TURBULENT TRANSPORT IN THE ATMOSPHERIC BOUNDARY LAYER WITH APPLICATION TO WIND FARM DYNAMICS

by

SCOTT B. WAGGY

B.S., Colorado School of Mines, 2007

M.S., University of Colorado at Boulder, 2009

A thesis submitted to the

Faculty of the Graduate School of the

University of Colorado in partial fulfillment

of the requirements for the degree of

Doctor of Philosophy

Department of Aerospace Engineering Sciences

2012

This thesis entitled:
Turbulent Transport in the Atmospheric Boundary Layer with Application to Wind Farm Dynamics
written by Scott B. Waggy
has been approved for the Department of Aerospace Engineering Sciences

Sedat Biringen

Peter Sullivan

Date

The final copy of this thesis has been examined by the signatories, and we find that both the content and the form meet acceptable presentation standards of scholarly work in the above mentioned discipline.

Waggy, Scott B. (Ph.D., Aerospace Engineering Sciences)

Turbulent Transport in the Atmospheric Boundary Layer with Application to Wind Farm Dynamics

Thesis directed by Prof. Sedat Biringen

With the recent push for renewable energy sources, wind energy has emerged as a candidate to replace some of the power produced by traditional fossil fuels. Recent studies, however, have indicated that wind farms may have a direct effect on local meteorology by transporting water vapor away from the Earth's surface. Such turbulent transport could result in an increased drying of soil, and, in turn, negatively affect the productivity of land in the wind farm's immediate vicinity.

This numerical study will analyze four scenarios with the goal of understanding turbulence transport in the wake of a turbine: the neutrally-stratified boundary layer with system rotation, the unstably-stratified atmospheric boundary layer, and wind turbine simulations of these previous two cases. For this work, the Ekman layer is used as an approximation of the atmospheric boundary layer and the governing equations are solved using a fully-parallelized direct numerical simulation (DNS). The in-depth studies of the neutrally and unstably-stratified boundary layers without introducing wind farm effects will act to provide a concrete background for the final study concerning turbulent transport due to turbine wakes.

Although neutral stratification rarely occurs in the atmospheric boundary layer, it is useful to study the turbulent Ekman layer under such conditions as it provides a limiting case when unstable or stable stratification are weak. In this work, a thorough analysis was completed including turbulent statistics, velocity and pressure autocorrelations, and a calculation of the full turbulent energy budget.

The unstably-stratified atmospheric boundary layer was studied under two levels of heating: moderate and vigorous. Under moderate stratification, both buoyancy and shearing contribute significantly to the turbulent dynamics. As the level of stratification increases, the role

of shearing is shown to diminish and is confined to the near-wall region only. A recent, multi-equation closure model, used to model the third and fourth velocity-temperature moments, performed well for the unstable cases. Optimal model coefficients found for the DNS data are shown to agree with atmospheric observations as well as LES data. Finally, the effects of top-down diffusion (entrainment-induced flux at the temperature inversion) and bottom-up diffusion (non-zero surface flux) were studied and improvements to correlation functions are suggested.

This thesis concludes by analyzing the neutral and unstable cases under the effects of wind turbine wakes. A unique means of converting a periodic simulation into a spatially evolving flow in the wake of a turbine is demonstrated; present results under neutral stratification are shown to agree with wind tunnel experiments under similar conditions. By introducing a scalar (humidity) into the flow field, the effect of a turbine wake on scalar transport in a wind farm is uncovered. The results show a clear drying effect under both neutral and unstable stratification given a wet surface. An investigation of energy and flux budgets gives guidance as to why such a phenomena occurs.

Observe the motion of the water surface, which resembles that of hair, that has two motions: one due to the weight of the shaft, the other to the shape of the curls; thus, water has eddying motions, one part of which is due to the principal current, the other to the random and reverse motion.

Leonardo da Vinci, 1510 ‡

‡ Translation provided by Piomelli et al. (2001).

ACKNOWLEDGEMENTS

First and foremost I would like to thank my advisor, Dr. Sedat Biringen, for the support he has shown over my five years of graduate studies. He provided consistent encouragement and motivation throughout the entire process. Moreover, this work would not have been possible without the vast amount of knowledge and experience I had readily available through him.

I would like to thank Dr. Peter Sullivan of NCAR for his help in brainstorming a worthwhile topic for my research. Thanks, also, for the engaging discussions as well as the constructive comments you have provided on written material. Thanks to the rest of my committee members for the support they have shown: Drs. Ken Jansen, Tom Manteuffel, Stuart Marlatt, and Kurt Maute.

Thanks to the Department of Aerospace Engineering Sciences for providing me financial support over the course of my graduate studies. Additional thanks to the NSF and NICS for providing computational resources with which I completed my research.

Some additional thanks are in order: to the fellow graduate students who understood when the post-work beer was not optional, thank you; to the great roommates I had over my college career, thank you; to the lifelong friends I made over the last five years, thank you; to my family who insisted we have a doctor in the family, thank you; to Casey, for all the encouragement and support, thank you.

Lastly, I want to thank my Creator for the opportunities He has laid out before me, the beauty with which He has filled my surroundings, and the people He has placed in my life.

CONTENTS

TABLES

Table

FIGURES

Figure

CHAPTER 1

INTRODUCTION

The case for studying turbulence has been made. The Nobel laureate physicist Richard Feynman is known for having described turbulence as "the most important unsolved problem in classical physics" (Feynman et al., 1963). Arguments can be made as to whether it truly is the "most important" or whether it is, in fact, "unsolved" (Nelkin, 1992). Regardless, Feynman clearly is highlighting the fundamental importance of the subject. With that in mind, motivating the study of turbulence is simple since turbulence happens all around us. In fact, one can argue that it is more difficult to escape turbulence than it is to create it.

Turbulent fluid flows – or as Osborne Reynolds referred to it, "sinuous" (Reynolds, 1883) – are apparent in every aspect of our daily lives. In nature, turbulent rivers carve canyons through mountains while winds and storms in the atmosphere impact how and where humans can populate. Instead of simply falling victim to the effects of turbulence, humans have used the properties of turbulent fluid flows to benefit societies. Although some applications of turbulence are simply for our enjoyment (e.g. dimples on a golf ball), many uses are necessary for us to live in the manner we have grown accustomed: the cooling of electronics via fans, promoting turbulence to increase combustion efficiency, improving lift/drag characteristics of flow of airplane wings. Since turbulence is coupled to many of the activities in our daily lives, the ability to control such a powerful force of nature would unveil countless advances in science and engineering.

The study of turbulence is the study of scales. The cascade of energy from large to small

scales is a well known turbulent phenomenon. As the different scales of turbulence are connected, large eddies tend to energize smaller eddies. These small scales then act to energize even smaller scales. This process continues until a limit is reached, at which, turbulent energy is destroyed and converted into heat. The length, velocity, and time scales that this occurs at are referred to as the Kolmogorov scales (see §2.6). Kolmogorov (1991) demonstrated that these scales are uniquely determined by the viscosity and energy dissipation rate. Although it seems that turbulence has a known 'smallest scale,' the large scales of turbulence appear to be limitless. In channel flow, the largest scales tend to be on the order of the channel height (Kim et al., 1987); in atmospheric turbulence, the eddies can reach many kilometers in size (Obukhov, 1962). These are dwarfed when one considers turbulent characteristics occurring in astrophysics problems (Brandenburg and Nordlund, 2011). Given the broad spectrum of ways that turbulence manifests itself, it is no surprise that Dr. Feynman held so much regard for this problem.

1.1 Wind Energy and the Atmospheric Boundary Layer

The focus of this dissertation will concern the atmospheric boundary layer (ABL) and the manner in which wind turbine wakes affect atmospheric turbulence. The ABL is a constantly evolving system, driven by many processes including (but not limited to):

- temporal variation due to surface heating during the day (Kaimal and Finnigan, 1994, pp. 7–9) and surface cooling at night (Hunt et al., 1996).
- surface topography (Kaimal and Finnigan, 1994, pp. 155-206).
- vegetation coverage and surface roughness (Finnigan and Belcher, 2004).
- urban effects caused by localized heating (Oke, 1982).
- a wide range of scales due to the inherently high Reynolds number of the turbulent field (Atta and Wyngaard, 1975).

- the Coriolis effect associated with rotation of the Earth.

Combining the above influences results in a system that varies depending on the time of day, time of year, surface geometry, surface foliage, proximity to urban centers, and climate of the region. Needless to say, no explanation is required as to why weather forecasting is an inexact science.

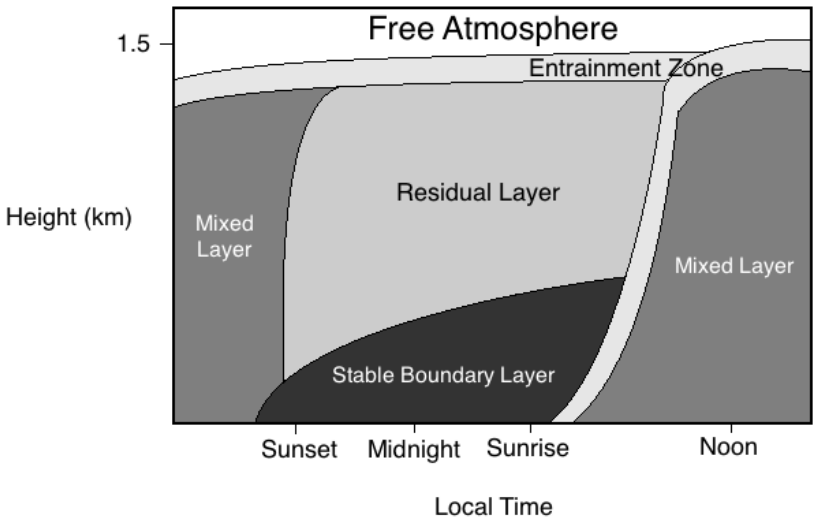

Figure 1.1: Structure of the boundary layer. Reproduction of figure from Stull (1988).

Considering an idealized scenario, temporal variations of the ABL are indicated in the cartoon presented in Fig. 1.1. The daytime boundary layer is characterized by a tall mixed layer that is capped by a temperature inversion and an entrainment zone. When the sun sets, radiative heating of the Earth's surface is eliminated resulting in a cooling effect. As a result, a boundary layer under stable thermal stratification grows during the early evening until the sun rises the following day. Above the stable boundary layer, remnants of the mixed layer persist in the residual layer.

While a great deal of the research that is presented in this thesis deals with characterizing and parameterizing the turbulence found in the atmosphere, the second focus of this investigation concerns the effect of wind turbines on atmospheric turbulence. So as to present wind energy as an effective alternative to typical fossil fuels, a great deal of research is currently being pursued

by a number of researchers. Wind energy possesses two key traits which make it so appealing as an alternative energy source:

(1) Renewability – The source of energy that a turbine utilizes (the key to its success) is wind. Unless the wind ceases to blow, wind farms will continue to have an endless supply of energy.

(2) Low environmental impact – A major concern of fossil fuels and nuclear energy are the waste products produced as a consequence of generating power. For wind energy, these bi-products are nearly eliminated. Thus, it is believed that wind turbines are much less invasive on their surrounding environment.

This work will explore how turbulence is modified by a wind farm. As the goal of a wind turbine is to convert energy in the fluid into energy for consumer consumption, it is plain to see that the flow will be modified in some manner as fluid passes between the turbine blades. Because of the impact of turbines on the velocity field, recent studies have indicated that wind farms may affect the environment around them in both a local (Calaf et al., 2011, Roy and Pacala, 2004, Zhou et al., 2012) and, in the case of large-scale wind farm energy production, global sense (Keith et al., 2004, Wang and Prinn, 2010).

Wind farms are not suitable for all locations. In order to have an effective source of energy for the turbine to draw from, the wind must be relatively consistent. Simply put: power is only generated if the wind is strong enough to turn the turbine. Thus, it is optimal to employ wind technologies in areas of consistent high-speed wind. As the kinetic energy in a flow goes as the velocity squared, the most readily available wind energy coincides with some of the least populated states (Kansas, Nebraska, North and South Dakota, Montana). This is beneficial in the sense that there is plenty of space to install large wind farms; however, it is vital that the effect of wind turbines on the surrounding environment is understood before large scale implementations are integrated.

The primary role of many of these high-wind regions is agricultural. A significant amount of the nations food (corn, wheat, etc.) is produced in the band of states from upper Texas through Michigan. Two observations can be made: (1) wind farms are much easier to install is less populated rural areas than dense metropolitans, (2) any secondary impacts from the wind turbines on the environment may impact crop production in the wind farms immediate vicinity. It has been suggested that wind turbines may adversely affect farmland in unforeseen ways.

Calaf et al. (2011) demonstrates an increase in scalar transport when an infinite wind turbine is simulated. If humidity is transported away from the Earth's surface in the vicinity of a wind farm, this could result in a drying of the soil as water is lifted and transported away from the wind farm. For large-scale wind farm applications, the implications of an adverse effect on water content in the soil could have major repercussions since much of the land that is ideal for wind farming is used for agricultural purposes.

Prior research concerning the different states of the ABL and wind turbine dynamics are outlined in the following sections. These summaries represent only a small selection of the studies performed on each subject.

1.1.1 The Unstable Boundary Layer

The mixed layer formed during the daytime hours is a consequence of unstable stratification (i.e. surface heating is applied to an overlying turbulent field) and an elevated temperature inversion which caps the unstable regime. Under weak unstable stratification, it is expected that the flow would exhibit organized roll vortices (see Figs. 1 and 2 in Etling and Brown, 1993). Coleman and Ferziger (1994) note that a vigorously heated large-eddy simulation (LES) of the convective boundary layer exhibits more isotropy than the neutrally stratified flow due to an increase in vertical kinetic energy. As the strength of stratification was moderated (reduced), the field began to demonstrate the roll structures. A comparable low Reynolds number direct numerical simulation (DNS) study showed that rotation does not affect the large convective eddies caused by unstable

stratification (Coleman and Ferziger, 1996).

The review by Etling and Brown (1993) discusses the development of rolls using observational, theoretical as well as numerical studies. Via two-dimensional simulations of atmospheric turbulence, Mason and Sykes (1980, 1982) show that rolls should be capable of developing as a consequence of friction alone. Etling and Brown (1993) note, however, that the lack of vortices in numerical simulations suggests that either 2D stability theory is not applicable to the three dimensional rotating boundary layer, or that the instability which causes the rolls is weak. The interesting study of Le et al. (2000) studied the three-dimensional boundary layer by impulsively moving a wall on a fully developed 2D flow. They find that the imposed three-dimensionality tends to break up the symmetry and alignment of vortical structures near the wall. Hence, the three-dimensional nature of turbulence in the ABL results in an added level of complexity in comparison with 2D flows.

1.1.2 The Stable Boundary Layer

Turbulent dynamics during the daytime and nighttime hours are fundamentally different. Stably stratified flows tend to suppress the production of turbulence and, in strong stratification, relaminarize the flow. Stable stratification is enforced by a coupling between the temperature inversion at the top of the boundary layer as well as surface cooling. In specific instances, the resulting nocturnal boundary layer (NBL) displays unique characteristics in which a low-level jet of high energy fluid is formed (Poulos et al., 2002). The work of Banta (2008) characterizes different regimes of the stable ABL based on the local Richardson number, a function of the strength of stratification in hopes of better understanding the mechanism which promotes the generation of the jet. Small-scale turbulence was studied by Frehlich et al. (2004) to compare turbulence in the nocturnal jet with Kolmogorov's theory. The results demonstrate that the inertial region scales with fully developed turbulence, specifically, the spectrum maintains a $-5/3$ slope.

A DNS of an externally stratified flows was performed by Coleman et al. (1992) and demon-

strated that the most significant effects of buoyancy were evident in the outer regions of the flows, where shear is weakest. They also showed that the stratification tends to decrease the kinetic energy and Reynolds stress near the wall and effectively decreases the height of the boundary layer, consequently increasing the shear. The energy budgets computed for the stably stratified case by Marlatt (1994) correlate well with the neutrally stratified case in the near-wall region. However, at the height of the inversion kinetic energy is destroyed by an additional buoyancy term.

Taylor and Sarkar (2008) addressed the externally stratified Ekman layer using both DNS and LES. Their results agreed with Coleman et al. (1992) and found a noticeable increase in shear when stratification is applied. The comparison made by Taylor and Sarkar (2008) showed differences between the two methods, specifically, that the unresolved scales of the LES that were not represented in the sub-grid model were responsible for entrainment of fluid into the boundary layer. This results from the inadequate resolution required to capture the unresolved turbulent heat flux, thus demanding a finer mesh resolution. Further LES work for the stably stratified Ekman layer include the work of Kosović and Curry (2000) and the comparison of models made by Beare et al. (2006).

1.1.3 Neutral Ekman Layer

Neutral stratification refers to the scenario where no buoyant forcing exists in the flow field. In such a case, turbulence is generated only through shearing and destroyed through dissipation. Typically, neutral stability is more of a transitional state as the atmosphere passes from unstable to stable (or vice versa) stratification. However, studies concerning the neutrally-stratified ABL are important since these results supply a limiting case as buoyant forces become very weak.

An approximation of the ABL under neutral stratification is typically approximated using the turbulent Ekman layer. The effect of the Ekman layer was first realized by the explorer and scientist Fridtjob Nansen while on a cruise heading north. He noticed that ice drifted not with the wind direction, but rather at a systematic angle to the downwind direction (e.g. see Fig. 2.1).

Upon studying the problem, his student, Vagn Walfrid Ekman, later published his results detailing the dynamics of the well known Ekman layer (Ekman, 1905). His work develops the solution of the horizontally homogeneous, laminar oceanic flow without thermal effects. The development of the laminar Ekman profile is discussed further in §2.5. The Ekman spiral was first used as an approximation of the ABL by Akerblom (1908). Since then, the Ekman approximation has been used widely for oceanic and atmospheric simulations.

Early DNS of the turbulent Ekman layer was completed by Coleman et al. (1990). This work concerning the neutrally stratified ABL used a low Reynolds number ($\mathrm{Re} = 400$) at varying latitudes. The results demonstrated a dependence of shear angle on the specified latitude while the surface friction velocity remained relatively constant. Marlatt (1994) and Marlatt et al. (2010) furthered this work by computing the turbulent energy budgets for the neutrally stratified field at the same Reynolds number ($\mathrm{Re} = 400$). A conclusion of this work was that the inter-component energy transfer between the horizontal velocity components is not negligible for rotating boundary layers. Thus, closure models which neglect the streamwise-spanwise covariance term might be erroneous.

Due to the lack of an inertial subrange at low Reynolds numbers, recent work has focused on increasing the Reynolds number to better approximate atmospheric dynamics. Coleman (1999) increased the Reynolds number of his study to $\mathrm{Re} = 1000$. An attempt was made to map the friction velocity and shear angle using the classic similarity theory of Csanady (1967). Although the surface friction velocity mapped well, the shear angle demonstrated a Reynolds number dependence and required a modification of similarity theory to better predict results. This indicates that the total velocity gradient at the wall (and consequently, the friction velocity) shows little low Reynolds number effects. However, the contribution from each velocity component does demonstrate such a dependence as is evidenced by the shear angle discrepancy.

The study by Miyashita et al. (2006) further increased the Reynolds number to $\mathrm{Re} = 1393$. This work confirms an increase in the log-law region of the flow with increased Reynolds number

(as expected) as well as a Reynolds number dependence of both diffusion and production terms in energy budgets. They speculate that the sweep event (high speed fluid moving towards wall) is more dominant in the near wall flow for the turbulent Ekman layer when compared with non-rotating flow fields.

Laboratory studies of the neutral Ekman layer can be performed using turn-table setups. Such work includes transition studies (Caldwell and Atta, 1970) as well as research concerning fully developed turbulence (Caldwell et al., 1972).

1.1.4 Wind Turbine Fluid Dynamics

Wind turbines have a pronounced effect on ABL dynamics. The most notable difference is evident in the velocity deficit in the wake of the turbine (Vermeer et al., 2003). As kinetic energy is extracted from the flow, it is expected that the velocity is decreased. This deficit is not maintained, however, as high energy fluid is transported back into the wake. This recovery is of particular interest as it determines the efficiency of downstream turbines. If the flow is not fully recovered, subsequent turbines have a lower energy flow to work with. A second characteristic of the turbine wake is the helical vortex tubes shed from the tips of the turbine blades (Hand et al., 2001, Vermeer et al., 2003).

A common simulation technique for wind-turbine arrays uses the drag-disk model. This model penalizes the velocity as it passes through the disk in an attempt to recreate the resulting velocity deficit found in the wake of a turbine. The size of the disk is determined by the radius of the turbine blades and the penalty is weighted in such a manner to represent actual turbine effects. The recent work by Calaf et al. (2010) employs such a method via LES for an infinite wind turbine array. In such a case, the flow must recover before each subsequent turbine. For the flow in steady conditions, Calaf et al. (2010) find that the total power extracted by the turbines is approximately 90% of the vertically transported kinetic energy. Moreover, they find that the array has a direct impact on the surface friction velocity.

The study by Keith et al. (2004) focuses on the effect large-scale wind power would have on the global climate by altering the surface roughness over large land masses. This method essentially imposes a drag over the land and, for large arrays, was found to impact climate patterns. Wang and Prinn (2010) attribute the increase in temperature to a reduction in the horizontal transport of heat caused by the increased drag attributed to the wind turbines (see also Roy and Pacala, 2004). The LES by Porté-Agel et al. (2010) simulated a single turbine and were able to reproduce the mean velocity deficit and tip vortices with good agreement to wind-tunnel experiments. This work also notices an increased surface flux for scalar transport.

A vast amount of experimental research has been conducted concerning wind turbine aerodynamics. Maalouf et al. (2009) studied tip vortices that were shed at the ends of rotor blades. Some of these results will be used in modeling different aspects of the turbine wake in this work. Additional experimental research is discussed in the review by Vermeer et al. (2003).

1.2 Problem Statement

The goal of this work is to study turbulent transport in the atmospheric boundary layer under varying thermal conditions. Using the turbulent Ekman layer as an approximation of the ABL, a direct simulation of neutrally and unstably-stratified boundary layers will be evaluated. Three baseline test cases will be performed to parameterize the flow field:

- Turbulent Ekman layer under neutral stratification.
- Unstably-stratified Ekman layer with moderate heating.
- Unstably-stratified Ekman layer with vigorous heating.

The above three cases will give evidence of the role buoyancy plays in atmospheric dynamics. Furthermore, the above cases will be used as a baseline for addressing the question of how humidity is transported in the wake of a wind farm. A unique means of introducing a wake into the flow

field will be presented which allows scalar transport to be monitored closely. It is hypothesized that, given a constant humidity density at the wall, humidity is transported upwards when the freestream concentration of humidity is less than that of the surface. Furthermore, it is believed that this is caused by an increase in the turbulent transport of scalars. When a turbine extracts energy from the velocity field, the resulting velocity wake will produce higher levels of turbulence given the sharper mean velocity gradients. As the vertical component of kinetic energy is excited, vertical transport is increased such that a drying effect should be seen near the wall.

In order to test the scenarios presented above, a DNS was utilized for this research. The decision was made to perform DNS (as opposed to LES) so that turbulence could be monitored down to the wall. Since surface flux is of vital importance for this study (i.e. what is humidity flux at the wall), the DNS allows the simulation of turbulence over a smooth surface to be performed such that turbulent and viscous effects are both accounted for. No unresolved scales require closures. Although the use of DNS relegates this study to only modest Reynolds numbers, results (as it will be shown later) demonstrate a clear connection between the simulations completed in conjunction with this research and other high Reynolds number studies using LES and Reynolds-averaged models.

The DNS of the turbulent Ekman layer with thermal variation includes the following characteristics:

- Momentum, energy, and scalar transport equations to solve for the velocity, temperature, and humidity respectively.
- Sufficient resolution of all relevant scales of motion.
- A means of initializing a turbine wake into a fully developed turbulent flow.

To determine its effect on scalar transport, this study will simplify the complex dynamics associated with flow through a wind turbine. Rather than modeling the complexities associated with the turbine aerodynamics, the wake is simplified such that only the velocity deficit (a consequence

of the turbine removing energy from the velocity field) and a rotational velocity component (imparted onto the flow by the turbine blades) are considered.

Specific humidity will be introduced as the scalar of interest. As opposed to a passive scalar which has no influence on the flow dynamics (i.e. neutral stratification), this scalar will be also introduced as an active scalar such that a change in the specific humidity at some point will influence the potential temperature at that point. Addressing the influence of the turbine wake on the scalar transport will be accomplished by an array of analyses: downstream evolution of turbulent stresses, turbulent energy budgets (inter-component energy transfer), turbulent flux budgets, and closure model evaluations.

1.3 Outline of Dissertation

A brief overview of the research completed is given below:

- Chapter 2 – Starting from first principles, the governing equations that describe the physics associated with the problem are developed. These governing principles include conservation of momentum, mass, and thermal energy, as well as a transport equation for scalars introduced into the field (e.g. humidity). The equations are then nondimensionalized by relevant scales. The chapter concludes by presenting the laminar solution of the Ekman layer obtained by Ekman (1905) and giving a brief overview of some of the turbulent scales that are used throughout this work.

- Chapter 3 – This chapter consists of two parts. First, the numerical method employed to directly solve the governing equations presented in Chap. 2 is outlined. A semi-implicit time integration scheme (second-order accuracy in time) is used in tandem with finite-difference spatial operators (fourth-order accuracy in space). Conservation of mass is imposed by a pressure correction step. The second half of the chapter is devoted to outlining the parallelization scheme used in the development of the code. A case used to validate

the code is presented, and code performance (scalability) is discussed.

- Chapter 4 – The turbulent Ekman layer under neutral stratification is simulated. Results are analyzed by computing typical turbulent statistics (Reynolds stresses, high-order moments, etc.), using autocorrelations to determine the characteristic shape of turbulent structures, and presenting energy budgets for the various Reynolds stresses. Finally, the popular $k - \varepsilon$ closure model is analyzed to determine its applicability in flows where system rotation is evident.

- Chapter 5 – Two unstably stratified simulations are presented: modest and vigorous heating. Results show a clear deviation from the neutral case where no buoyant forcing occurs through the calculation of kinetic energy budgets. Comparisons are made between the current data and other relevant atmospheric studies. A model for the third and fourth-order vertical velocity-temperature moments is analyzed to demonstrate the sensitivity of model constants. It is found that the coefficients are relatively independent of both the strength of stratification and the Reynolds number of the field. The concept of top-down and bottom-up diffusion in the convective boundary layer (Wyngaard and Brost, 1984) is addressed with the remainder of the chapter. Specifically, data are used to determine how gradient functions and scalar variances change when a smooth surface (rather than a rough wall) is present.

- Chapter 6 – The means by which turbine wakes will be analyzed is presented at the outset of this chapter. By directly imposing a wake onto the mean velocity field, it is possible to analyze turbulent characteristics of a spatially evolving wake. Turbulent statistics under neutral and unstable stratification are compared with wind tunnel results to assess the ability of the method for studying wind turbine wake characteristics. Once agreement has been shown, the effect of the turbine on the transport of humidity is discussed and analyzed. The chapter concludes by revisiting a few of the turbulence closure models introduced earlier.

- Chapter 7 – An overview of the work is presented. Two sections are devoted to highlighting significant findings of the research, as well as recommendations of future research that build upon the work completed here.

CHAPTER 2

GOVERNING EQUATIONS

The Ekman layer describes a system in which Coriolis forces, the pressure gradient, and friction forces are all in balance. First proposed by Ekman (1905) to describe the drift of sea-ice in ocean currents, the turbulent Ekman layer is commonly used as a model (Coleman et al., 1990) for the atmospheric boundary layer (ABL). The unique dynamics are triggered by the inclusion of system rotation in the conservation of momentum equation. In their basic form, the governing equations for mass, momentum, and energy conservation with system rotation are

$$\frac{\partial \rho}{\partial t} + \nabla \cdot (\rho \mathbf{u}) = 0 \tag{2.0.1a}$$

$$\rho \left(\frac{\partial \mathbf{u}}{\partial t} + \mathbf{u} \cdot \nabla \mathbf{u} + 2\boldsymbol{\Omega} \times \mathbf{u} - \Omega^2 \mathbf{R} \right) = -\nabla \hat{p} + \mu \nabla^2 \mathbf{u} + \rho \mathbf{g} \tag{2.0.1b}$$

$$\rho \frac{\partial \left(c_p T^* \right)}{\partial t} + \rho \mathbf{u} \cdot \nabla \left(c_p T^* \right) = k \nabla^2 T^* \tag{2.0.1c}$$

where ρ is the fluid density, t is time, $\mathbf{u}$ is the velocity vector, $\boldsymbol{\Omega}$ is the rotation vector, $\mathbf{R}$ is the vector perpendicular to the axis of rotation, $\hat{p}$ is the pressure, μ is the dynamic viscosity of the fluid, and $\mathbf{g}$ is the gravitational vector. For the energy equation, T^* is the temperature of the fluid, c_p is the specific heat at constant pressure, and k is the molecular conductivity. The wall normal direction – the $\hat{k}$ direction – corresponds to the z (or x_3) spatial coordinate and the w (or u_3) velocity component. The horizontal coordinates are defined similarly such that the right-hand-rule is obeyed.

2.1 Simplifications and Approximations

The complexity and number of variables associated with Eqs. 2.0.1 are reduced by introducing several suitable approximations. Equation 2.0.1b demonstrates the effect of both Coriolis acceleration ($2\boldsymbol{\Omega} \times \mathbf{u}$) and centrifugal acceleration ($-\Omega^2\mathbf{R}$). For this work, the effect of centrifugal acceleration will be incorporated into the pressure gradient such that a new pressure gradient is defined

$$-\frac{1}{\rho}\nabla\hat{p} + \Omega^2\mathbf{R} = -\frac{1}{\rho}\nabla\tilde{p} \tag{2.1.1}$$

where $\tilde{p}$ now accounts for any centrifugal effects. Additionally, the rotation vector will be confined to align with the vertical direction. Making such an assumption allows the rotation rate $\boldsymbol{\Omega}$ to be written as $\boldsymbol{\Omega} = \Omega_z\hat{k} = \Omega_0\hat{k}$. Coleman et al. (1990) tested the low Reynolds number Ekman layer with both vertical and horizontal rotational components. From their work they demonstrated that a positive horizontal component of $\boldsymbol{\Omega}$ acts to increase the difference between the vertical and streamwise turbulent kinetic energy resulting in an increase in production of turbulent energy via the vertical turbulent shear stresses. The converse is true for a negative horizontal rotation. By confining the rotation vector to the wall-normal direction, the effect on the results by the change of latitude is removed at the cost of a decrease in accuracy concerning the levels of turbulence under specific rotational conditions.

For this work, it is assumed that gravity will only act in the negative vertical direction: $\mathbf{g} = -g\hat{k}$. This is a good assumption for this work; deviation from the alignment of the gravity vector and wall-normal direction is confined to flow over topography and small variations due to the slight spheroid shape of the Earth.

Finally, it is assumed that the flow is incompressible ($\rho = \rho_0 =$ constant). The Boussinesq approximation is introduced to provide thermal effects to the momentum equation. Under the Boussinesq approximation it is assumed that small density changes that occur due to changes in temperature only affect the buoyancy term in the vertical momentum equation. Concerning

humidity effects, the change in density that results from water vapor will be accounted for by adjusting the potential temperature to account for added thermal energy. Using a reference density ρ_0 which corresponds to a temperature T_0, the Boussinesq approximation is given as

$$\rho = \rho_0 \left[1 - \alpha \left(T^* - T_0\right)\right] \tag{2.1.2}$$

where α is the coefficient of thermal expansion for the fluid. Therefore, the term $\rho\mathbf{g}$ in Eq. 2.0.1b can be written $\rho\mathbf{g} = \rho_0 \left[1 - \alpha \left(T^* - T_0\right)\right] \mathbf{g}$. Assuming that air behaves as an ideal gas, $\alpha = 1/T_0$ completing the Boussinesq approximation:

$$\rho\mathbf{g} = \rho_0\mathbf{g}\left[1 - \frac{\left(T^* - T_0\right)}{T_0}\right] \tag{2.1.3}$$

Combining the simplifications given above with Eqs. 2.0.1 yields the following simplified governing equations:

$$\nabla \cdot \mathbf{u} = 0 \tag{2.1.4a}$$

$$\frac{\partial \mathbf{u}}{\partial t} + \mathbf{u} \cdot \nabla \mathbf{u} + 2\Omega\hat{k} \times \mathbf{u} = -\frac{1}{\rho_0}\nabla p + \nu\nabla^2\mathbf{u} + g\frac{\left(T^* - T_0\right)}{T_0}\hat{k} \tag{2.1.4b}$$

$$\frac{\partial T^*}{\partial t} + \mathbf{u} \cdot \nabla T^* = \kappa\nabla^2 T^* \tag{2.1.4c}$$

In the above energy equation, ν is the kinematic viscosity and κ is the coefficient of thermal diffusion where $\kappa = k/c_p\rho$. The variable ∇p is defined such that it accounts for the pressure gradient, the centrifugal acceleration, and the constant term in the Boussinesq approximation:

$$\nabla p = \nabla\hat{p} + \Omega^2\mathbf{R} + \rho_0 g\hat{k}$$

As will be discussed in §2.3, the temperature variables T^* and T_0 represent potential temperatures. A change in T^* will necessarily result in buoyant forcing.

2.2 Nondimensionalization

Nondimensionalization is accomplished by defining characteristic velocity, length, temperature, and density scales. As this is an incompressible simulation, the density ρ_0 is a logical reference parameter. Similarly, the temperature T_0 will be a sufficient temperature scale.

In choosing a reference velocity it is customary to scale the problem on the velocity at the outer edge of the boundary layer. For the Ekman problem, this farfield velocity is given by the geostrophic velocity U_g. As will be demonstrated in §2.5, a unique feature of the Ekman layer is that the geostrophic velocity is perpendicular to the pressure gradient because system rotation is included (Holton, 2004).

A proper length scale for the turbulent Ekman layer is the Ekman depth δ_E. This characteristic length is a function of the fluid properties (ν) as well as the rate of rotation (Ω_0). The Ekman depth is defined as

$$\delta_E = \sqrt{\frac{\nu}{\Omega_0}} \tag{2.2.1}$$

Typical Ekman depths found in the atmosphere are approximately 0.45 m: $\Omega_0 = 2\pi/1\,\text{day} \approx 7.3 \times 10^{-5}\,\text{s}^{-1}$ and $\nu \approx 1.5 \times 10^{-5}\,\text{m}^2/\text{s}$ at 20 °C and 1 atm (Kundu and Cohen, 2004).

The dimensionless variables are given below. Starred terms correspond to physical quantities.

$$x = \frac{x^*}{\delta_E} \tag{2.2.2a}$$

$$\mathbf{u} = \frac{\mathbf{u}^*}{U_g} \tag{2.2.2b}$$

$$\Omega = \frac{\Omega^*}{\Omega_0} \tag{2.2.2c}$$

$$t = \frac{t^* U_g}{\delta_E} \tag{2.2.2d}$$

$$p = \frac{p^*}{\rho_0 U_g^2} \tag{2.2.2e}$$

$$\tilde{\theta} = \frac{T^* - T_0}{T_0} \tag{2.2.2f}$$

Substitution of these dimensionless variables into Eq. 2.1.4 yields the nondimensionalized gov-

erning equations for the turbulent Ekman layer.

$$\nabla \cdot \mathbf{u} = 0 \tag{2.2.3a}$$

$$\frac{\partial \mathbf{u}}{\partial t} + \mathbf{u} \cdot \nabla \mathbf{u} + \frac{1}{\mathrm{Ro}} \hat{k} \times \mathbf{u} = -\nabla p + \frac{1}{\mathrm{Re}} \nabla^2 \mathbf{u} + \theta \hat{k} \tag{2.2.3b}$$

$$\frac{\partial \tilde{\theta}}{\partial t} + \mathbf{u} \cdot \nabla \tilde{\theta} = \frac{1}{\mathrm{Pr\,Re}} \nabla^2 \tilde{\theta} \tag{2.2.3c}$$

Note that a new dimensionless temperature θ is defined by

$$\theta = \gamma_\theta \tilde{\theta} \tag{2.2.4}$$

The dimensionless factor $\gamma_\theta = g\delta_E / U_g^2$ that appears in the vertical momentum equation stipulates the strength of buoyant forces relative to inertial forces. However, dependence upon this specific dimensionless (and constant) quantity is easily removed. Multiplying Eq. 2.2.3c by γ_θ simply scales the entire expression by some constant. The resulting energy equation can be solved for θ, a newly defined dimensionless temperature (or buoyancy variable):

$$\frac{\partial \theta}{\partial t} + \mathbf{u} \cdot \nabla \theta = \frac{1}{\mathrm{Pr\,Re}} \nabla^2 \theta \tag{2.2.5}$$

In Eq. 2.2.3, Ro is the Rossby number, Re is the Reynolds number, and Pr is the Prandtl number. These dimensionless numbers are defined as follows:

$$\mathrm{Re} = \frac{U_g \delta_E}{\nu} \tag{2.2.6a}$$

$$\mathrm{Ro} = \frac{U_g}{2\Omega_0 \delta_E} \tag{2.2.6b}$$

$$\mathrm{Pr} = \frac{\nu}{\kappa} \tag{2.2.6c}$$

The Reynolds number is the ratio of inertial forces to viscous forces. A low Reynolds number flow is dominated by the diffusion term while a high Re confines viscous effects to very small scales.

The Rossby number defines the ratio of inertial to Coriolis forces. For a non-rotating flow, $\mathrm{Ro} = \infty$. Conversely, a case in which the effects of rotation dominate will occur as $\mathrm{Ro} \to 0$. An alternative means of writing the Rossby number is

$$\mathrm{Ro} = \frac{U_g}{f \delta_E}$$

or

$$\mathrm{Ro} = \frac{U_g \delta_E}{2\nu}$$

where f is the Coriolis parameter. Here it is clear that $\mathrm{Ro} = \mathrm{Re}/2$. The Coriolis parameter f is commonly used in Ekman studies. The formal definition of f is $f = 2\Omega_0 \sin\phi$, where ϕ gives the latitude. As stated earlier, rotation is confined to the x/y plane. Consequently, the $\sin\phi$ in the definition of f is irrelevant. For this work, f and $2\Omega_0$ will be used interchangeably.

The Prandtl number (Pr) is the ratio of viscous to thermal diffusivity. This parameter is fluid specific and temperature dependent. For small temperature changes, however, this ratio can be treated as a constant (Melling et al., 1997). For dry air, $\mathrm{Pr} \approx 0.7$.

2.3 Scalar Transport Equation for Humidity

The scalar transport equation for a quantity c in a fluid flow is given by

$$\frac{\partial \rho_c}{\partial t} + \mathbf{u} \cdot \nabla \rho_c = D_c \nabla^2 \rho_c \tag{2.3.1}$$

where ρ_c and D_c are the density and molecular diffusivity of the scalar respectively. A relative density with respect to the ambient fluid is defined as

$$q_c = \frac{\rho_c}{\rho} \tag{2.3.2}$$

where ρ is the density of the surrounding fluid. For this work, the ambient fluid is incompressible and taken to be dry air ($q_c = \rho_c/\rho_0$). Thus, q_c is a function of ρ_c only. Substituting Eq. 2.3.2 into Eq. 2.3.1 and simplifying yields

$$\frac{\partial q_c}{\partial t} + \mathbf{u} \cdot \nabla q_c = D_c \nabla^2 q_c$$

This work assumes that the transported quantity of scalar c is the specific humdity q_w. Nondimensionalizing by the parameters given in Eq. 2.2.2 gives

$$\frac{\partial q_w}{\partial t} + \mathbf{u} \cdot \nabla q_w = \frac{1}{\mathrm{Re\,Sc}} \nabla^2 q_w \tag{2.3.3}$$

where $\mathrm{Sc} = \nu/D_w$ gives the Schmidt number, the ratio of momentum to mass diffusion. This completely defines the transport equation for the specific humidity of water vapor. For standard temperature and pressure, $D_w = 0.217$ cm^2/s for water vapor in dry air (Massman, 1998). The corresponding Schmidt number is $\mathrm{Sc} = 0.7336$. Although D_w is a function of temperature and pressure, Massman (1998) demonstrated that the changes in diffusivity are negligible for small variation in T or p.

While Eq. 2.3.3 sufficiently describes water vapor transport, without a coupling between this relationship and one of the conservation equations in Eq. 2.2.3, the transport would be passive; the specific humidity will not influence the velocity field in any manner. Stated another way, no buoyancy effects due to humidity would exist.

A commonly used coupling between the specific humidity and temperature, as discussed by Khandekar (1977), is given by

$$T_v = T^*(1 + 0.61 q_w) \tag{2.3.4}$$

where T^* is a potential temperature and T_v is the corresponding virtual potential temperature. The potential temperature T^* defines the temperature a parcel of dry air would have if adiabatically brought to a reference pressure. As opposed to the thermodynamic temperature, changes in the potential temperature will necessarily result in buoyant forcing. Similar to the stably stratified simulation by Coleman et al. (1992), T^* and T_0 in Eq. 2.2.2f represent potential temperatures. The definition of the dimensionless temperature $\tilde{\theta}$ in Eq. 2.2.2f is in terms of these potential temperatures. Therefore, $\tilde{\theta}$ represents a dimensionless potential temperature.

The virtual potential temperature accounts for water vapor content in air by modifying the dry air temperature to compensate for the added thermal energy of the water vapor. Specifically, the virtual potential temperature T_v is the temperature of dry air if its pressure and density were equal to those of a parcel of moist air. This allows the dry air temperature to reflect the heat content of the water vapor. Equation 2.3.4 can be linearized about a reference temperature (T_0) and specific

humidity (q_0):

$$T_v\left(T^*, q_w\right) = T_v\left(T_0, q_0\right) + \left(T^* - T_0\right)\left.\frac{\partial T_v\left(T^*, q_w\right)}{\partial T^*}\right|_{T_0,q_0} + \left(q_w - q_0\right)\left.\frac{\partial T_v\left(T^*, q_w\right)}{\partial q_w}\right|_{T_0,q_0}$$

$$T_v\left(T^*, q_w\right) = T_0\left(1 + 0.61q_0\right) + \left(T^* - T_0\right)\left(1 + 0.61q_0\right) + \left(q_w - q_0\right)\left(0.61T_0\right)$$

$$T_v\left(T^*, q_w\right) = T^* + 0.61T_0q_w + 0.61q_0T^* - 0.61T_0q_0$$

Defining

$$\tilde{\theta}_v\left(T^*, q_w\right) = \frac{T_v\left(T^*, q_w\right) - T_0}{T_0}$$

and substituting yields

$$\tilde{\theta}_v\left(T^*, q_w\right) = \frac{T^* - T_0}{T_0} + 0.61\left(q_w - q_0\right) + 0.61q_0\frac{T^*}{T_0}$$

Assuming small values of q_w and setting $q_0 = 0$,

$$\tilde{\theta}_v\left(T^*, q_w\right) = \frac{T^* - T_0}{T_0} + 0.61q_w$$

or

$$\tilde{\theta}_v = \tilde{\theta} + 0.61q_w \tag{2.3.6}$$

Multiplying Eq. 2.3.6 by the constant γ_θ gives

$$\theta_v = \theta + 0.61\gamma_\theta q_w \tag{2.3.7}$$

Like the energy equation, γ_θ is easily incorporated into the scalar transport equation (Eq. 2.3.3) by solving for the new variable $(\gamma_\theta q_w)$. Recall from earlier the Boussinesq approximation:

$$\rho\mathbf{g} = \rho_0\mathbf{g}\left[1 - \frac{\left(T^* - T_0\right)}{T_0}\right]$$

Substitution of $\left(T_v - T_0\right)/T_0$ for $\left(T^* - T_0\right)/T_0$ ensures that buoyant forcing will only occur if the virtual potential temperature is higher than the ambient virtual potential temperature (note that the ambient virtual potential temperature is equal to the reference temperature T_0 since $q_0 = 0$). The Boussinesq approximation can then be rewritten as:

$$\rho\mathbf{g} = \rho_0\mathbf{g}\left[1 - \frac{\left(T_v - T_0\right)}{T_0}\right] \tag{2.3.8}$$

Notice that this assumes the coefficient of thermal expansion does not change due to humidity. Substitution of Eq. 2.3.8 into the Navier-Stokes and nondimensionalizing yields a new momentum equation which accounts for changes in specific humidity.

$$\frac{\partial \mathbf{u}}{\partial t} + \mathbf{u} \cdot \nabla \mathbf{u} + \frac{1}{\mathrm{Ro}} \hat{k} \times \mathbf{u} = -\nabla p + \frac{1}{\mathrm{Re}} \nabla^2 \mathbf{u} + \theta_v \hat{k} \tag{2.3.9}$$

2.4 Complete Governing Equations in Conservative Form

For an incompressible flow, the governing equations given by Eq. 2.2.3 and 2.3.3 can be written such that the advective terms are the derivative of a flux. Transcribing the relationships in this manner yields the complete set of governing equations for a thermally stratified turbulent flow with scalar transport.

$$\frac{\partial u_i}{\partial x_i} = 0 \tag{2.4.1a}$$

$$\frac{\partial u_i}{\partial t} + \frac{\partial u_i u_j}{\partial x_j} + \frac{1}{\mathrm{Ro}} \varepsilon_{3ji} u_j = -\frac{\partial p}{\partial x_i} + \frac{1}{\mathrm{Re}} \frac{\partial^2 u_i}{\partial x_j \partial x_j} + \theta_v \delta_{i3} \tag{2.4.1b}$$

$$\frac{\partial \theta}{\partial t} + \frac{\partial u_j \theta}{\partial x_j} = \frac{1}{\mathrm{Re}\,\mathrm{Pr}} \frac{\partial^2 \theta}{\partial x_j \partial x_j} \tag{2.4.1c}$$

$$\frac{\partial q_w}{\partial t} + \frac{\partial u_j q_w}{\partial x_j} = \frac{1}{\mathrm{Re}\,\mathrm{Sc}} \frac{\partial^2 q_w}{\partial x_j \partial x_j} \tag{2.4.1d}$$

$$\theta_v = \theta + 0.61 \gamma_\theta q_w \tag{2.4.1e}$$

The above set of equations use Einstein notation where a repeated indices implies summation over all components. The Kronecker delta δ_{ij} is 1 if $i = k$ or 0 if $i \neq k$. The permutation symbol ε_{ijk} is $+1$ for cyclic values of ijk, -1 for anti-cyclic values, or 0 if an index is repeated.

2.5 Laminar Base Solution

For a low enough Reynolds number an exact solution can be developed for the laminar Ekman layer. Assuming that the flow is spatially homogeneous in the horizontal plane enforces $\partial/\partial x = \partial/\partial y = 0$. Since $\partial u/\partial x = \partial v/\partial y = 0$, the the continuity equation stipulates that $\partial w/\partial z =$

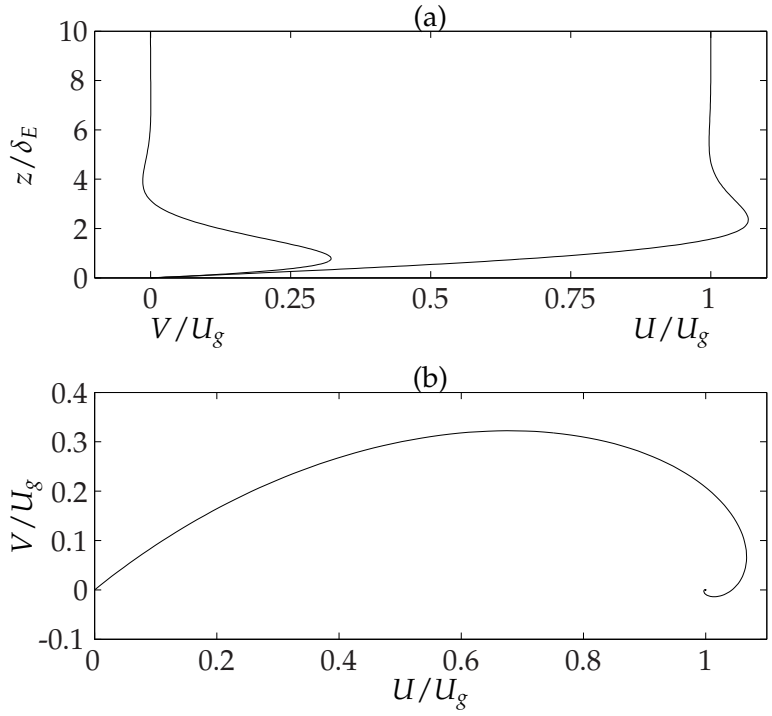

Figure 2.1: The laminar velocity profile presented (a) as a function of the distance from the wall and (b) in hodograph form.

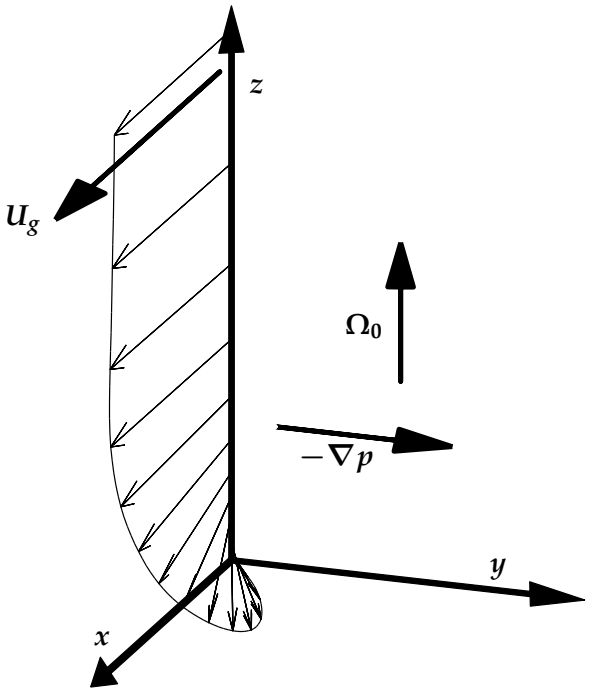

Figure 2.2: Laminar hodograph superimposed over coordinate axes. Demonstrates orientation of domain with respect to mean flow.

0. With $w = 0$ at the wall, the vertical velocity is zero throughout the domain. If it is assumed the flow has reached a steady state, all time derivatives are zero ($\partial/\partial t = 0$). Assuming that there are no temperature gradients, the governing equations reduce to the following x and y momentum equations.

$$-\frac{v}{\mathrm{Ro}} = -\frac{\partial p}{\partial x} + \frac{1}{\mathrm{Re}}\frac{\mathrm{d}^2 u}{\mathrm{d}z^2} \tag{2.5.1a}$$

$$\frac{u}{\mathrm{Ro}} = -\frac{\partial p}{\partial y} + \frac{1}{\mathrm{Re}}\frac{\mathrm{d}^2 v}{\mathrm{d}z^2} \tag{2.5.1b}$$

Imposing a no-slip boundary condition at $z = 0$, the laminar solution is given by the following (Holton, 2004):

$$u = 1 - cos(z)e^{-z} \tag{2.5.2a}$$

$$v = sin(z)e^{-z} \tag{2.5.2b}$$

Solving for the resulting pressure gradients yield

$$\frac{\partial p}{\partial x} = 0 \tag{2.5.3a}$$

$$\frac{\partial p}{\partial y} = \frac{2}{\mathrm{Re}} \tag{2.5.3b}$$

Equation 2.5.3 will be used as an approximation of the mean turbulent pressure gradient ($\partial P/\partial x = 0$ and $\partial P/\partial y = 2/\mathrm{Re}$) when numerically solving Eq. 2.4.1. The laminar velocity profile is shown in Fig. 2.1. The hodograph in subplot (b) demonstrates the typical Ekman spiral; the local direction of shear stress is tangent to this curve at every point. The effect of rotation is also clearly evident in Fig. 2.2 where the rotation vector $\Omega\hat{k}$, geostrophic velocity direction, and pressure gradient are included to orientate the reader with the three coordinate directions.

2.6 Characteristic Scales

Throughout the dissertation there are many characteristic scales that will be introduced. They all typically serve to obtain some sort of 'universal scaling' between different flow geometries

or conditions. In this section, a few of the fundamental scales used will be introduced. Additional characteristic lengths, velocities, and times will be introduced as needed.

The smallest scales of turbulence are characterized by the Kolmogorov scales (see Pope, 1993). These scales are functions of the kinematic viscosity ν and the turbulent dissipation ε. The smallest length, velocity, and time scales are given by

$$\eta = \left(\frac{\nu^3}{\varepsilon}\right)^{1/4} \tag{2.6.1}$$

$$u_\eta = (\nu\varepsilon)^{1/4} \tag{2.6.2}$$

and

$$\tau_\eta = \left(\frac{\nu}{\varepsilon}\right)^{1/2} \tag{2.6.3}$$

Dissipation of turbulent energy occurs at the above Kolmogorov scales. The size of large eddies is given by

$$\mathcal{L} = \frac{k^{3/2}}{\varepsilon} \tag{2.6.4}$$

The computational domain must be at least of size $\mathcal{L}$ for a given Reynolds number. If the domain is smaller than the largest eddies, the field is pinched and not allowed to evolve naturally.

The time associated with the eddies of size $\mathcal{L}$ is known as the large eddy turn-over time. The turn-over time $\mathcal{T}$ is given by

$$\mathcal{T} = \frac{k}{\varepsilon} \tag{2.6.5}$$

The inertial time period of the turbulent Ekman layer under neutral stratification is given by

$$\tau = \frac{1}{f} \tag{2.6.6}$$

Scaling the dimensional time t^* by the inertial time period yields the dimensionless time

$$t^* f = \frac{2t}{\mathrm{Re}} \tag{2.6.7}$$

While the above discussion offers a few of the characteristic scales of turbulence that will be used in this work, many more quantities will be introduced later in the thesis. Relevancy of additional scales is more apparent when they are introduced during a pertinent discussion.

CHAPTER 3

NUMERICAL METHOD AND PARALLELIZATION SCHEME

No closed-form solution of the full Navier-Stokes equations currently exists. Like the laminar solution of the Ekman problem, a select number of solutions exist when simplifications (e.g. steady with time, homogeneous in specific directions, etc.) are made. For direct numerical simulations, the full governing equations are approximated (or solved) numerically. This chapter describes the numerical scheme used (§3.1), the parallelization of the code (§3.2), results from the validation test case (§3.3), and gives parallel scalability results in §3.4. Some recommendations on code usage, and a brief summary concludes the chapter in §3.5.

3.1 Mathematical Model of Governing Equations

The domain geometry for the Ekman problem can be resolved using a Cartesian mesh. As the turbulent Ekman layer is a wall-bounded flow, it is efficient to employ a stretched mesh in the wall-normal direction allowing clustering of points near the lower boundary where both $\mathcal{L}$ and η are smallest. In the present work, the mesh has been staggered in the vertical direction to allow improved coupling between the pseudo-pressure and the vertical velocity component. The code and numerical method is based on earlier work by Marlatt (1994); however, significant changes to the time integration and spatial differencing scheme were made.

3.1.1 Time Integration Scheme

The numerical method used to integrate Eq. 2.4.1 is semi-implicit, applying the implicit Crank-Nicolson scheme (Crank and Nicolson, 1947) for the vertical diffusion terms in the conservation equations. Because mesh stretching results in a very small spacing near the lower domain boundary, using an implicit scheme for the diffusion terms allows time-step requirements for numerical stability to be relaxed. For the model equation

$$\frac{\partial u_i}{\partial t} \approx \frac{1}{\mathrm{Re}} \frac{\partial^2 u_i}{\partial x_3^2} \tag{3.1.1}$$

the Crank-Nicolson scheme can be written as

$$\frac{\hat{u}_i - u_i^n}{\Delta t} \approx \frac{1}{2\mathrm{Re}} \frac{\partial^2 \hat{u}_i}{\partial x_3^2} + \frac{1}{2\mathrm{Re}} \frac{\partial^2 u_i^n}{\partial x_3^2} + \mathcal{O}\left(\Delta t^2\right) \tag{3.1.2}$$

where $\mathcal{O}\left(\Delta t^2\right)$ implies that the solution is second-order accurate in time. The predicted velocity $\hat{u}_i$ is obtained from the solution of the linear system

$$\left(1 - \frac{\Delta t}{2\mathrm{Re}} \frac{\partial^2}{\partial x_3^2}\right) \hat{u}_i \approx u_i^n + \frac{\Delta t}{2} M_i^n \tag{3.1.3}$$

where

$$M_i^n = \frac{1}{\mathrm{Re}} \frac{\partial^2 u_i^n}{\partial x_3^2} \tag{3.1.4}$$

For the temperature equation, advancement of θ^n to θ^{n+1} is accomplished by substituting (Re) with $(\mathrm{Re\,Pr})$, u_i^n with θ^n, and $\hat{u}_i$ with θ^{n+1} in Eq. 3.1.3 and 3.1.4.

Remaining terms in Eq. 2.4.1b, 2.4.1c, and 2.4.1d (advection, horizontal diffusion, Coriolis, and mean pressure gradient) are advanced using the fully explicit Adams-Bashforth method (see Ferziger and Perić, 2002, pg. 138–140), which utilizes a two-level integration technique:

$$\frac{\hat{u}_i - u_i^n}{\Delta t} \approx \frac{3}{2} L_i^n - \frac{1}{2} L_i^{n-1} + \mathcal{O}\left(\Delta t^2\right) \tag{3.1.5}$$

where

$$L_i^n = -\frac{\partial u_i^n u_j^n}{\partial x_j} - \frac{1}{\mathrm{Ro}} u_j^n \varepsilon_{ji3} - \frac{\partial P}{\partial x_i} + \frac{1}{\mathrm{Re}} \left(\frac{\partial^2 u_i^n}{\partial x_1^2} + \frac{\partial^2 u_i^n}{\partial x_2^2} \right) + \theta_v^n \delta_{i3} \tag{3.1.6}$$

Equations 3.1.5 and 3.1.6 are fully explicit; this allows each node to independently advance the solution in time completing the predictor step. Combining Eq. 3.1.3, 3.1.4, 3.1.5, and 3.1.6 yields the following linear system of equations for the predictor velocity:

$$\left(1 - \frac{\Delta t}{2\mathrm{Re}}\frac{\partial^2}{\partial x_3^2}\right)\hat{u}_i = u_i^n + \Delta t\left(\frac{1}{2}M_i^n + \frac{3}{2}L_i^n - \frac{1}{2}L_i^{n-1}\right) \tag{3.1.7}$$

where L_i^n and M_i^n are given by Eq. 3.1.6 and 3.1.4 respectively. A similar time advancement is used for the conservation of energy and scalar transport equations. The time integration scheme for these two equations are given by

$$\left(1 - \frac{\Delta t}{2\mathrm{Re\,Pr}}\frac{\partial^2}{\partial x_3^2}\right)\theta^{n+1} = \theta^n + \Delta t\left(\frac{1}{2}M_\theta^n + \frac{3}{2}L_\theta^n - \frac{1}{2}L_\theta^{n-1}\right) \tag{3.1.8}$$

and

$$\left(1 - \frac{\Delta t}{2\mathrm{Re\,Sc}}\frac{\partial^2}{\partial x_3^2}\right)q_w^{n+1} = q_w^n + \Delta t\left(\frac{1}{2}M_{q_w}^n + \frac{3}{2}L_{q_w}^n - \frac{1}{2}L_{q_w}^{n-1}\right) \tag{3.1.9}$$

where the explicit terms are given by

$$M_\theta^n = \frac{1}{\mathrm{Re\,Pr}}\frac{\partial^2\theta^n}{\partial x_3^2} \tag{3.1.10}$$

$$M_{q_w}^n = \frac{1}{\mathrm{Re\,Sc}}\frac{\partial^2 q_w^n}{\partial x_3^2} \tag{3.1.11}$$

$$L_\theta^n = -\frac{\partial u_j^n\theta^n}{\partial x_j} + \frac{1}{\mathrm{Re\,Pr}}\left(\frac{\partial^2\theta^n}{\partial x_1^2} + \frac{\partial^2\theta^n}{\partial x_2^2}\right) \tag{3.1.12}$$

and

$$L_{q_w}^n = -\frac{\partial u_j^n q_w^n}{\partial x_j} + \frac{1}{\mathrm{Re\,Sc}}\left(\frac{\partial^2 q_w^n}{\partial x_1^2} + \frac{\partial^2 q_w^n}{\partial x_2^2}\right) \tag{3.1.13}$$

Note that no Coriolis, buoyancy, or pressure gradient terms appear for the temperature and scalar transport equations. The coupling between the momentum, energy and scalar transport equations given in Eq. 2.4.1e is explicitly computed using the potential temperature and specific humidity at the n^{th} time step. The last term in Eq. 3.1.6 is therefore

$$\theta_v^n = \theta^n + 0.61\gamma_\theta q_w^n \tag{3.1.14}$$

While the energy and scalar equations will have been integrated successfully using the above methods, a zero divergence for the velocity field has not yet been enforced. The velocity field at the advanced time step $(n+1)$ is obtained by a pressure corrector step to the predicted velocity field.

$$\frac{u_i^{n+1} - \hat{u}_i}{\Delta t} = -\frac{\partial \phi}{\partial x_i} \tag{3.1.15}$$

The variable ϕ acts as a pseudopressure to account for small fluctuations in the turbulent field that are not accounted for when applying a mean pressure gradient. Taking the divergence of Eq. 3.1.15 yields

$$\frac{1}{\Delta t}\left(\frac{\partial u_i^{n+1}}{\partial x_i} - \frac{\partial \hat{u}_i}{\partial x_i}\right) = -\frac{\partial^2 \phi}{\partial x_i \partial x_i}.$$

Continuity is enforced by stipulating that the advanced field be divergence free (i.e. $\partial u_i^{n+1}/\partial x_i = 0$). This results in the following linear system for ϕ based only on the fraction step velocity $\hat{u}_i$:

$$-\Delta t \frac{\partial^2 \phi}{\partial x_i \partial x_i} = \frac{\partial \hat{u}_i}{\partial x_i} \tag{3.1.16}$$

The updated velocity is then found using a rearranged form of Eq. 3.1.15.

$$u_i^{n+1} = \hat{u}_i - \Delta t \frac{\partial \phi}{\partial x_i} \tag{3.1.17}$$

In summary, advancing from the time level n to level $n+1$ requires solving 3 linear systems for the fractional velocity components ($\hat{u}$, $\hat{v}$, and $\hat{w}$), 2 linear system for the updated temperature (θ) and humidity (q_w) fields, and 1 linear system for the pseudo pressure (ϕ).

3.1.2 Spatial Differences

Spatial derivatives of the DNS are approximated using high order finite differences. The horizontal plane in this simulation is homogeneous in the context that there are no extraneous features requiring a concentrated mesh (such as topography). Therefore, the employed mesh in the horizontal plane is uniform. However, due to small scales of turbulence near the wall, a uniform mesh in the z direction is impractical. A sufficient resolution which captures the small

scales near the wall would be extraneous in the far-field. Conversely, using a uniform spacing which adequately resolved scales away from the boundary would be insufficient near the surface. Instead, a stretched grid is employed which clusters points near the lower boundary and allows a larger grid spacing in the outer flow field (where the gradients are shallower). An exponential grid spacing is employed by specifying the location of 2 points in the domain and iterating until a smooth distribution mesh nodes is achieved in the z direction (Marlatt, 1994). Alternatively, the code allows for the user to specify a uniform z distribution or upload a specific grid spacing file.

A staggering of the mesh is employed in the vertical direction resulting in the generation of 2 meshes. The mesh which coincides with the wall is defined as the z_w mesh while the cell centered mesh is termed the z_c mesh. The z_c mesh is easily determined from the z_w mesh by centering nodes between the wall bounded grid. For a vertical mesh (z_w) using n_z points, the cell centered mesh (z_c) of size $n_z + 1$ points is defined as

$$z_{c,k} = \frac{1}{2}\left(z_{w,k} + z_{w,k+1}\right), k = 0 : n_z - 1 \tag{3.1.18a}$$

$$z_{c,n_z} = z_{w,n_z-1} + \frac{1}{2}\left(z_{w,n_z-1} + z_{w,n_z-2}\right) \tag{3.1.18b}$$

$$z_{c,-1} = -z_{c,0} \tag{3.1.18c}$$

where $z_{w,0}$ is the point on the wall, $z_{c,-1}$ is the staggered point below the wall, and z_{c,n_z} is the point above the top of the domain. Figure 3.1 demonstrates the alignment of the various meshes. The variables u, v, and ϕ are defined on the z_c mesh while w, θ, and q_w are defined on z_w.

The uniform mesh in the x and y direction allows finite difference coefficients to be computed for each coordinate which are valid at any point. The arbitrary vertical mesh requires that a unique set of coefficients be computed for each z_c and z_w point. Furthermore, it is necessary to interpolate between meshes for the advective terms as well as the pressure correction step. Finite difference coefficients as well as interpolation coefficients are stored to reduce the computational effort at each time step.

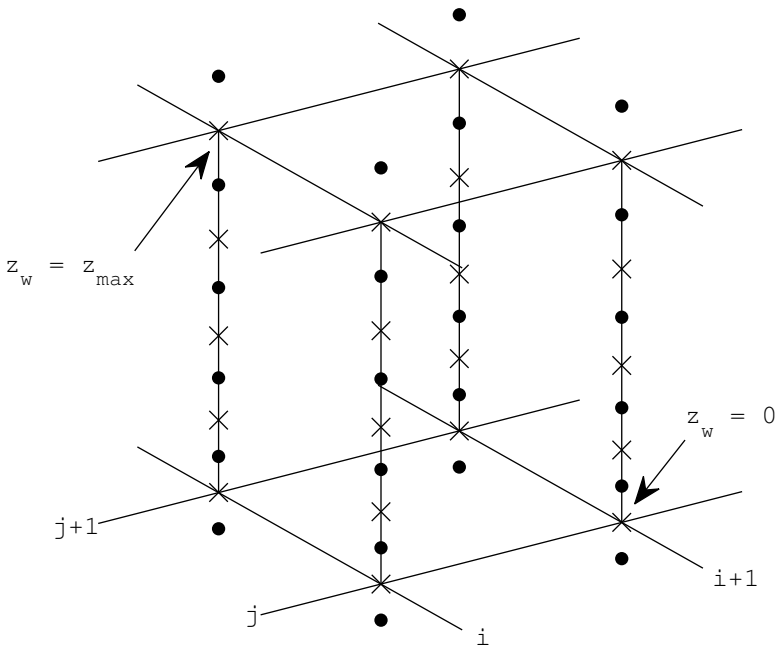

Figure 3.1: Staggered mesh. Uniform mesh in horizontal plane and stretched mesh in vertical direction. z_w nodes denoted by $\times$ and z_c nodes by $\bullet$.

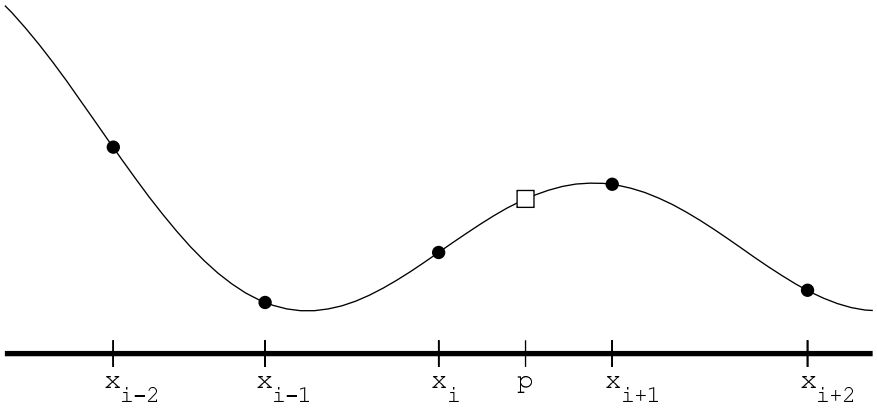

Figure 3.2: Example interpolation scheme of point p (denoted by $\square$) using points $x_{i-2} \leq x_i \leq x_{i+2}$ (denoted by $\bullet$).

Lagrangian Polynomials

Computation of finite difference coefficients and interpolation between the z_w and z_c meshes (or vice-versa) is accomplished by means of Lagrangian polynomials. A Lagrangian interpolation polynomial is defined by $l_i(x)$ as follows (Atkinson, 1989, Cheney and Kincaid, 2004):

$$l_k(x) = \prod_{\substack{j=0 \\ j \neq k}}^{m} (x - x_j) \tag{3.1.19}$$

Here x represents an arbitrary point while x_j denotes a set of $m+1$ points on a mesh. Interpolation of a function $f(x_j)$ onto an arbitrary point $f(x)$ is accomplished with the Lagrangian interpolation polynomial.

$$f(x) \approx \sum_{k=0}^{m} \frac{l_k(x)}{l_k(x_k)} f(x_k) \tag{3.1.20}$$

Generalized to a set of nodes $x_{i+il} \leq x_i \leq x_{i+ih}$ about point x (see example in Fig. 3.2), the interpolation polynomial becomes

$$f(x) \approx \sum_{k=il}^{ih} \frac{l_k(x)}{l_k(x_{i+k})} f(x_{i+k}) \tag{3.1.21}$$

where

$$l_k(x) = \prod_{\substack{j=il \\ j \neq k}}^{ih} (x - x_{i+j}) \tag{3.1.22}$$

Although there is not necessarily a relationship between x and the points x_i, increased accuracy is obtained when x is within the bounds of $x_{i+il} \leq x \leq x_{i+ih}$. If x is outside these bounds, the approximation is an extrapolation rather than an interpolation.

Approximating derivatives of the function $f(x)$ is also accomplished from the Lagrangian polynomials. A first derivative is computed by taking the derivative of the basis function in the numerator of Eq. 3.1.21.

$$\frac{df(x)}{dx} = \sum_{k=il}^{ih} \frac{dl_k(x)}{dx} \frac{f(x_{i+k})}{l_k(x_{i+k})} \tag{3.1.23a}$$

$$\frac{dl_k(x)}{dx} = \sum_{\substack{m=il \\ m\neq k}}^{ih} \prod_{\substack{j=il \\ j\neq m \\ j\neq k}}^{ih} (x - x_{i+j}) \tag{3.1.23b}$$

Taking the derivative of the basis function reduces the order of the polynomial by one degree. Therefore, an approximation of the first derivative requires (at least) a polynomial of order 1. The 2$^{\text{nd}}$ derivative, requiring a polynomial of at least 2 (3 mesh points), is computed in a similar manner.

$$\frac{d^2f(x)}{dx^2} = \sum_{k=il}^{ih} \frac{d^2l_k(x)}{dx^2} \frac{f(x_{i+k})}{l_k(x_{i+k})} \tag{3.1.24a}$$

$$\frac{d^2l_k(x)}{dx^2} = \sum_{\substack{m=il \\ m\neq k}}^{ih} \sum_{\substack{n=il \\ n\neq m \\ n\neq k}}^{ih} \prod_{\substack{j=il \\ j\neq n \\ j\neq m \\ j\neq k}}^{ih} (x - x_{i+j}) \tag{3.1.24b}$$

Equation 3.1.23 is used for computing the advective terms while Eq. 3.1.24 is used for the diffusive terms. The fourth-order artificial dissipation used to ensure numerical stability is approximated by continuing the expansion two more levels.

$$\frac{d^4f(x)}{dx^4} = \sum_{k=il}^{ih} \frac{d^4l_k(x)}{dx^4} \frac{f(x_{i+k})}{l_k(x_{i+k})} \tag{3.1.25a}$$

$$\frac{d^4l_k(x)}{dx^4} = \sum_{\substack{m=il \\ m\neq k}}^{ih} \sum_{\substack{n=il \\ n\neq m \\ n\neq k}}^{ih} \sum_{\substack{q=il \\ q\neq n \\ q\neq m \\ q\neq k}}^{ih} \sum_{\substack{r=il \\ r\neq q \\ r\neq n \\ r\neq m \\ r\neq k}}^{ih} \prod_{\substack{j=il \\ j\neq r \\ j\neq q \\ j\neq n \\ j\neq m \\ j\neq k}}^{ih} (x - x_{i+j}) \tag{3.1.25b}$$

Although these expressions can be simplified to reduce computational requirements, the use of a fixed mesh allows the coefficients to be stored. The effort to computationally optimize the fourth-order difference would prove to return minimal gains in startup time.

3.1.3 Artificial Dissipation, Rayleigh Friction, and Courant Number

When finite difference methods are employed, dealiasing in the Fourier space has to be replaced with numerical smoothing by artificial viscosity in the physical space in order to dissipate excess energy that cannot be resolved by the grid. This can be accomplished by adding an explicit high-order dissipation term to the explicit time advancement equations given by Eq. 3.1.6, 3.1.12, and 3.1.13, viz.,

$$L_{u_i}^n = \cdots + \beta \Delta x_j^4 \frac{\partial^4 u_i^n}{\partial x_j^4} \tag{3.1.26}$$

The coefficient β controls the strength of the dissipation and is bounded by $0 < \beta \leq 1$ (Anderson et al., 1984). In the present work, artificial dissipation is applied to both the velocity and temperature. For neutral stratification ($\theta = 0$ throughout the domain), numerical stability was maintained with β as low as $\beta = 0.05$. For unstably stratified cases (hot wall) β had to be increased to values as high as $\beta = 0.2$ for moderate heating or $\beta = 0.8$ for strong heating. The smallest scales (η) tend to decrease for the heated wall case in comparison with the neutral field, thus requiring higher values of β. A reduction in β for the stratified cases could be achieved by increasing the mesh resolution, or, for some problems, using upwind biased differences (Rai and Moin, 1991).

Secondly, a Rayleigh friction layer (e.g. Marlatt, 1994) is used at the top of the domain to prevent the reflection of gravity waves off the top boundary. This additional term is added to the explicit term $L_{u_i}^n$ for the three momentum equations. The basic form is

$$L_{u_i}^n = \cdots - \alpha_{rf} \left(\hat{u}_i - u_{i,\text{top}} \right) \tag{3.1.27}$$

The coefficient α_{rf} controls the strength of the Rayleigh friction. The user controls two parameters ($\alpha_{rf,\max}$ and z_{rf}) which effectively determines α_{rf}. $\alpha_{rf,\max}$ is the maximum damping that is applied

at the top of the domain; z_{rf} is the height at which damping should start. A simple sinusoid is used to specify α_{rf} for points above z_{rf}:

$$\alpha_{rf} = \alpha_{rf,\max} \sin\left[\frac{\pi}{2}\frac{(z - z_{rf})}{(z_{\max} - z_{rf})}\right] \tag{3.1.28}$$

If $z > z_{rf}$, $\alpha_{rf} = 0$.

As a guideline for determining the time step to use given a specific spatial discretization, the Courant number of the flow is given by

$$CN_{\max} = \frac{|u_i|_{\max}\,\Delta t}{\Delta x_i} \tag{3.1.29}$$

Note that the repeated index implies a summation over all three velocity components and spatial directions. The exact value of $CN_{\max}$ at which the simulation becomes unstable depends on both the governing equations as well as the numerical scheme used. For this work, it was found that keeping $CN_{\max} < 0.5$ was required to ensure stability.

3.2 Parallelization of DNS

The numerical algorithm outlined in §3.1 was programmed using the Portable, Extensible Toolkit for Scientific Computation (PETSc) libraries (Balay et al., 1997, 2011). These routines are specifically designed for solving large systems using massively parallel algorithms. The term 'massively' is used in this context to emphasize that each processor holds only a small portion of the total problem, where hundreds or thousands of processors work in parallel to accomplish the task.

While developing the present code, easy optimization and adjustable domain configurations were enabled when possible. Concerning optimization, PETSc allows the user to specify tolerances, the choice of the linear solution procedure, and other computation parameters directly from the command line. This allows a level of versatility for quickly tuning simulations.

Configuration restrictions were relaxed by avoiding 'hardwires' (statements applicable to a

specific case only) in the code. Examples of such are evident in allowing $N_1 \neq N_2$, i.e. unequal number of grid points in different coordinate directions. Moreover, the number of points for N_1, N_2, or N_3 is not constricted to be a power of 2 (as with some pseudo-spectral codes) thus allowing fine tuning of the grid.

A flowchart for the program is provided in Fig. 3.3. The shaded boxes indicate portions of the code where each individual process can work relatively independent. A white box indicates an action which has extensive interprocess communication. The lower half of the flowchart (below the dashed line) represents the time integration sequence. One complete cycle will advance the velocity and temperature from time step n to $n + 1$. Given that the solution of the scalar transport equations is optional and mimic the solution of the temperature equation, they have been removed from this discussion for clarity. Any number of scalars are easily added and the actions required for solving these equations mirror those of the temperature equation. In what follows, we will discuss the parallelism associated with each block shown in Fig. 3.3.

3.2.1 Initialization

The initialization routine of the code generates the computational mesh, obtains finite difference and interpolation coefficients, and allocates storage. Flow variables are stored on all processors in a vector structure. This is accomplished by a Distributed Array (DA) through PETSc which controls the three-dimensional indexing for transmitting data between neighboring processors. The DA structure allows the user to control the number of neighboring points to be shared as well as the periodicity of the domain (in this case, the x_1/x_2 plane).

In total, 25 vectors are declared (as outlined in Table 3.1) leading to a large amount of storage due to the allocation of each right-hand-side (RHS) individually (including staggered velocities). By allocating additional storage it is possible to compute all quantities at the same time rather than having to perform a step-through process where each RHS is computed and solved sequentially. Ultimately, storage savings could be generated at the expense of added computational time. The

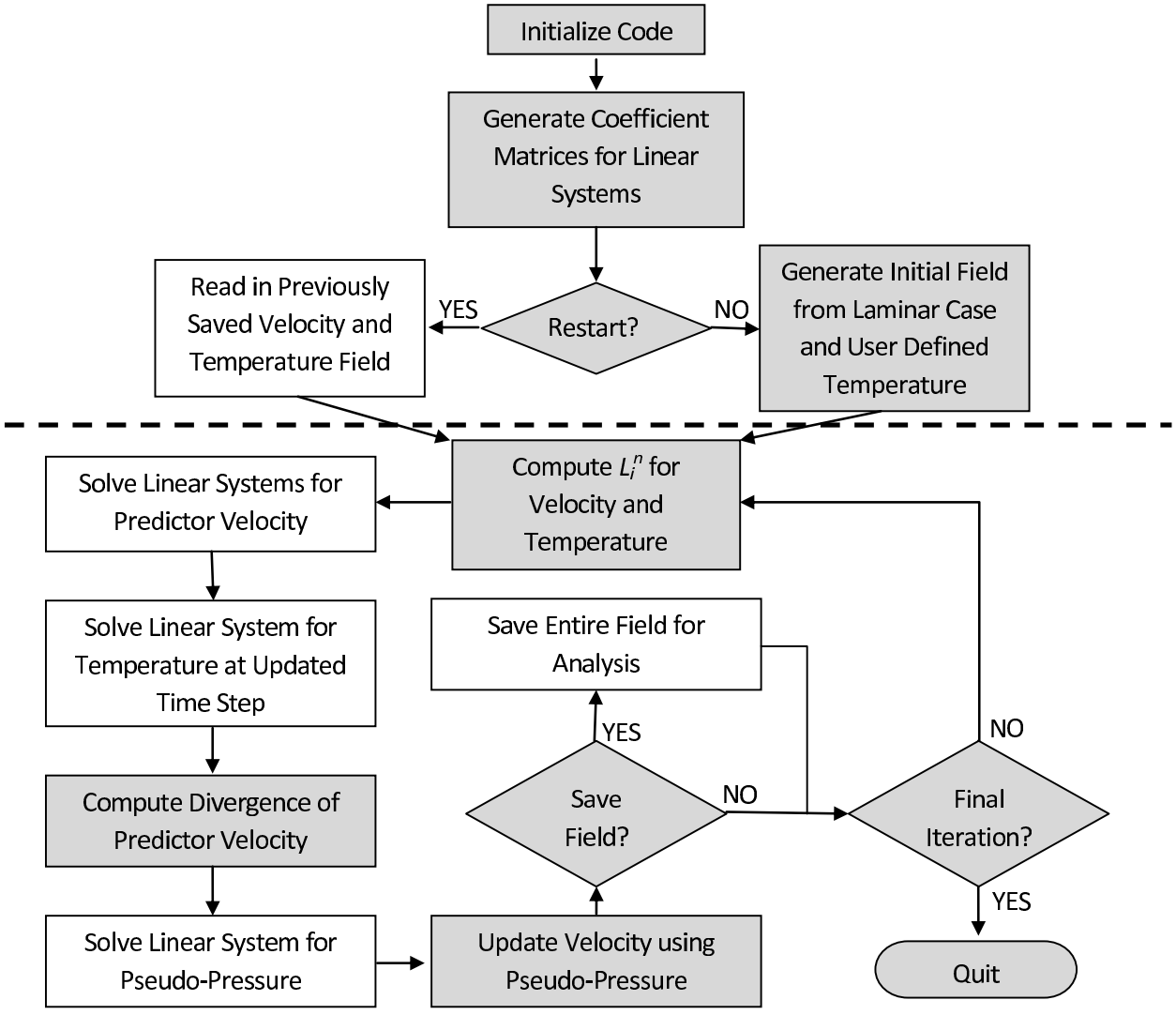

Figure 3.3: Direct Numerical Simulation Flowchart: Shaded box, each process works independent; White box, global communication. Dashed line separates startup and time integration sequences.

Table 3.1: Vector Storage.

# of Vectors	Description
3	Full-step velocity
1	Temperature
3	Velocity on staggered mesh
1	Temperature on staggered mesh
1	Pseudo-pressure
6	L_i^n and L_i^{n-1} for velocity
2	L_θ^n and L_θ^{n-1} for temperature
3	RHS of velocity predictor equation
1	RHS of temperature equation
1	RHS of pseudo-pressure equation
3	Fractional velocities

allocation of vectors is a local action in the sense that each process much allocate its own storage to hold these variables. Although swapping of boundary points needed for the finite differences is initialized when declaring the DA, no passing occurs during initialization.

The initialization concludes by computing the laminar Ekman flow and user specified base temperature profile. The analytical Ekman layer solution can be used as an initial condition for high Reynolds turbulent simulations with Coriolis forcing.

3.2.2 Generating Linear Operators

Linear solvers are required to advance the velocity in the predictor step and to compute the pseudo-pressure. All solutions are obtained using the Krylov subspace methods (Trefethen and Bau, 1997) of the PETSc library, specifically, using the GMRES iterative algorithm to solve the linear system $Ax = b$. However, PETSc allows for multiple solution algorithms to be employed; algorithm optimization has not been attempted in the present work and is a topic for future research.

Equations 3.1.7 and 3.1.16 result in $N^2 \times N^2$ systems of equations where $N = N_1 N_2 N_3$. A row in the coefficient matrix A for the system $Ax = b$ is locally owned by the processor which

stores the flow variables for the row's corresponding gridpoint. The coefficient matrices for the linear systems are stored in parallel in the same manner as velocity and temperature vectors. For large systems, storage savings are obtained by preallocating non-zeros in the banded matrix. This operation proves trivial with PETSc where storage is allocated based on the DA generated earlier. Care was taken to ensure that no additional allocation of memory for each matrix is needed. Setting coefficients which are not preallocated results in a significant computational slow-down.

Boundary conditions are imposed directly through the A matrix. No 'folding-in' occurs as this operation would require allocating a smaller matrix to store coefficients. Either Dirichlet or Neumann conditions are easily imposed.

3.2.3 Generate Initial Conditions

Initial conditions are created by either reading a previously saved velocity and temperature field or generating an initial condition based on the laminar Ekman profile. Restarting from a saved field is a global operation; all processes must read their portion of data from a single file. Although it is possible to have each process write their stored data to a separate file, this would limit the ability of the code to stop and start using various numbers of processors (e.g. Case 1a uses 16 processors, Case 1b uses 32 processors).

When starting a new simulation, an initial condition is generated by perturbing the laminar Ekman profile. The perturbations can be random noise, which will eventually transition into turbulence through growth of primary and secondary instabilities, or user defined functions depicting an unstable solution of the linearized equations (see §3.3).

3.2.4 Compute L_i^n for Velocity and Temperature

The explicit terms for the velocity and temperature given by L_i^n are computed from flow variables at iteration n. For each node stored on a processor, the finite differences require sur-

rounding points to compute spatial derivatives. Near the processor boundaries this requires that data be transmitted between the processor and its neighbor. PETSc routines are used which transmit neighboring data (including periodic boundaries) for a given finite difference stencil width. Typically the communication is between 2 processors and no global communication is required.

In order for the terms outlined in Eq. 3.1.6 and 3.1.26 to be computed, a grid transform using fourth-order Lagrange polynomials is performed for each variable to allow products such as $u_1 u_3$ to be computed on either z_w or z_c. The RHS of the u_3 and θ linear system must be on the z_w mesh, and consequently, the advective terms are also defined on the z_w mesh by interpolating u_1 and u_2 onto z_w (hence the additional storage shown in Table 3.1). Conversely, u_1 and u_2 explicit terms require the RHS to be on the z_c mesh; variables u_3 and θ are interpolated from z_w to z_c.

Once the velocity and temperature are defined on both z_w and z_c mesh systems, the explicit terms are computed locally for each process. Since each process has been updated with the necessary boundary data, no further communication between processors is required. The term M_i^n given by Eq. 3.1.4 is computed in a similar manner and no additional inter-process communication is necessary. The RHS is computed locally by Eq. 3.1.7. The explicit term L_i^n is saved for the next iteration since Eq. 3.1.7 requires the term L_i^{n-1}.

By allocating additional storage and computing L_i^n for each velocity component and the temperature simultaneously, the amount of computational work is decreased. Instead of each process looping over all locally owned grid-points four times, the code only loops once.

3.2.5 Solve for Fractional Velocity and Temperature

The fractional velocity $\hat{u}_i$ and updated temperature θ^{n+1} are solved using the linear operator previously defined and the newly computed RHS. For this purpose, the GMRES algorithm is employed which, in these situations, drops the residual by over five orders of magnitude in a few iterations (typically $3-6$). For the system $Ax = b$, the residual can be defined as $r = Ax - b$. PETSc allows the convergence criteria as well as the measure of the residual (e.g.: 2-norm) to be

controlled by the user.

The code currently uses the previous solution of $\hat{u}$ as the first guess of the solution in the next time step; if Δt is small, the solution does not vary greatly over one time step. Thus, the number of iterations is reduced by supplying a good initial condition to the solver. The GMRES algorithm could be replaced with incomplete LU factorization, algebraic multigrid, or others.

3.2.6 Solve for Pseudo-Pressure / Updating Velocity

The divergence of the predictor velocity, $\partial \hat{u}_i / \partial x_i$, is a simple operation which requires updating boundary points of each processor in a similar manner as discussed for the explicit terms. Since the pseudo-pressure ϕ is defined on the z_c mesh, u_3 is interpolated from its original z_w grid onto z_c. Upon interpolating and updating boundary points for each processor, the RHS of Eq. 3.1.16 is computed locally.

Solving Eq. 3.1.16 uses the same GMRES algorithm used for the velocity and temperature equations. Neumann conditions ($\partial \phi / \partial x_3 = 0$) are imposed at both the lower and upper boundaries. This system is ill-conditioned since a null-space exists in the solution. PETSc provides an easily implemented function which removes the null-space by setting the mean of the pressure field to 0. In mathematical terms, the null-space of vector $\mathbf{v}$ is removed by

$$\mathbf{v} = \mathbf{v} - \frac{\langle \mathbf{v}, \mathbf{1} \rangle}{\langle \mathbf{1}, \mathbf{1} \rangle} \tag{3.2.1}$$

where $\langle \mathbf{a}, \mathbf{b} \rangle$ denotes the inner product between the vectors $\mathbf{a}$ and $\mathbf{b}$. Since the gradient of the pseudo-pressure is of interest (both for time advancement as well as analysis), removing the null-space is sufficient to obtain an accurate pressure gradient.

Once the pseudo-pressure is calculated, the velocity field at the advanced timestep, u_i^{n+1}, is computed via Eq. 3.1.17. Note that the accuracy to which $\nabla \cdot u_i^{n+1} \approx 0$ is dependent upon the accuracy of the solution for ϕ. Simulations indicate that decreasing the residual of ϕ by five orders of magnitude generally results in an average divergence of approximately 10^{-5}.

3.2.7 Field Saves

Field saves are conducted at a frequency defined by the user. For example, if statistical turbulent averages are of interest, a field is typically saved every hundred or thousand iterations. If time varying analysis is to be completed, the frequency would increase to every few iterations. To facilitate stopping and starting with different numbers of processors, each flow variable is written to one file (as opposed to n processors saving a file each for a total of n files). The drawback is that writing data is computationally expensive as all processors must communicate with a single file. Furthermore, the data files become quite large for high Reynolds number problems. For a $512 \times 512 \times 256$ mesh required for the current $\mathrm{Re} = 1000$ simulations, the velocity, temperature, and pressure files are 515 MB each for a total of 2.6 GB per field save. Transferring data becomes a problem if many iterations are to be moved.

After saving the field, the code checks to determine if the last iteration has been reached. If so, all parallel vectors and matrices are deallocated and the computation concludes. If not, the code begins computing the explicit terms for the next time step, thus closing the iterative loop.

3.3 Code Validation

In an effort to validate the accuracy of the parallel code, numerical solutions are compared with the hydrodynamic linear stability theory for the plane channel (Poiseuille) flow. For this purpose, least-damped eigenvalues of the Orr-Sommerfeld equation for plane channel flow were used as the initial conditions for the full Navier-Stokes equations on a horizontally doubly-periodic computational domain. By measuring the growth rate and phase speed of the primary two-dimensional disturbance from the computation and comparing these values to the eigenvalues of the Orr-Sommerfeld equation, the accuracy of the code was assessed. The Orr-Sommerfeld equation in dimensionless form is given by

$$(U^* - c^*)\left(\varphi'' - {\alpha_\delta}^2\varphi\right) - U^{*\prime\prime}\varphi + \frac{i}{\alpha_\delta \mathrm{Re}}\left(\varphi'''' - 2{\alpha_\delta}^2\varphi'' + {\alpha_\delta}^4\varphi\right) = 0 \tag{3.3.1}$$

Table 3.2: Validation Test: Top - Linear Theory; Bottom - Present DNS.

Case	$\mathrm{Re} = \frac{U_0\delta}{\nu}$	α_δ	c_r^*	c_i^*	Amplitude Growth $(0 \leq t \leq 10)$
V1	7500	0.98	0.2476 0.2439	0.0023 0.0029	1.0233 1.0294
V2	10000	0.94	0.2309 0.2316	0.0044 0.0048	1.0450 1.0492

where $U^* = U/U_0$, $c^* = c/U_0$, $\alpha_\delta = \alpha\delta$, $\mathrm{Re} = U_0\delta/\nu$, $\varphi = w/U_0$, w is the wall-normal perturbation velocity, α is the wavenumber along the streamwise (x) direction, c is the dimensional wave speed, δ is the channel half-height, and U_0 is the centerline velocity in the channel. The prime, $(\cdot)'$, is used to indicate differentiation with respect to the wall normal (z) direction. Boundary conditions of Eq. 3.3.1 for plane-channel flow are

$$\varphi\left(x, y, \pm\delta, t\right) = 0 \tag{3.3.2}$$

The solution of Eq. 3.3.1 consists of solving the eigenvalue problem $\mathcal{F}\left(\mathrm{Re}, c^*, \alpha_\delta\right) = 0$ for the specific boundary conditions given by Eq. 3.3.2. For the temporally evolving case, Re and α_δ are real and the eigenvalues will correspond to the complex wave speed $c^* = c_r^* + c_i^* i$ (note $i = \sqrt{-1}$) where c_r^* is the phase velocity and c_i^* is the temporal growth rate of the wave (see White, 1991, pg. 410). Solutions of the linearized Navier-Stokes equations are expected to be valid while wave amplitudes are still small.

Using an Orr-Sommerfeld solver (Trefethen, 2000), α_δ was selected such that it corresponds to the least stable eigenvalue (largest value of c_i^*) for a specified Re. Two Reynolds numbers ($\mathrm{Re} = 7500$ and $\mathrm{Re} = 10000$) have been chosen for this stability analysis; the computed eigenvalues corresponding to the least stable wave-number α_δ for each Reynolds number are shown in Table 3.2 (top numbers).

The eigenfunctions corresponding to these eigenvalues are used as initial conditions for the numerical simulation; maximum amplitudes of the initial disturbances were set to $0.01U_0$. The

Table 3.3: Case Parameters.

Case	$\mathrm{Re} = \frac{U_g \delta_E}{\nu}$	Stratification	N_1	N_2	N_3	N
T1	400	Neutral	128	128	128	2.10×10^6
T2	1000	Unstable	512	512	256	6.71×10^7

perturbed field is then integrated forward in time by the Navier-Stokes solver. Comparisons between observed values of the complex wave speed, c^*, in the computational model and theoretical predictions are displayed in Table 3.2. For both Reynolds numbers strong agreement between theoretical predictions of c^* and DNS results is observed. The wave speed (c_r^*) is within 1.5% of its predicted value for both Case V1 and V2. Similar to the work of Orszag and Kells (1980), the growth of the disturbance amplitude demonstrates small deviation (less than 1%) with the linear stability theory over the integration time $0 \leq t \leq 10$ (see Table 3.2). The accuracy of the growth rates and wave speeds gives confidence to the viability of this code for solving the unsteady incompressible Navier-Stokes equations for the simulation of wave propagating problems.

3.4 Scalability Results

Two test cases were used to assess the strong scaling capabilities of the code. Specifics regarding each case are presented in Table 3.3. Each simulation is integrated 200 steps forward in time. The first 4 time steps display significant startup lag when compared with subsequent iterations and are not considered in this analysis. Furthermore, time required to write the field to a file is not considered in the scaling results. Both cases were run on the Kraken Cray XT5: peak performance of 1.17 PetaFLOPs, 112,896 compute cores, 147 TB of compute memory.

Strong scaling describes the ability of a parallel code to decrease the wall-time for a problem of specific size. For each case, the size of the problem (or number of gridpoints) was held constant while varying the number of processors assigned to the simulation. Figure 3.4 shows scaling results for Case T1. The number of processors varies between 12 and 768 (multiples of 12

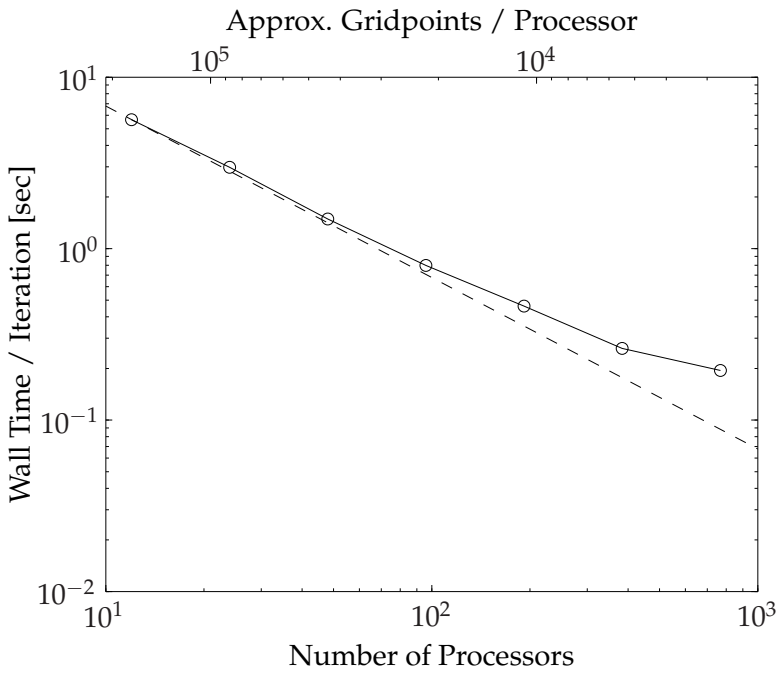

Figure 3.4: Strong scaling for Case T1: Re $=$ 400, $128 \times 128 \times 128$, neutrally stratified. Timing averaged over 196 iterations; startup effects are ignored. Dashed line, theoretical strong scaling; solid line / circles, DNS results.

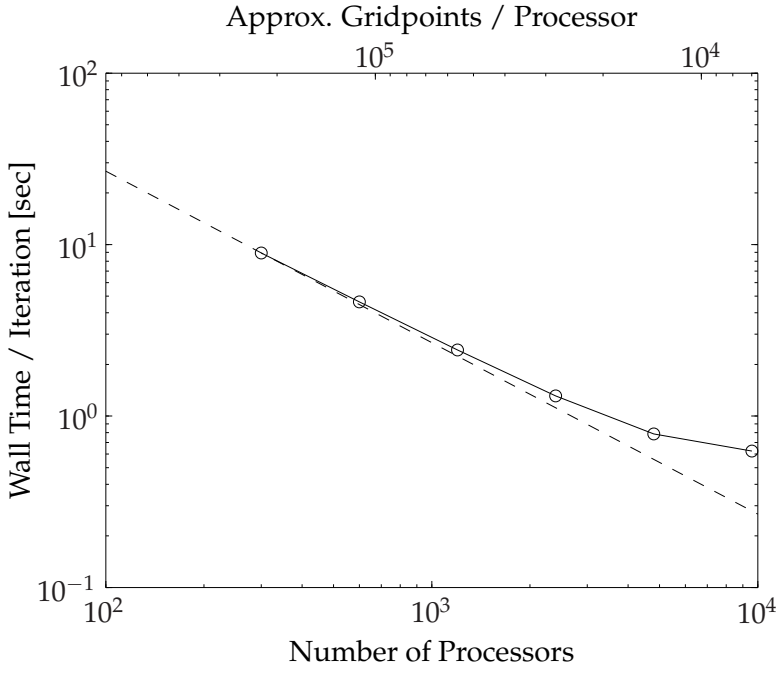

Figure 3.5: Strong scaling for Case T2: Re $=$ 1000, $512 \times 512 \times 256$, unstably stratified. Timing averaged over 196 iterations; startup effects are ignored. Dashed line, theoretical strong scaling; solid line / circles, DNS results.

required for Kraken) and the corresponding number of mesh points per processor is displayed along the top axis. Note that this is an approximate measure since the PETSc DA is left to determine how many nodes are assigned to each process. In general, the DA will work to balance the load equally. The dashed line in Fig. 3.4 represents ideal strong scaling where the time required is inversely proportional to the number of processors working on the problem. The results in Fig. 3.4 demonstrate strong scaling relatively consistently up until 384 processors are implemented. The 768 process simulation shows a clear decrease in efficiency, a consequence of the increased interprocess communication.

The strong scaling results for Case T2 are shown in Fig. 3.5. For this test the number of processors was allowed to vary between 300 and 9600. The DNS diverges from ideal scaling near the test cases with 2400 and 4800 processors. Although the test using 9600 processors converges faster than the 4800 test, the variance from ideal strong scaling represents a decrease in efficiency. Performing the simulation with 9600 as opposed to 4800 cores is a less efficient use of computational resources.

As demonstrated by the above examples, the number of processors will change between runs based on the overall problem size. It would seem that the number of variables per processor is a more logical choice for assessing scalability. Comparing the results from Case T1 and T2 (Fig. 3.4 and 3.5 respectively), the number of processors assigned to the task varies greatly. However, the top axis of each plot represents the number of unknowns per process. Both cases show divergence from ideal strong-scaling near 10000 unknowns per process. Decreasing the number of unknowns beyond this point causes a clear loss in efficiency. Based on the results from Fig. 3.4 and 3.5, the user should allocate no less than 14000 unknowns (meshpoints) per processor to ensure an efficient simulation.

Improving the efficiency of the code and decreasing the time required per iteration depends upon optimizing the most computationally expensive portion of the code. Monitoring the time required to perform each operation demonstrates the amount of effort spent at each step of the

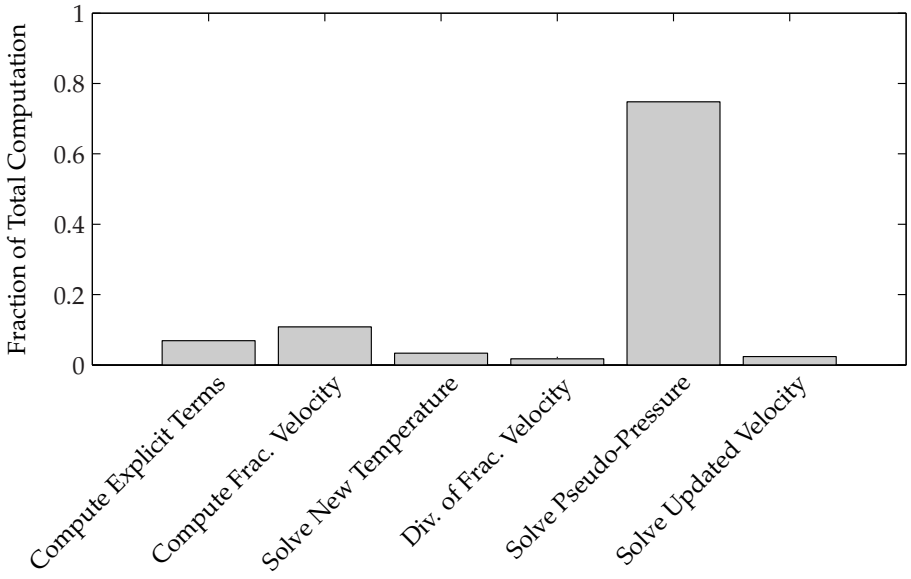

Figure 3.6: Computational Effort for Case T2: Re $= 1000$, $512 \times 512 \times 256$, unstably stratified. Results averaged over $300 \leq N_{\text{procs}} \leq 9600$.

code. A comparison of routines is provided in Fig. 3.6 for Case T2; as before, startup routines have been ignored since these represent a one-time expense and should be small when compared with the total run. The results have been averaged over the seven different parallel simulations. The chart clearly demonstrates that the solution of ϕ is by far the most computationally expensive portion of the code accounting for 75% of the total computational time. Due to the stiffness of the problem, the number of iterations required to solve the linear system given by Eq. 3.1.16 dramatically increases over the time required to solve for the velocity and temperature field (Eq. 3.1.7). While the GMRES algorithm decreased the residual of the velocity and temperature equation by over 5 orders of magnitude in as little as 10 iterations, the pseudo-pressure equation converges much slower. Figure 3.7 demonstrates a typical convergence curve for solving ϕ. Note that for a given solution procedure (such as GMRES) it is possible to decrease the time required to solve the pseudo-pressure equation by relaxing the convergence criteria. Of course, because this criteria directly affects the residual divergence of the velocity field, it must be selected such that the

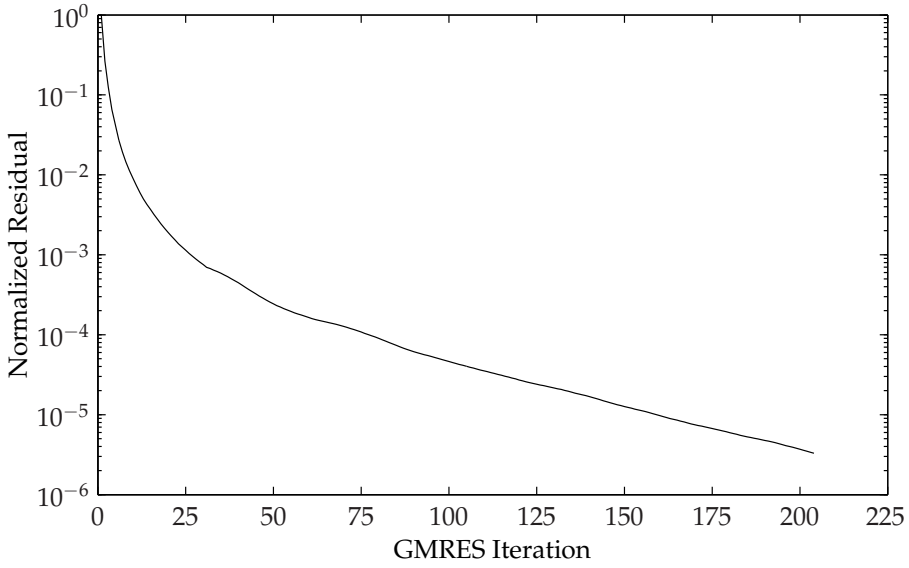

Figure 3.7: Example solution of pseudo-pressure (ϕ) using GMRES algorithm for Case T1. Residual normalized by initial value.

magnitude of the quantity remains small. For the simulations presented in this dissertation,

$$\left|\left|\nabla \cdot u_i^{n+1}\right|\right| < 10^{-5} \tag{3.4.1}$$

3.5 Recommendations

The code exhibits good strong scaling over a finite range of unknowns per processor. It is recommended that the number of meshpoints per process is kept at 14000 or above to maintain computational efficiency.

The use of finite differences in the lateral directions does not impose a 2^n requirement concerning the number of meshpoints and allows for nonuniform spacing in all directions which is especially important if periodic sidewall boundary conditions are replaced by solid boundaries (e.g. duct flow). Furthermore, only slight modifications are required to address other problems including spatially evolving transition problems that require non-periodic inflow/outflow boundary problems.

Future improvements are aimed at decreasing the computational cost of each simulation. Attention should be paid to finding a suitable preconditioner for the GMRES algorithm. This could substantially reduce the computational effort required to solve for each time step. Also, storage savings can be realized by coarsening the mesh in the lateral (x_1/x_2) directions away from the wall. In much the same manner that the vertical mesh is stretched, a step-wise resolution change for the horizontal directions will reduce the total number of unknowns. Finally, the simulation currently advances forward in time using a constant Δt. A variable time-stepping algorithm would require fewer steps (and less resources) to reach a predetermined convergence criteria.

Although the code has recently been running on the Kraken supercomputer at the University of Tennessee (and previously on Frost at NCAR), the initial development and debugging was performed on a personal PC. The PETSc libraries (Balay et al., 2010) are widely available, well supported, and have proven to be easy to implement.

CHAPTER 4

TURBULENT EKMAN LAYER: NEUTRAL STRATIFICATION

The ABL typically exhibits either unstable or stable stratification during daytime or nighttime hours respectively. Neutral stability of the ABL is a rare occurrence and usually occurs as a transient state between the unstable and stable stratifications (or vice-versa). Nevertheless, the neutrally stratified turbulent Ekman layer allows a unique look into the dynamics of the ABL if thermal forcing is removed. Without buoyant forcing, turbulence in the neutral Ekman layer is generated by mean shear alone. The flow field is unique, however, from turbulent flows without system rotation. As will be demonstrated, the Coriolis effect due to rotation generates a three-dimensional mean velocity field. This results in energy production in both horizontal components.

Like the laminar case, the turbulent Ekman layer still represents a balance between pressure gradient, Coriolis forces, and shear stresses. Given a high enough Reynolds number, the flow will transition to turbulence when perturbed. Previous studies have indicated that turbulence in the Ekman layer occurs at Reynolds numbers as low as $\mathrm{Re} = 400$ (Coleman et al., 1990, Marlatt, 1994). Turbulence in the boundary layer resulted in significant vertical growth of the mean velocity. Furthermore, the three-dimensional nature of the mean flow generates complex inter-component velocity interactions.

Although neutral stratification is a rare occurrence in atmospheric flows, it is frequently achieved in wind tunnel experiments. Recent wind tunnel studies have analyzed the wake of a wind turbine under neutral stratification (Chamorro and Porté-Agel, 2009, 2010). The LES of

Porté-Agel et al. (2010) studies how accurately different models represent actual turbine wake dynamics. Both Calaf et al. (2010) and Johnstone and Coleman (2012) model the fully-developed (infinite) wind turbine array using LES and DNS respectively.

To better compare neutrally stratified results with wind farm effects, a thorough analysis of the neutrally stratified Ekman boundary layer is presented here as a baseline for comparison. Details concerning the setup of the computation are provided in §4.1, mean flow statistics are presented in §4.2, and turbulent kinetic energy budgets are analyzed in §4.3. The characteristic shape of velocity and pressure structures in the turbulent Ekman layer are discussed in §4.4. Finally, an analysis of the popular $k - \varepsilon$ closure model is provided in §4.5.

4.1 Simulation Specifications

The turbulent Ekman layer simulation was initialized using the laminar Ekman layer velocity profile given in Eq. 2.5.2. Geostrophic balance was assumed and the mean pressure gradient was set by Eq. 2.5.3 with a Reynolds number of $\mathrm{Re} = 1000$. Random disturbances – with a strength of $\Delta = \pm 0.1$ – were added to the laminar velocity profile to trip the flow to turbulence. So as to save computational resources, the flow was initialized on a horizontally coarse mesh. The velocity field was subsequently interpolated onto a finer and finer mesh until no buildup of energy occurred at the highest wavenumbers. The final mesh had a resolution of $512 \times 512 \times 256$ corresponding to the x, y, and z directions respectively. At this resolution, an artificial dissipation coefficient (see Eq. 3.1.26) of $\beta = 0.05$ was sufficient to ensure stability. The Rayleigh friction had a maximum strength of $\alpha_{rf,\max} = 0.01$ with $z_{rf}/L_z = 5/6$.

Domain parameters (in terms of the turbulent depth δ, see §4.2.1) are given in Table 4.1 along with a comparison with a similar DNS study of Miyashita et al. (2006). It is clear that the mesh spacing and domain size are comparable to other Ekman layer DNS studies. Furthermore, DNS of Ekman layer turbulence at $\mathrm{Re} = 400$ showed that the majority of the largest turbulent structures

Table 4.1: Case A Domain Parameters

	NEW	Miyashita et al. (2006)
Re	1000	1140
Ro	500	570
$L_x/\delta = L_y/\delta$	2.08	1.92
$N_x = N_y$	512	512
$\Delta x^+ = \Delta y^+$	5.48	6.60
L_z/δ	2.31	1.92
N_z	256	512
Δz^+_{min}	0.477	0.147

are captured when L_x and L_y are greater than 2δ (Waggy et al., 2011). The time step which allowed for stability to be maintained was $\Delta t U_g/\delta_E = 0.01$ or $\Delta t f = 2 \times 10^{-5}$.

Once the final grid resolution was reached, the flow was integrated until a statistical steady state was reached based on the maximum turbulent kinetic energy and the surface friction velocity. The maximum turbulent kinetic energy is given by

$$E_{\text{max}} = \frac{1}{2} \left\langle u'u' + v'v' + w'w' \right\rangle \Big|_{\text{max}} \tag{4.1.1}$$

where $\langle \cdot \rangle$ denotes an average over horizontal planes. Thus, E_{max} is the maximum turbulent energy in the field at some distance from the wall z. The change of E_{max} with time is shown in Fig. 4.1 where $tf = 0$ corresponds to the start of the averaging period (after a statistical steady state had been reached). Given that the inertial time period of the flow field is f, an integration window of $0 \leq tf \leq 0.8$ captures almost a full inertial time period. Over the period $tf = 0.8$, 200 flow realizations were captured for analysis.

The friction velocity u_* is given by (Pope, 1993)

$$u_* = \sqrt{\frac{\tau_w}{\rho}} \tag{4.1.2}$$

and τ_w is the total shear stress at the wall. Note that τ_w is a function of both the streamwise and spanwise velocity components. In dimensionless form, the friction velocity u_*/U_g is given by

$$\frac{u_*}{U_g} = \left[\frac{1}{\text{Re}} \left\langle \sqrt{\left(\frac{\partial u}{\partial z}\right)^2 + \left(\frac{\partial v}{\partial z}\right)^2} \right\rangle \right]^{1/2} \tag{4.1.3}$$

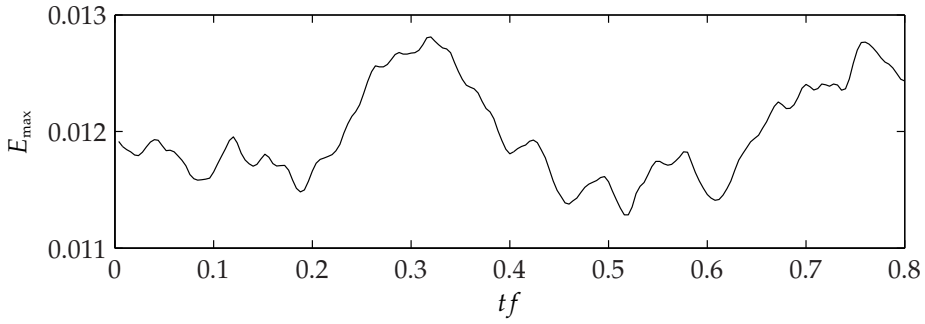

Figure 4.1: Time variation of maximum kinetic energy for Case A over averaging period.

or

$$\frac{u_*}{U_g} = \left[\frac{1}{\mathrm{Re}}\frac{\mathrm{d}}{\mathrm{d}z}\sqrt{\langle u\rangle^2 + \langle v\rangle^2}\right]^{1/2} \tag{4.1.4}$$

Both Eq. 4.1.3 and 4.1.4 are valid and give comparable results. As u_* is an averaged quantity, the friction velocity is only a function of the mean velocity field. The solid line in Fig. 4.2 shows the results from the DNS over the averaging window; the dashed line indicates the mean value of $u_*/U_g = 0.0520$ computed by averaging the 200 realizations over the time period. The mean value is within 4% of other Re $= 1000$ neutral Ekman layer simulations (see Table 4.2).

As with the friction velocity, the surface shear angle α_0 is computed by averaging the local shear angle spatially or computing the mean shear angle based on the mean velocity profiles:

$$\alpha_0 = \left\langle \tan^{-1}\left(\frac{\partial v/\partial z}{\partial u/\partial z}\right)\right\rangle \tag{4.1.5}$$

or

$$\alpha_0 = \tan^{-1}\left(\frac{\mathrm{d}\langle v\rangle/\mathrm{d}z}{\mathrm{d}\langle u\rangle/\mathrm{d}z}\right) \tag{4.1.6}$$

Table 4.2: Friction Velocity and Shear Angle Comparison for Case A

Case	Re	u_*/U_g	α_0 (deg)
A	1000	0.0520	18.56
Coleman (1999)	1000	0.0539	19.00
Miyashita et al. (2006)	775	0.0561	21.2
Miyashita et al. (2006)	1140	0.0520	19.4
Spalart et al. (2008)	1000	0.0535	19.36

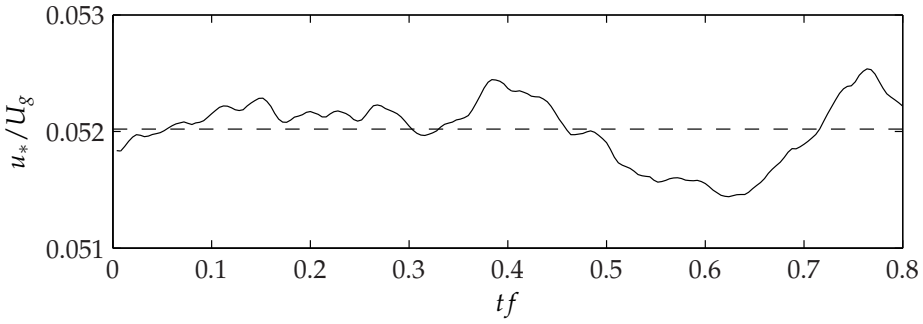

Figure 4.2: Time variation of friction velocity for Case A over averaging period. Mean friction velocity denoted by dashed line: $u_*/U_g = 0.052$.

The shear angle shown in Fig. 4.3 was computed via Eq. 4.1.5. The time series show fluctuations about the mean $\alpha_0 = 18.56^\circ$ as large as 0.7°. The $\mathrm{Re} = 1000$ cases of Coleman (1999) and Spalart et al. (2008) both demonstrate slightly higher surface shear angles. The deviation may be due, in part, to the size of the sampling window used for this case.

4.2 Mean Flow Statistics

Spatially and temporally averaged statistics were computed from the 200 flow realizations saved over the time period shown in Figs. 4.1-4.3. To accomplish this, the velocity field at some instance in time can be broken down into the sum of a mean and fluctuating velocity component

$$u_i = \langle u_i \rangle + u_i' \tag{4.2.1}$$

where $\langle u_i \rangle$ is the instantaneous mean component and $u_i' = u_i - \langle u_i \rangle$ is the fluctuating component. The instantaneous mean velocity $\langle u_i \rangle$ can then be temporally averaged to yield $\langle\langle u_i \rangle\rangle$. The double bracket $\langle\langle \cdot \rangle\rangle$ denotes a time average (over the period $tf = 0.8$) of a quantity that has been spatially averaged over the horizontal planes. For convenience, the temporal and spatial averaged will be denoted $\overline{(\cdot)} = \langle\langle \cdot \rangle\rangle$. This convention of using angle brackets to denote a spatial average and the overbar to denote an addition temporal average will be used throughout the dissertation unless

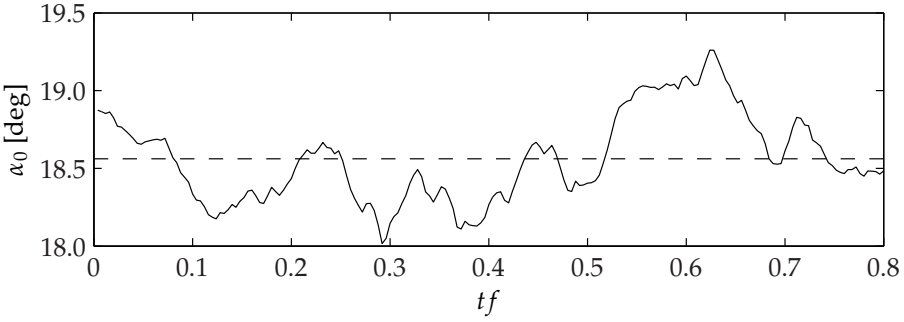

Figure 4.3: Time variation of surface shear angle for Case A over averaging period. Mean shear angle denoted by dashed line: $\alpha_0 = 18.56\,^\circ$.

otherwise noted. Mean velocities $\overline{u_i}$ will be denoted with a capital letter:

$$U_i = \overline{u_i} \tag{4.2.2}$$

Since the turbulent Ekman layer is not a spatially evolving flow (the boundary layer does not grow), spatial and temporal averaging are applicable. The wall-normal mean velocity component W is effectively zero: $\max(W) < 10^{-10}$.

4.2.1 Mean velocity profile

The mean velocity field for Case A is shown in comparison with the laminar solution in Fig. 4.4. The mean profile demonstrates growth in the vertical direction due to turbulent mixing. In the near wall region, the gradient of the mean velocity increases. The vertical coordinate in Fig. 4.4 has been normalized by the turbulent depth δ:

$$\delta = u_*/f \tag{4.2.3}$$

Blackadar and Tennekes (1968) proposed a velocity-defect law for neutrally barotropic planetary boundary layers such that the velocity-defect is Reynolds number independent and a function of (z/δ) only, specifically,

$$\frac{U - U_g}{u_*} = F_u\left(\frac{z}{\delta}\right) \tag{4.2.4a}$$

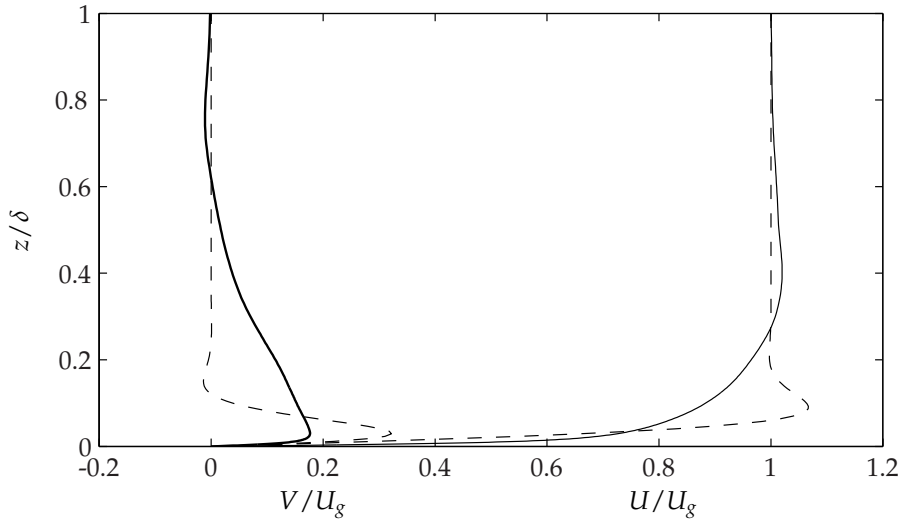

Figure 4.4: Mean velocity profile. Solid line, Re = 1000; dashed line, laminar.

$$\frac{V - V_g}{u_*} = F_v\left(\frac{z}{\delta}\right) \tag{4.2.4b}$$

where F_u and F_v are universal functions. The velocity-defect is shown in Fig. 4.5 after rotating the mean velocity to align with the surface shear angle α_0. These results are shown in comparison with the experimental work of Caldwell et al. (1972) and the Re = 400 Ekman simulation of Marlatt (1994). For the rotated V velocity component in Fig. 4.5(b), the agreement between the three sets of data is good. Both the Re = 400 and Re = 1000 DNS fall within the range of experimental data. However, less agreement is noted for the rotated U component. The current DNS velocity-defect falls outside of the experimental work. Although the Re = 400 shows agreement near $z/\delta = 0.1$, the Case A results show closer agreement to experimental work in the near-wall region. Furthermore, it appears the high Reynolds number DNS if offset from Caldwell's work by a factor of approximately 2.5 over the range $10^{-2} \leq z/\delta \leq 10^{-1}$. While the data do not directly confirm or invalidate the existence of universal functions F_u and F_v, the characteristic scale δ appears to be the appropriate length scale for the neutrally stratified turbulent Ekman layer. As such, it will be used frequently in scaling the spatial coordinates for the neutrally stratified case.

The velocity hodograph for Case A is shown in comparison with the characteristic laminar

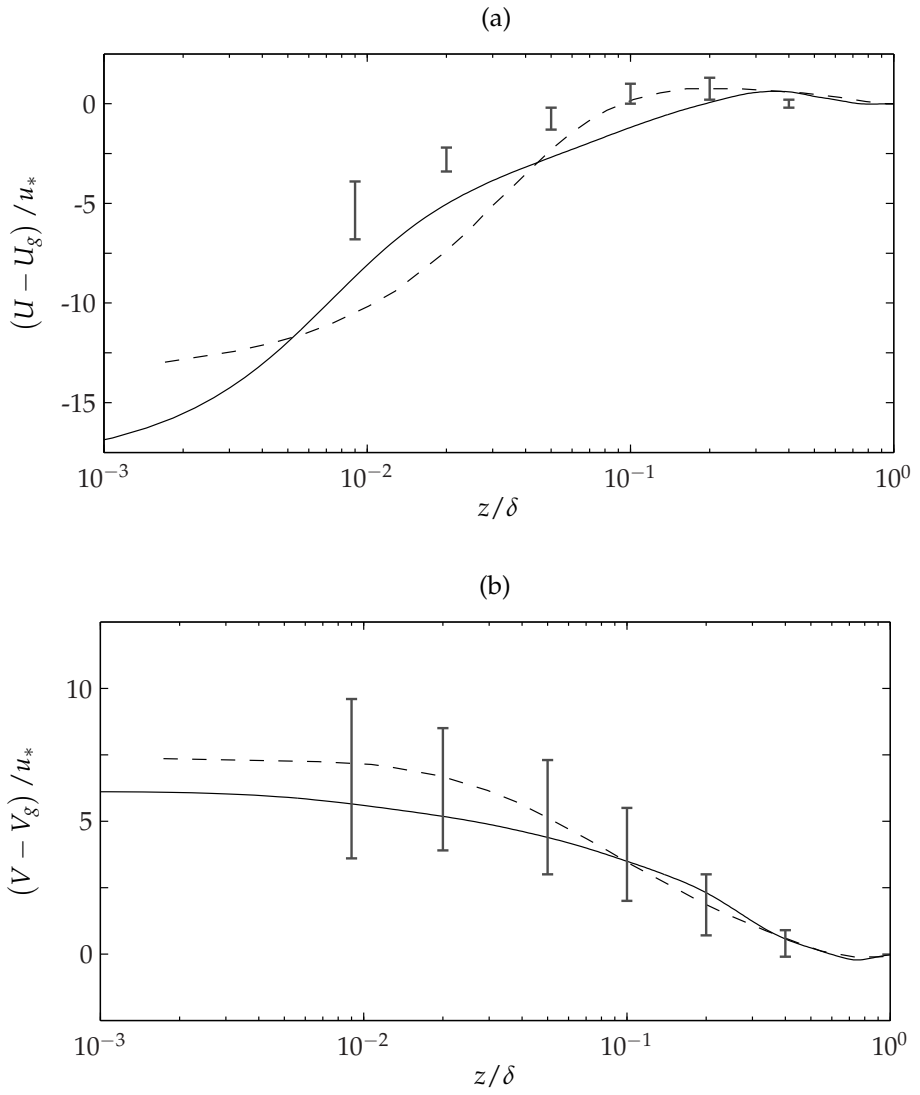

Figure 4.5: Case A velocity-defect. (a) U, (b) V. Note that the coordinates axes have been rotated for both figures such that U is aligned with the surface shear direction. Solid line, DNS at Re $= 1000$; dashed line, DNS at Re $= 400$ (Marlatt, 1994); error bars, range of data in Ekman experiment (Caldwell et al., 1972).

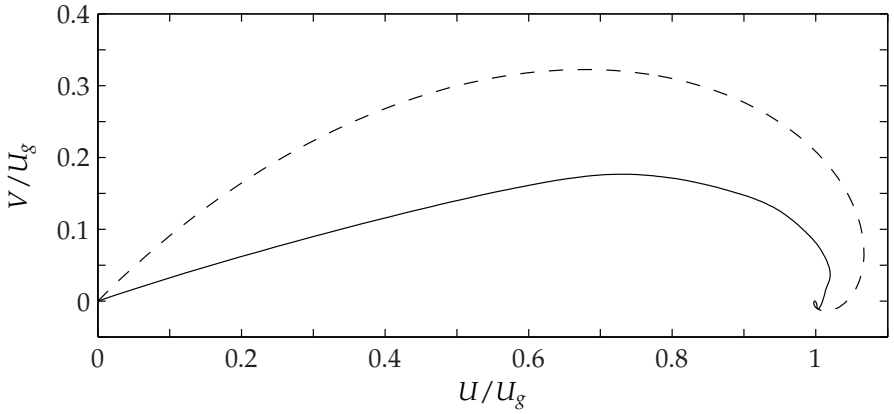

Figure 4.6: Case A velocity hodograph. Solid, Re = 1000; dashed, laminar Ekman spiral.

Ekman spiral in Fig. 4.6. The shear angle at the surface is decreased with the onset of turbulence and continues to decrease with an increase in Re (Marlatt et al., 2010, Miyashita et al., 2006). It is believed the kink seen at the top of the boundary layer for the Re = 1000 data is a consequence of the averaging window used. Since length and time scales increase with distance from the wall, it is speculated that the curve would maintain a smooth curl if a larger sample was used.

In order to better compare the turbulent Ekman boundary layer with other turbulent flows it is beneficial to plot the results in terms of the wall units

$$u^+ = \frac{u}{u_*} \tag{4.2.5}$$

and

$$z^+ = \frac{z u_*}{\nu} \tag{4.2.6}$$

In terms of dimensionless variables, these can be written as

$$u^+ = \frac{u/U_g}{u_*/U_g} \tag{4.2.7}$$

and

$$z^+ = \frac{z}{\delta_E}\frac{u_*}{U_g}\mathrm{Re} \tag{4.2.8}$$

Given the three-dimensional nature of the Ekman flow it is important to account for both the U

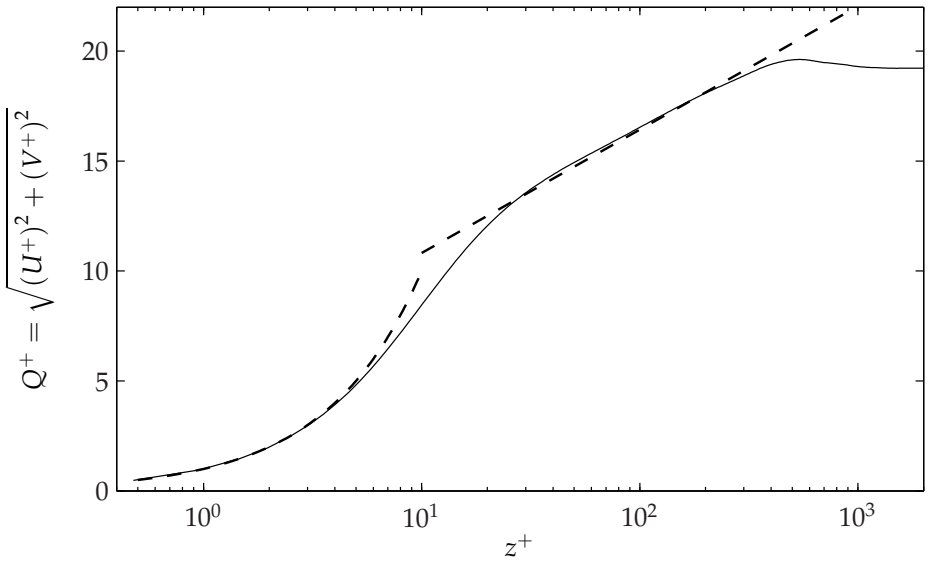

Figure 4.7: Mean velocity profile in terms of wall units. Solid,DNS data; dashed, $Q^+ = z^+$ for $z^+ < 10$ and $Q^+ = 1/\kappa \ln(z^+) + B$ for $z^+ > 10$. $\kappa = 0.41$ and $B = 5.2$.

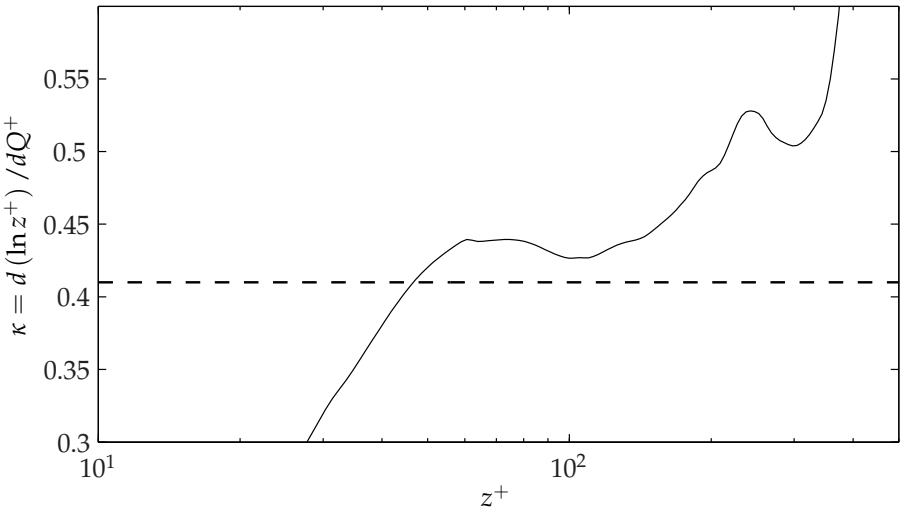

Figure 4.8: Calculated value of von Kármán 'constant'. Dashed line indicates $\kappa = 0.41$.

and V velocity components. Here a total velocity Q is defined as

$$Q = \sqrt{U^2 + V^2}, \tag{4.2.9}$$

or, in terms of wall units,

$$Q^+ = \sqrt{(U^+)^2 + (V^+)^2} \tag{4.2.10}$$

Figure 4.7 gives Q^+ as a function of z^+. Note that Q^+ is accurately represented in the near-wall region by $Q^+ = z^+$ for $z^+ \leq 5$. At this Reynolds number a log-law region develops and appears to be well approximated by $Q^+ = (1/\kappa)\ln(z^+) + B$ where the Kármán constant is taken to be $\kappa = 0.41$ and $B = 5.2$. A more precise measure of the Kármán constant is evaluated using

$$\kappa = \frac{\mathrm{d}(\ln z^+)}{\mathrm{d}Q^+} \tag{4.2.11}$$

Figure 4.8 shows the 'constant' over the logarithmic region where κ exhibits nearly constant behavior over approximately a half decade of z^+. This agrees with previously published results for comparable Reynolds numbers (Miyashita et al., 2006, Spalart et al., 2008). Comparing with the widely accepted value of $\kappa = 0.41$, the computed κ from the DNS appears to be slightly higher with the constant closer to $\kappa = 0.44$.

4.2.2 Second-order Moments

The importance of the fluctuating velocity component u_i' is clearly evident in the Reynolds-averaged Navier-Stokes equations (RANS, see App. A) where the governing equation for the mean flow U_i is independent of fluctuating components except for the term $\partial\overline{u_i'u_j'}/\partial x_j$. The second order moments of the fluctuating velocity components are termed Reynolds stresses where the product of aligned velocity components ($\overline{u'u'}$, $\overline{v'v'}$, and $\overline{w'w'}$) represent normal stresses and the cross-correlated products ($\overline{u'v'}$, $\overline{u'w'}$, and $\overline{v'w'}$) are shear stresses. Furthermore, the turbulent kinetic energy of the turbulent field k is given by the sum of the normal Reynolds stresses:

$$k = \frac{1}{2}\left(\overline{u'u'} + \overline{v'v'} + \overline{w'w'}\right) \tag{4.2.12}$$

Normal Reynolds stresses for Case A are shown in Fig. 4.9. Each stress component reaches a maximum at slightly different distances from the wall. The streamwise Reynolds stress $\overline{u'u'}$ reaches a maximum below the start of the log-law region at approximately $z/\delta \approx 0.011$ ($z^+ \approx 15$). A 'hump' which can be seen in $\overline{u'u'}$ – Fig. 4.9(b) – is also noted in the Re $= 775$ and Re $= 1140$ results of Miyashita et al. (2006). The strength of this artifact has been found to increase with an increase in Reynolds number until a local maximum becomes present for both pipe flow (Morrison et al., 2004) as well as flat-plate boundary layers (Marusic and Kunkel, 2003). $\overline{v'v'}$ peaks at a magnitude less than $1/3$ that of $\overline{u'u'}$ at $z/\delta \approx 0.023$ ($z^+ \approx 29$). For $0.25 < z/\delta < 0.7$ ($350 < z^+ < 800$), $\overline{v'v'}$ is the dominant stress. This region corresponds to the location where U reaches a maximum and dU/dz is nearly zero. Like the streamwise normal stress, $\overline{v'v'}$ displays an inflection (arguably more prominent than $\overline{u'u'}$) above $z/\delta > 0.1$. The location relative to the streamwise inflection is further from the wall and corresponds to a region of the flow where the gradient of the mean spanwise velocity is nearly constant. The effect of the wall is very pronounced in the $\overline{w'w'}$ profile as growth of vertical Reynolds stresses is heavily suppressed. Only when $z^+ > 50$ is the magnitude of $\overline{w'w'}$ within a factor of two of either horizontal energy component. Unlike the streamwise and spanwise normal Reynolds stresses, the vertical stress does not display as prominent of an inflection.

Computing k from Eq. 4.2.12 for Case A gives the distributions shown in Fig. 4.10. The maximum turbulent intensity is found at $z/\delta = 0.012$, very near the location of maximum $\overline{u'u'}$ (which is expected given that the streamwise Reynolds stress is the dominant term in the near wall region). Unlike the streamwise component which displays inflections in the middle region of the boundary layer, k is well represented by $k/u_*^2 = -\ln(z/\delta)$ for $0.02 \leq z/\delta \leq 1$. From Fig. 4.7 and 4.10(b) it appears that both the mean velocity and turbulent kinetic energy may be governed by some form of log-law outside of the near-wall region for low Reynolds number flows.

Reynolds shear stresses (Fig. 4.11) are defined by $-\overline{u_i'u_j'}$ when $i \neq j$. The convention of showing the negative of the shear stress stems from the fact that a negative stress, in association

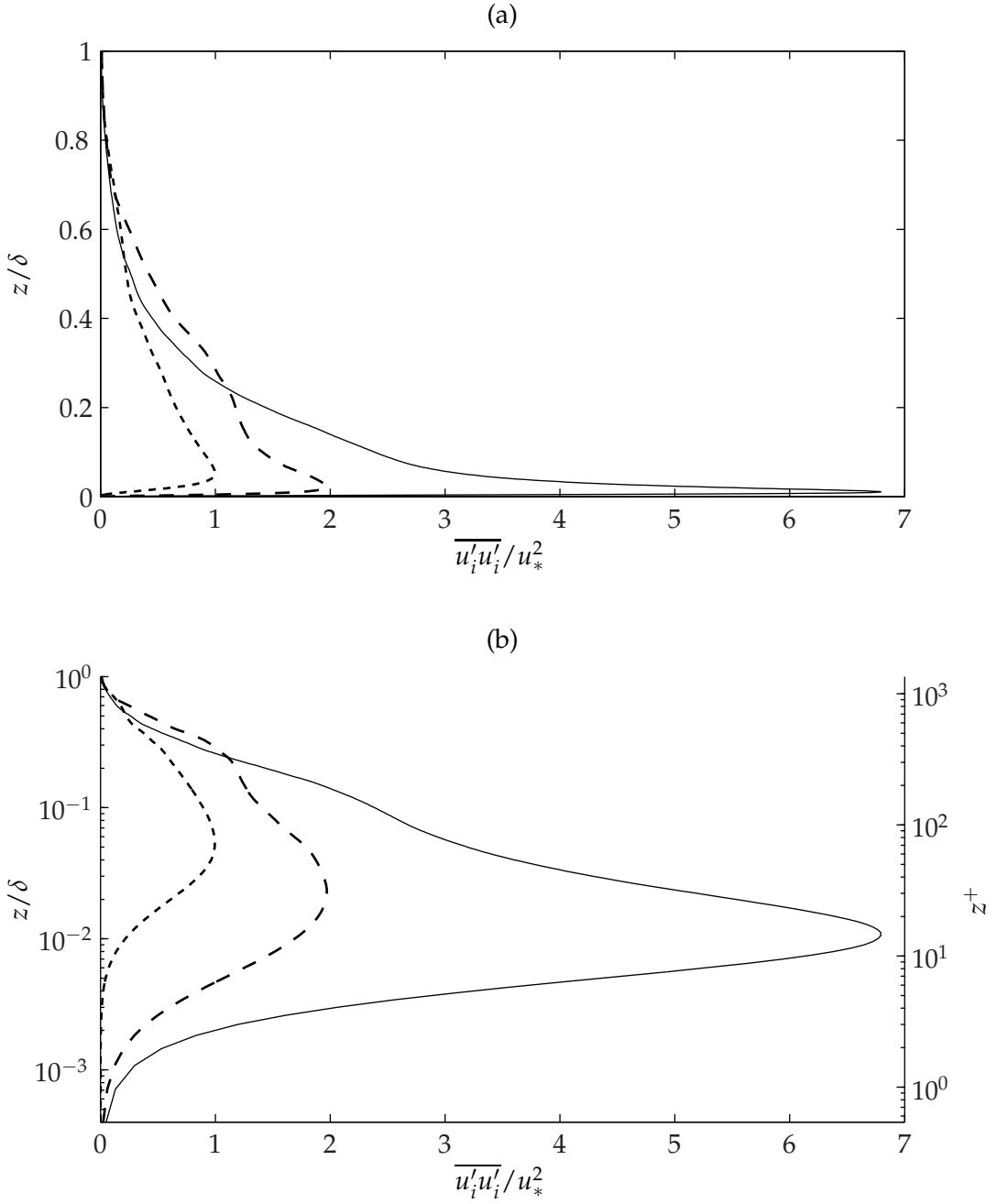

Figure 4.9: Normal Reynolds stresses: solid line, $\overline{u'u'}$; dashed line, $\overline{v'v'}$; dotted line, $\overline{w'w'}$. Note that repeated indices do not imply a summation.

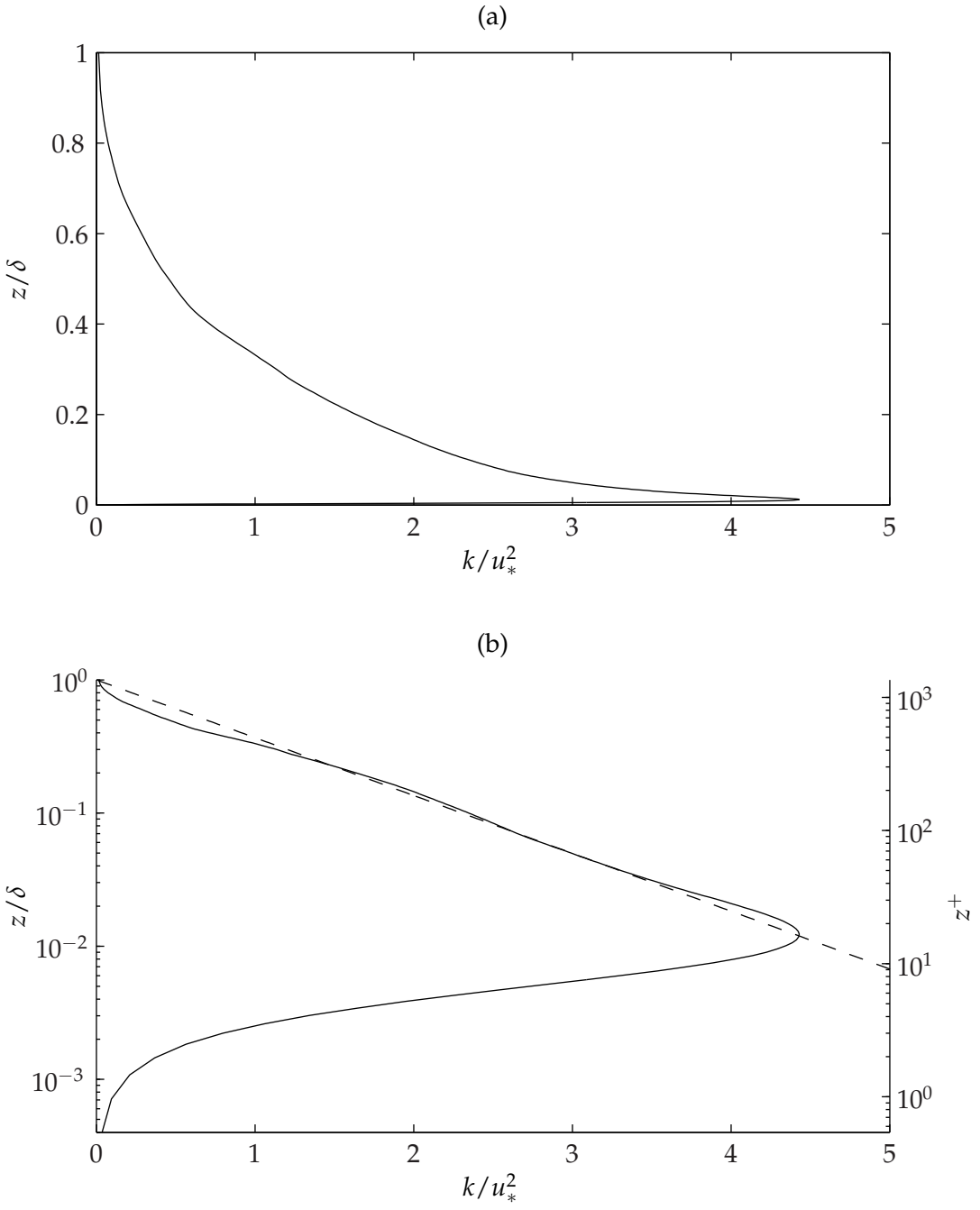

Figure 4.10: Turbulent kinetic energy for Case A: solid line, DNS; dashed line, $k/u_*^2 = -\ln(z/\delta)$.

with a positive velocity gradient, will produce (rather than destroy) turbulent energy. The largest contribution in the near-wall region comes from $-\overline{u'v'}$. A minimum at $z/\delta = 0.009$ ($z^+ \approx 12$) is comparable to the magnitudes of the normal Reynolds stresses presented in Fig. 4.9. Contribution by $-\overline{u'v'}$ Reynolds shear stress is caused by rotation and is not observed in nonrotating flows (Mansour et al., 1988); even at Re $= 400$, Marlatt et al. (2010) demonstrated the significant contribution of $-\overline{u'v'}$ to the energy budgets for the Ekman layer. Accordingly, $-\overline{u'v'}$ does not contribute turbulent kinetic energy production and simply provides a means of redistributing energy. The $-\overline{u'w'}$ term remains positive for the majority of the boundary layer indicative of turbulence kinetic energy production by means of sweeps and ejections. Similar behavior was noted for the Re $= 400$ turbulent Ekman layer (Marlatt et al., 2010). The $-\overline{v'w'}$ term shows a small positive region near the wall before switching signs at $z^+ \approx 58$. The point of crossover roughly correlates with the sign change of $-\overline{u'v'}$.

4.2.3 Third and Fourth-order Moments

The Reynolds-averaged Navier-Stokes equations give rise to 6 second-order moments that must be modeled in order to close the system of equations. If an attempt is made to derive a governing equation for the $\overline{u_i'u_j'}$ terms, third-order moments appear. The dependence of order n moments on those of order $n+1$, or $m^n = f\left(m^{n+1}\right)$, represents an infinite regression. This phenomena, first recognized by Keller and Friedmann (1924), represents the 'closure problem' of turbulence: how do the fluctuating velocity components relate to the mean?

Here several higher-order velocity statistics are calculated. The third-moment of a velocity component normalized by the cube of the root-mean-square of the fluctuating velocity component is termed the skewness:

$$S_{u_i} = \frac{\overline{u_i'u_i'u_i'}}{\left(\overline{u_i'u_i'}\right)^{3/2}} \tag{4.2.13}$$

Note that no summation is implied by repeated indices and that, by definition, the skewness is a dimensionless quantity. The skewness provides a measure of the frequency at which either

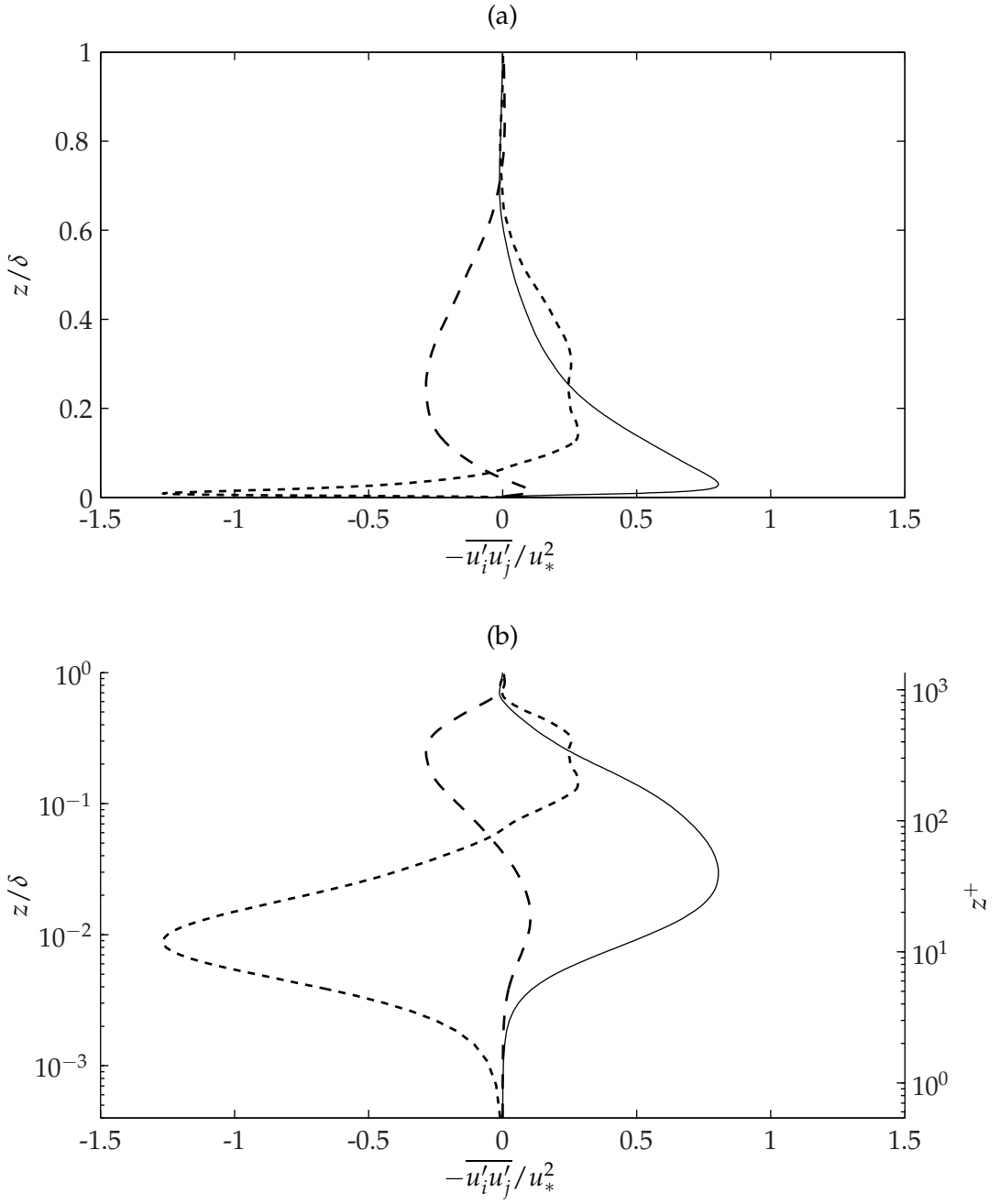

Figure 4.11: Shear Reynolds stresses for Case A: solid line, $-\overline{u'w'}$; dashed line, $-\overline{v'w'}$; dotted line, $-\overline{u'v'}$.

positive or negative extreme events occur in the fluctuating velocity field. A positive skewness indicates that large amplitude positive fluctuations are more likely to occur than negative fluctuations of a similar strength (Tennekes and Lumley, 1972). Zero skewness implies that extreme high or low-momentum events are equally likely to take place.

The skewness for Case A is shown in Fig. 4.12. All three velocity components show a positive skewness in the very near wall region where high speed streaks and vertical bursts are evident (see §4.4). The skewness of the wall-normal velocity (S_w) changes sign between $0.003 < z/\delta < 0.023$ ($4.1 < z^+ < 31.1$) and then remains positive with $S_w \approx 0.5$ throughout the boundary layer. The streamwise skewness S_u remains negative between $0.01 < z/\delta < 0.75$ with minima at $z/\delta = 0.023$ and $z/\delta = 0.42$. The minimum skewness $S_u \approx -0.8$ at $z/\delta \approx 0.42$ matches closely with the location of maximum streamwise velocity (see Fig. 4.4). It is interesting to note a local maximum in the vertical skewness at the same height as the minimum in S_u. This suggests the existence of strong ejections ($+w'$, $-u'$) where $\partial U/\partial z = 0$. The spanwise velocity skewness S_v is positive for the majority of the boundary layer, and, interestingly, the crossover from positive to negative skewness occurs at the same location as the crossover for S_u ($z/\delta = 0.75$). Moreover, the point where $S_v = S_u = 0$ corresponds to the minimum in the spanwise velocity profile where $\partial V/\partial z = 0$. The maximum spanwise skewness of $S_v = 0.86$ is located at the point where $V = 0$.

The kurtosis – or 'flatness' (Tennekes and Lumley, 1972) – represents the normalized fourth-order moment of the velocity components:

$$K_{u_i} = \frac{\overline{u_i' u_i' u_i' u_i'}}{\left(\overline{u_i' u_i'}\right)^2} \tag{4.2.14}$$

As with the skewness, the kurtosis is a normalized function and gives an estimate for the frequency at which extreme events occur. However, K_{u_i} will always be positive since the order of the moment is even. A high value of kurtosis ($K > 3$) indicates a high probability of small fluctuations about the mean coupled with an increase in extreme events (large positive or negative fluctuating velocities) with respect to a Gaussian distribution. A low kurtosis ($K < 3$) signifies a flatter distribution with respect to the Gaussian. The flatness of the Gaussian distribution is $K = 3$.

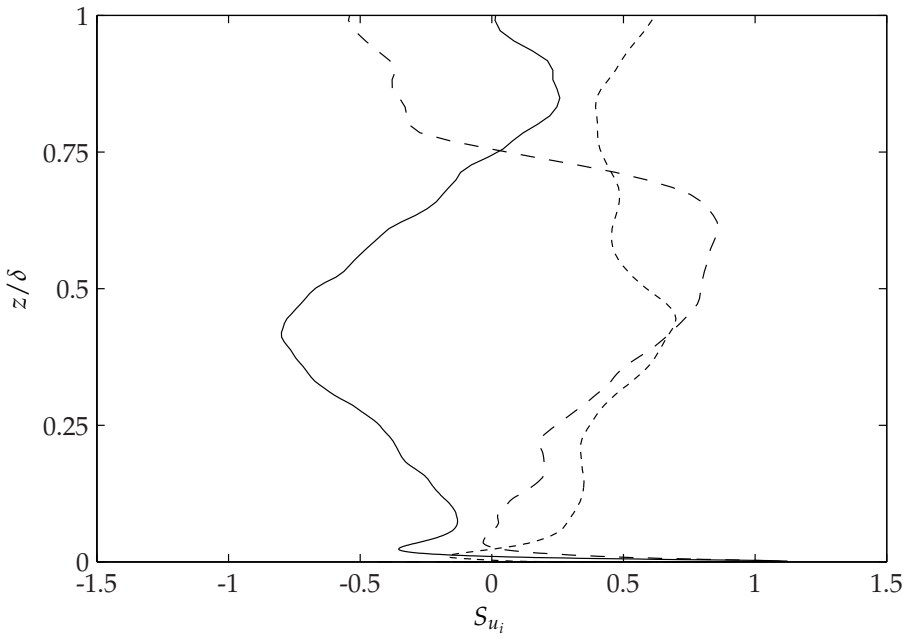

Figure 4.12: Velocity skewness for Case A: solid line, S_u; dashed line, S_v; dotted line, S_w.

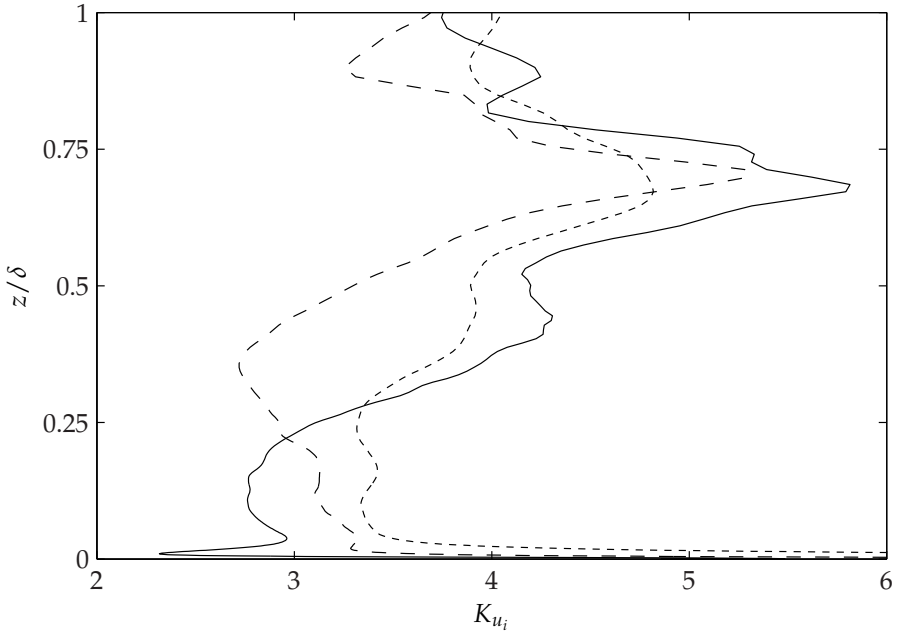

Figure 4.13: Velocity kurtosis (flatness) for Case A: solid line, K_u; dashed line, K_v; dotted line, K_w.

Figure 4.13 shows the kurtosis for the three velocity components. The very near-wall region is characterized by large kurtosis for all three components ($K_u = 5.46$, $K_v = 9.73$, and $K_w = 39.60$ at $z^+ = 0.4767$). The very large value of K_w is a consequence of being oriented in the wall-normal direction. The streamwise kurtosis decreases to a minimum of $K_u = 2.3$ at $z^+ = 12.9$. Apart from two inflections near $z/\delta \approx 0.1$ and $z/\delta \approx 0.5$ the streamwise kurtosis increases until a maximum flatness of $K_u = 5.815$ is reached near $z/\delta = 0.7$. The spanwise kurtosis is greater than 3 for the majority of the boundary layer indicating a high probability for low amplitude fluctuations and localized outbursts of high amplitude fluctuations. The vertical kurtosis (apart from the near wall region) increases until all three components of kurtosis share the same peak at $z/\delta \approx 0.7$.

Given that the skewness and kurtosis are high-order moments, statistical convergence is harder to obtain than the second-order statistics. This is clearly evident in the small fluctuations occurring in the data sets presented in Fig. 4.12 and 4.13. Furthermore, these statistics are difficult to measure accurately in the ABL due to data noise and sampling constraints (Lenschow et al., 1994, 2000). Recent research has been conducted concerning different methods of modeling the velocity kurtosis as a function of the velocity skewness (Sattin et al., 2009, Schopflocher and Sullivan, 2005). Tampieri et al. (2000) and Alberghi et al. (2002) evaluate wind tunnel and sodar data respectively to determine a value of α such that

$$K_{u_i} = \alpha \left(S_{u_i}^2 + 1 \right) \tag{4.2.15}$$

The quadratic relationship given in Eq. 4.2.15 was first proposed by Mole and Clarke (1995) and it can be shown that $\alpha = 1$ is the lower limit of the relationship (J. Ernest Wilkins, 1944). For the purely shear driven flows, Tampieri et al. (2000) proposed $\alpha = 2.3$ for the streamwise velocity and $\alpha = 3.3$ for vertical velocity. Figures 4.14 – 4.16 show plots of kurtosis versus skewness below $z^+ < 600$ (this covers the viscous sublayer, buffer region, and log-law region).

From Fig. 4.14 it is clear that the approximation of kurtosis as the square of the skewness is good. While $\alpha = 2.3$ does well at capturing the very near-wall region, a better approximation of the log-law regime is characterized by $\alpha = 2.6$. The largest deviation from the parabolic profiles

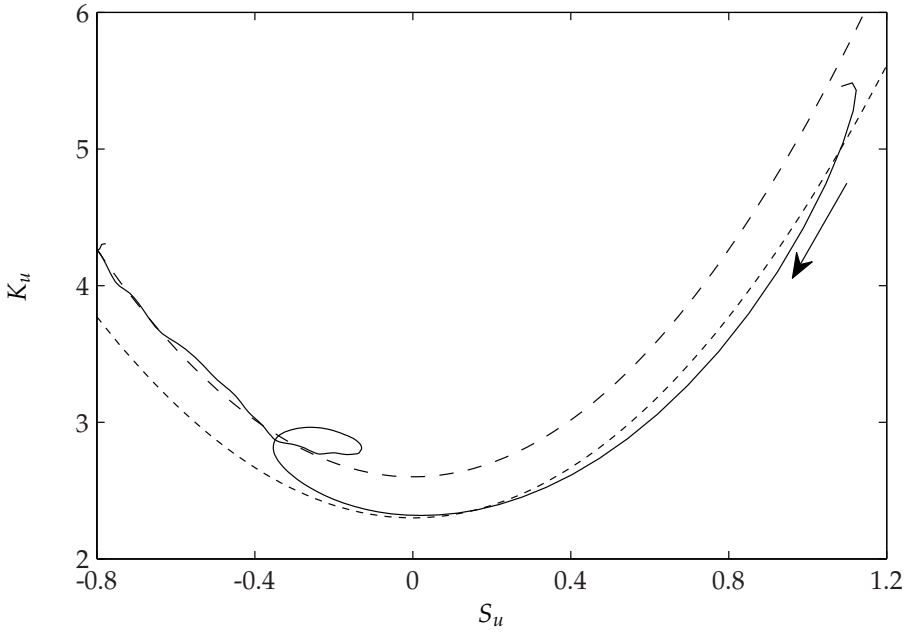

Figure 4.14: Skewness vs. Kurtosis for streamwise velocity component, Case A: solid line, DNS ($z^+ < 600$); dashed line, $\alpha = 2.6$; dotted line, $\alpha = 2.3$. Arrow indicates increasing z.

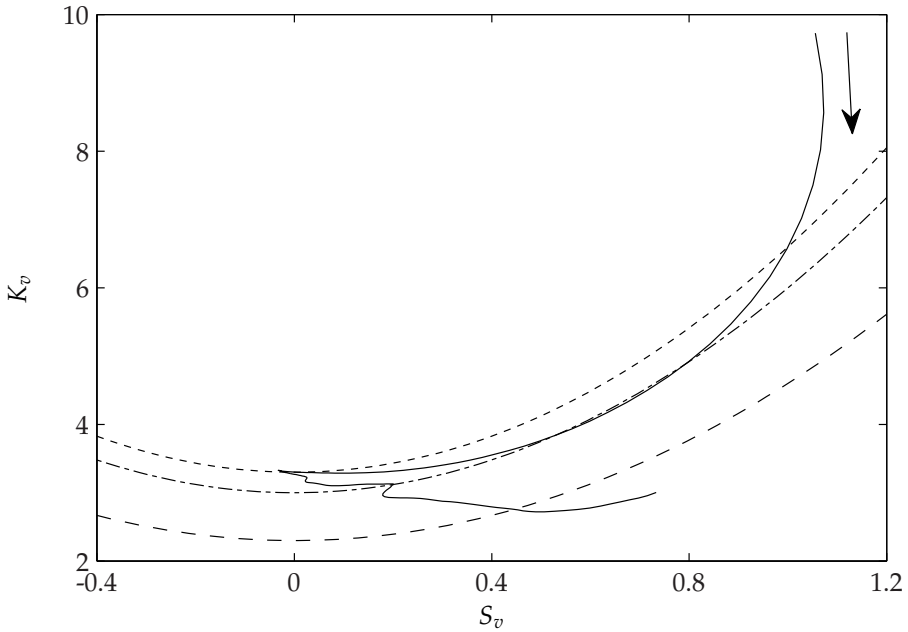

Figure 4.15: Skewness vs. Kurtosis for spanwise velocity component, Case A: solid line, DNS ($z^+ < 600$); dashed line, $\alpha = 2.3$; dotted line, $\alpha = 3.3$; dash-dot line, $\alpha = 3$. Arrow indicates increasing z.

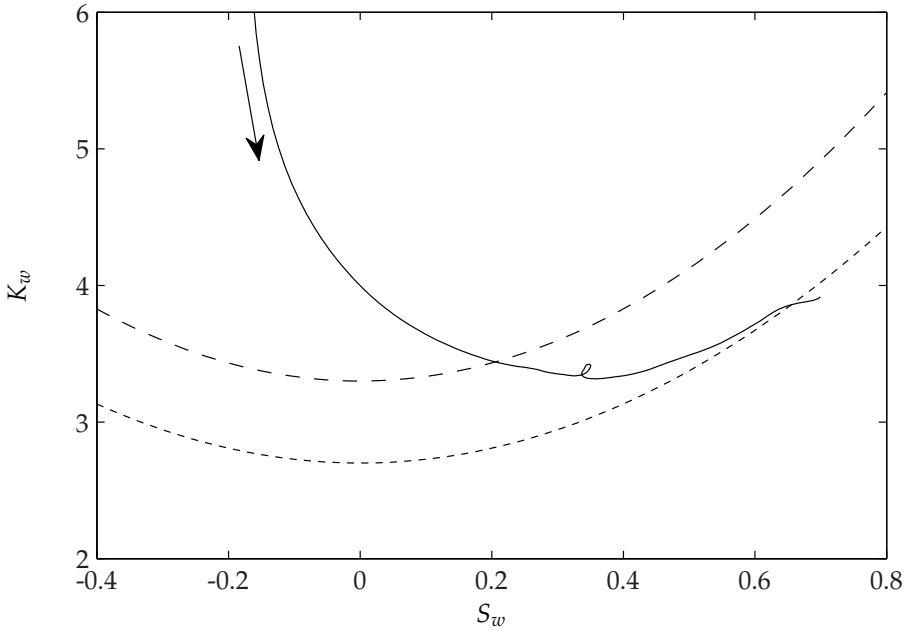

Figure 4.16: Skewness vs. Kurtosis for vertical velocity component, Case A: solid line, DNS ($z^+ < 600$); dashed line, $\alpha = 3.3$; dotted line, $\alpha = 2.7$. Arrow indicates increasing z.

occur at the near-wall inflection that occurs in both the kurtosis and skewness. These inflections manifest themselves in Fig. 4.14 as the closed loop. Regardless, the $\alpha = 2.6$ model still does a decent job of predicting the kurtosis based on the skewness of the streamwise velocity. The excellent agreement noted with the streamwise velocity component between the model and DNS is less evident for the spanwise component. Much of the data is bounded within the curves set by $\alpha = 2.3$ and $\alpha = 3.3$. The kurtosis through the log-law region does not appear to be a parabolic function of the skewness. Tampieri et al. (2000) note that $\alpha = 3.3$ for the vertical velocity component in a shear driven flow field. The data shown in Fig. 4.16 demonstrates that this value is too high outside of the near-wall region. A better estimate to the data is given by $\alpha = 2.7$, which is in agreement with the estimate $\alpha = 2.4 \pm 0.3$ given by Alberghi et al. (2002) for the convective boundary layer.

4.3 Turbulent Kinetic Energy Budgets

The RANS equations are heavily dependent upon the second-order Reynolds stresses $\overline{u_i' u_j'}$. Equations governing the dynamics associated with these terms can be developed from the momentum equation for the fluctuating component (see Appendix B). The resulting budget accounts for energy redistribution among various energy sources and sinks. Equation 4.3.1 gives the general form of energy budget for the three variance (normal stress) and three covariance (shear stress) terms.

$$\underbrace{\frac{\partial \overline{u_i' u_k'}}{\partial t}}_{0} = 0 = \underbrace{-U_j \frac{\partial \overline{u_i' u_k'}}{\partial x_j}}_{\text{I}} \underbrace{+\overline{u_i' \theta_v'} \delta_{k3} + \overline{u_k' \theta_v'} \delta_{i3}}_{\text{II}} \underbrace{-\overline{u_i' u_j'} \frac{\partial U_k}{\partial x_j} - \overline{u_k' u_j'} \frac{\partial U_i}{\partial x_j}}_{\text{III}}$$

$$\underbrace{-\frac{\partial \overline{u_i' u_j' u_k'}}{\partial x_j}}_{\text{IV}} \underbrace{-\frac{2}{\mathrm{Re}} \overline{\frac{\partial u_i'}{\partial x_j} \frac{\partial u_k'}{\partial x_j}}}_{\text{V}} \underbrace{+\frac{1}{\mathrm{Re}} \frac{\partial^2 \overline{u_i' u_k'}}{\partial x_j \partial x_j}}_{\text{VI}} \underbrace{+\overline{p' \left(\frac{\partial u_i'}{\partial x_k} + \frac{\partial u_k'}{\partial x_i} \right)}}_{\text{VII}} \tag{4.3.1}$$

$$\underbrace{-\frac{\partial \overline{u_i' p'}}{\partial x_k} - \frac{\partial \overline{u_k' p'}}{\partial x_i}}_{\text{VIII}} \underbrace{+\frac{1}{\mathrm{Ro}} \left(\varepsilon_{kj3} \overline{u_i' u_j'} + \varepsilon_{ij3} \overline{u_k' u_j'} \right)}_{\text{IX}}$$

The ten terms which make up the energy budget are (0) temporal variation; (I) advection by mean shear, $A_{i,k}$; (II) buoyant production of turbulent energy, $\beta_{i,k}$; (III) production by mean shear stresses, $P_{i,k}$; (IV) transport via turbulent diffusion, $T_{i,k}$; (V) viscous dissipation, $\varepsilon_{i,k}$; (VI) molecular diffusion, $D_{i,k}$; (VII) pressure strain, $\Phi_{i,k}$; (VIII) pressure diffusion, $\Theta_{i,k}$; and (IX) Coriolis redistribution, $C_{i,k}$.

For the statistically-steady, neutrally-stratified, and horizontally-homogeneous turbulent Ekman layer, some simplifications to Eq. 4.3.1 are relevant. Temporal variation of the Reynolds stress (term 0) is assumed to be zero since the solution has reached a quasi-steady state. Furthermore, the enforcement of periodicity in the spanwise and streamwise directions ensures that no mean gradients exist in either direction: $\partial/\partial x = \partial/\partial y = 0$. Given that the wall-normal mean

velocity $W = 0$, the advection by mean shear $A_{i,k} = 0$ for all i and k. Finally, neutral stratification dictates that no buoyant forcing occurs, thus, $\beta_{i,k} = 0$.

The seven remaining terms in the energy budget were computed for each Reynolds stress term and are presented in the following sections. Due to the absence of buoyant forcing, the production by mean shear, $P_{i,k}$ is the only means of producing turbulent kinetic energy. The driving force behind production is the gradient in the mean velocity profile, without which, the turbulent kinetic energy will decay. Destruction of turbulent kinetic energy is accomplished only through viscous dissipation, $\varepsilon_{i,k}$. The five remaining terms in the energy budget ($T_{i,k}$, $D_{i,k}$, $\Phi_{i,k}$, $\Theta_{i,k}$, and $C_{i,k}$) account for both redistribution as well as energy transport between various Reynolds stresses. Diffusion of turbulent energy is accomplished through three distinct mechanisms: pressure, molecular, and turbulent diffusion. At high Reynolds number, the diffusion by molecular interactions is typically orders of magnitude smaller than diffusion by turbulent motions (Tennekes and Lumley, 1972). This is a consequence of the fact that $D_{i,k}$ occurs at a much smaller length scale than $T_{i,k}$. For the relatively low Reynolds number presented here, both terms prove important. The pressure diffusion and pressure strain terms can be combined into a single term which accounts for all pressure effects:

$$-\overline{u'_k \frac{\partial p'}{\partial x_i}} - \overline{u'_i \frac{\partial p'}{\partial x_k}} = \overline{p' \left(\frac{\partial u'_i}{\partial x_k} + \frac{\partial u'_k}{\partial x_i} \right)} - \frac{\partial \overline{u'_i p'}}{\partial x_k} - \frac{\partial \overline{u'_k p'}}{\partial x_i} \tag{4.3.2}$$

or

$$\Pi_{i,k} = \Phi_{i,k} + \Theta_{i,k} \tag{4.3.3}$$

The pressure strain term is commonly referred to as the return-to-isotropy component. A summation over all three normal Reynolds stresses is zero through application of the continuity equation (i.e. $\Phi_{i,i} = 0$). Therefore, pressure strain acts as an avenue through which energy is redistributed between normal stresses. Like $\Phi_{i,i}$, the sum of the normal components of Coriolis redistribution is also zero: $C_{i,i} = 0$.

4.3.1 Variance Budgets

The kinetic energy budgets for the three velocity variances, $\overline{u'u'}$, $\overline{v'v'}$, and $\overline{w'w'}$ are presented in Fig. 4.17, 4.18, and 4.19 respectively. All terms have been nondimensionalized by u_*^3/δ. The majority of the boundary layer $0.05 \leq z/\delta \leq 1$ is shown in the top panel; the bottom plot provides details in the near wall region.

Streamwise Variance Budget: $\overline{u'u'}$

The variance budget for the streamwise turbulent kinetic energy highlights the presence of production by mean shear. $P_{1,1}$ peaks near $z^+ = 11.5$, closely matching the $\mathrm{Re} = 400$ results of Marlatt et al. (2010) who note peak production at $z^+ \approx 12$. This location correlates closely with the location of the maximum $\overline{u'u'}$ as shown in Fig. 4.9(b). Production decreases steadily until the gradient of the mean velocity changes sign, at which point, the production acts as a sink. Meanwhile, dissipation acts as the primary sink throughout the boundary layer. The small inflection in $\varepsilon_{1,1}$ near $z^+ \approx 10$ is also evident other neutral Ekman (Marlatt et al., 2010) and channel flow (Mansour et al., 1988) simulations. It seems the rate of dissipation is reduced due to the increased transport through both turbulent and molecular diffusion. The ability of these terms to transfer energy away from the region of peak production relaxes the dissipation rate necessary to maintain balance.

The maximum dissipation at the wall is matched by the small-scale molecular diffusion which transfers energy away from regions of high production and towards the wall. While turbulent diffusion also plays a minor role in moving energy to the wall, $T_{1,1}$ is largely responsible for transporting energy upwards into the boundary layer.

Pressure diffusion is not present in the budget equation for $\overline{u'u'}$ given the assumption of horizontal homogeneity. Consequently, pressure effects manifest themselves only through the return-to-isotropy term which attempts to restore isotropic balance to the flow field. Given that

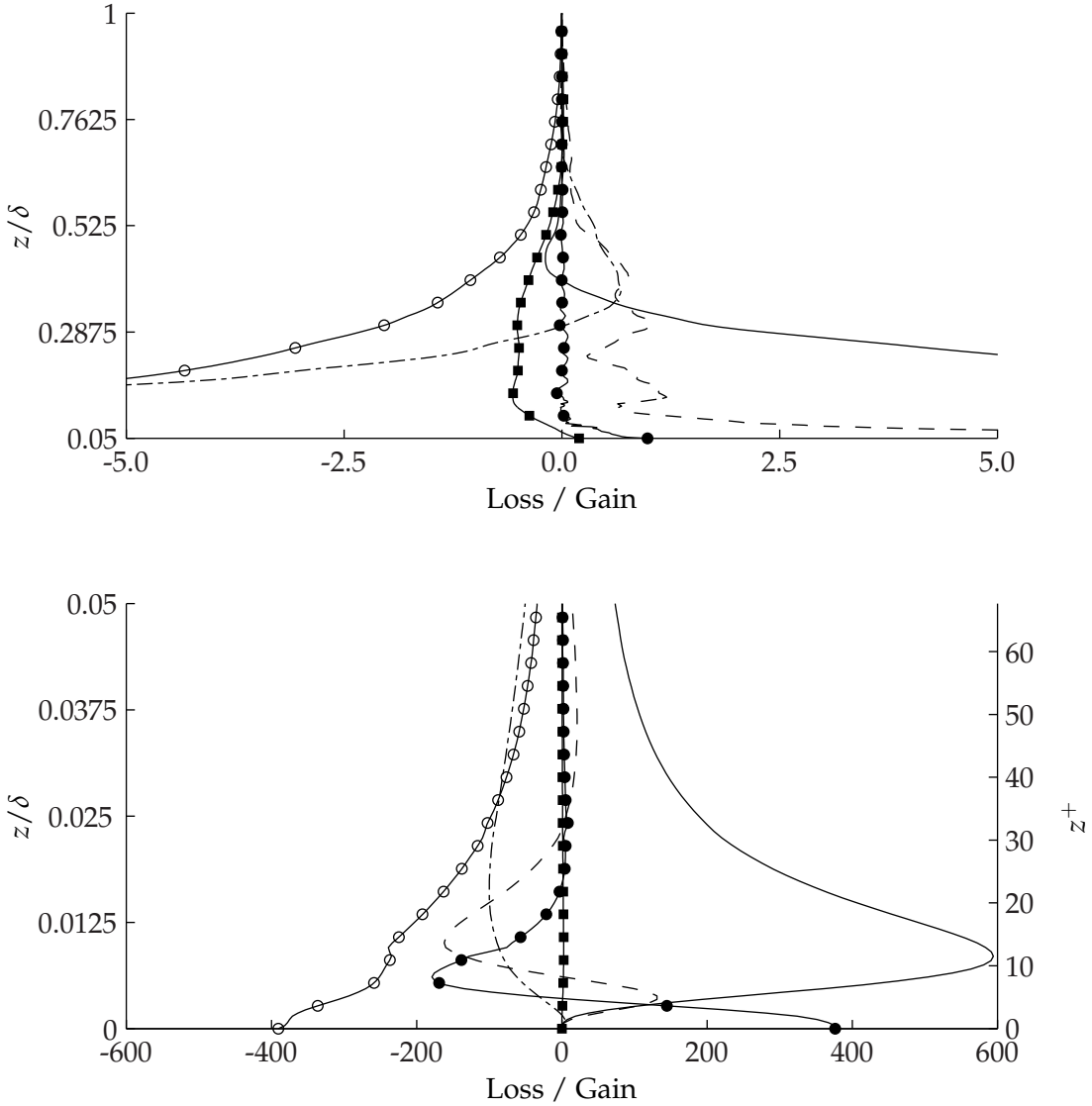

Figure 4.17: Case A turbulent kinetic energy budget for $\overline{u'u'}$ component. Production, solid; turbulent diffusion, dashed; pressure strain, dot-dash; molecular diffusion, solid circle; viscous dissipation, open circle; Coriolis redistribution, square. All terms have been normalized by u_*^3/δ.

the streamwise variance is the major producer of turbulent kinetic energy, it is no surprise that pressure strain acts as a sink when $z/\delta < 0.3$. This confirms that $\overline{u'u'}$ is supplying energy to the other variance terms. For $z/\delta > 0.3$, $\Phi_{1,1}$ and $T_{1,1}$ are the main suppliers of energy for the streamwise turbulent kinetic energy component. Coriolis redistribution is negligible in the near wall region and plays only a minor role in the far-field; the negative value indicates that energy is being redistributed to $\overline{v'v'}$ through $-\overline{u'v'}$.

Spanwise Variance Budget: $\overline{v'v'}$

The budget for the $\overline{v'v'}$ velocity variance is shown in Fig. 4.18. Like the streamwise budget, a nonzero mean shear ($\partial V/\partial z \neq 0$) introduces energy production into the field. However, production by mean shear is not the primary energy source in the near wall region for $\overline{v'v'}$. The peak production of $P_{2,2} \approx 27$ occurs near the same location as the peak streamwise production, $z^+ \approx 10.1$, although the strength of $P_{2,2}$ is over an order of magnitude smaller than $P_{1,1}$. At this same distance from the wall, the return-to-isotropy term is $\Phi_{2,2} \approx 89.2$; this accounts for the transport of energy from $\overline{u'u'}$ into the spanwise Reynolds stress component. Away from the wall, a second peak is noted in the production term at $z/\delta = 0.22$. This corresponds to the location where the amplitude of the spanwise velocity gradient is at a local maximum. At this distance from the wall, $P_{1,1}$ and $P_{2,2}$ are comparable in magnitude. As the streamwise production decays faster, spanwise production becomes the main turbulent energy source for $z/\delta > 0.22$.

Energy dissipation is the dominant energy sink in the near-wall region of the boundary layer. The nonzero dissipation at the wall is balanced by the downward transport of energy by molecular diffusion. The inflection in $\varepsilon_{2,2}$ is even more pronounced than that found in $\varepsilon_{1,1}$. The local minimum correlates well with the location where $D_{2,2}$ is taking the most energy out of the field. Pressure strain replaces dissipation as the dominant sink near the local maximum in production near $z/\delta = 0.22$. Since the $P_{2,2}$ becomes the dominant source of energy for all variance components, the return-to-isotropy term acts to provide energy to $\overline{u'u'}$ and $\overline{w'w'}$. In the work of

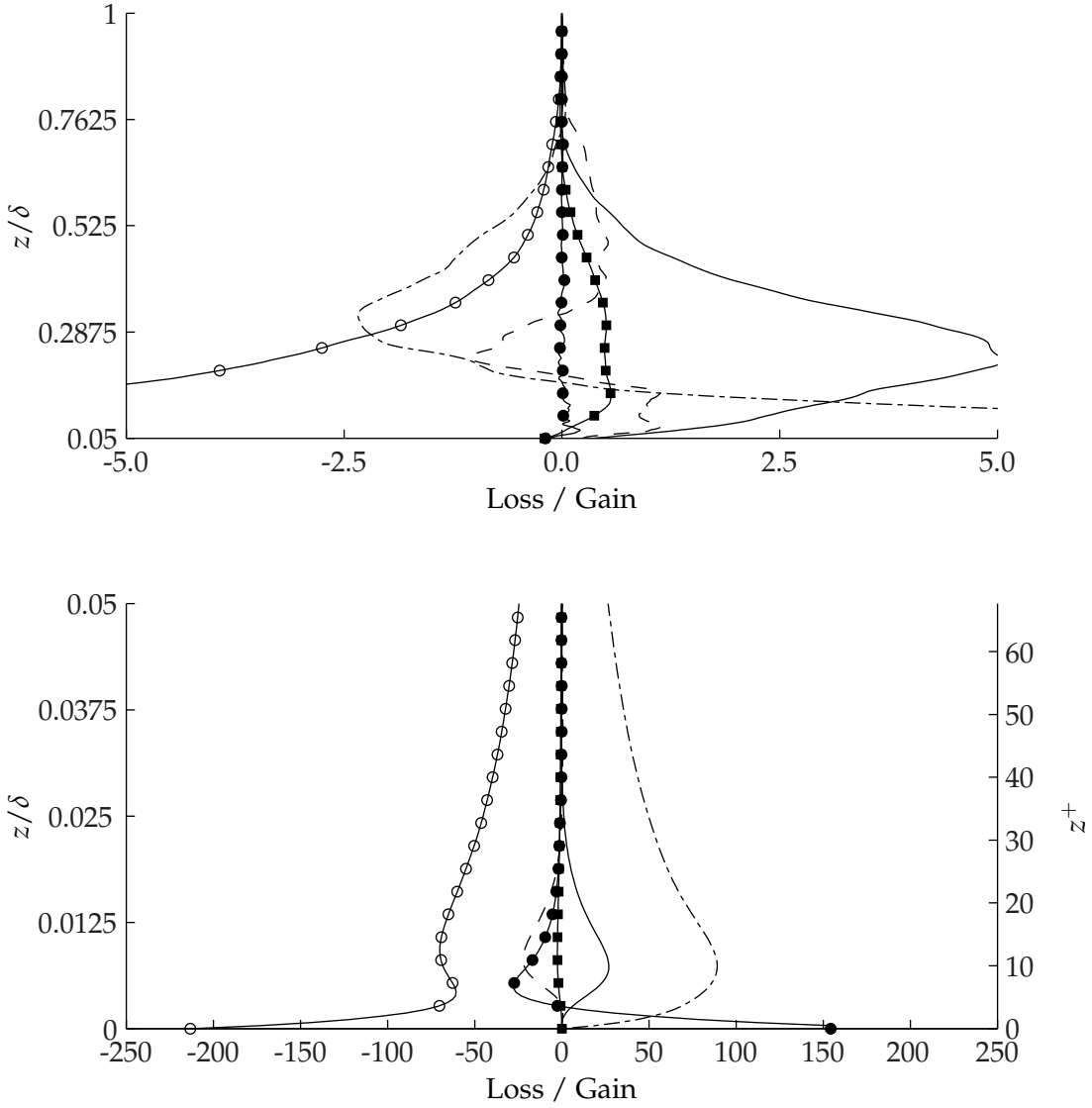

Figure 4.18: Case A turbulent kinetic energy budget for $\overline{v'v'}$ component. Production, solid; turbulent diffusion, dashed; pressure strain, dot-dash; molecular diffusion, solid circle; viscous dissipation, open circle; Coriolis redistribution, square. All terms have been normalized by u_*^3/δ.

Marlatt et al. (2010), dissipation remained the dominant energy sink and the effect of $\Phi_{2,2}$ was less severe. At the increased Reynolds number, the return-to-isotropy term plays a much more pronounced role in redistributing energy.

Apart from the downward transport of energy by $D_{2,2}$ below $z^+ < 10$, molecular diffusion does not affect the $\overline{v'v'}$ budget. Turbulent diffusion, $T_{2,2}$ shows a slight sink near the wall at the location of maximum production and return-to-isotropy. However, unlike the streamwise variance, very little of the energy is transported towards the wall. Instead, the energy is transported upwards and energizes the regions between the two peaks in production, $0.026 < z/\delta < 0.19$. $T_{2,2}$ also acts to transport energy upwards from the second peak in the production that occurs away from the wall. The Coriolis term $C_{2,2}$ is a mirror image of $C_{1,1}$ as energy is gained by $\overline{v'v'}$ at the expense of $\overline{u'u'}$. Comparing these results with those of Marlatt et al. (2010), it appears the increase in Reynolds number decreases the importance of Coriolis redistribution.

Vertical Variance Budget: $\overline{w'w'}$

The vertical variance budget is fundamentally different from either the streamwise or spanwise budget as given in Fig. 4.19. The first notable difference is the absence of energy production by mean shear. Furthermore, since rotation is aligned with the wall-normal direction, $C_{3,3} = 0$. Finally, the pressure diffusion term is nonzero throughout the entire domain.

The primary source of energy for $\overline{w'w'}$ comes from the two pressure transport terms, $\Phi_{3,3}$ and $\Theta_{3,3}$. Above $z^+ > 15$ the return-to-isotropy pressure strain $\Phi_{3,3}$ acts to supply energy from both the streamwise and spanwise variances. Judging by the other budgets, $\overline{u'u'}$ is the prime source when $z/\delta < 0.22$ and $\overline{v'v'}$ takes over when $z/\delta > 0.22$. In the very near-wall region ($z^+ < 15$), pressure diffusion ($\Theta_{3,3}$) transports energy towards the wall from the overlying flow as pressure strain ($\Phi_{3,3}$) then redistributes this energy to $\overline{u'u'}$ and $\overline{v'v'}$. This phenomena was referred to as 'splatting' by Moin and Kim (1982) since the impingement of the vertical velocity on the wall tends to energize the horizontal energy components. As shown in Fig. 4.20(c), the pressure

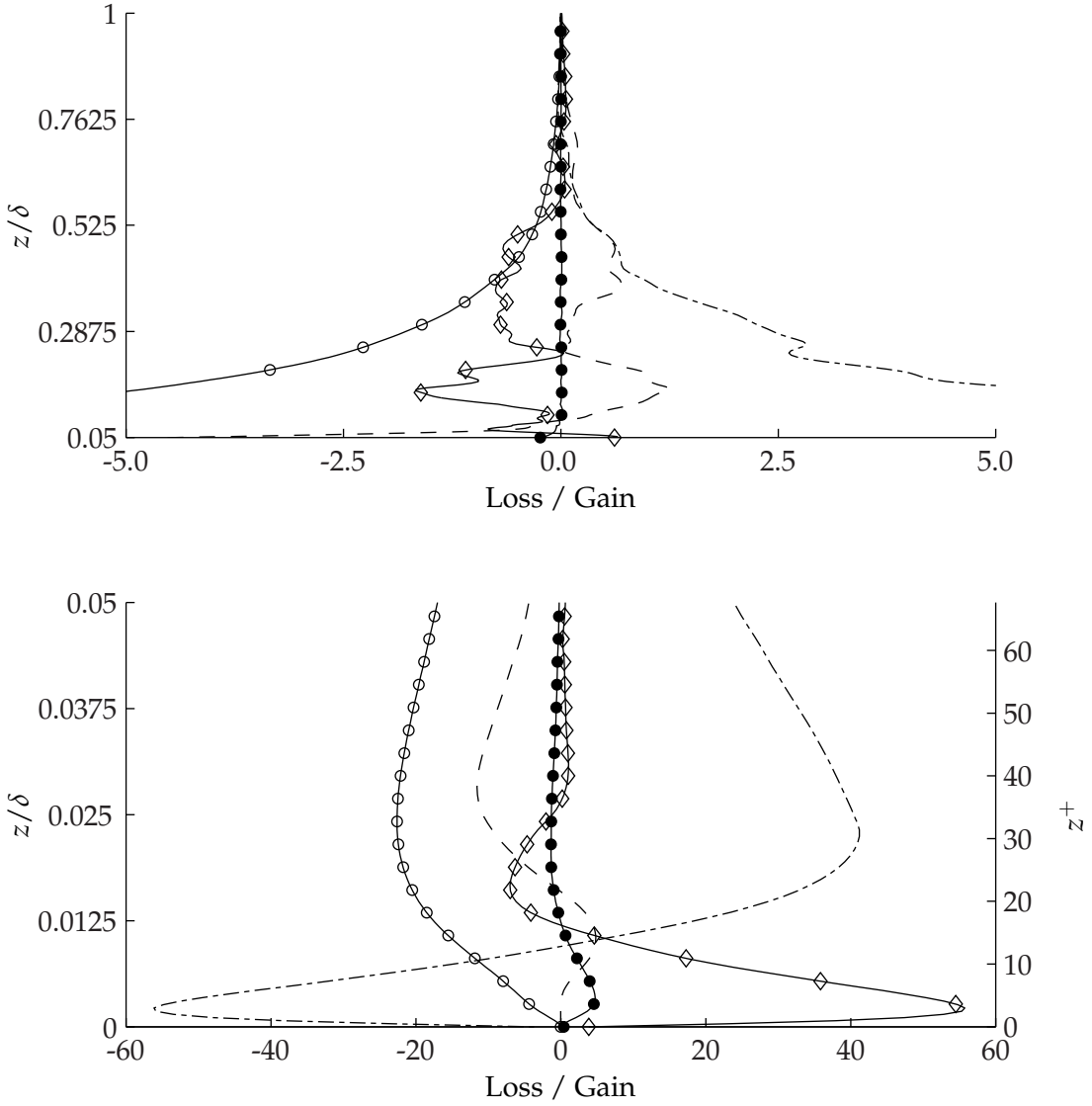

Figure 4.19: Case A turbulent kinetic energy budget for $\overline{w'w'}$ component. Turbulent diffusion, dashed; pressure strain, dot-dash; pressure diffusion, diamond; molecular diffusion, solid circle; viscous dissipation, open circle. All terms have been normalized by u_*^3/δ.

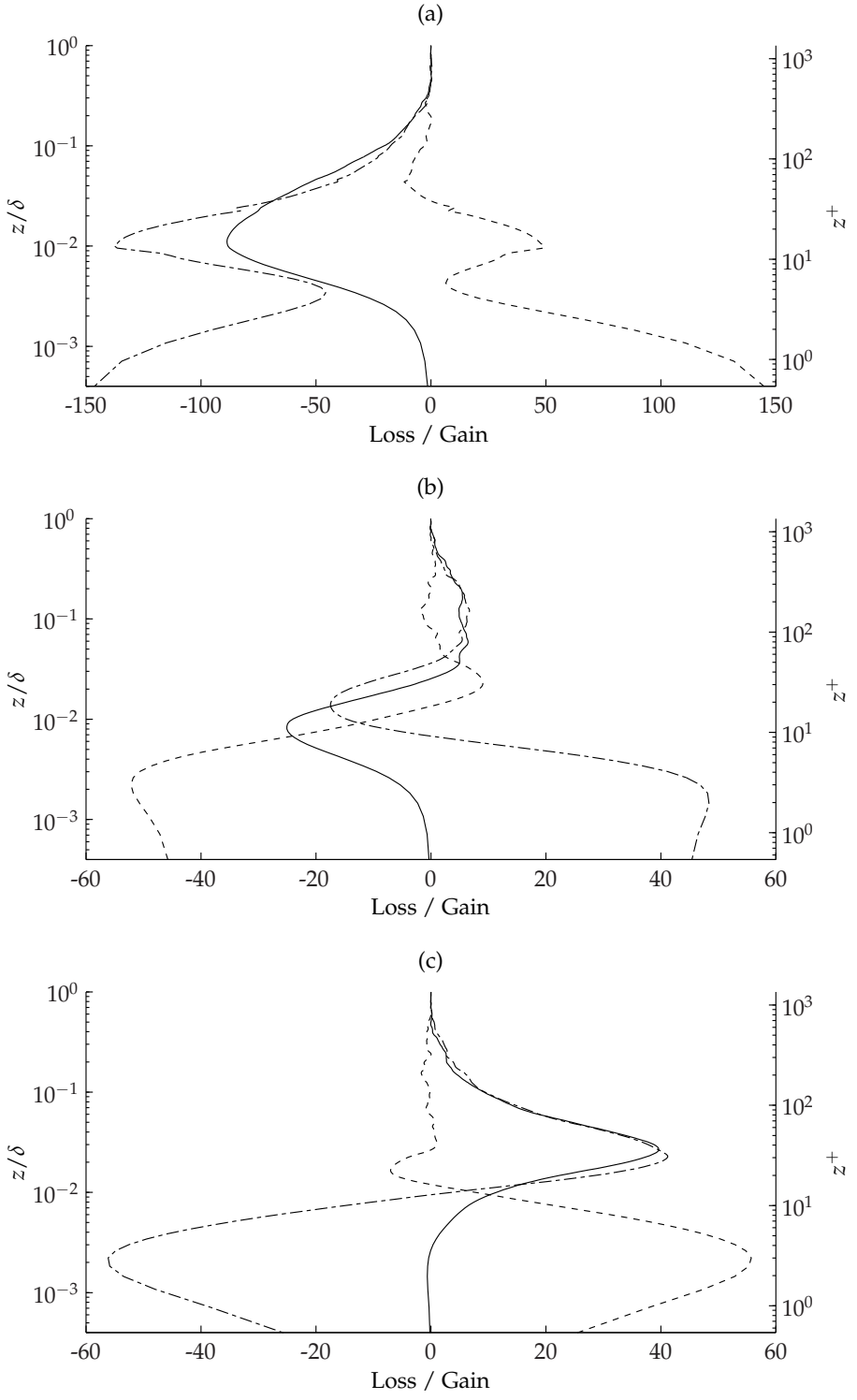

Figure 4.20: Case A pressure transport terms: (a) $\overline{u'w'}$, (b) $-\overline{v'w'}$, (c) $\overline{w'w'}$. Solid, total pressure transport ($\Pi_{i,k}$); dotted, pressure diffusion ($\Theta_{i,k}$); dot-dash, pressure strain ($\Phi_{i,k}$).

strain and diffusion balance each other in the near wall region such that the total contribution from pressure terms to the energy balance is small. Only when pressure strain becomes positive at $z^+ > 12.5$ does the energy gain from the pressure terms become substantial. Consequently, $\Pi_{3,3}$ acts to supply energy throughout the entire boundary layer.

Molecular diffusion and turbulent diffusion are responsible for energizing the very near wall region. $T_{3,3}$ moves energy towards the wall from above $z^+ \approx 22$. It appears in Fig. 4.19 that $D_{3,3}$ then takes energy from $T_{3,3}$ and $\Pi_{3,3}$ and transports it down to the wall. In the very near-wall region, molecular diffusion is the only process supplying energy to the flow field, hence, the small amplitude of the Reynolds stress (see Fig. 4.9).

Dissipation is the dominant sink throughout the domain for $\overline{w'w'}$ and balances the pressure terms. Unlike the previous various budgets, $\varepsilon_{3,3} = 0$ at the wall.

4.3.2 Covariance Budgets

Though the velocity variance terms are directly responsible for the turbulent kinetic energy of the field, the covariances are primary contributors to the production of kinetic energy through $P_{i,k}$ in Eq. 4.3.1. Classification of the covariances can be categorized into primary, those responsible for energy production, and secondary, those which only act as an avenue for energy redistribution. Given the non-zero spanwise velocity that results from including Coriolis rotation, both $\overline{u'w'}$ and $\overline{v'w'}$ act as primary covariances. $\overline{u'v'}$ does not appear in any production terms, but will be analyzed regardless due to its important role in energy transport. As with the velocity variances presented earlier, all terms have been nondimensionalized by u_*^3/δ. Note that the budgets for the covariance terms are presented for $-\overline{u_i'u_k'}$ when $i \neq k$. The analysis is carried out in this manner since $P_{i,k} > 0$ if $\overline{u_i'u_j'} < 0$ when $\partial U_k/\partial x_j > 0$.

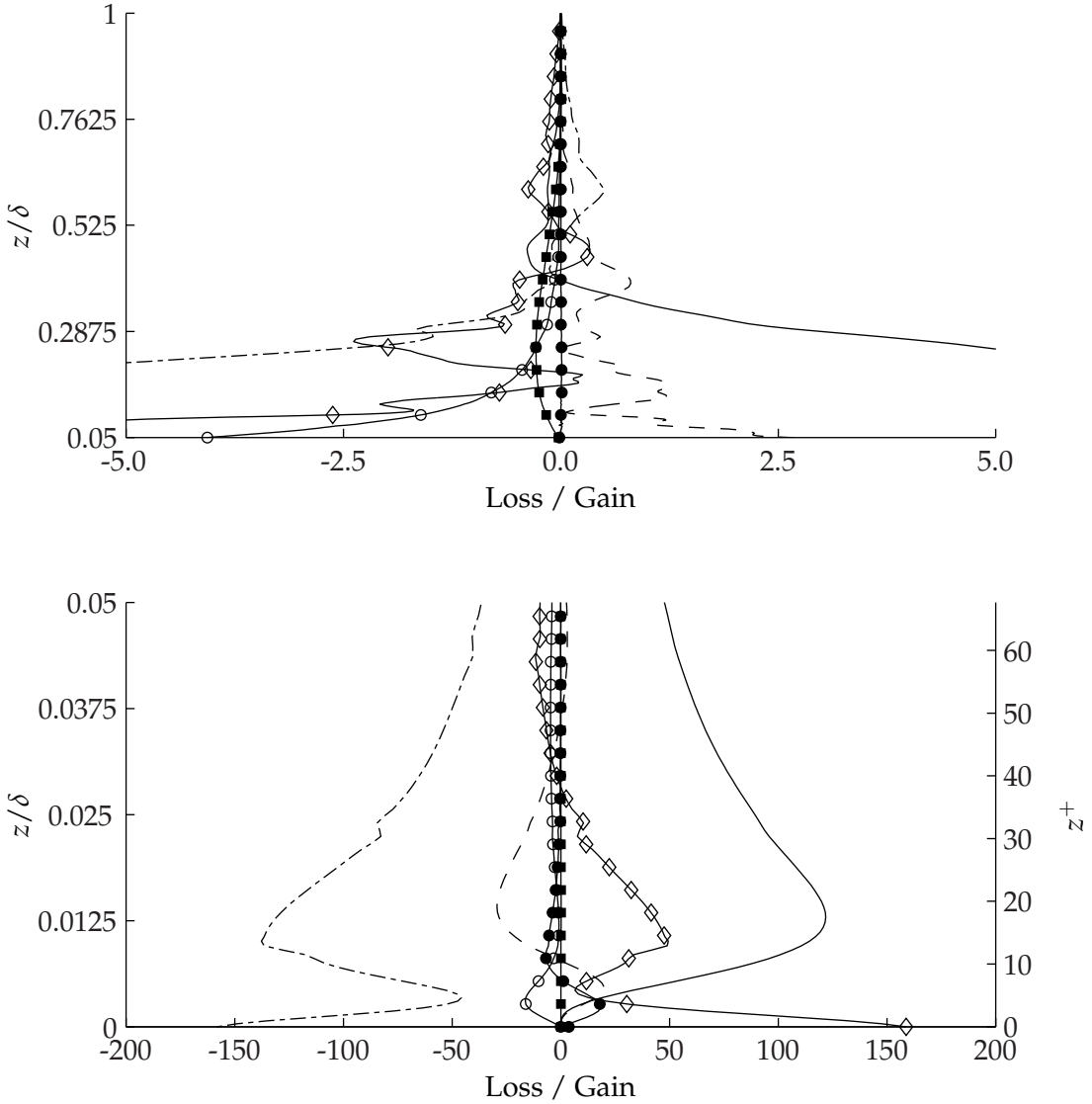

Figure 4.21: Case A turbulent kinetic energy budget for $-\overline{u'w'}$ component. Production, solid; turbulent diffusion, dashed; pressure strain, dot-dash; pressure diffusion, diamond; molecular diffusion, solid circle; viscous dissipation, open circle; Coriolis redistribution, square. All terms have been normalized by u_*^3/δ.

Primary Covariance Budgets: $-\overline{u'w'}$ and $-\overline{v'w'}$

Presented in Fig. 4.21 is the energy budget for $-\overline{u'w'}$. The gain from production is nearly in balance with pressure strain for most of the boundary layer. From Eq. 4.3.1 it is clear that $P_{1,3}$ involves an interaction between the vertical velocity variance and streamwise mean velocity gradient. Given that $\overline{w'w'}$ is always positive, the nature of the production term to act as a source or sink of $-\overline{u'w'}$ is dependent upon the sign of $\partial U/\partial z$. A budget gain, in the context of the primary covariances, tends to enhance sweeps and ejections, both of which are responsible for the generation of turbulent energy (Pope, 1993).

Dissipation and molecular diffusion are small outside of $z^+ < 10$. Once again, molecular interactions tend to transport turbulent producing events towards the wall while dissipation acts to destroy energy. Pressure strain is the dominant sink for $-\overline{u'w'}$ and nearly balances the production term on its own. $\Phi_{1,3}$ does not dissipate the turbulence producing events (sweeps and ejections), but rather acts as a redistribution mechanism to transport energy between various velocity variance components. The total pressure transport term $\Pi_{1,3}$ acts as a sink throughout the boundary layer as shown in Fig. 4.20(a).

The statistics above $z/\delta > 0.5$ suffer from an increase in noise. The uncertainty of the results may be a consequence of the small role the covariance term plays in the farfield, or a simple artifact of the slow convergence of these particular statistics.

Figure 4.22 shows that production of turbulence for $-\overline{v'w'}$ is over almost a factor of four smaller than the corresponding streamwise covariance. Like $-\overline{u'w'}$, the sign of $P_{2,3}$ changes when the corresponding mean velocity is at a maximum. Above $z^+ \approx 40$, $P_{2,3}$ destroys turbulent events and is balanced by the redistribution caused by pressure strain. Since pressure strain represents an inter-component energy transfer, $-\overline{v'w'}$ likely is using $\Phi_{1,3}$ as its source. Pressure diffusion balances pressure strain at the wall and then acts as a source when production changes sign. The combined effect of pressure shown in Fig. 4.20(b) demonstrates the same effect.

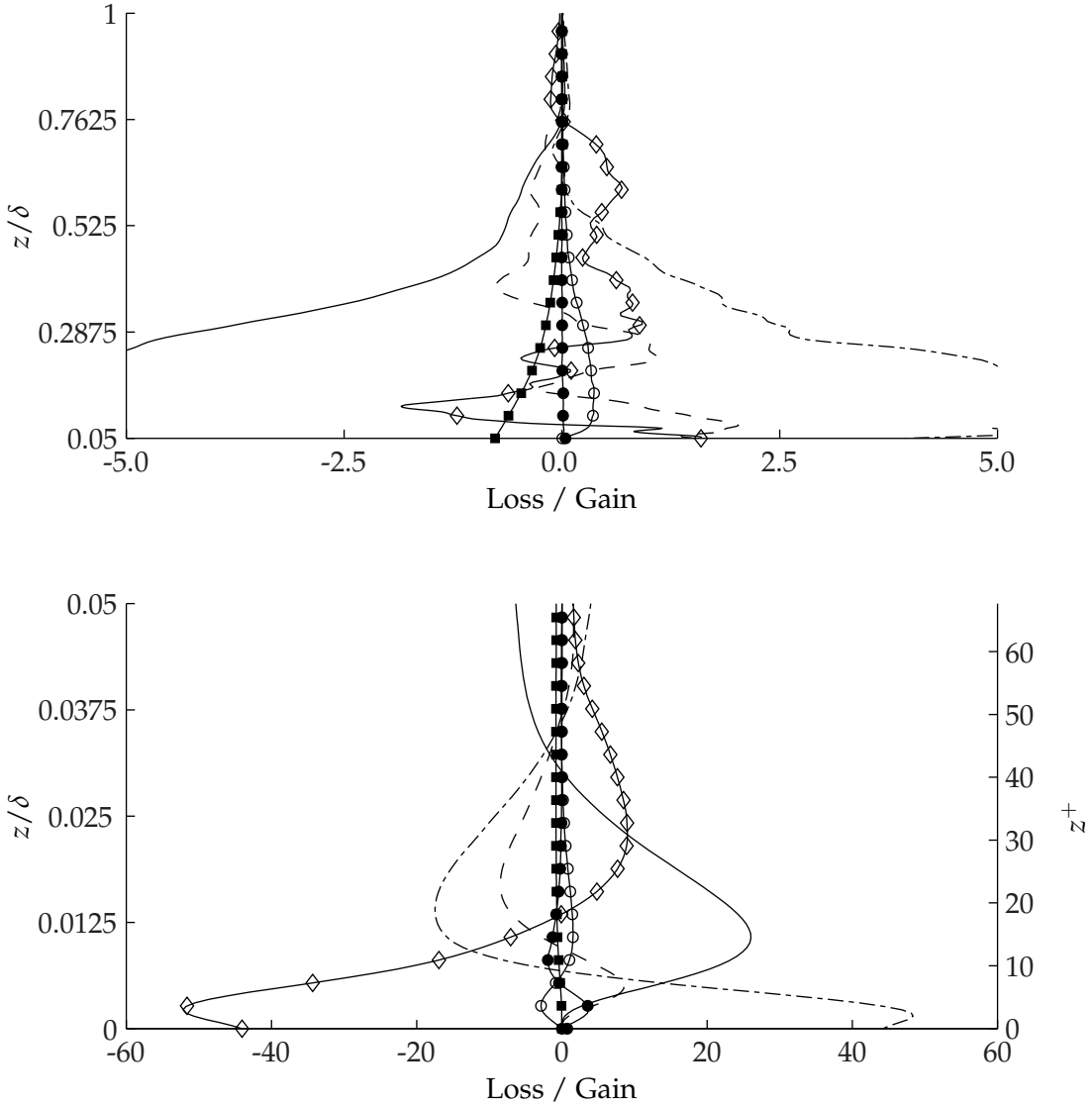

Figure 4.22: Case A turbulent kinetic energy budget for $-\overline{v'w'}$ component. Production, solid; turbulent diffusion, dashed; pressure strain, dot-dash; pressure diffusion, diamond; molecular diffusion, solid circle; viscous dissipation, open circle; Coriolis redistribution, square. All terms have been normalized by u_*^3/δ.

The dissipation term acts in a unique manner for the spanwise covariance in that the dissipation acts as a source for most of the flow field. Although quite a few of the terms show heavy oscillations due to statistical noise ($\Theta_{2,3}$, $T_{2,3}$), the dissipation appears to be well converged and acts as a gain for this particular budget. However, the magnitude of this term (as well as the Coriolis redistribution) is small in comparison with production by mean shear and pressure strain.

Secondary Covariance Budget: $-\overline{u'v'}$

For the flow that is homogeneous in the horizontal domain, $-\overline{u'v'}$ does not explicitly act to produce turbulence like $-\overline{u'w'}$ or $-\overline{v'w'}$. Consequently, the effects of this term are commonly overlooked. However, the total energy redistribution that occurs within this term is on the same order of magnitude as other variance and covariance terms. Should horizontal homogeneity not be enforced, the covariance between horizontal components could act to produce turbulent energy directly. In this study, the secondary covariance simply acts as a means of energy redistribution. The budget for this term is presented in Fig. 4.23.

As with the other velocity covariances, the data presented represent a budget for the negative of the covariance term. This is done so that production (in the most common case) will act to produce turbulence while dissipation acts to destroy turbulence for the primary covariances. As can be seen in Fig. 4.23, the roles of the budget terms have been reversed for the sign convention used. Production is a sink for $z^+ < 45$ at which point it changes sign and acts to provide energy to the $-\overline{u'v'}$ covariance. Dissipation also acts as a source throughout the domain, although its presence is only notable near the wall.

Pressure strain is a source for the term near the wall but changes sign near $z^+ \approx 30$. Above this $\Phi_{1,2}$ balances the gain provided by the mean shear production.

The roles of molecular and turbulent diffusion are reversed from what is seen in other variance and covariance budgets. $D_{1,2}$ and $T_{1,2}$ move energy in $-\overline{u'v'}$ towards the point of minimum production.

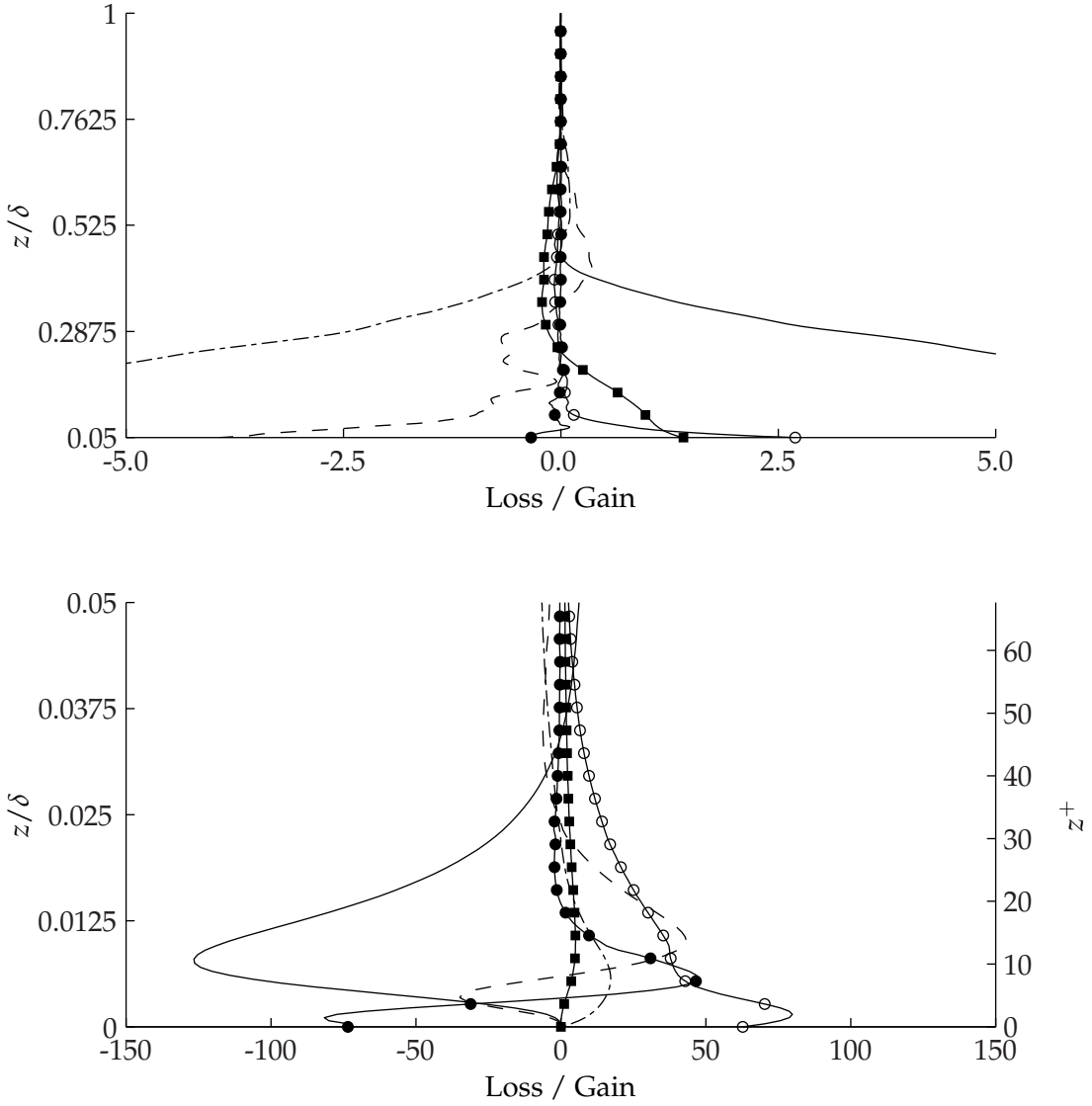

Figure 4.23: Case A turbulent kinetic energy budget for $-\overline{u'v'}$ component. Production, solid; turbulent diffusion, dashed; pressure strain, dot-dash; molecular diffusion, solid circle; viscous dissipation, open circle; Coriolis redistribution, square. All terms have been normalized by u_*^3/δ.

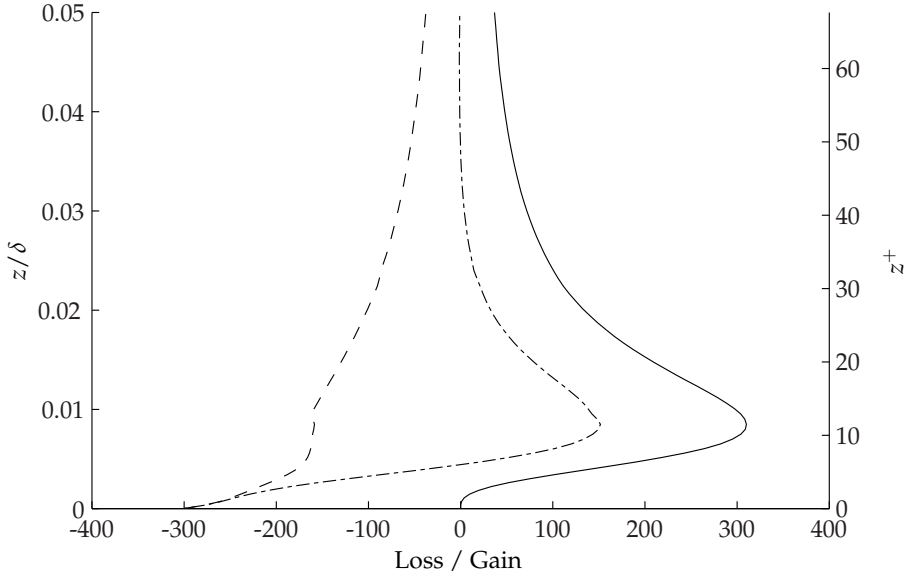

Figure 4.24: Case A production/dissipation balance: k production (P), solid line; k dissipation (ε), dashed line; balance ($P + \varepsilon$), dash-dot.

4.3.3 Balance of Production and Dissipation

The neutrally stratified turbulent Ekman layer reaches a statistical steady-state since no thermal forcing is applied. Over a long enough averaging window, the total level of kinetic energy should not change in the domain. The total production P and total energy dissipation ε of kinetic energy k are defined by

$$P = 0.5 P_{i,i} \tag{4.3.4a}$$

$$\varepsilon = 0.5 \varepsilon_{i,i} \tag{4.3.4b}$$

which stem from the kinetic energy definition in Eq. 4.2.12. Note the repeated indices imply a summation over the diagonal components of the tensors. If the level of energy in the flow does not change over time then the integral of P and ε over the domain should be in balance:

$$\int_0^\infty P \, \mathrm{d}z + \int_0^\infty \varepsilon \, \mathrm{d}z = 0 \tag{4.3.5}$$

P, ε, and the sum of the two are shown in Fig. 4.24. The sum of production and dissipation demonstrates that the dissipation of energy occurs near the wall, where length scales are smallest.

Above $z^+ \approx 13$ the dissipation decreases rapidly with increased height. The inflection point noted earlier in the buffer layer at $z^+ = 10$ is particularly interesting as it appears to correlate with the atmospheric data presented by Balsley et al. (2003). In their work they demonstrate that the dissipation exhibits a small region of constant dissipation before decreasing with an increase in altitude. However, no measurements were reported in the region nearest the wall. From Fig. 4.24 we can speculate that there would be an increase in dissipation through the viscous sublayer of the Ekman layer. The agreement between the atmospheric data of Balsley et al. (2003) and the Case A unstratified DNS suggests that the effect of buoyancy on dissipation in the near-wall region is minor. The channel flow analysis by Mansour et al. (1988) demonstrated a similar inflection in ε at $z^+ \approx 10$ indicating that in the wall region where viscous effects dominate, small scale motions are not affected by Coriolis forces.

Integrating the production and dissipation shown in Fig. 4.24 over the entire domain, the balance of production and dissipation is computed by

$$\frac{\int_0^\infty P\mathrm{d}z + \int_0^\infty \varepsilon \mathrm{d}z}{\int_0^\infty P\mathrm{d}z} = \text{TKE balance} \tag{4.3.6}$$

The balance of k production and destruction is within 9.3% of equilibrium. It is believed that this discrepancy is a consequence of statistical sampling. While production and dissipation of k should be in balance, the total energy transported at any distance from the wall z for all $\overline{u_i' u_k'}$ budgets should also be near equilibrium. A measure of equilibrium is given by

$$\frac{P_{i,k} + T_{i,k} + \varepsilon_{i,k} + D_{i,k} + \Pi_{i,k} + C_{i,k}}{|P_{i,k}| + |T_{i,k}| + |\varepsilon_{i,k}| + |D_{i,k}| + |\Pi_{i,k}| + |C_{i,k}|} = r_{i,k} \tag{4.3.7}$$

Equation 4.3.7 normalizes the residual energy for a given Reynolds stress budget by the amount of energy transfer occurring. The budget should be in balance ($r_{i,k} = 0$) over the entire boundary layer. The results shown in Fig. 4.25 show that the three energy components are nearly in balance (within 10%) when $z/\delta < 0.5$. Furthermore, the $\overline{u'u'}$ budget is within 5% of equilibrium for $z/\delta < 0.64$. This is reassuring given that the streamwise variance is the primary supplier of energy to the flow.

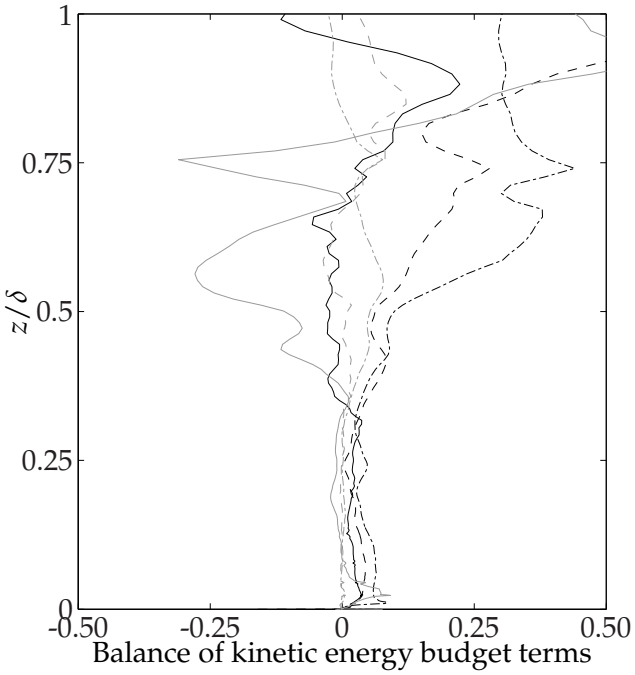

Figure 4.25: Case A turbulent kinetic energy budget balance: $\overline{u'u'}$, solid black; $\overline{v'v'}$, dashed black; $\overline{w'w'}$, dash-dot black; $-\overline{u'v'}$, solid gray; $-\overline{u'w'}$, dashed gray; $-\overline{v'w'}$, dash-dot gray. Terms computed as residual energy in budget terms normalized by total energy in all terms. 0 - complete balance, 1 - complete imbalance.

The largest unbalance for the covariance terms is noted in $\overline{u'w'}$ (solid gray line). When $z/\delta > 0.5$, the balance of all terms deteriorates. In this outer region of the boundary layer the length and time scales are large. It is possible that the integration period of $tf = 0.8$ was insufficient to accurately converge the budget statistics in this region.

4.4 Turbulent Structures

To gain insight concerning the shapes of typical turbulent structures throughout the boundary layer, two-point velocity and pressure autocorrelations are presented. For two arbitrary variables a and b, the normalized autocorrelation R_{ab} is given by

$$R_{ab}\left(\Delta x, \Delta y, z_1, z_2\right) = \frac{\int_0^{\tau}\int_0^{L_y}\int_0^{L_x} a(x,y,z_1,t)\, b(x+\Delta x, y+\Delta y, z_2, t)\,\mathrm{d}x\,\mathrm{d}y\,\mathrm{d}t}{\tau L_x L_y\, a_{\mathrm{rms}}(z_1)\, b_{\mathrm{rms}}(z_2)} \tag{4.4.1}$$

This definition of an autocorrelation can be applied to either velocity or pressure and is written in such a manner to emphasize that the results are averaged both spatially and temporally. The spatial integration limits of L_x and L_y imply that the entire x/y plane is averaged over for all values of x and y. The time interval over which the statistics are averaged is denoted by τ; for Case A, $\tau f = 0.8$. Due to periodicity, R_{ab} is a function of neither x or y, but rather the spatial separations Δx and Δy. The definition of Eq. 4.4.1 implies that $R_{aa}\,(0, 0, z_1, z_1) = +1$.

The four-dimensional structure generated by R_{ab} is difficult to visualize without simplifying the autocorrelation. Instead, the autocorrelations across three separate planes are given:

- Projection of the x/y plane at $z = z_1$: $R_{ab}\,(\Delta x, \Delta y, z_1, z_1)$
- Projection of the x/z plane centered at $z = z_1$: $R_{ab}\,(\Delta x, 0, z_1, z)$
- Projection of the y/z plane centered at $z = z_1$: $R_{ab}\,(0, \Delta y, z_1, z)$

Through the three projections it is possible to infer the 'average' shape of a turbulent structure at different distances from the wall.

4.4.1 x/y Projections

The near wall ($z^+ = 2.48$) velocity and pressure fields – and their accompanying in-plane autocorrelation – are presented in Fig. 4.26 through 4.29. The instantaneous fields encompass nearly the entire domain while the autocorrelation is zoomed-in to show detail concerning the structure. For the streamwise component shown in Fig. 4.26, the near wall field is characterized by elongated structures inclined with the local direction of shear. The autocorrelation R_{uu} indicates that the autocorrelation is very narrow in the direction normal to shear. Mean flow shear acts to stretch the coherent structures. Note that the autocorrelation in 4.26(b) does not align exactly with the local shear but is instead biased towards the x coordinate direction.

The spanwise correlation R_{vv} shows a different trend (Fig. 4.27) in that the autocorrelation is slightly biased in the y coordinate direction. This is evident in both the instantaneous field

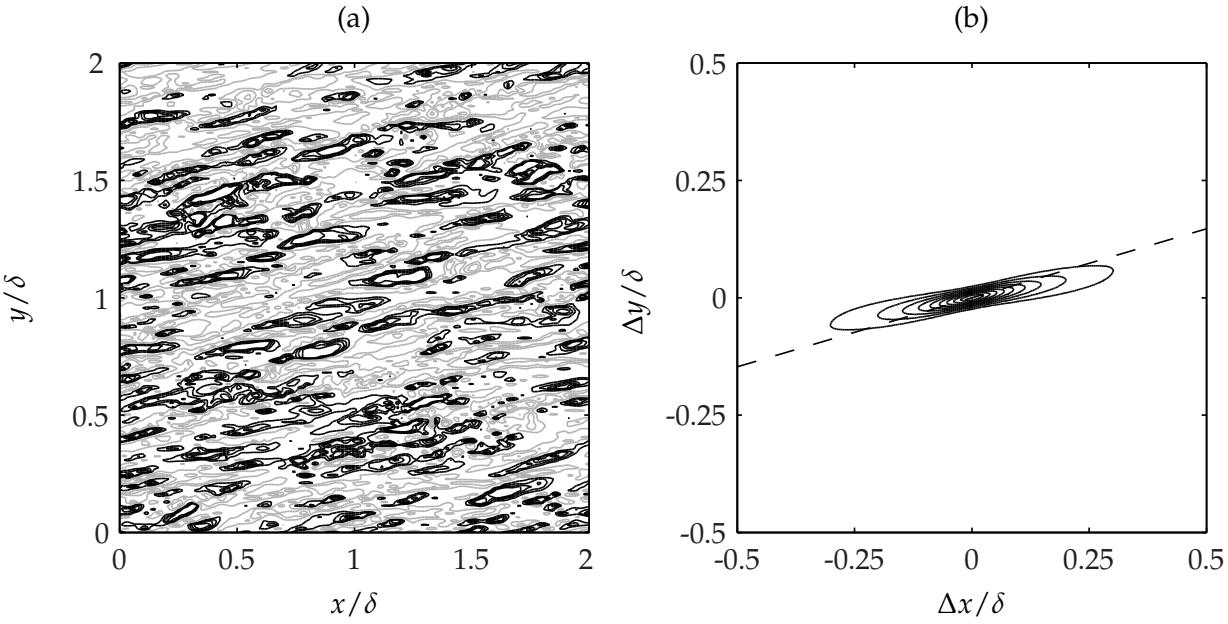

Figure 4.26: Case A, $z_1^+ = 2.48$: (a) u'/u_* at $tf = 0.4$, (b) $R_{uu}(\Delta x, \Delta y, z_1, z_1)$. Contour interval for instantaneous field and autocorrelation is $\Delta = 0.457$ and $\Delta = 0.1$ respectively. Black contours denote positive values while gray indicate negative values; the zero contour is not shown. The dashed line indicates the direction of local shear.

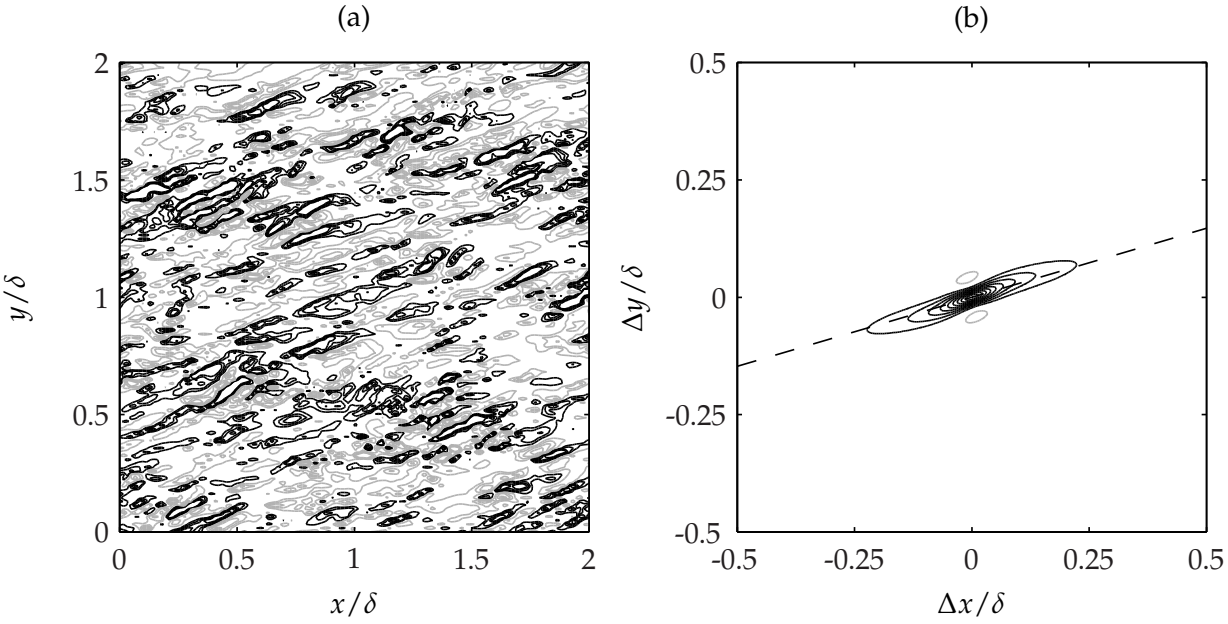

Figure 4.27: Case A, $z_1^+ = 2.48$: (a) v'/u_* at $tf = 0.4$, (b) $R_{vv}(\Delta x, \Delta y, z_1, z_1)$. Contour interval for instantaneous field and autocorrelation is $\Delta = 0.283$ and $\Delta = 0.1$ respectively. Black contours denote positive values while gray indicate negative values; the zero contour is not shown. The dashed line indicates the direction of local shear.

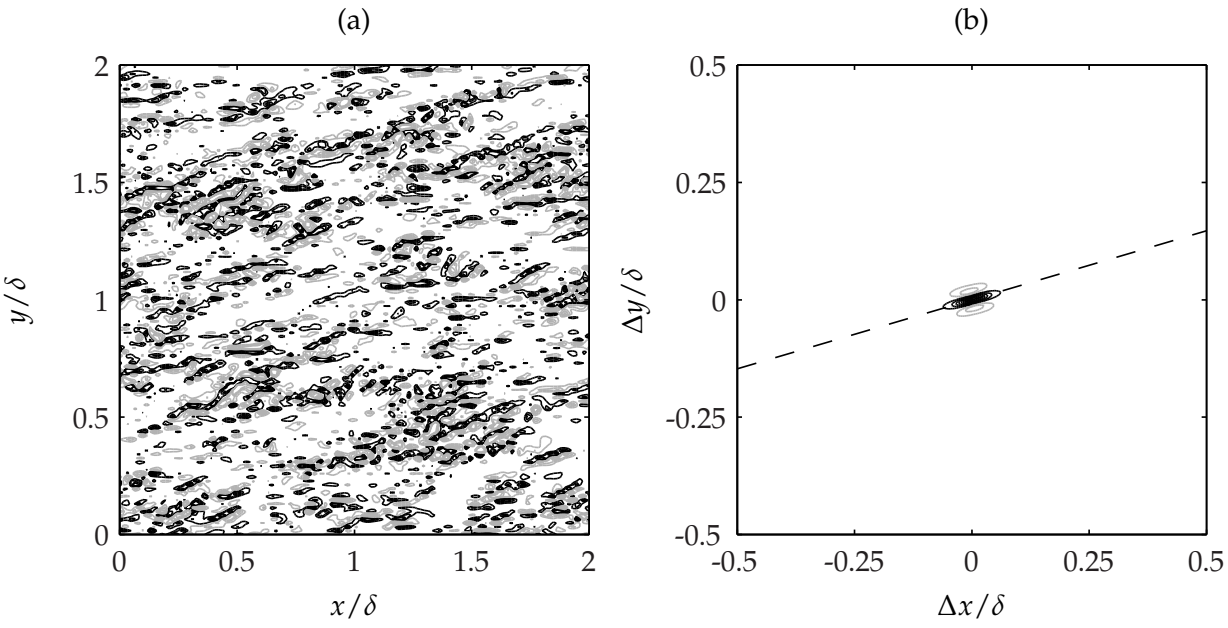

Figure 4.28: Case A, $z_1^+ = 2.48$: (a) w'/u_* at $tf = 0.4$, (b) $R_{ww}(\Delta x, \Delta y, z_1, z_1)$. Contour interval for instantaneous field and autocorrelation is $\Delta = 0.0256$ and $\Delta = 0.1$ respectively. Black contours denote positive values while gray indicate negative values; the zero contour is not shown. The dashed line indicates the direction of local shear.

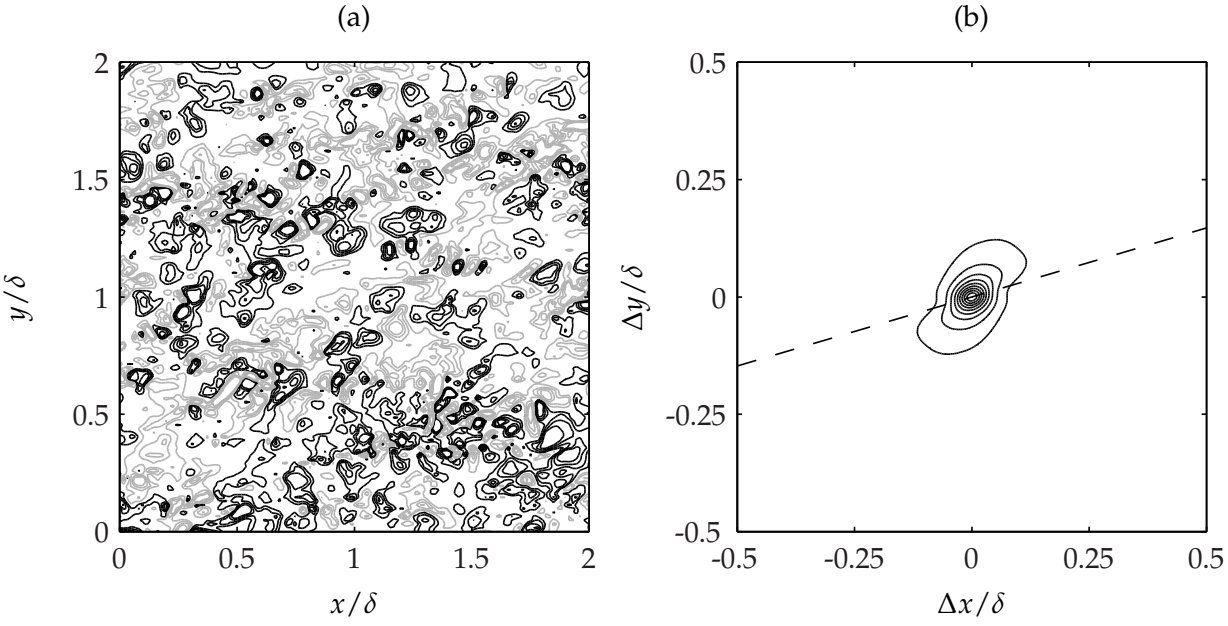

Figure 4.29: Case A, $z_1^+ = 2.48$: (a) p'/u_*^2 at $tf = 0.4$, (b) $R_{pp}(\Delta x, \Delta y, z_1, z_1)$. Contour interval for instantaneous field and autocorrelation is $\Delta = 1.21$ and $\Delta = 0.1$ respectively. Black contours denote positive values while gray indicate negative values; the zero contour is not shown. The dashed line indicates the direction of local shear.

as well as the autocorrelation function. It appears the autocorrelations tend to align with their corresponding coordinate direction as the flow becomes more isotropic away from the wall. The biasing of the structures indicates that pressure strain attempts to overcome the strong anisotropic mean shear. Like the streamwise autocorrelation, the function is elongated in the shear direction, though slightly shorter in length. The width of the region of positive correlation is smaller for R_{vv} when compared with R_{uu}. A small region of negative correlation exists with small Δy.

The instantaneous field for w', as seen in Fig. 4.28(a), indicates the existence of narrow elongated 'worm-like' structures in specific locations throughout the domain. The strength of these fluctuations are substantially lower than the corresponding streamwise and spanwise fluctuations as indicated by the very small contour interval. The autocorrelation demonstrates a narrow band of positive correlation that aligns with the local shear direction. Two regions of negative correlation are found on either side. While R_{uu} is biased towards x and R_{vv} towards y, the vertical autocorrelation shows no biasing in either horizontal direction.

The instantaneous pseudo-pressure field and corresponding autocorrelation shown in Fig. 4.29(a) and (b) respectively are fundamentally different from the three velocity components. The stretching in the shear direction is non-existent at small scales as demonstrated by the nearly circular contours in subplot (b) for small values of Δx. Only at the large scales of the structure does mean shear tend to affect the pressure.

The next set of autocorrelations presented are located near the start of the log-law region, $z^+ = 39.4$. The streamwise autocorrelation in Fig. 4.30(b) shows growth of the u' velocity structure in both the spanwise and streamwise direction. The autocorrelation is still stretched in the streamwise direction and tends to align with structures close to the wall. The spanwise autocorrelation in Fig. 4.31(b) shows significant broadening in the y direction and a slight contraction in x. Like R_{uu}, the spanwise autocorrelation shows a residual angle which aligns with the structures in the viscous sublayer. w' and R_{ww} are shown in Fig. 4.32. The structures have grown significantly with an increased separation with the wall. The regions of negative correlation still exist though they

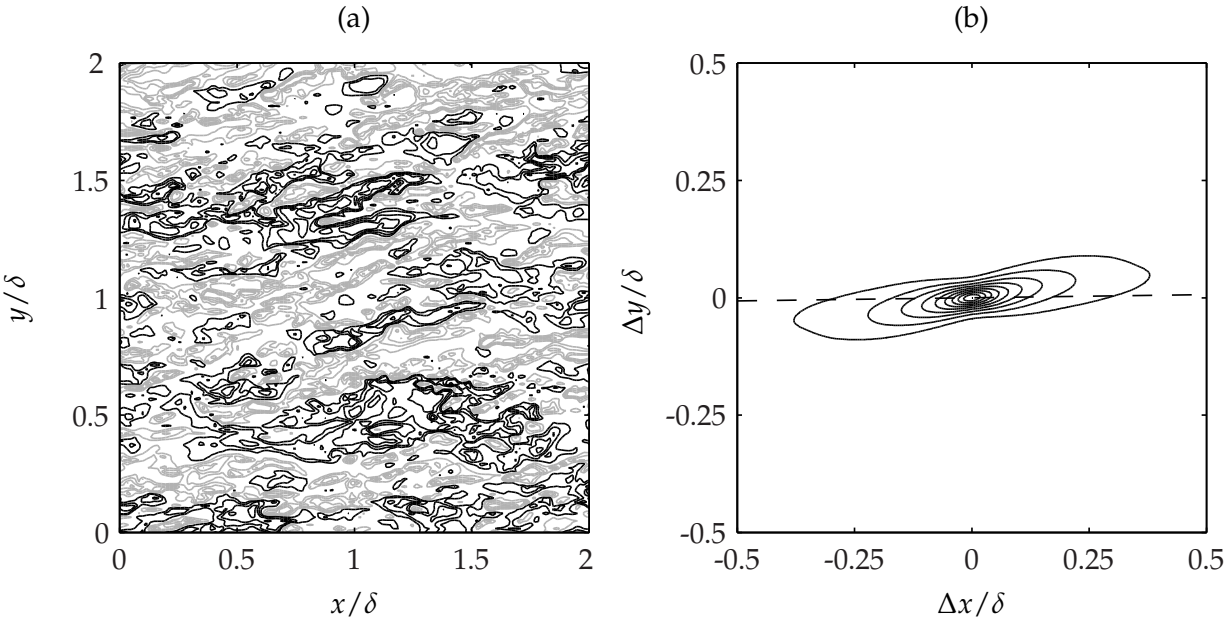

Figure 4.30: Case A, $z_1^+ = 39.4$: (a) u'/u_* at $tf = 0.4$, (b) $R_{uu}(\Delta x, \Delta y, z_1, z_1)$. Contour interval for instantaneous field and autocorrelation is $\Delta = 1.06$ and $\Delta = 0.1$ respectively. Black contours denote positive values while gray indicate negative values; the zero contour is not shown. The dashed line indicates the direction of local shear.

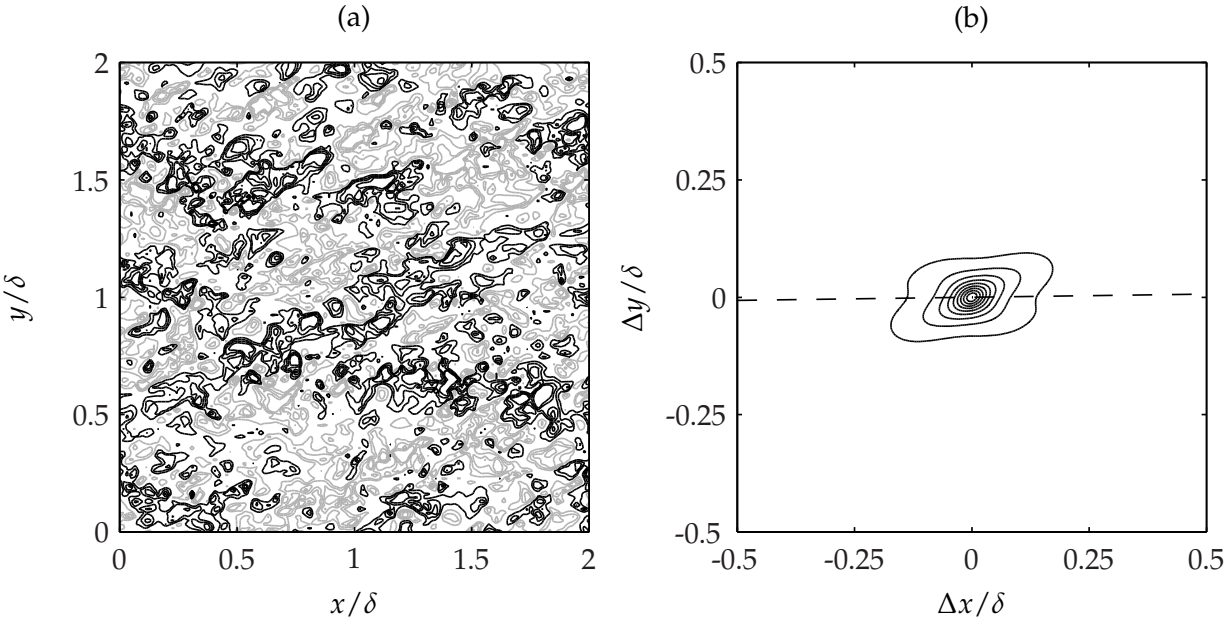

Figure 4.31: Case A, $z_1^+ = 39.4$: (a) v'/u_* at $tf = 0.4$, (b) $R_{vv}(\Delta x, \Delta y, z_1, z_1)$. Contour interval for instantaneous field and autocorrelation is $\Delta = 0.700$ and $\Delta = 0.1$ respectively. Black contours denote positive values while gray indicate negative values; the zero contour is not shown. The dashed line indicates the direction of local shear.

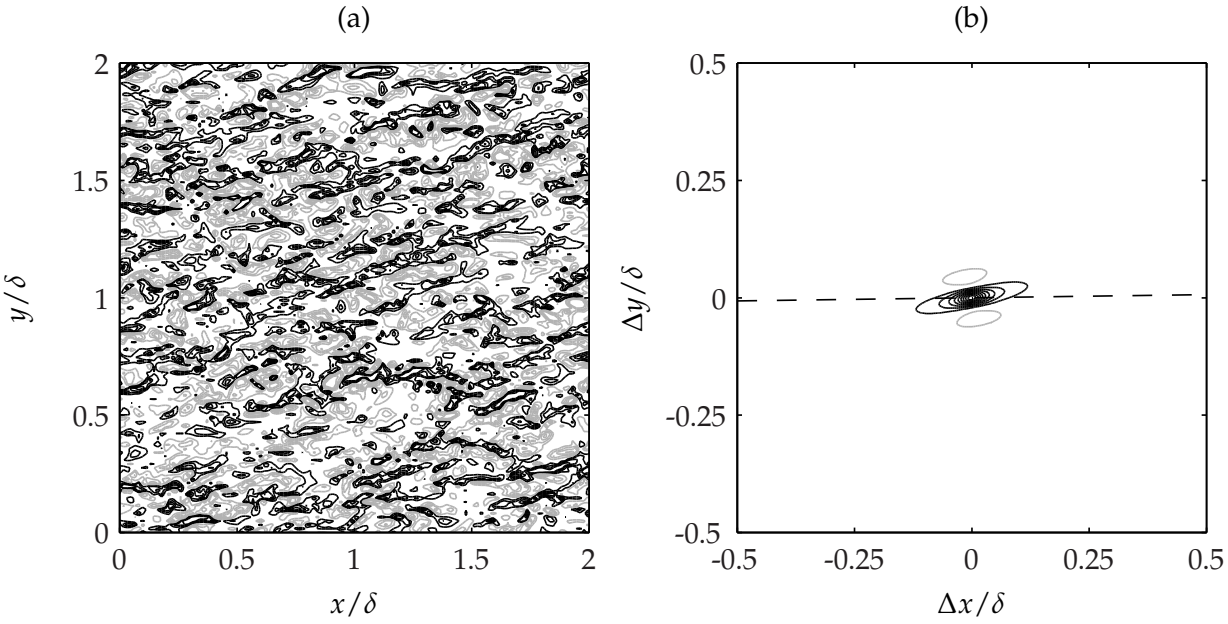

Figure 4.32: Case A, $z_1^+ = 39.4$: (a) w'/u_* at $tf = 0.4$, (b) $R_{ww}(\Delta x, \Delta y, z_1, z_1)$. Contour interval for instantaneous field and autocorrelation is $\Delta = 0.456$ and $\Delta = 0.1$ respectively. Black contours denote positive values while gray indicate negative values; the zero contour is not shown. The dashed line indicates the direction of local shear.

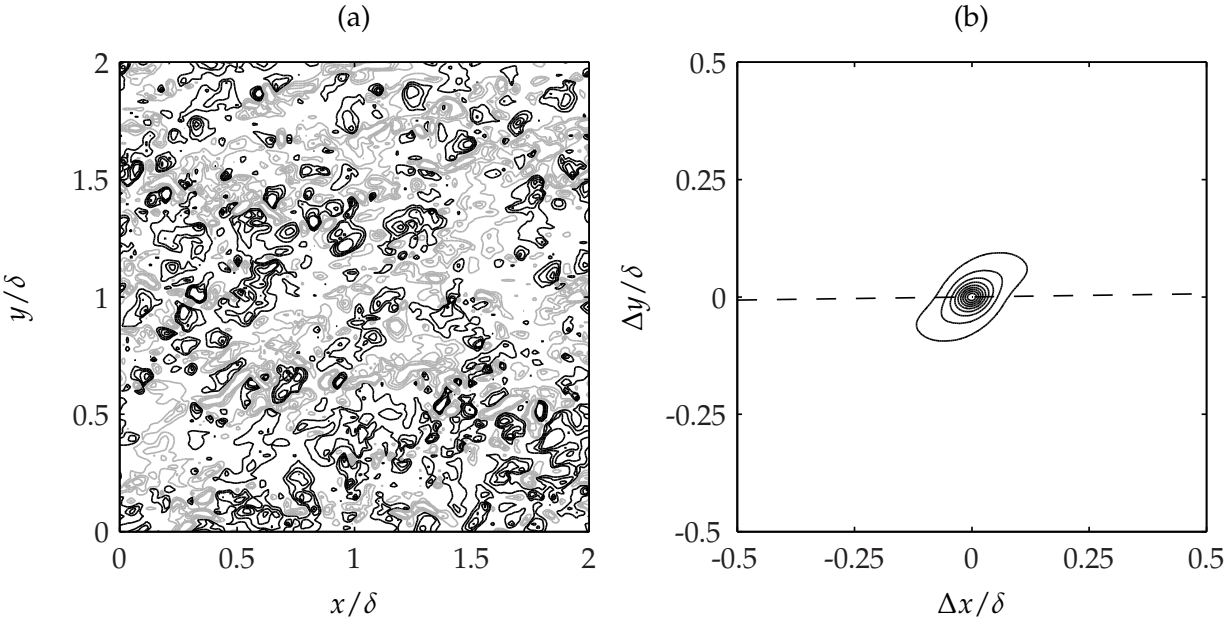

Figure 4.33: Case A, $z_1^+ = 39.4$: (a) p'/u_*^2 at $tf = 0.4$, (b) $R_{pp}(\Delta x, \Delta y, z_1, z_1)$. Contour interval for instantaneous field and autocorrelation is $\Delta = 1.36$ and $\Delta = 0.1$ respectively. Black contours denote positive values while gray indicate negative values; the zero contour is not shown. The dashed line indicates the direction of local shear.

have decreased in strength relative to the center of the structure. The fluctuating pseudo-pressure and corresponding autocorrelation remain approximately the same size as the structures in the near wall region (Fig. 4.33). The smallest scales show little directional preference as the contours are roughly circular.

The final set of autocorrelations presented were taken at $z^+ = 218$ in Fig. 4.34 through 4.37. The autocorrelations show a large increase in structure size and changes in the alignment of structures. Close to the wall, the R_{uu} structure tended to align with the shear direction at the wall. Moving into the boundary layer, however, the inclination has changed such that the autocorrelation shown in Fig. 4.34(b) is aligned between the x coordinate direction and the local shear direction. Two regions of negative correlation now exist as the size of the structures has grown considerably. The R_{vv} autocorrelation also demonstrates alignment with the direction of the velocity component in the autocorrelation. For the spanwise autocorrelation R_{vv}, the structure is stretched in the y direction. The influence of the local shear is evident as the structure is biased in that direction at the largest separation distances. The vertical autocorrelation takes on a roughly circular shape as the distance from the wall increases indicating that w' does not prefer the x or y directions. The slight directional preference that is demonstrated is nearly perfectly aligned with the direction of shear. As will be shown later, the R_{ww} also aligns with its coordinate direction and is stretched vertically. The pressure autocorrelation in Fig. 4.37(b) shows an alignment of the structure in the direction perpendicular to the local shear direction. As pressure transport is partly responsible for the redistribution of energy, the alignment of the pressure structure may be a consequence of pressure acting to diffuse energy into different components. If the structure is aligned as such to promote the return-to-isotropy, we would expect to see the pressure structure also stretched in the vertical direction.

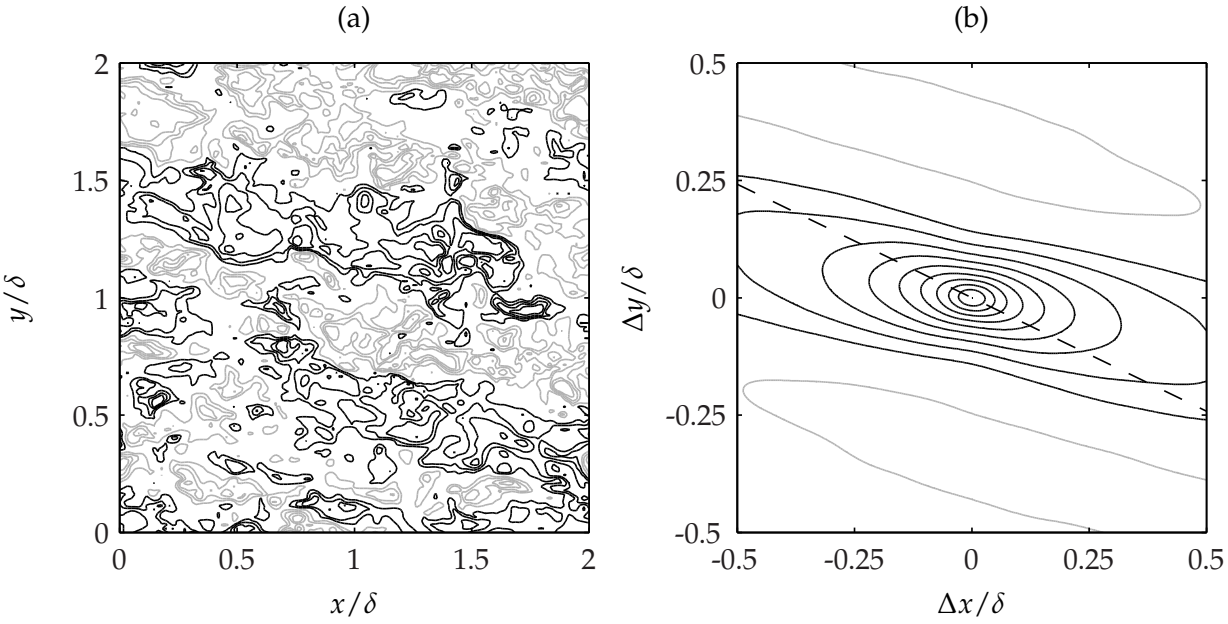

Figure 4.34: Case A, $z_1^+ = 218$: (a) u'/u_* at $tf = 0.4$, (b) $R_{uu}(\Delta x, \Delta y, z_1, z_1)$. Contour interval for instantaneous field and autocorrelation is $\Delta = 0.679$ and $\Delta = 0.1$ respectively. Black contours denote positive values while gray indicate negative values; the zero contour is not shown. The dashed line indicates the direction of local shear.

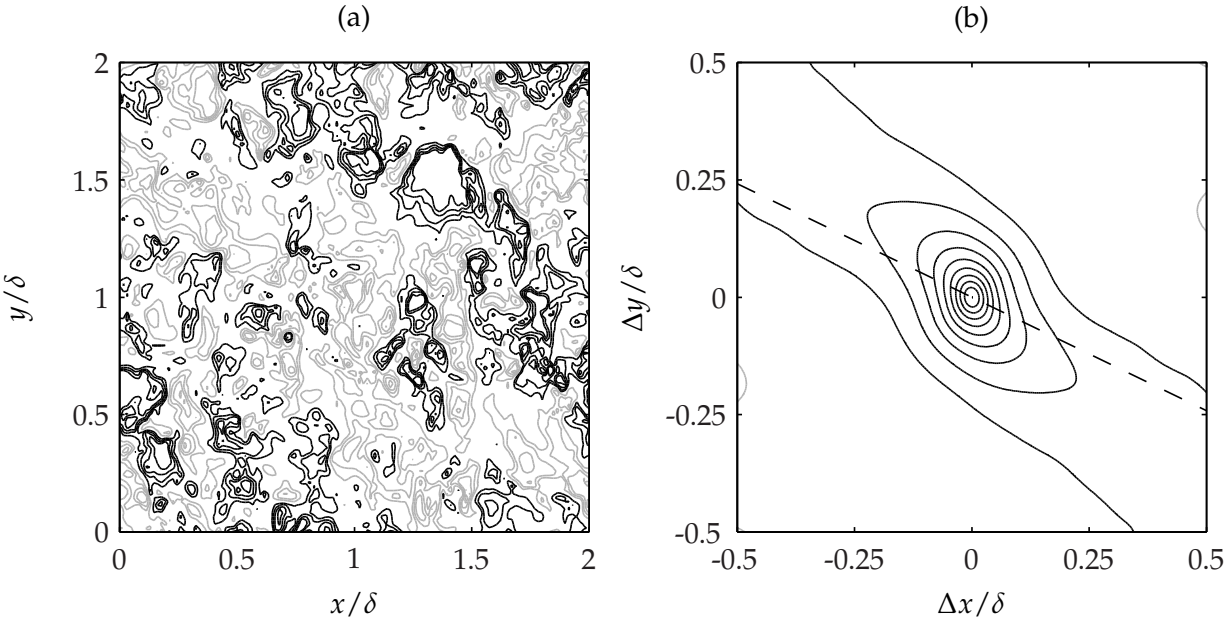

Figure 4.35: Case A, $z_1^+ = 218$: (a) v'/u_* at $tf = 0.4$, (b) $R_{vv}(\Delta x, \Delta y, z_1, z_1)$. Contour interval for instantaneous field and autocorrelation is $\Delta = 0.547$ and $\Delta = 0.1$ respectively. Black contours denote positive values while gray indicate negative values; the zero contour is not shown. The dashed line indicates the direction of local shear.

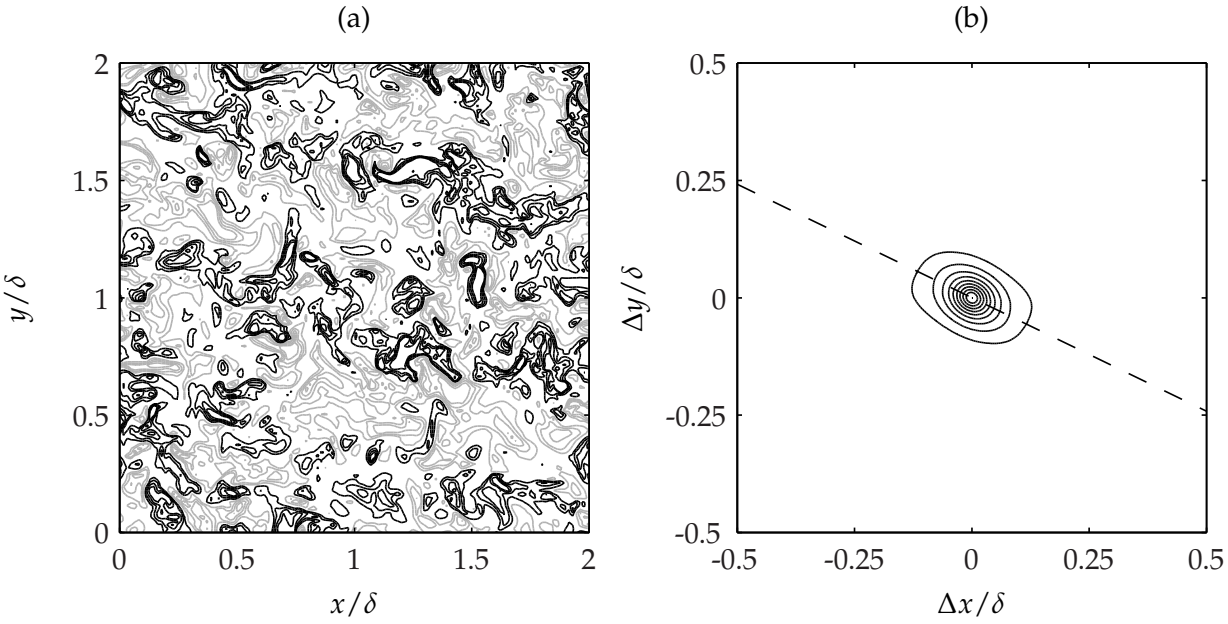

Figure 4.36: Case A, $z_1^+ = 218$: (a) w'/u_* at $tf = 0.4$, (b) $R_{ww}(\Delta x, \Delta y, z_1, z_1)$. Contour interval for instantaneous field and autocorrelation is $\Delta = 0.436$ and $\Delta = 0.1$ respectively. Black contours denote positive values while gray indicate negative values; the zero contour is not shown. The dashed line indicates the direction of local shear.

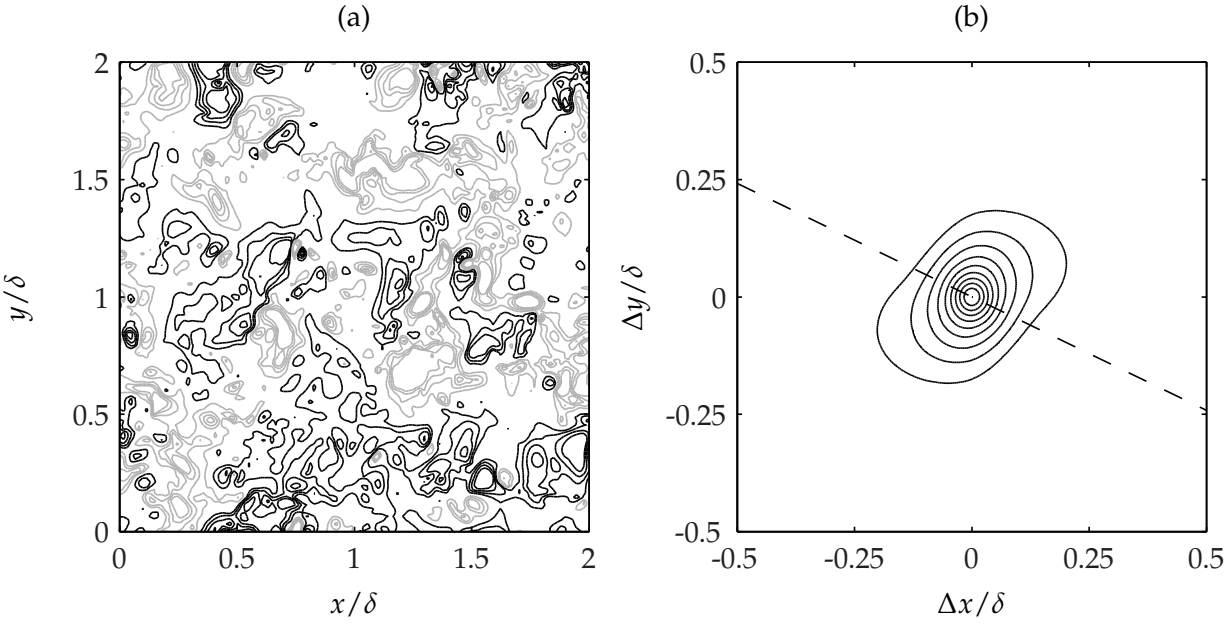

Figure 4.37: Case A, $z_1^+ = 218$: (a) p'/u_*^2 at $tf = 0.4$, (b) $R_{pp}(\Delta x, \Delta y, z_1, z_1)$. Contour interval for instantaneous field and autocorrelation is $\Delta = 0.801$ and $\Delta = 0.1$ respectively. Black contours denote positive values while gray indicate negative values; the zero contour is not shown. The dashed line indicates the direction of local shear.

Taylor Microscale

Although only three locations were shown for the in-plane autocorrelations, statistics were computed at 10 vertical locations in total. From the various autocorrelations it is easy to find the Taylor microscale by (Pope, 1993, pg. 198)

$$\lambda_{u_i,x_j} = \left[-\frac{1}{2} \frac{\partial^2 R_{u_j u_i}}{\partial x_j^2} \right]^{-1/2} \tag{4.4.2}$$

where λ_{u_i,x_i} is the Taylor microscale of the u_i velocity component in the x_i direction (no summation is implied). This particular scale of turbulence is between the Kolmogorov scale η and the size of the large eddies $\mathcal{L}$. Taylor microscales are shown for all three velocity components in Fig. 4.38. Near the wall, the streamwise microscale for all three velocities is larger than the corresponding spanwise microscale as structures are stretched in the direction of the surface shear. Moving further into the boundary layer a growth in λ is evident. Furthermore, the spanwise microscale for v becomes larger than the streamwise microscale indicating the structure is aligning with the y coordinate direction. For isotropic turbulence, the ratio of the microscale aligned with the velocity to component to the scale in the perpendicular direction should have a ratio of $\sqrt{2}$ (≈ 1.41) (Pope, 1993, pg. 199):

$$\frac{\lambda_{u,x}}{\lambda_{u,y}} = \frac{\lambda_{v,y}}{\lambda_{v,x}} = \sqrt{2} \tag{4.4.3}$$

At the point furthest from the wall in Fig. 4.38, the ratios for the u and v microscales are 1.38 and 1.46 respectively. This demonstrates the level of isotropy is increased with an increased distance from the wall. The Taylor microscale can also be expressed as (Marlatt, 1994, Tennekes and Lumley, 1972, pg. 66)

$$\lambda = \sqrt{\frac{\nu k}{\varepsilon}} \tag{4.4.4}$$

which stems from the isotropic approximation (Pope, 1993)

$$\lambda = \sqrt{\frac{15 \nu \overline{u'^2}}{\varepsilon}} \tag{4.4.5}$$

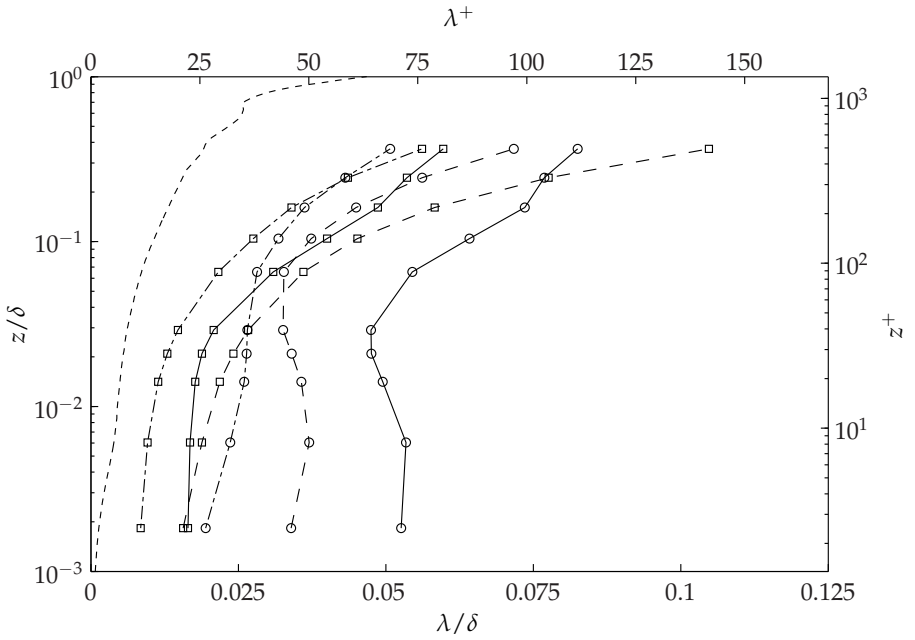

Figure 4.38: Taylor microscale for Case A: λ_u, solid line; λ_v, dashed line; λ_w, dot-dash line. Circles and squares denote streamwise (x) and spanwise (y) microscale respectively. Dotted line indicates microscale λ computed from Eq. 4.4.4.

In Fig. 4.38 it is clear that the microscale computed via the autocorrelations is significantly larger than that computed by Eq. 4.4.4. Constructing a Reynolds number based on the Taylor microscale,

$$\mathrm{Re}_\lambda = \frac{\lambda k^{1/2}}{\nu} \tag{4.4.6}$$

the results indicate a maximum value of $\mathrm{Re}_\lambda \approx 25$ when the microscale is taken from Eq. 4.4.4.

Energy Spectrum

From the x/y autocorrelations the turbulent kinetic energy spectrum was computed. Since the velocity correlations have been normalized such that $R_{ab}(0, 0, z_1, z_1) = 0$ for all velocity components, the spectrum has been computed as such:

$$E(\kappa) = \mathrm{FFT}\left[\frac{k}{3}\left(R_{uu} + R_{vv} + R_{ww}\right)\right] \tag{4.4.7}$$

E is then a measure of the energy in the flow as a function of specific wavenumbers. The results shown in Fig. 4.39 are located at $z^+ = 330$. This location corresponds to the distance from the wall

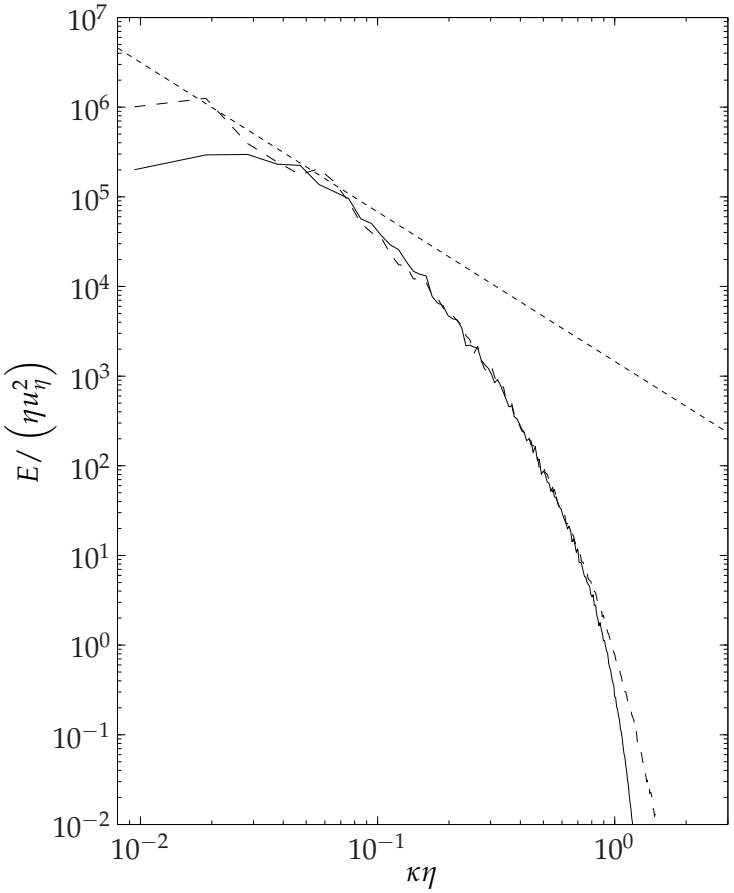

Figure 4.39: Normalized energy spectrum at $z^+ = 330$: solid line, $\kappa_x\eta$; dashed line, $\kappa_y\eta$; dotted line, $\propto \kappa^{-5/3}$.

where the separation of scales ($\mathcal{L}/\eta$) is near a maximum. At the location chosen, $\mathcal{L}/\eta = 123.6$; the maximum in the entire domain is $\mathcal{L}/\eta = 124.9$.

The spectrum in Fig. 4.39 has been normalized by the Kolmogorov scales given by Eqs. 2.6.1 and 2.6.2. Given the Reynolds number of the flow, agreement with the $-5/3$ spectrum is limited.

4.4.2 x/z Projections

A snapshot of the instantaneous velocity and pressure fields is shown in Fig. 4.40. Note that the vertical and horizontal scales are not equal so as to show detail in the wall region. The streamwise and spanwise instantaneous fluctuating velocities in Fig. 4.40(a) and (b) respectively show elongated structures in the near wall region that tend to lift with an increase in x. The vertical and pressure fluctuations in subplots (c) and (d) respectively tend to stretch in z with little elongation in the x direction.

Representative structures in the viscous sublayer are shown in Fig. 4.41 where $z^+ = 2.48$. The streamwise autocorrelation – subplot (a) – appears symmetric for positive and negative Δx apart from the $R_{uu} = 0.1$ contour (which may be a byproduct of sampling). The spanwise autocorrelation is more compact and demonstrates significant lifting with $+\Delta x$. Even when centered very near the wall, the pressure autocorrelation shows a structure that extends far into the boundary layer with a broadening in the structure as z increases.

Moving further away from the wall allows the turbulent structures to grow substantially. Figure 4.42(a) gives R_{uu} at $z^+ = 39.4$. Note how the extent of the autocorrelation is no longer symmetric for $\pm\Delta x$. Instead, R_{uu} shows significant correlation for large $+\Delta x$ and a noticeable lift of the structure with an increased spacing. Conversely, the upstream portion of the autocorrelation ($-\Delta x$) is truncated. This result indicates that turbulent fluctuations generated near the wall are passed downstream and slowly move away from the wall. The spanwise correlation in subplot (b) provides similar behavior except that the lifting is more drastic and a region of negative correlation exists for $-\Delta x$. The vertical velocity and pressure contours show only a slight lifting downstream

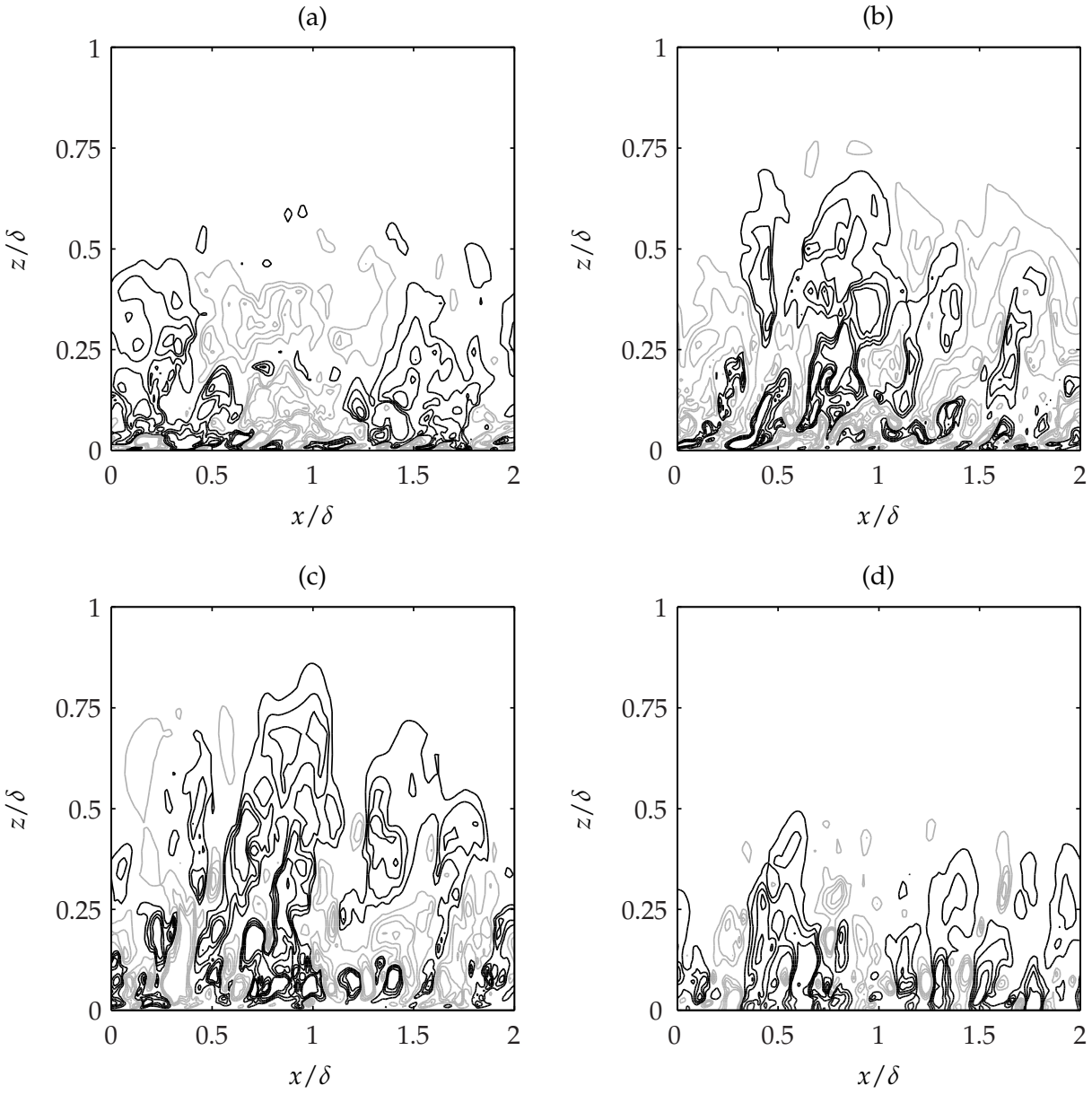

Figure 4.40: Instantaneous velocity and pressure field for Case A, $y/\delta = 0.0203$: (a) u'/u_*, $\Delta = 0.592$; (b) v'/u_*, $\Delta = 0.406$; (c) w'/u_*, $\Delta = 0.327$; p'/u_*^2, $\Delta = 0.757$.

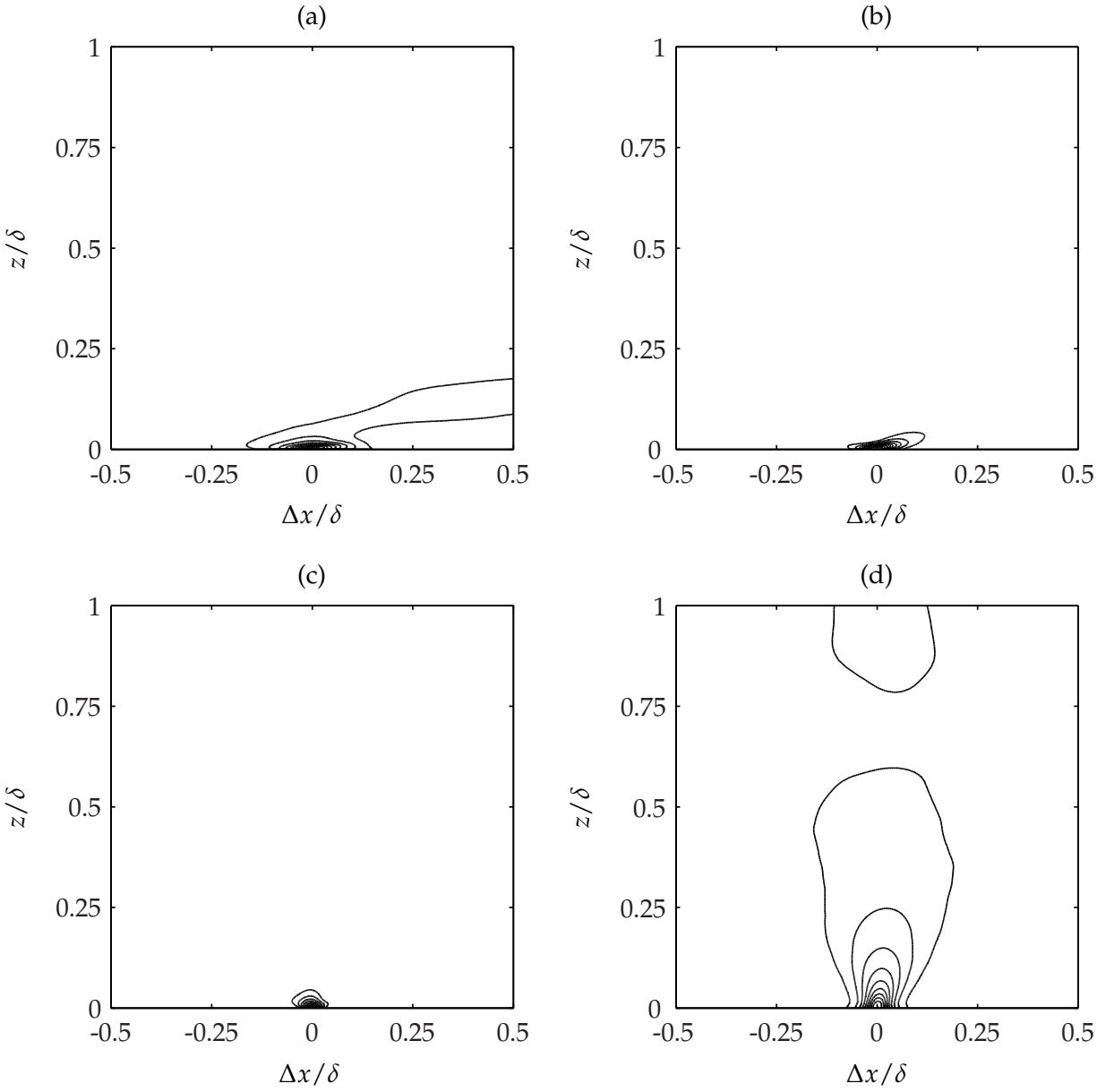

Figure 4.41: Case A, $z_1^+ = 2.48$ ($z/\delta = 0.00183$): (a) $R_{uu}(\Delta x, 0, z_1, z)$, (b) $R_{vv}(\Delta x, 0, z_1, z)$, (c) $R_{ww}(\Delta x, 0, z_1, z)$, (d) $R_{pp}(\Delta x, 0, z_1, z)$. Contour interval is $\Delta = 0.1$. Black contours denote positive values while gray indicate negative values; the zero contour is not shown.

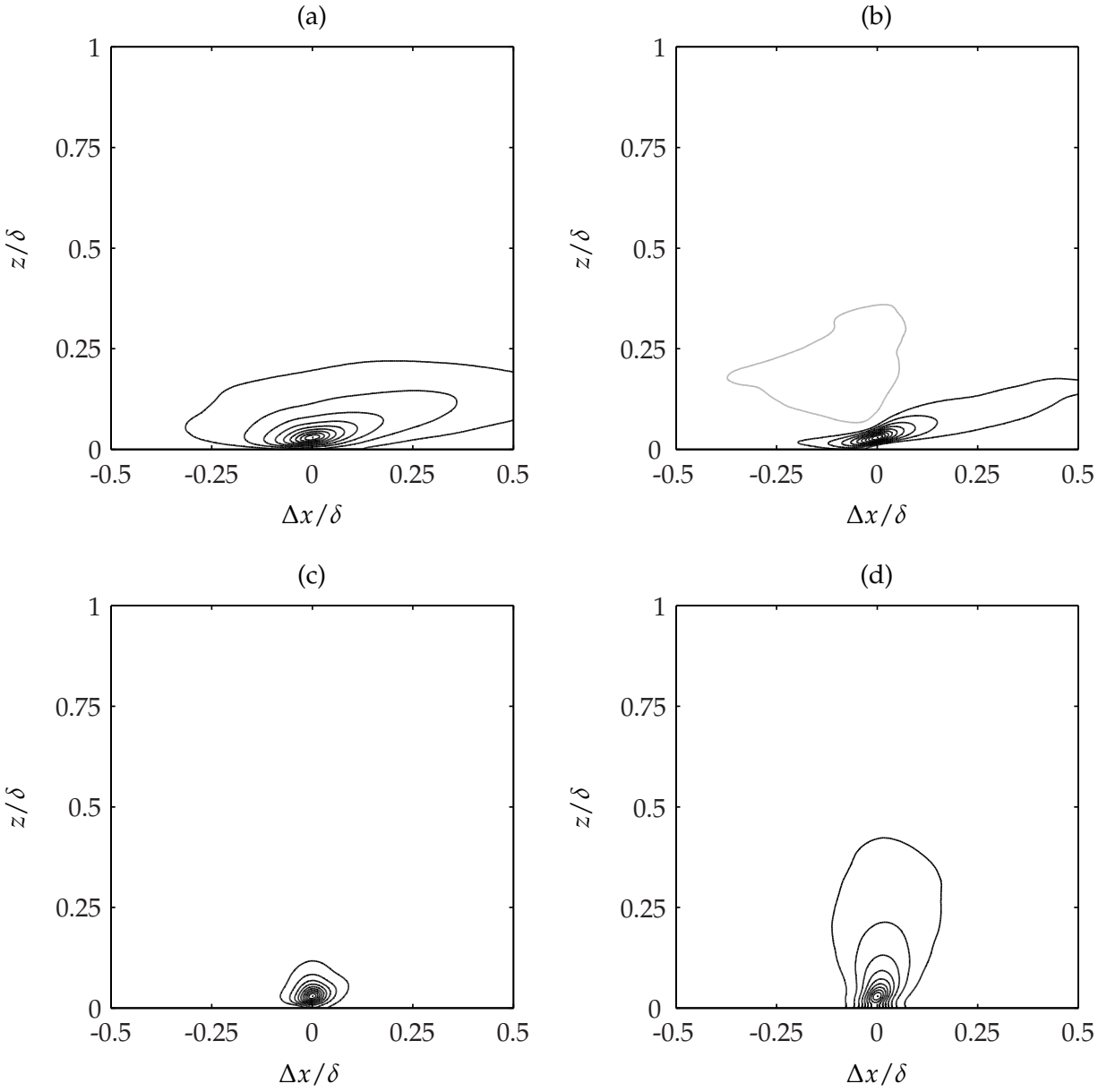

Figure 4.42: Case A, $z_1^+ = 39.4$ ($z/\delta = 0.029$): (a) $R_{uu}(\Delta x, 0, z_1, z)$, (b) $R_{vv}(\Delta x, 0, z_1, z)$, (c) $R_{ww}(\Delta x, 0, z_1, z)$, (d) $R_{pp}(\Delta x, 0, z_1, z)$. Contour interval is $\Delta = 0.1$. Black contours denote positive values while gray indicate negative values; the zero contour is not shown.

of the structure center. Concerning the pressure autocorrelation, it is peculiar that the vertical extent of the structure is reduced as the center of the structure is moved further from the wall.

Shown in Fig. 4.43 are the autocorrelations centered at $z^+ = 218$. The transport of near-wall turbulence away from the wall is clearly evident in the R_{vv} autocorrelation (and to a smaller extend, R_{uu}). The vertical velocity autocorrelation elongates in the vertical direction with an increased separation from the wall. As the flow becomes more isotropic the autocorrelations tend to align themselves in the direction of the velocity component.

4.4.3 y/z Projections

An instantaneous velocity and pressure field across the y/z plane is shown in Fig. 4.44. From the perturbation contours it is hard to surmise anything about the general structures except for that the length scales of velocity structures is significantly shorter in the y direction than in the x direction (which was plainly obvious from the x/y instantaneous fields and autocorrelations), and the instantaneous spanwise and vertical velocity in subplot (b) and (c) respectively tend to roughly correlate with each other for $z/\delta < 0.25$.

The near-wall autocorrelation in Fig. 4.45 demonstrate the narrow shape of the typical turbulent structures. A slight rightward inclination is noted in R_{uu}. Though hard to see in the figures, negative correlation regions exist near the wall for both R_{vv} and R_{ww}. Once again, the pressure exhibits stretching in the wall-normal direction.

Moving further from the wall the rightward tilt in the streamwise autocorrelation is corrected and the structure stands nearly vertical. The vertical velocity still exhibits regions of negative correlation, but R_{vv} now shows a slight lifting with $+\Delta y$ and a region of negative correlation above the structure.

At $z^+ = 218$, the autocorrelations shown in Fig. 4.47 show significant tilting. R_{uu} now shows a leftward tilt. It is believed that the tilt is directly related to the gradient of the spanwise mean

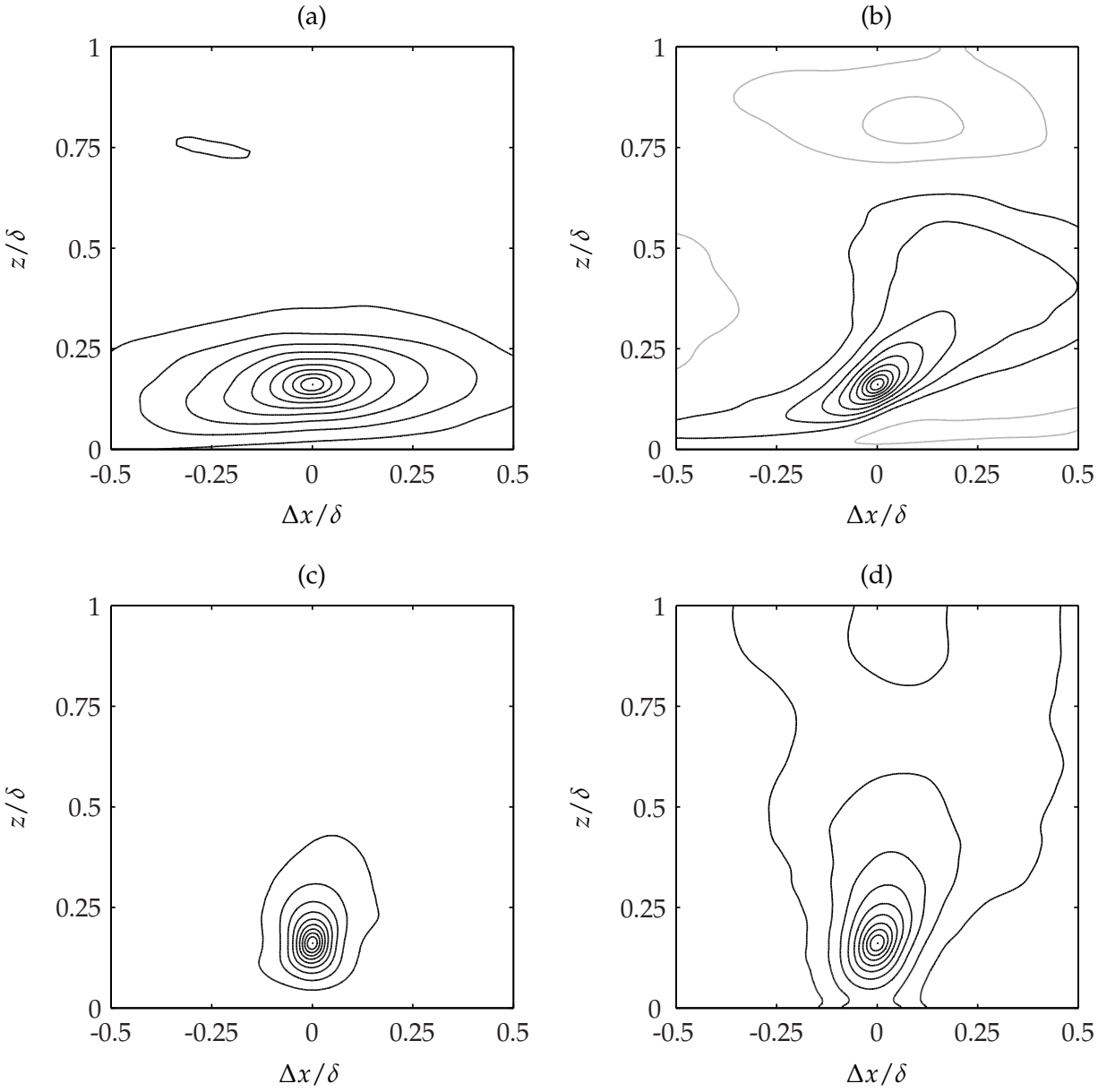

Figure 4.43: Case A, $z_1^+ = 218$ ($z/\delta = 0.16$): (a) $R_{uu}(\Delta x, 0, z_1, z)$, (b) $R_{vv}(\Delta x, 0, z_1, z)$, (c) $R_{ww}(\Delta x, 0, z_1, z)$, (d) $R_{pp}(\Delta x, 0, z_1, z)$. Contour interval is $\Delta = 0.1$. Black contours denote positive values while gray indicate negative values; the zero contour is not shown.

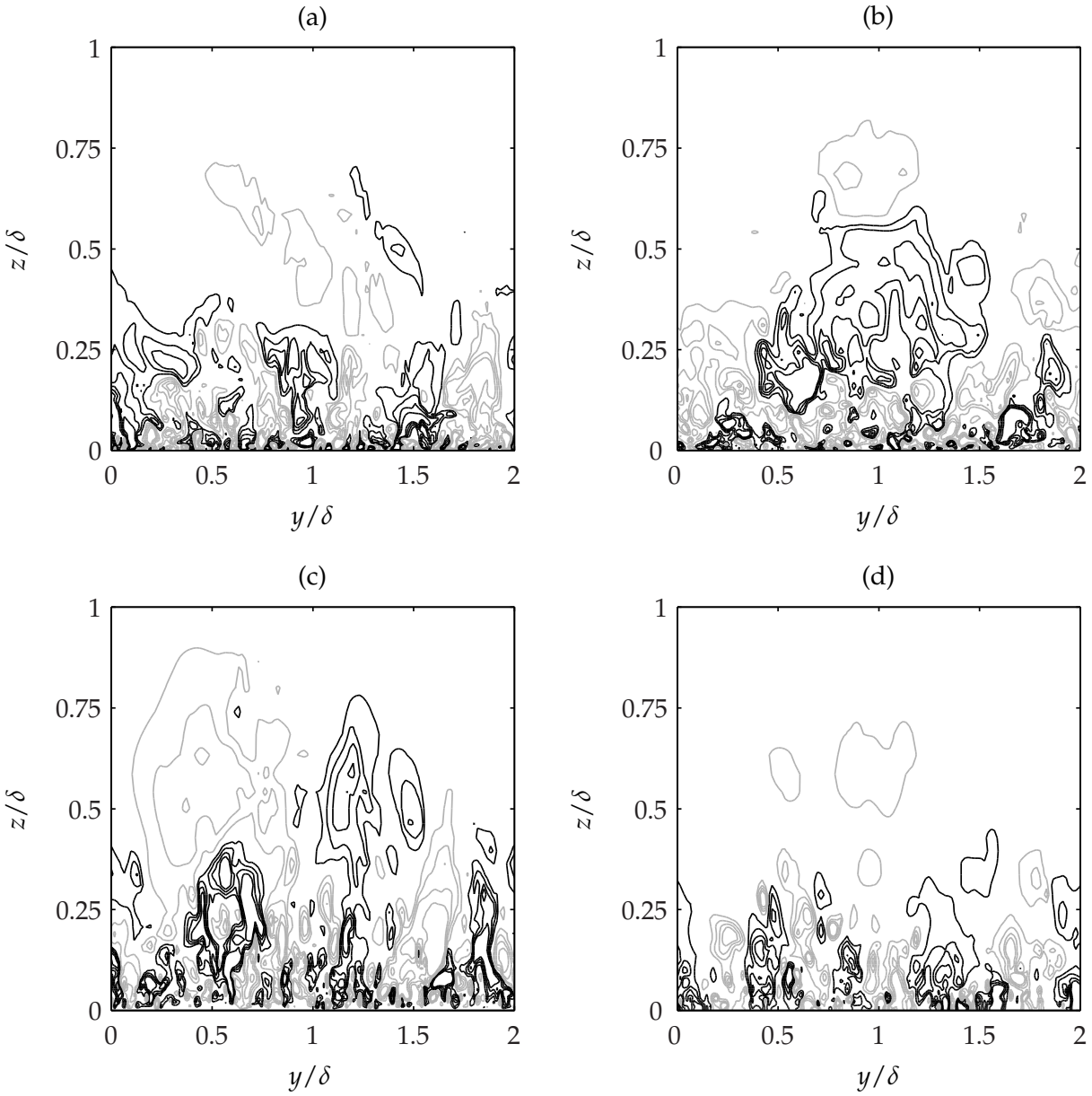

Figure 4.44: Instantaneous velocity and pressure field for Case A, $x/\delta = 0.0203$: (a) u'/u_*, $\Delta = 0.673$; (b) v'/u_*, $\Delta = 0.472$; (c) w'/u_*, $\Delta = 0.334$; p'/u_*^2, $\Delta = 0.711$.

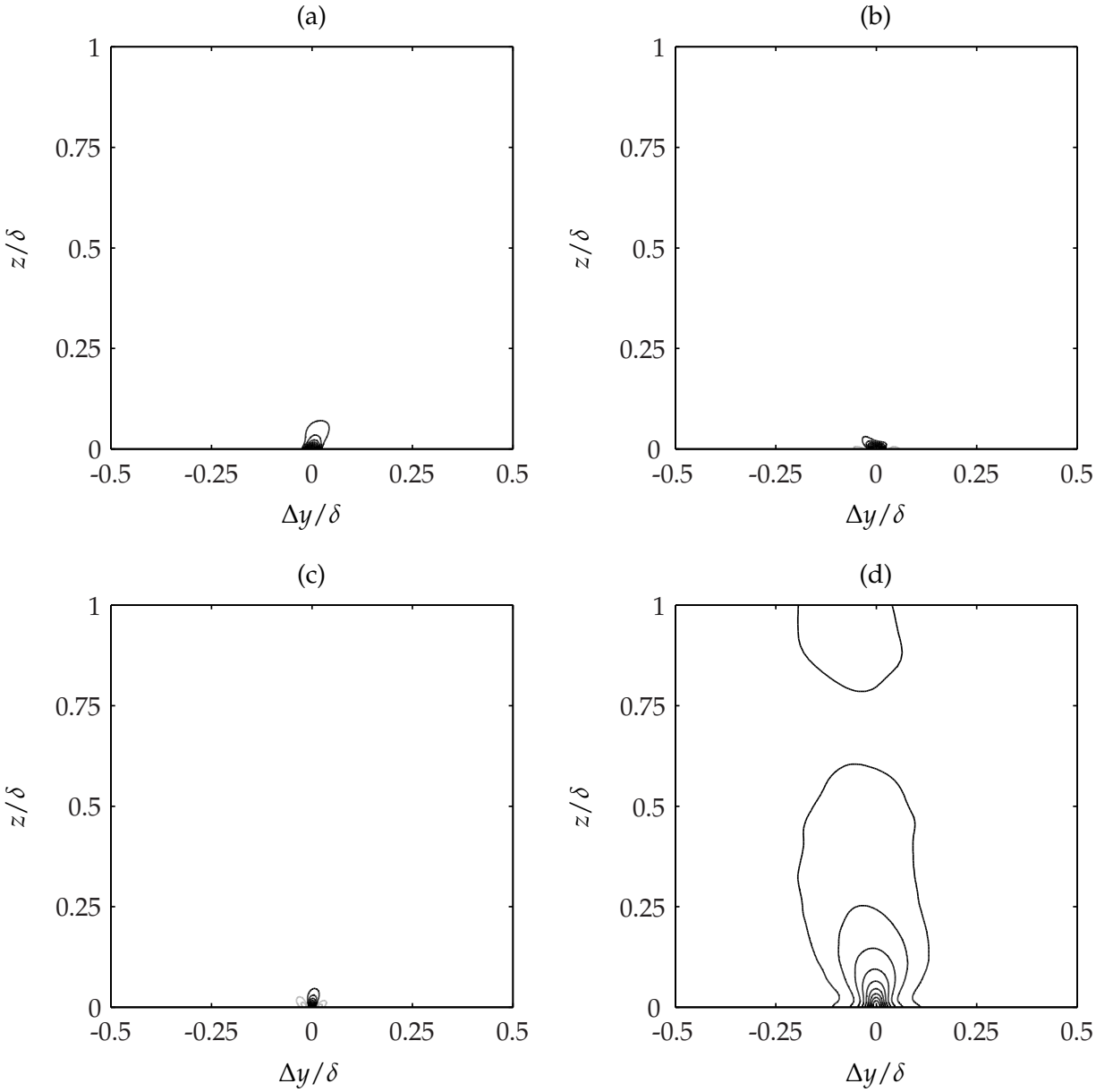

Figure 4.45: Case A, $z_1^+ = 2.48$ ($z/\delta = 0.00183$): (a) $R_{uu}(0, \Delta y, z_1, z)$, (b) $R_{vv}(0, \Delta y, z_1, z)$, (c) $R_{ww}(0, \Delta y, z_1, z)$, (d) $R_{pp}(0, \Delta y, z_1, z)$. Contour interval is $\Delta = 0.1$. Black contours denote positive values while gray indicate negative values; the zero contour is not shown.

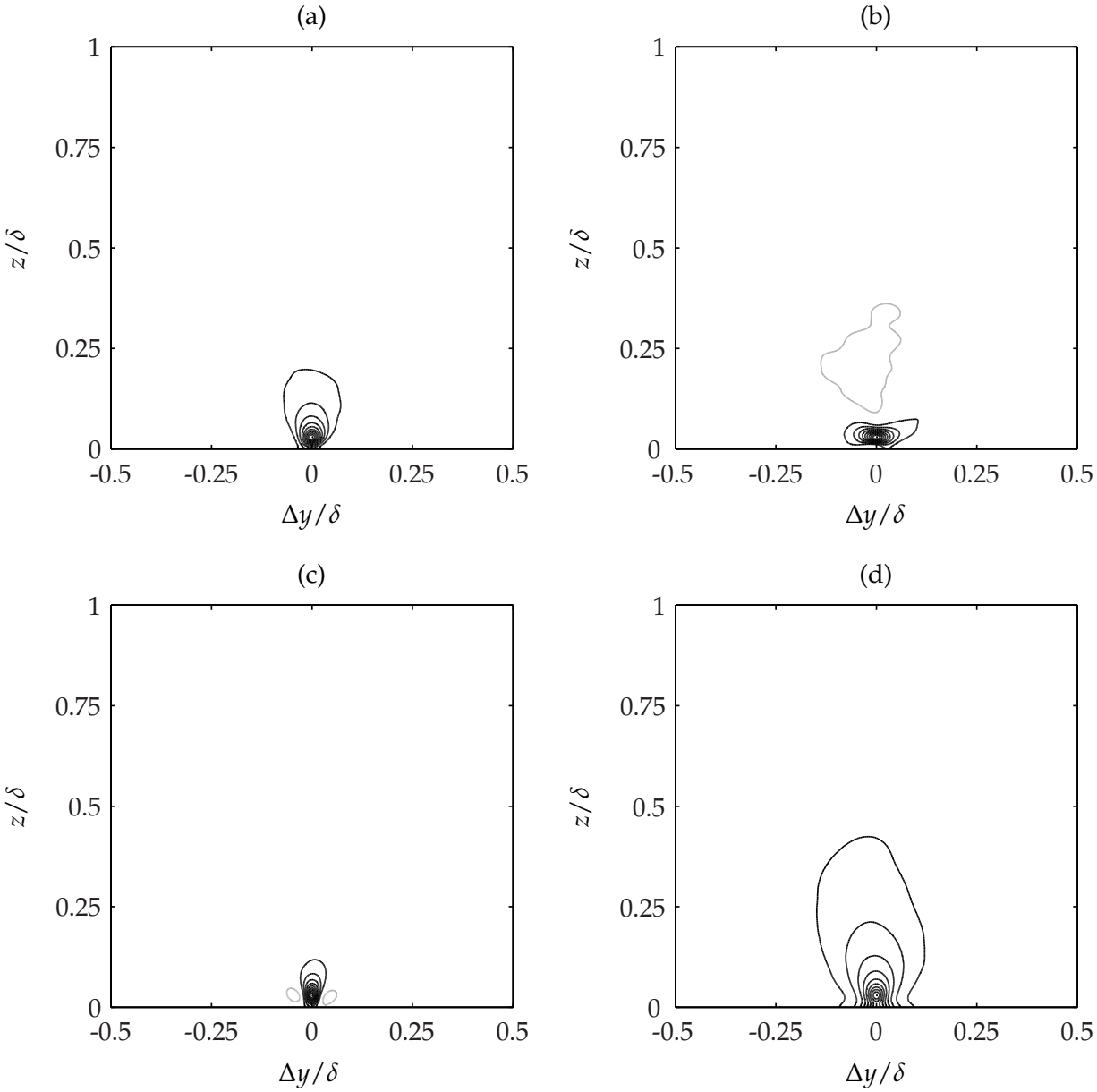

Figure 4.46: Case A, $z_1^+ = 39.4$ ($z/\delta = 0.029$): (a) $R_{uu}(0, \Delta y, z_1, z)$, (b) $R_{vv}(0, \Delta y, z_1, z)$, (c) $R_{ww}(0, \Delta y, z_1, z)$, (d) $R_{pp}(0, \Delta y, z_1, z)$. Contour interval is $\Delta = 0.1$. Black contours denote positive values while gray indicate negative values; the zero contour is not shown.

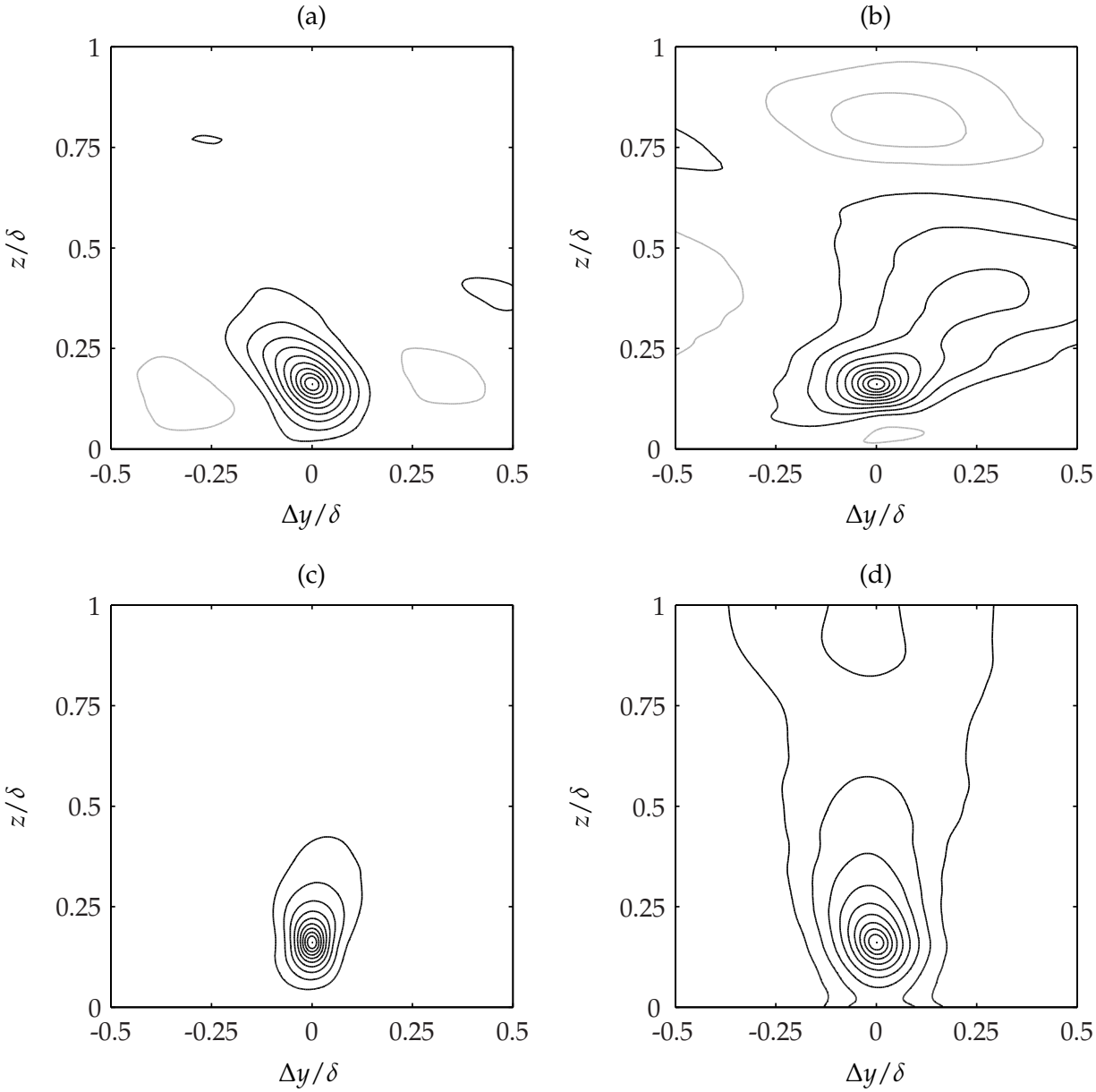

Figure 4.47: Case A, $z_1^+ = 218$ ($z/\delta = 0.16$): (a) $R_{uu}(0, \Delta y, z_1, z)$, (b) $R_{vv}(0, \Delta y, z_1, z)$, (c) $R_{ww}(0, \Delta y, z_1, z)$, (d) $R_{pp}(0, \Delta y, z_1, z)$. Contour interval is $\Delta = 0.1$. Black contours denote positive values while gray indicate negative values; the zero contour is not shown.

velocity: $\partial V/\partial z$. This would explain the change in tilt of the streamwise structure at the different locations in the boundary layer. Moreover, the autocorrelation shape is a direct consequence of the inclusion of Coriolis rotation given the nonzero V component. The spanwise autocorrelation once again lifts in the downstream region.

4.5 Evaluation of closure model: $k - \varepsilon$

Turbulence close models are required to close the governing momentum equations given the existence of the $\overline{u_i' u_j'}$ velocity correlations that appear in the Reynolds-averaged equations (App. A). While further governing equations can be derived for these second-order moments, more third-order moments are generated resulting in an unclosed system. Closure models are used to relate these unknown moments back to some known quantity in the flow field through both theoretical and empirical devices. The order of the model typically refers to the order of the moment that will be approximated by some prognostic equations. If second-order Reynolds stresses are modeled, the closure is termed second-order (e.g. Umlauf and Burchard, 2005); if third-order moments are modeled, the closure is third-order (e.g. Zilitinkevich et al., 1999). The model will typically relate high-order terms back to known quantities. For example, the fourth-order moment $\overline{w'^4}$ is typically a function of the second-order moment $\overline{w'^2}^2$.

Although current meteorological closures typically utilize high-order models (e.g. Lappen et al., 2010), many methods of relating the mean-flow to the Reynolds stresses are based upon an analogy with molecular viscosity and assume a form of down-gradient diffusion by the turbulent stresses:

$$\overline{u_i' u_j'} - \frac{2}{3} k \delta_{ij} = -K_m \left(\frac{\partial U_i}{\partial x_j} + \frac{\partial U_j}{\partial x_i} \right) \tag{4.5.1}$$

where K_m is known by a variety of names, such as 'eddy viscosity', 'eddy diffusivity', or 'turbulent diffusivity,' and k is the turbulent kinetic energy. For the horizontally homogeneous Ekman problem under consideration, Eq. 4.5.1 is identically zero for all normal stresses. To avoid uncertainties

regarding coordinate system rotation, the data presented here consider the parameterization of the total Reynolds vertical momentum flux

$$\sqrt{\overline{u'w'}^2 + \overline{v'w'}^2} = -K_m \sqrt{\left(\frac{\partial U}{\partial z}\right)^2 + \left(\frac{\partial V}{\partial z}\right)^2} \tag{4.5.2}$$

which follows directly from $\overline{u'w'} = -K_{m1}\,(\partial U/\partial z)$ and $\overline{v'w'} = -K_{m2}\,(\partial V/\partial z)$. Note that this assumes isotropic turbulent diffusion (i.e. $K_m = K_{m1} = K_{m2}$). The definition in Eq. 4.5.2 will be used to compute the eddy diffusivity from DNS data for comparison with model predictions.

The $k-\varepsilon$ model, which was first introduced by Jones and Launder (1972, 1973), is a typical variant of the second-order closure scheme. Instead of six prognostic equations for the six components of the Reynolds stress tensor, the $k-\varepsilon$ closure model utilizes a governing equation for the turbulent kinetic energy k (Eq. 4.2.12) and the dissipation rate ε (Eq. 4.3.1 and 4.3.4b). Various forms of the $k-\varepsilon$ model have been applied to a variety of atmospheric flow problems including boundary layer flow over a tree canopy (Liang et al., 2006), neutral atmospheric boundary layer flows (Hargreaves and Wright, 2007), and dispersion in urban environments (Kim and Baik, 2004).

As presented for the model, these equations have the form

$$\frac{Dk}{Dt} = -\overline{u'w'}\frac{dU}{dz} - \overline{v'w'}\frac{dV}{dz} - \frac{d\left(\overline{w'p'} + \overline{w'k'}\right)}{dz} - \varepsilon \tag{4.5.3a}$$

$$\frac{D\varepsilon}{Dt} = C_{\varepsilon 1}\left(\frac{\varepsilon}{k}\right)\left[-\overline{u'w'}\frac{dU}{dz} - \overline{v'w'}\frac{dV}{dz}\right] - \frac{d\overline{w'\varepsilon'}}{dz} - C_{\varepsilon 2}\left(\frac{\varepsilon^2}{k}\right) \tag{4.5.3b}$$

where $D/Dt = \partial/\partial t + \mathbf{u}\cdot\nabla$ is the total derivative and the effects of buoyancy are at present neglected. For the steady-state, horizontally-homogeneous simulation presented here, $D/Dt = 0$. The terms k' and ε' are used to denote instantaneous turbulent kinetic energy and kinetic energy dissipation respectively. The equations are then closed using the assumptions (Beljaars et al., 1987, Stull, 1988)

$$K_m = \frac{(\alpha_m k)^2}{\varepsilon} \tag{4.5.4a}$$

$$\overline{w'p'} + \overline{w'k'} = -K_m\frac{dk}{dz} \tag{4.5.4b}$$

$$\overline{w'\varepsilon'} = -\frac{K_m}{C_{\varepsilon 3}}\frac{d\varepsilon}{dz} \tag{4.5.4c}$$

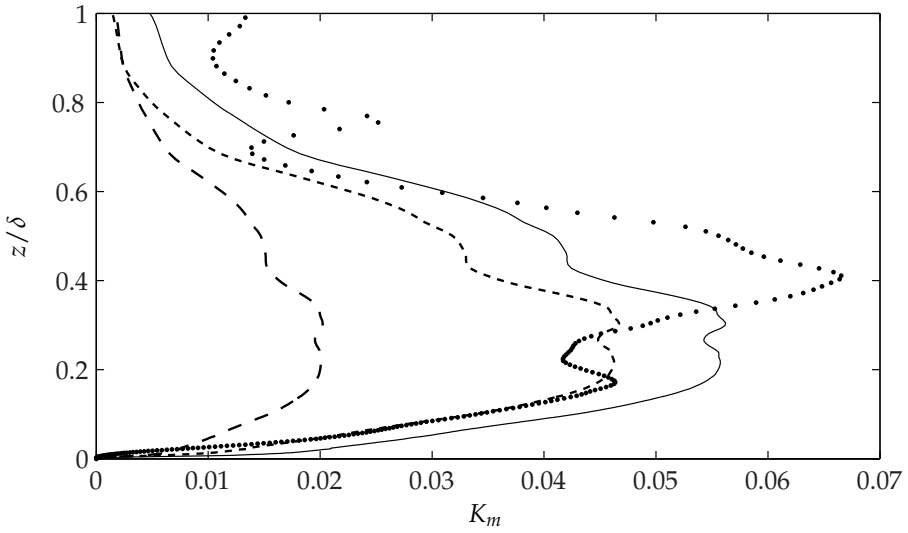

Figure 4.48: Eddy diffusivity for $k-\varepsilon$ model: solid line, $\alpha_m = 0.3$; dashed line, $\alpha_m = 0.18$; short-dash line, $\alpha_m = f(\mathrm{Re}_T)$; dots, DNS.

The constants are defined, primarily on the basis of empirical evidence, by $C_{\varepsilon 1} = 1.44$ and $C_{\varepsilon 2} = 1.92$, $C_{\varepsilon 3} = 1.30$, and $\alpha_m = 0.3$. The value $\alpha_m = 0.3$ was originally recommended by Jones and Launder; Panofsky and Dutton (1984) recommend a value of 0.18 as more appropriate for the ABL. For low Reynolds number turbulence, Jones and Launder (1973) recommend several modifications (see White, 1991). Without revisiting the prognostic equations, the most interesting is the modification to α_m:

$$\alpha_m = \left[0.09 \exp\left(\frac{-2.5}{1 + \mathrm{Re}_T/50}\right)\right]^{1/2} \tag{4.5.5}$$

where Re_T is the turbulent Reynolds number defined $\mathrm{Re}_T = \hat{k}^2/\hat{\varepsilon}\nu$ (the 'hat' denotes a dimensional quantity), or, in terms of the dimensionless kinetic energy and dissipation, $\mathrm{Re}_T = \mathrm{Re}(k^2/\varepsilon)$. k and ε are nondimensionalized by $k = \hat{k}/U_g^2$ and $\varepsilon = \hat{\varepsilon}\delta_E/U_g^3$ respectively. In the present simulation this value varies across the boundary layer and peaks at $\mathrm{Re}_T = 624.6$ near $z/\delta = 0.305$.

Comparison between the modeled eddy diffusivities (Eq. 4.5.4a) and those from the DNS (Eq. 4.5.2) are presented in Fig. 4.48, while the resulting Reynolds stress profiles are shown in Fig. 4.49. Qualitatively the profiles are correct; however, the location of the maximum diffusivity

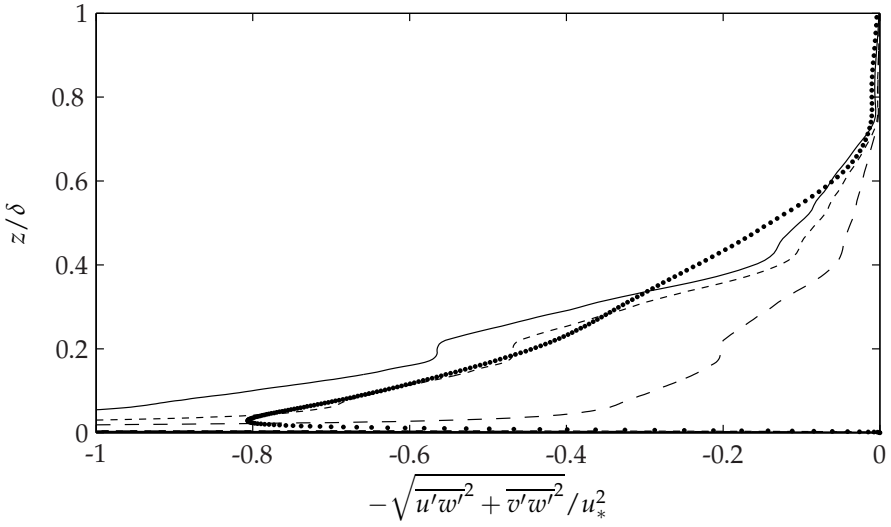

Figure 4.49: Reynolds stress for $k-\varepsilon$ model: solid line, $\alpha_m = 0.3$; dashed line, $\alpha_m = 0.18$; short-dash line, $\alpha_m = f(\mathrm{Re}_T)$; dots, DNS.

is off by approximately 0.1δ regardless of the value of α_m. For $\alpha_m = 0.3$, the model over-predicts the Reynolds stress in the lower half of the boundary layer and under-predicts in the upper half. Reducing α_m to 0.18 results in poor model performance across the entire flow field. The variable coefficient where $\alpha_m = f(\mathrm{Re}_T)$ yields the best results with great accuracy for $z/\delta < 0.3$ and $z/\delta > 0.6$. The middle region of the boundary layer is underpredicted by all three values of α_m, and performance of the models in the near-wall region is poor. Referring to the normal stress budgets presented in Figs. 4.17 – 4.19, a significant source of energy in the near-wall region is molecular diffusion. The formulation given by Eq. 4.5.3 ignores this term and may be the source of inaccuracy close to the wall.

To better assess the $k-\varepsilon$ model with respect to the simulation data, comparisons were made of the kinetic energy production and transport terms in Eq. 4.5.3a and the transport term in Eq. 4.5.3b. The kinetic energy production is parameterized, using Eq. 4.5.4a, as

$$-\overline{u'w'}\frac{dU}{dz} - \overline{v'w'}\frac{dV}{dz} \approx K_m \left[\left(\frac{dU}{dz}\right)^2 + \left(\frac{dV}{dz}\right)^2 \right] \tag{4.5.6}$$

and the transfer terms are modeled by Eq. 4.5.4b and 4.5.4c, respectively.

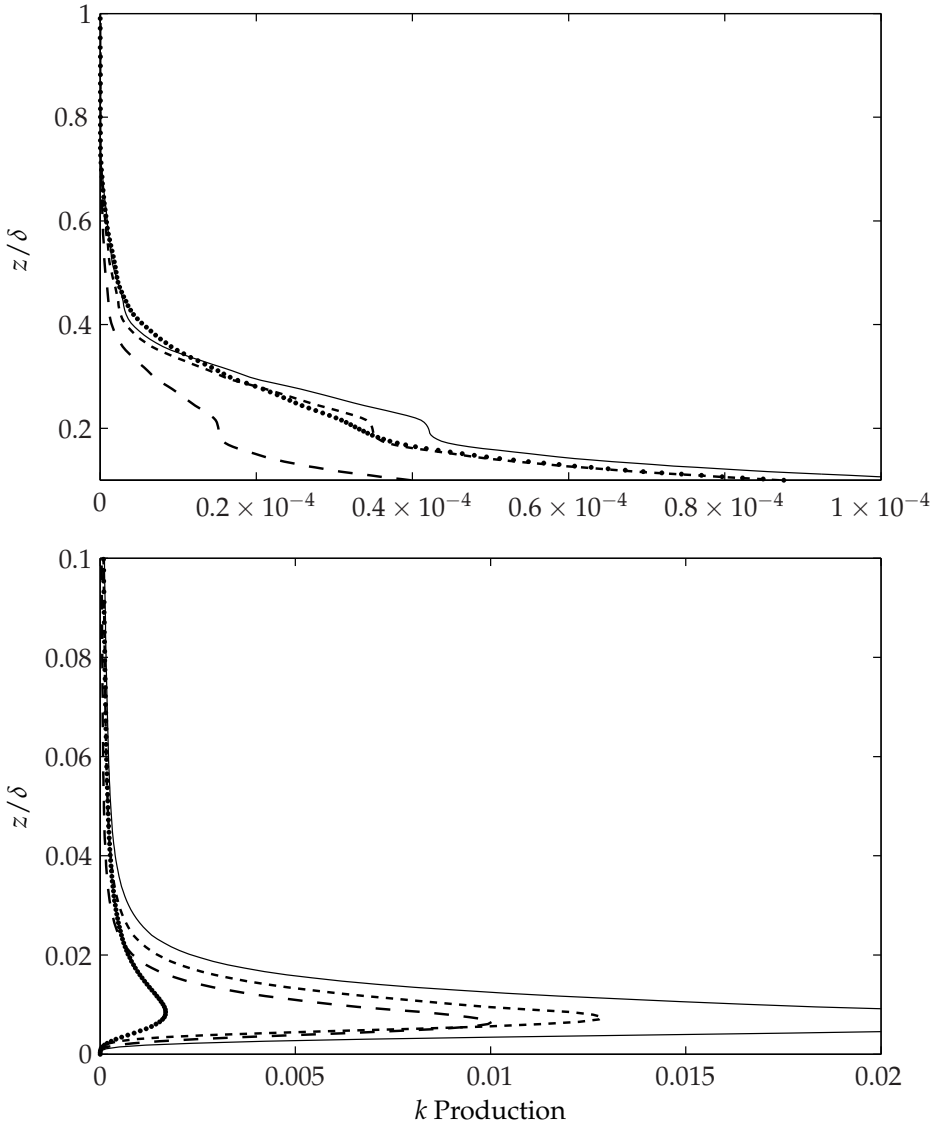

Figure 4.50: Production term for $k-\varepsilon$ model: solid line, $\alpha_m = 0.3$; dashed line, $\alpha_m = 0.18$; short-dash line, $\alpha_m = f(\mathrm{Re}_T)$; dots, DNS.

The vertical profiles of kinetic energy production (Fig. 4.50) demonstrate that this term is overestimated by all three forms of the model in the near-wall region. However, the location of maximum production is well captured and relatively good agreement is achieved above $z/\delta \approx 0.1$, especially when α_m is a function of Re_T. Apart from the near-wall region (where the best model is off by over a factor of 4), the variable value of α_m performs quite well.

The transport model is qualitatively correct throughout the entire boundary layer. The crossover is well captured (Fig. 4.51, bottom) for all 3 values of α_m. The location of the minimum ($z/\delta \approx 0.01$) is accurately predicted; however, each model overshoots the actual value. The maxima at $z/\delta = 0.3$ is modeled slightly nearer the wall than DNS results, but the $\alpha_m = f(\mathrm{Re}_T)$ curve is quite accurate with predicting the actual maximum value. However, all models underpredict the transport terms above $z/\delta = 0.4$. Pressure transport and turbulent diffusion are modeled together as a down-gradient diffusion of kinetic energy. Although pressure diffusion does transport energy away from the wall as suggested by Eq. 4.5.4b (see Fig. 4.19), modeling both transport terms together may be the cause of the discrepancies noted.

The vertical profiles of the dissipation (Fig. 4.52) are qualitatively well represented by the models except in the near-wall region where the models behave poorly due to an inflection in the mean dissipation profile. None of the models capture the small negative region below $z/\delta = 0.01$. However, the curve for $\alpha_m = f(\mathrm{Re}_t)$ shows good agreement above $z/\delta = 0.05$. All models underpredict the dissipation in the middle parts of the boundary layer $(0.35 < z/\delta < 0.7)$.

4.6 Summary

The neutral Ekman layer results presented here were carried out at the Reynolds number of $\mathrm{Re} = 1000$. At this modest Reynolds number, approximately half-a-decade of log-law behavior is evident in the mean velocity profile. However, the ratio of the largest to smallest turbulent scales is only $\mathcal{L}/\eta = 123.6$; little evidence of a $-5/3$ behavior can be seen in the turbulent kinetic energy

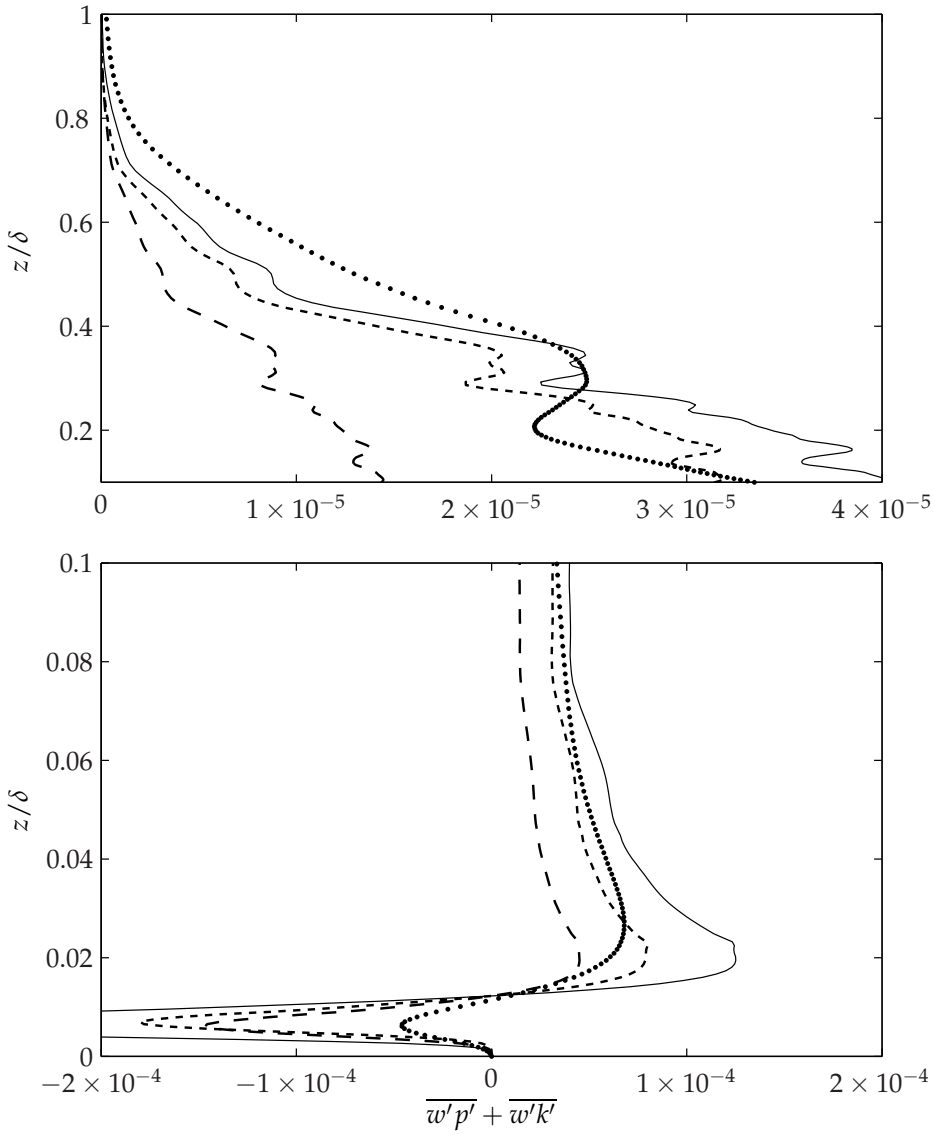

Figure 4.51: Transport terms for $k - \varepsilon$ model: solid line, $\alpha_m = 0.3$; dashed line, $\alpha_m = 0.18$; short-dash line, $\alpha_m = f(\mathrm{Re}_T)$; dots, DNS.

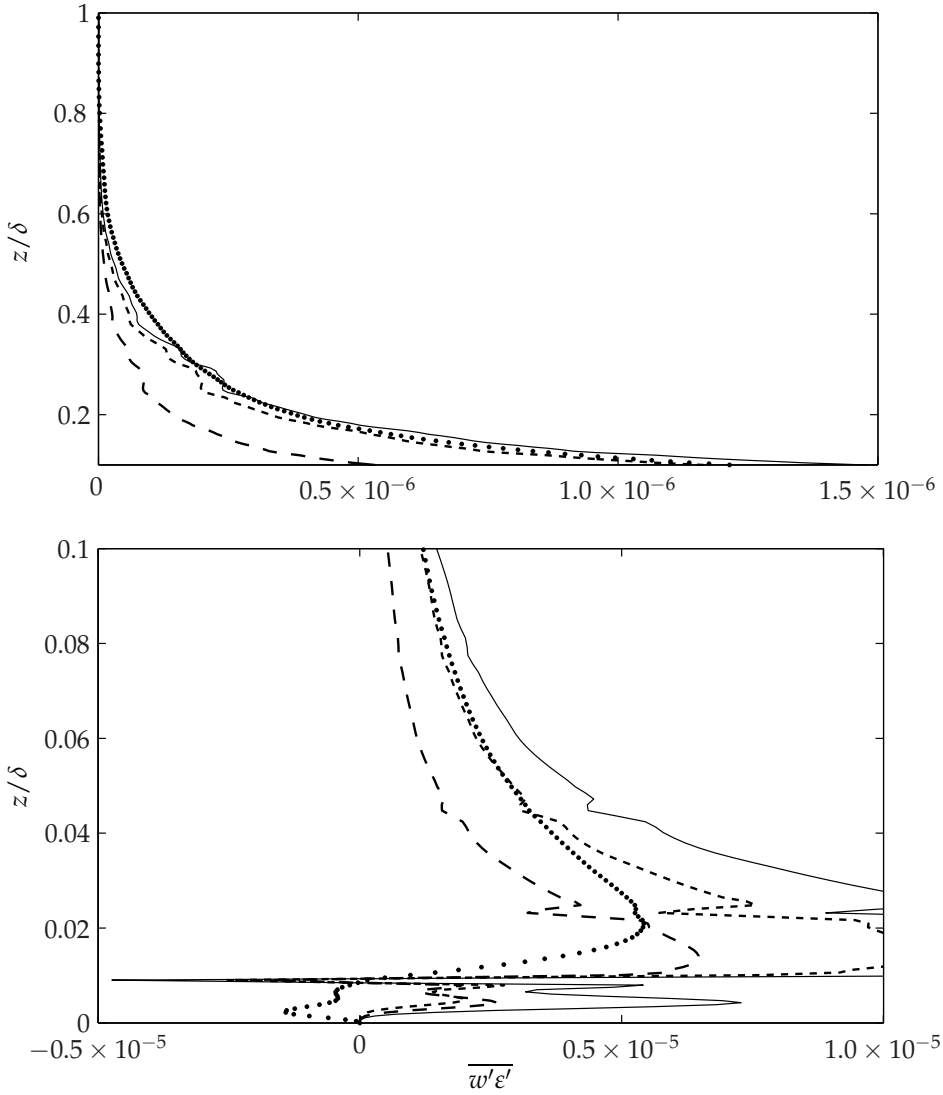

Figure 4.52: Dissipation term for $k - \varepsilon$ model: solid line, $\alpha_m = 0.3$; dashed line, $\alpha_m = 0.18$; short-dash line, $\alpha_m = f(\mathrm{Re}_T)$; dots, DNS.

spectrum.

The kinetic energy budgets indicate a complex exchange of energy between the 3 variance and 3 covariance Reynolds stresses. Given the absence of buoyant forcing, production by mean shear for the $\overline{u'u'}$ stress is the primary source of turbulent energy. A small contribution by $\overline{v'v'}$ exists, but is secondary to the streamwise production in the near-wall region. Away from the wall, however, spanwise production becomes a primary source of energy. The return-to-isotropy component energizes the vertical Reynolds stress by taking energy from both horizontal components. This is true apart from the near-wall region where the 'splatting' effect redistributes energy from the vertical to horizontal components. The local minimum seen in ε for both horizontal components appears to coincide with the location at which molecular diffusion acts as a sink. Instead of being dissipated, the energy is transfered down to the wall. Finally, comparing the results with those of Marlatt et al. (2010), it appears the effect of Coriolis redistribution decreases with an increase in Reynolds number.

Autocorrelation structures were computed from the data set. Results indicate that the structures near the wall are all inclined at the shear angle at the wall. As the flow becomes more isotropic, the autocorrelations tend to align with their specific coordinate. The most notable difference between the turbulent Ekman layer and other boundary layers is apparent in the R_{uu} correlation. The opposite tilting evident in the presented contours is attributed to the vertical variation in the mean velocity gradient.

Two different closure models have been analyzed. As a means of closing the fourth-order moments, the kurtosis of the streamwise velocity is well approximated by the square of the skewness as shown in Fig. 4.14. Spanwise and vertical velocities demonstrate less agreement with the model given by Eq. 4.2.15. The evaluation performed of the $k-\varepsilon$ closure model supports its use in modeling rotating flows. Specifically, the parameterization of α_m as a function of the turbulent Reynolds number (Re_T) dramatically improved the results over the models utilizing a constant value for α_m. The underprediction of the Reynolds stresses in the outer region of the boundary

layer appears to be a consequence of the underestimation of the transport terms coupled with a slight difference in the modeled and actual dissipation. Comparing the magnitude of the pressure diffusion term $\overline{w'p'}$ and the kinetic energy flux $\overline{w'k'}$ demonstrates that both terms make considerable contributions to the transport term. As the pressure strain terms are not included in the turbulent kinetic energy budget for the $k-\varepsilon$ model, it is possible that neglected inter-component energy redistribution is responsible for model errors. A more likely source of error, however, is the underestimation of the dissipation rate. As production and dissipation are nearly in balance, a low estimate of the dissipation will directly influence the modeled production through Eq. 4.5.4a and 4.5.4c. Figure 4.52 demonstrates the underprediction of the dissipation in the top portion of the boundary layer.

CHAPTER 5

THE UNSTABLY-STRATIFIED EKMAN LAYER

The unstably-stratified convective boundary layer is typical of the ABL during daytime hours. Density stratifications are created from the increase in temperature of the fluid close to the Earth's surface. As a result, surface heating causes a reduction in density near the wall ($\partial\rho/\partial z > 0$). Turbulent mixing corrects this density inversion by allowing hot fluid to rise through the ABL in thermal plumes: columns of rapidly ascending hot air. In conserving mass, downward drafts carrying dense air are found around the plumes. Turbulence is generated throughout this region due to substantial horizontal gradients in the vertical velocity as well as the viscous instability associated with neutrally stratified flow.

The top of the mixed layer has a well defined cap by means of a potential temperature inversion. An increase in potential temperature with height throughout the ABL – a positive temperature gradient – is characteristic of stable stratification. No buoyant forcing exists and turbulence tends to be suppressed in this region (Kosović and Curry, 2000, Marlatt, 1994). Depending on the strength of the temperature gradient, stable stratification can result in intermittent turbulence, or relaminarization of the flow field (Sun et al., 2002). The height of the temperature inversion is referred to as the 'inversion height' and will be represented as z_i.

In this simulation the density of the fluid is assumed to remain constant (incompressible flow assumption). Buoyant forcing is handled by incorporating the Boussinesq approximation which relates density changes to temperature gradients as discussed in Chapter 2.

Table 5.1: Case B Simulations Specifications

Case	Re	Pr	$\mathrm{Ri}_{0,0}$	tf	tw_*/z_i	N_{samples}
B1	1000	1	-0.08	0.152	1.53	39
B2	1000	1	-1.00	0.050	1.52	51

Specifications for the two unstably-stratified Ekman simulations are given in Table 5.1. For both simulations, the Reynolds number and Prandtl number are 1000 and 1 respectively and the only difference concerns the initial temperature gradient applied to the field. The initial temperature field was specified in the manner used by Coleman and Ferziger (1994):

$$\begin{aligned} \theta &= \frac{a_*}{\delta_E}\frac{\pi^{1/2}}{2c}\mathrm{Ri}_{0,0}\left[\mathrm{erf}\left(c\frac{z}{a_*}\right)+\mathrm{erf}\left(c\frac{b_*-z}{a_*}\right)\right] \qquad 0 \le \frac{z}{\delta_E} \le \frac{b_*}{\delta_E} \\ &= -\frac{a_*}{\delta_E}\frac{\pi^{1/2}}{2c}\mathrm{Ri}_{0,0}\mathrm{erf}\left(c\frac{z-b_*}{a_*}\right)+\theta_{z=0} \qquad \frac{z}{\delta_E} > \frac{b_*}{\delta_E} \end{aligned} \tag{5.0.1}$$

In the above expressions, $c = \sqrt{-\ln(0.01)}$, $a_*/\delta_E = 4$, $b_*/\delta_E = 10$, and $\mathrm{Ri}_{z,t}$ denotes a local Richardson number defined by

$$\mathrm{Ri}_{z,t} = \frac{\partial}{\partial z}\theta(z,t) \tag{5.0.2}$$

The $(0,0)$ subscript in $\mathrm{Ri}_{0,0}$ indicate that the Richardson number refers to a surface value at time $t = 0$. The initial temperature field given by Eq. 5.0.1 contains two key features of the convective ABL: surface heating and a temperature inversion. Since heating of the overlying fluid is expected to occur, the gradient near the wall will not remain constant. The extent to which this occurs will be demonstrated shortly.

The flow was initialized using the statistically-steady, neutrally-stratified field given by Case A (see Chapter 4). To start the simulation, the temperature field given by Eq. 5.0.1 was imposed on the velocity field at $tf = 0.3$ in Fig. 4.2. Velocity boundary conditions for Case B1 and B2 remained the same: no-slip walls and stress-free farfield. The temperature boundary conditions were specified such that the temperature on the wall remained constant. This assumes the heat removed from the wall is trivial in comparison to the total amount of energy contained 'within' the boundary.

5.1 Temporal variation

The velocity and temperature fields were integrated forward in time until the rate-of-change of the surface Richardson number, friction velocity (Eq. 4.1.3), and shear angle (Eq. 4.1.5) are approximately constant as shown in Figs. 5.1 – 5.3 respectively. In each figure, subplot (a) refers to Case B1 and subplot (b) refers to Case B2. It was found (through trial and error) that the time step used to integrate the neutrally stratified case was insufficient for the buoyantly forced cases. For both sets of data, Δt was set to $\Delta t = 0.01$ and $\Delta t = 0.0025$ for Cases B1 and B2 respectively. These time steps result in a maximum Courant number (see Eq. 3.1.29) that is less than 0.5. Furthermore, stability was maintained by increasing the fourth-order artificial dissipation such that the coefficient given in Eq. 3.1.26 was increased to $\beta = 0.2$ for Case B1 and $\beta = 0.8$ for B2.

The initial temperature profile undergoes large changes at the beginning of the integration period. The temperature gradient at the wall decreases with time until a minimum is reached. For each case (see Fig. 5.1), this extrema occurs near $tw_*/z_i \approx 0.6$ where the temperature inversion height z_i and the convective velocity w_* are taken as the characteristic scales of the convective ABL (Deardorff, 1972). The convective velocity is defined as (Deardorff, 1972)

$$w_* = \left(\frac{g Q_{\theta,0} z_i}{T_0} \right)^{1/3} \tag{5.1.1}$$

where $Q_{\theta,0}$ is the surface heat flux. At the wall, $\overline{w'\theta'} = 0$ due to the $w = 0$ wall boundary condition. Thus, the total heat flux at $z = 0$ is given by the viscous flux only:

$$Q_{\theta,0} = -\frac{k}{c_p \rho} \frac{\partial T}{\partial \tilde{z}} \tag{5.1.2}$$

or

$$\frac{Q_{\theta,0}}{U_g T_0} = -\frac{1}{\mathrm{Pr}\,\mathrm{Re}} \left. \frac{\partial \theta}{\partial z} \right|_{z_0} \tag{5.1.3}$$

The subscript $\theta, 0$ in Eq. 5.1.3 is used to indicate that $Q_{\theta,0}$ is the heat flux (θ) at the wall (0). Combining Eqs. 5.1.1 and 5.1.3, the convective velocity is written in dimensionless form by

$$\frac{w_*}{U_g} = \left[-\left(\frac{z_i}{\delta_E} \right) \left(\frac{1}{\mathrm{Pr}\,\mathrm{Re}} \right) \left(\frac{\partial \theta}{\partial z} \right)_{z=0} \right]^{1/3} \tag{5.1.4}$$

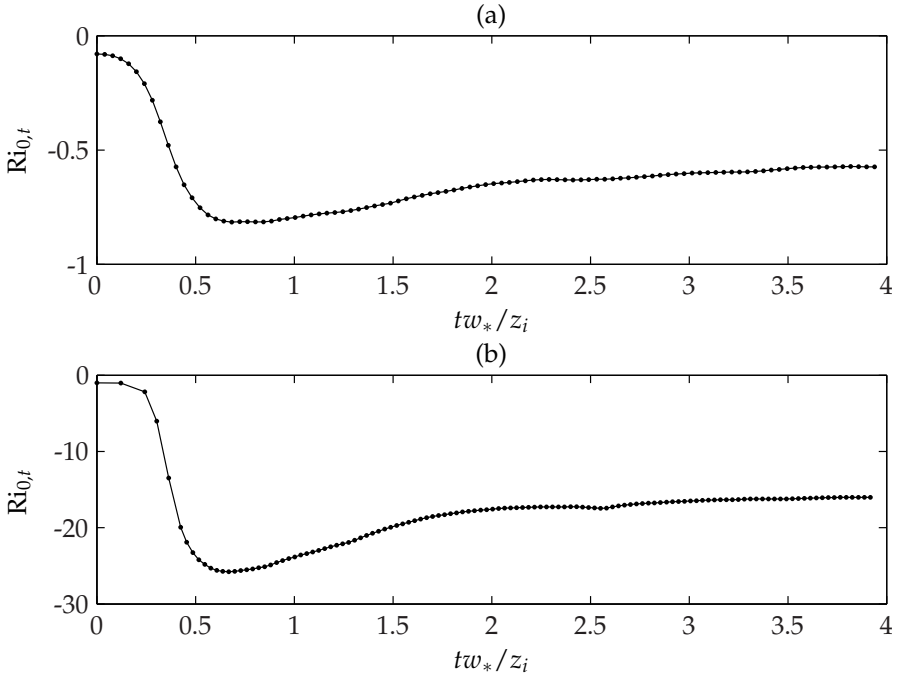

Figure 5.1: Variation of surface Richardson number with time: (a) Case B1, (b) Case B2. Dots denote a saved field.

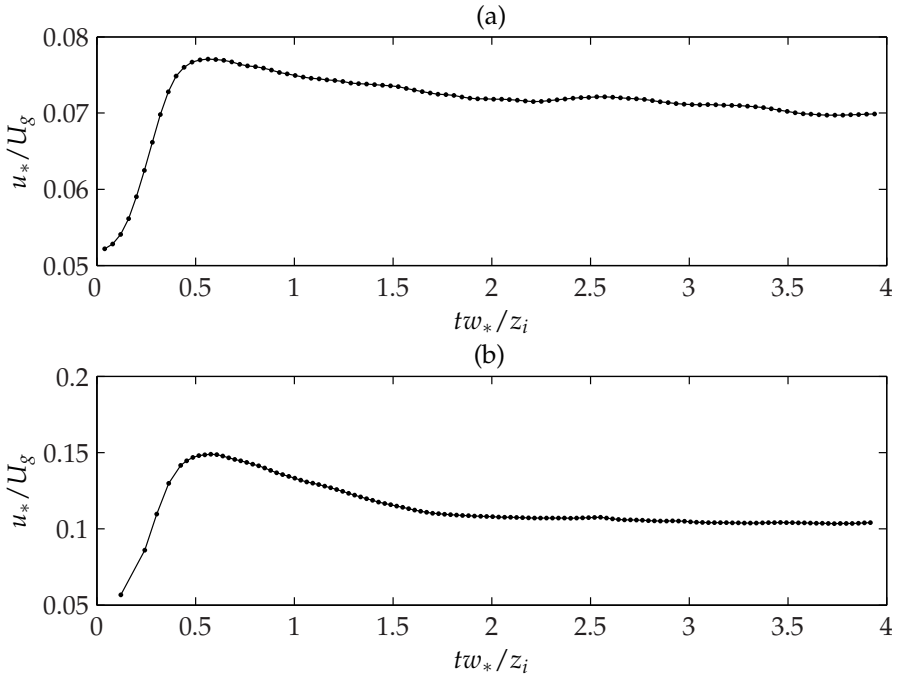

Figure 5.2: Variation of surface friction velocity u_*/U_g with time: (a) Case B1, (b) Case B2. Dots denote a saved field.

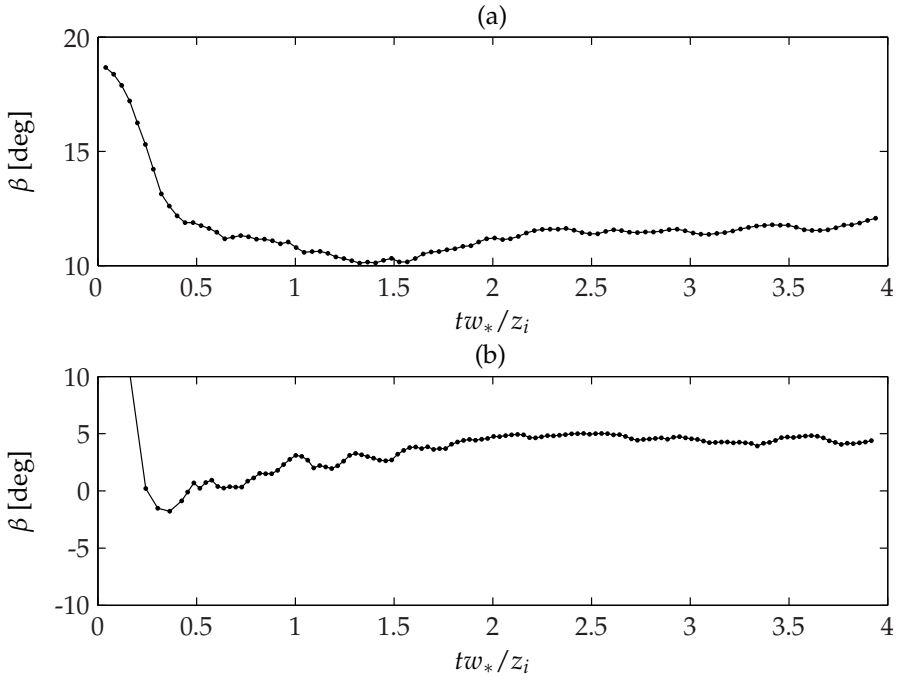

Figure 5.3: Variation of surface shear angle β with time: (a) Case B1, (b) Case B2. Dots denote a saved field.

The rapid changes in $\mathrm{Ri}_{0,t}$ indicate the flow is adjusting to the imposed temperature gradients. The initial Richardson numbers of -0.08 and -1.00 are quickly amplified by over an order of magnitude. Similar behavior was noted by Coleman and Ferziger (1994) for their $\mathrm{Re} = 400$ convective boundary layer with system rotation. The minimum value of $\mathrm{Ri}_{0,t}$ for their $\mathrm{Ri}_{0,0} = -0.08$ case is approximately -0.35. The magnitude of their surface Richardson number is over a factor of 2 smaller than the maximum surface Richardson number seen in Fig. 5.1(a). A similar relationship between the current DNS and the low Reynolds number convective boundary layer of Coleman and Ferziger (1994) is seen for the $\mathrm{Ri}_{0,0} = -1.00$ cases.

After the initial transient die out, the increase of the surface Richardson number remains nearly constant for both cases. Similarly, the friction velocity goes through rapid changes at the beginning of the integration period and then flattens out after the initial transients have passed. The surface shear angle (Fig. 5.3) decreases with the increased stratification.

Table 5.2: Characteristic Scales of Case B

Case	z_i/δ_E	u_*/U_g	w_*/U_g	u_*/w_*	β	$-z_i/L$	Re_c
B1	8.59	0.071	0.173	0.411	11.59°	5.90	1486
B2	8.59	0.104	0.521	0.201	4.53°	50.54	4475

5.2 Temporally Averaged Results

Unlike the neutrally stratified simulation, the convective Ekman layer will not reach an equilibrium. As the overlying fluid is heated, the temperature gradient at the wall will steadily return to zero (until neutral stratification is achieved). For this reason, the integration period over which results are averaged is significantly shorter than that of the neutral Ekman layer presented earlier. The total time integration period was chosen to be $tw_*/z_i \approx 4$ where the last $tw_*/z_i \approx 1.5$ would be used for averaging. This averaging period allows an entire eddy turnover time $\mathcal{T}$ (where $\mathcal{T} = z_i/w_*$) to be captured while ensuring that initial transients from imposing the temperature field have died out. From Table 5.1 it is clear that $w_*/z_i f \gg 1$. This indicates that the time scale of the convective eddies ($\mathcal{T}$) is much smaller than that of the eddies resulting from the inclusion of Coriolis (Coleman and Ferziger, 1994) which scale as $1/f$.

Averaging the data over the period specified yields the characteristic scales given in Table 5.2. The convective Reynolds number Re_c is formed from the characteristic scales z_i and w_*:

$$\mathrm{Re}_c = \frac{w_* z_i}{\nu} \tag{5.2.1}$$

or

$$\mathrm{Re}_c = \left(\frac{w_*}{U_g}\right)\left(\frac{z_i}{\delta_E}\right)\mathrm{Re} \tag{5.2.2}$$

As seen earlier, the stratification tends to increase the friction velocity while decreasing the shear angle. This indicates that the wall shear stress increases with an increase in heating while the shear angle tends to align more closely with the geostrophic direction under more vigorous heating conditions. Moreover, the convective velocity increases with an increase in the level of stratification. It is important to note, however, that u_* is not linearly proportional to w_*. The ratio u_*/w_* gives

an indication of the role of thermal forcing relative to shear. If $u_*/w_* \to \infty$, the flow is representative of turbulence generated by shearing alone (Chap. 4). As $u_*/w_* \to 0$, buoyancy dominates the field and shear generated turbulence becomes negligible.

Another measure of stratification is given by the Obukhov length L (Obukhov, 1971)

$$L = -\frac{u_*^3 T_0}{g\kappa Q_{\theta,0}} \tag{5.2.3}$$

where $\kappa = 0.41$ is the von Kármán constant. A dimensionless form of Eq. 5.2.3 is given by

$$\frac{L}{\delta_E} = \left(\frac{u_*}{U_g}\right)^3 \left(\frac{\mathrm{Re}\,\mathrm{Pr}}{\kappa}\right) \left(\frac{\partial\theta}{\partial z}\right)_{z=0}^{-1} \tag{5.2.4}$$

The ratio of the inversion height z_i to the Obukhov length L gives an indication of the strength of stratification. A positive value of L indicates unstable stratification while negative values characterize stably-stratified boundary layers. The inversion height to Obukhov length ratios for Case B1 and B2 are given in Table 5.2. Values of $-z_i/L$ for Case B1 indicate moderate heating on par with the work of Coleman and Ferziger (1994) who report $-zi/L = 2$ and Moeng and Wyngaard (1984) where $-z_i/L = 10$. The vigorously heated Case B2 is closer to the stratification level in the LES studies of Wang et al. (2007) ($-z_i/L = 17.9$) and Wyngaard and Brost (1984) ($-z_i/L = 64$). Also, Gryanik and Hartmann (2002) reported atmospheric measurements ranging from $9.9 \leq -z_i/L \leq 20.9$. The two cases presented here bound this interval and offer insight into how large changes in the stratification level might affect turbulence dynamics.

Both the lower and upper boundaries are set to a constant temperature. To ensure no internal waves are reflected off the top boundary by the numerical scheme (Coleman and Ferziger, 1994), the temperature gradient $\partial\theta/\partial z \to 0$ as $z \to \infty$ (see Eq. 5.0.1) is applied. Thus, the curvature in the temperature profile at the top of the domain is a consequence of the upper boundary condition. The shape of the capping inversion for $z > z_i$ is reminiscent of the convective tank experiments of Deardorff and Willis (1985) and Piper et al. (1995). The time-averaged temperature field is shown in Fig. 5.4. The temperature gradient near the wall is much steeper than that imposed in the initial field for both cases. For $0 < z < z_i$, the temperature is well mixed.

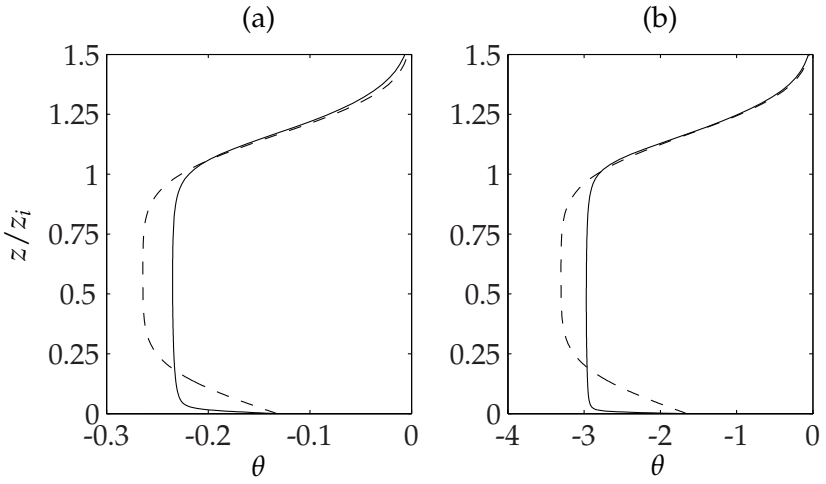

Figure 5.4: Mean temperature field: (a) Case B1, (b) Case B2. The solid line give time-averaged results; the dashed line indicates the initial temperature distribution imposed (Eq. 5.0.1).

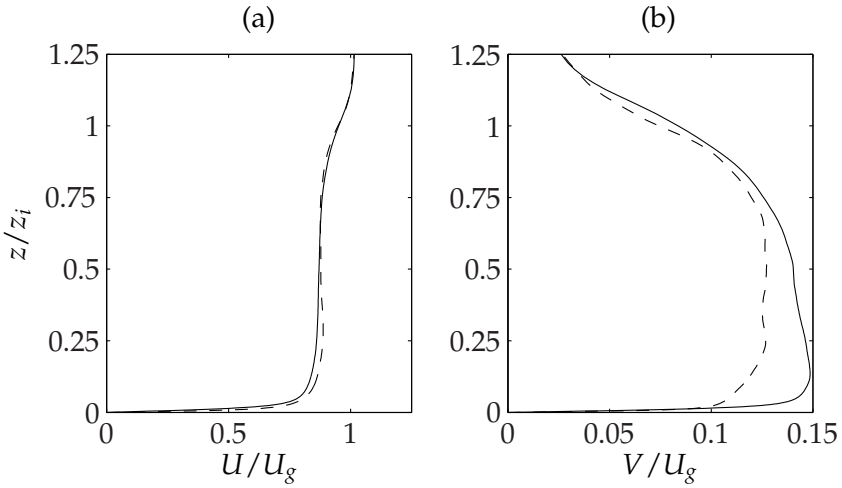

Figure 5.5: Mean velocity field: (a) streamwise velocity, (b) spanwise velocity. The solid and dashed lines represent Case B1 and B2 respectively.

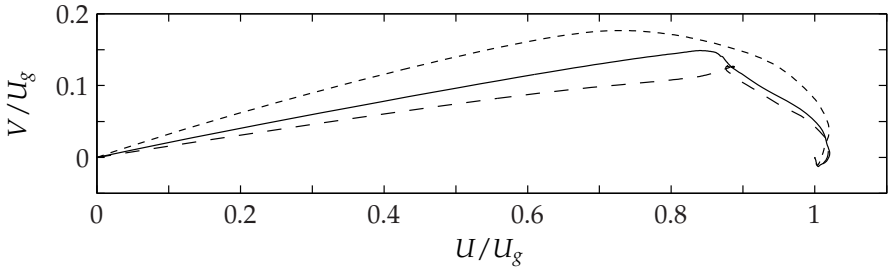

Figure 5.6: Mean velocity hodograph for Case B: solid, Case B1; dashed, Case B2; dotted, Case A, (neutral Ekman layer).

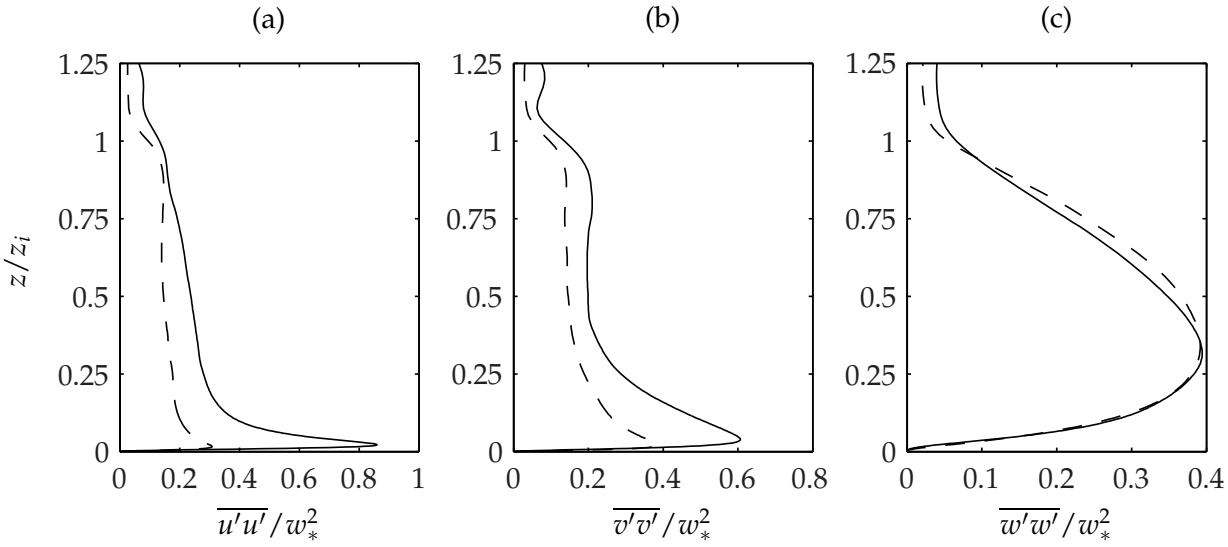

Figure 5.7: Variances of velocity fluctuations normalized by convective velocity w_*. (a) $\overline{u'u'}$, (b) $\overline{v'v'}$, (c) $\overline{w'w'}$. Solid line, Case B1; dashed line, Case B2.

Because of enhanced vertical transport, the mean velocity field (Fig. 5.5) also becomes well mixed. When $z/z_i > 0.75$ the mean fields for the two cases are approximately equal. However, for the majority of the boundary layer, an increase in stratification causes a reduction in the mean spanwise velocity component. Plotting the velocities in hodograph form (see Fig. 5.6) demonstrates the decrease in β with an increase in $-z_i/L$.

5.2.1 Statistics of Velocity Fluctuations

The velocity variances $\overline{u'u'}$, $\overline{v'v'}$ and $\overline{w'w'}$ are shown in Fig. 5.7. Streamwise and spanwise fluctuations are at a maximum near the wall. An increase in stratification tends to move this maximum closer to the wall while slightly decreasing the horizontal velocity variance across the mixed layer. Both $\overline{u'u'}$ and $\overline{v'v'}$ demonstrate a dependence upon $-z_i/L$. However, the vertical variance appears to scale well with w_*^2 regardless of the strength of stratification. The values seen across the mixed layer for $\overline{w'w'}/w_*^2$ are close to the laboratory experiments of Willis and Deardorff (1974) and Deardorff and Willis (1985). Given the differences in methodology, stratification level, and Reynolds number of the flow fields, the scaling of $\overline{w'w'}$ with w_*^2 appears to be universal in

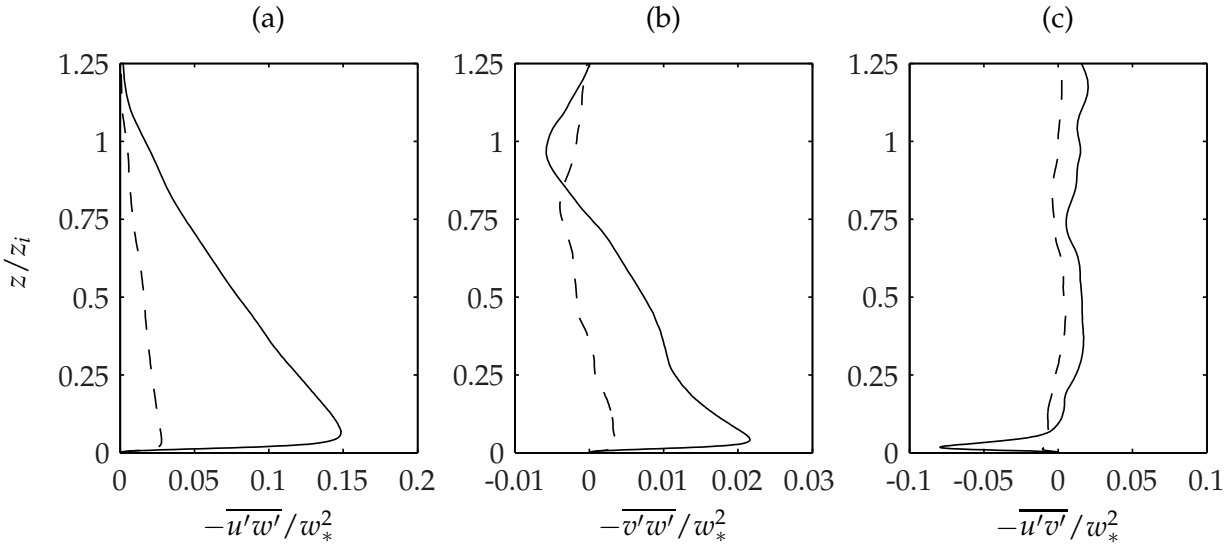

Figure 5.8: Covariances of velocity fluctuations normalized by convective velocity w_*. (a) $-\overline{u'w'}$, (b) $-\overline{v'w'}$, (c) $-\overline{u'v'}$. Solid line, Case B1; dashed line, Case B2.

convective flows.

Shear Reynolds stresses are shown in Fig. 5.8 and 5.9. The difference between the two sets of data is the characteristic velocity used to normalize the covariances. Results scaled by w_*^2 demonstrate significant differences in amplitude with changes in the level of stratification. Note the difference in amplitude of $-\overline{u'w'}$ for the two cases in Fig. 5.8(a). When scaled by the friction velocity, however, the $-\overline{u'w'}/u_*^2$ stress nearly collapses to the same curve (see Fig. 5.9). Moreover, the maximum amplitude is much closer to 1 indicating that the shear stresses scale better with the friction velocity rather than the convective velocity. Similar behavior is noted for the other shear stress terms; however, the similarity between Case B1 and B2 data depreciates for $-\overline{v'w'}$ and $-\overline{u'v'}$ in comparison with the primary shear stress.

Skewness (see Eq. 4.2.13) of the velocity components is shown in Fig. 5.10. The streamwise skewness S_u demonstrates a minimum near $z/z_i = 1$ which suggests the existence of streamwise streaks (bands of slow moving fluid). The negative skewness in the mixed layer for S_u decreases with an increase in stratification; Fig. 4.12 shows that the minimum skewness for the neutrally stratified case is $S_u \approx -0.8$. The amplitude of S_v is relatively small for both Case B1 and B2.

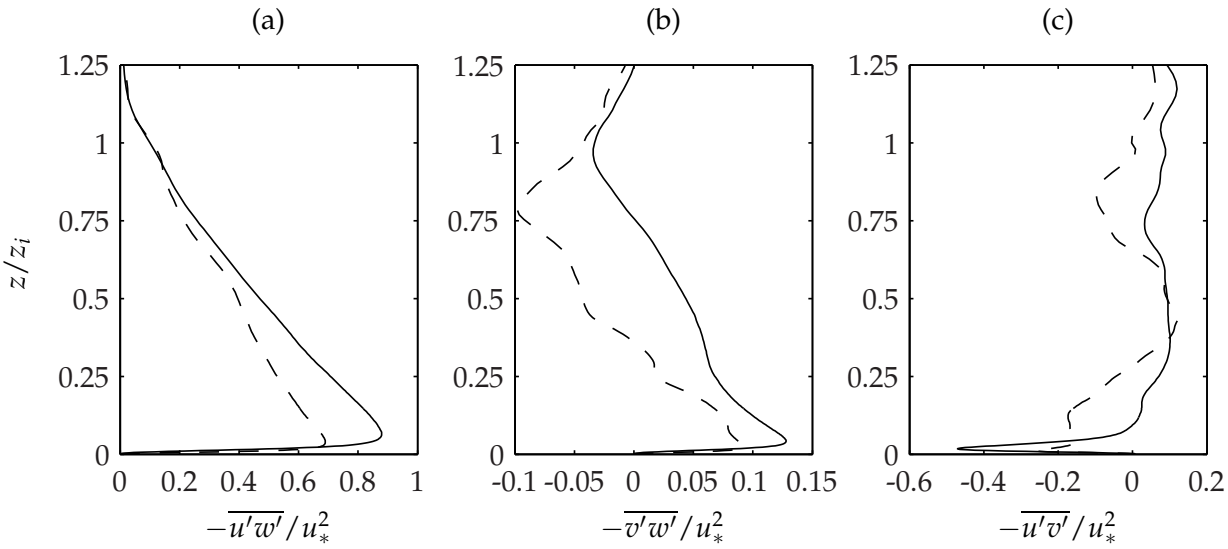

Figure 5.9: Same as Fig. 5.8 but normalized by u_*.

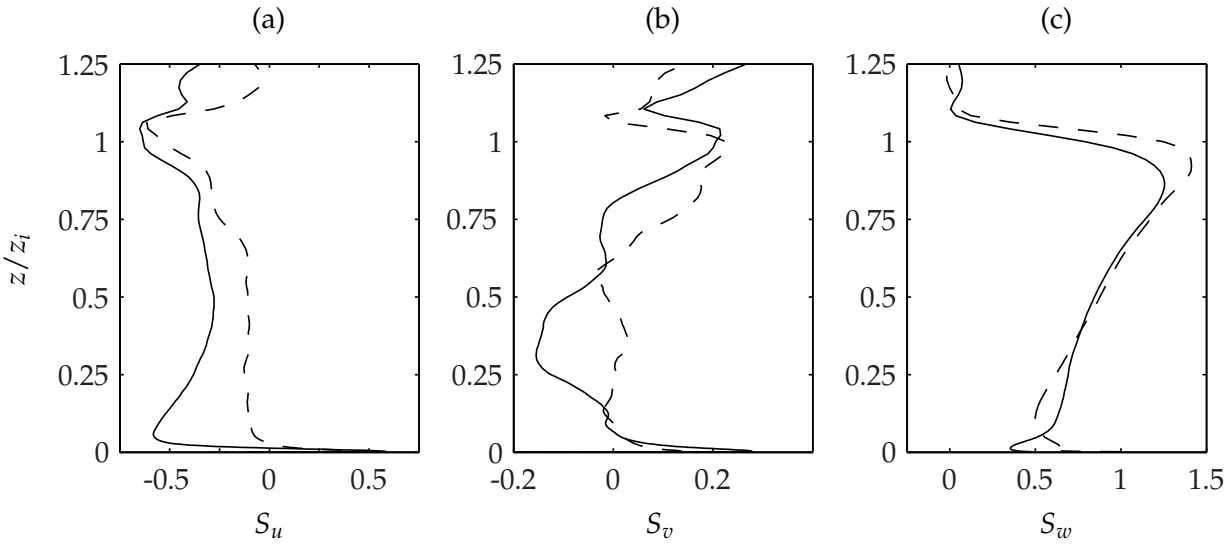

Figure 5.10: Skewness of velocity components for Case B1 (solid line) and Case B2 (dashed line). (a) S_u, (b) S_v, (c) S_w.

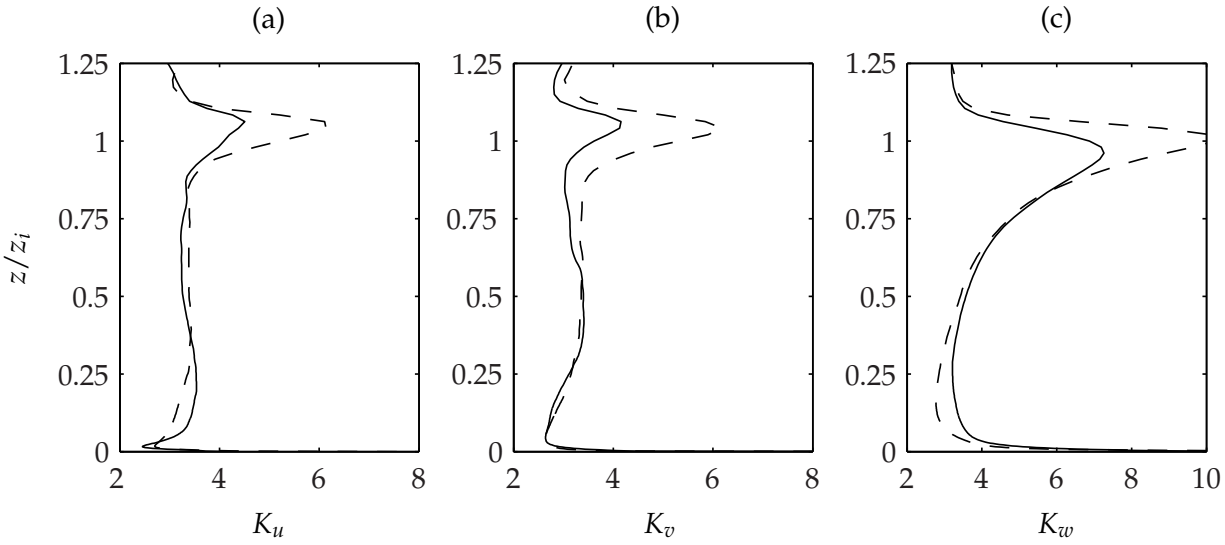

Figure 5.11: Same as Fig. 5.10 but for velocity kurtosis.

Skewness of the vertical velocity increases in comparison with the neutrally stratified Case A (Fig. 4.12). S_w for both Case B1 and B2 are nearly identical: positive skewness that increases linearly throughout the mixed layer. This agrees with LES data of Mason (1989), Mironov et al. (2000) and Gryanik and Hartmann (2002) but is not representative of convective ABL conditions (LeMone, 1990, Moeng and Rotunno, 1990). Instead, a decrease in skewness should occur as $z \to z_i$. LeMone (1990) argues that very large scale features of size > 10 km with near-zero skewness prohibit further increases in skewness in the vicinity of z_i. This DNS, as well as the LES noted earlier, are not capable of resolving these large scales resulting in the increased skewness near the inversion.

Figure 5.11 gives the kurtosis (see Eq. 4.2.14) of the three velocity components. Recall from §4.2.3 that $K_{u_i} = 3$ for normally distributed velocity components. Both K_u and K_v demonstrate a reduction relative to Case A (Fig. 4.13). With a kurtosis close to 3, both horizontal velocity components are close to a Gaussian distribution. At the inversion there is an increase in the kurtosis of the fluctuating velocity which is amplified by an increase in $-z_i/L$. K_w reaches a minimum of $K_w \approx 3$ at the bottom of the mixed layer but increases steadily until the peak at $z/z_i = 1$ for both

cases. As with the in-plane velocity components, increased stratification causes an increase in K_w at z_i.

5.2.2 Statistics of Temperature Fluctuations

The turbulent heat flux $\overline{w'\theta'}$ is shown in Figure 5.12 for both cases. Note that the flux has been normalized by the surface heat flux $Q_{\theta,0}$. Both cases show linear behavior through the mixed layer with a maximum at the surface such that $\overline{w'\theta'}/Q_0 \approx 1$. Although the turbulent flux goes to zero at the wall (due to the no-slip boundary condition), viscous heat flux is at a maximum at the wall. Refer to §5.5.2 for a discussion concerning the contribution of viscous and turbulent flux through both top-down and bottom-up diffusion processes.

Although the inversion height has already been used in presenting results, z_i is formally defined as the height where $\overline{w'\theta'}$ is a minimum. Other definitions for z_i exist and are discussed by Sullivan et al. (1998). Their results show less than 5% variation in z_i between the different methods used.

Given the convective velocity w_* and the surface heat flux $Q_{\theta,0}$ a characteristic temperature scale θ_* can be formed such that

$$w_*\theta_* = Q_{\theta,0} \tag{5.2.5}$$

or

$$\theta_* = \frac{Q_{\theta,0}}{w_*} \tag{5.2.6}$$

The variance of the temperature fluctuations is shown in Fig. 5.13 where $\overline{\theta'\theta'}$ has been normalized by θ_*^2. It seems $\overline{\theta'\theta'}$ does not scale with θ_*^2 (i.e. $\overline{\theta'\theta'}/\theta_*^2$ is not necessarily of order 1) near the wall or at the inversion. In fact, the case with vigorous heating shows an increase in the level of fluctuations in the near wall region. However, within the mixed layer, where temperature fluctuations are less severe, the temperature variance scales with the characteristic temperature in Eq. 5.2.6. Moene et al. (2006) propose a modified scaling which keeps the scaled variances on the order of $1-10$ throughout the boundary layer. So as to compare with other measurements and

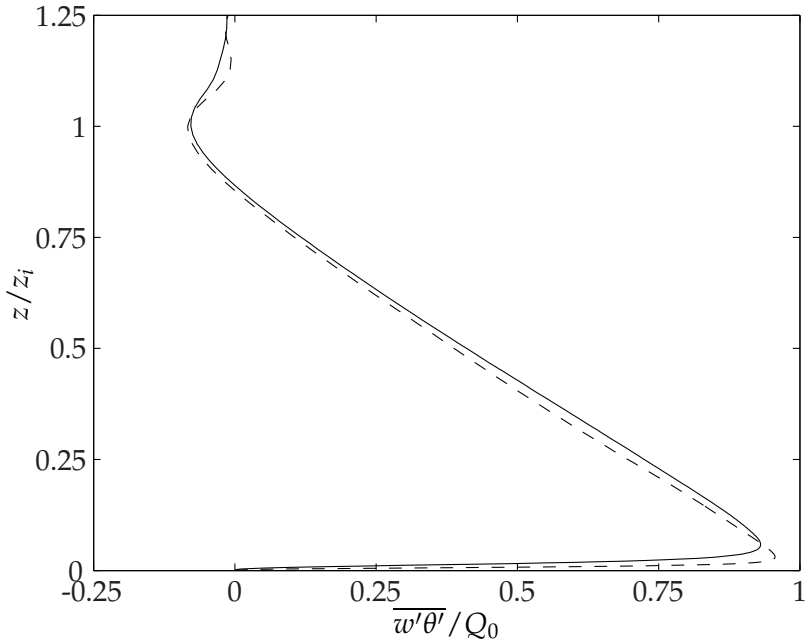

Figure 5.12: Temperature flux for Case B: Solid line, Case B1; dashed line, Case B2.

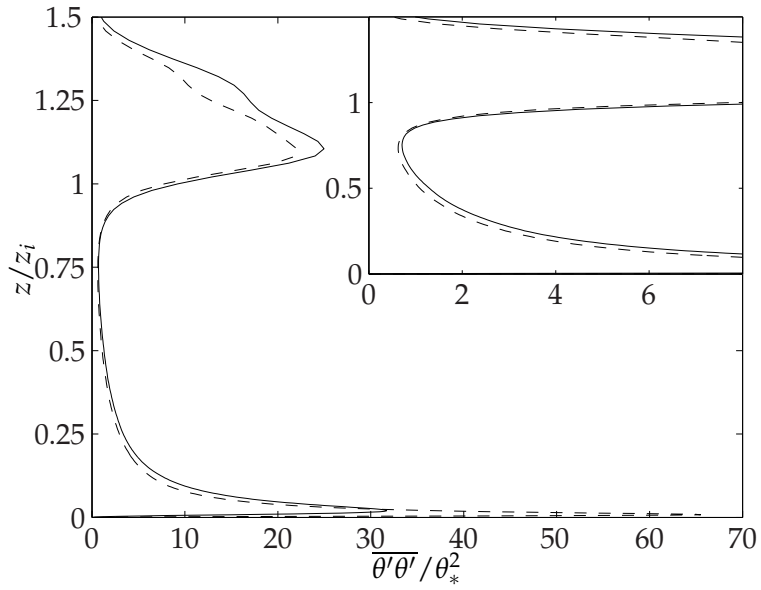

Figure 5.13: Variance of temperature fluctuations for Case B: Solid line, Case B1; dashed line, Case B2. Inset show detail in the mixed layer.

simulations, their scaling is not incorporated here. The minimum of $\overline{\theta'\theta'}/\theta_*^2$ is approximately unity (see inset of Fig. 5.13) and is located towards the top of the mixed layer. A significant increase in the level of temperature fluctuations is noted between $0.75 < z/z_i < 1.5$. A similar increase is not displayed in the velocity variances (Fig. 5.7). It may be that buoyant plumes carrying hot fluid from the wall region continue until they encounter the capping-inversion. No longer forced by a buoyant instability, these plumes continue to travel upwards carrying (relatively) cold fluid into the stably-stratified region by means of positive vertical velocity fluctuations. The difference between the mean temperature and the temperature of the plumes impacting into the inversion results in the large increase in $\overline{\theta'\theta'}$ near $z \approx z_i$. This reasoning agrees with the heat flux $\overline{w'\theta'}$ profile near z_i. Cold temperature fluctuations traveling upwards into the inversion would correspond with a negative heat flux. Scaling of the temperature variance is similar for both Case B1 and B2 suggesting that the strength of the temperature fluctuations may not be a function of $-z_i/L$. However, differences in the magnitude of $\overline{\theta'\theta'}$ exist between these data and that of Coleman and Ferziger (1994, 1996) who show $\overline{\theta'\theta'}/\theta_*^2 \approx 5$ or Mason (1989) where $\overline{\theta'\theta'}/\theta_*^2 \approx 17.5$. It is possible that the magnitude of the fluctuations at the inversion is more a function of the strength of the capping inversion $(\partial\theta/\partial z)$ at z_i than the surface parameter L.

Higher-order statistics, namely the skewness and kurtosis (Eq. 4.2.13 and 4.2.14 respectively), of the temperature fluctuations are shown in Fig. 5.14. The increase in heating tends to promote increased positive skewness and increased flatness. The positive skewness is characteristic of the buoyant plumes, or, relatively small regions of very high temperature fluid. An increased Richardson number promotes the existence of such plumes. It is expected that high temperatures will correlate with positive vertical velocities. However, the skewness of w' (which increases linearly between $0 < z/z_i < 1$) does not mirror the behavior of S_θ. Although the temperature fluctuations are skewed towards $+\theta'$ in the mixed layer, S_θ decreases as the inversion is approached. When hot upward traveling fluid encounters the inversion, the skewness is decreased since the 'hot' fluid from the mixed layer is encountering higher temperatures as it travels

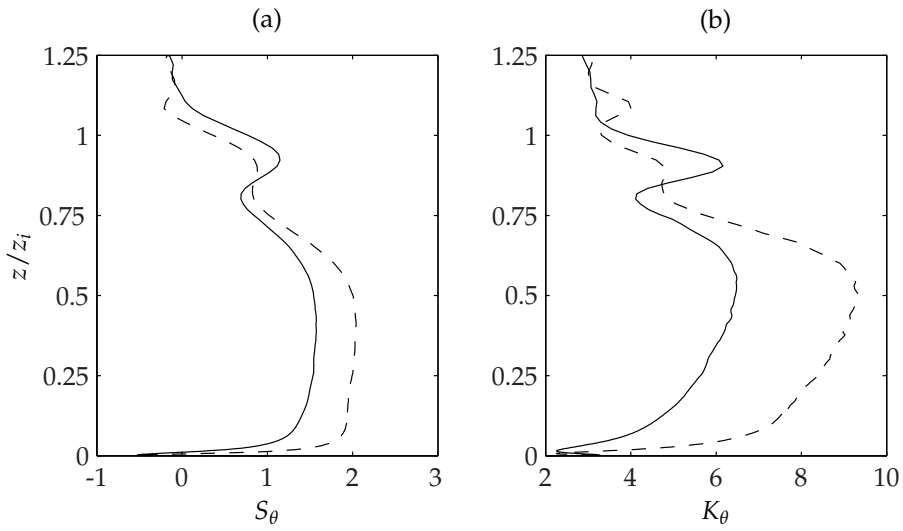

Figure 5.14: Skewness (a) and Kurtosis (b) of temperature field for Case B: Solid line, Case B1, dashed line, Case B2.

through the inversion. Thus, the temperature difference between $\overline{\theta}$ and θ' is reduced.

5.3 Turbulent Kinetic Energy Budgets

Turbulent kinetic energy budgets were computed for the velocity variance and covariance terms using Eq. 4.3.1. For cases B1 and B2, the production by buoyant forces, $\beta_{i,k}$ (term II) is nonzero for $\overline{w'w'}$, $-\overline{u'w'}$, and $-\overline{v'w'}$. The pressure term will be presented for these unstable cases using the total pressure transport ($\Pi_{i,k}$) rather than the pressure strain ($\Phi_{i,k}$) and the pressure diffusion ($\Theta_{i,k}$) as given by Eq. 4.3.3. In the budgets for $\overline{u'u'}$, $\overline{v'v'}$, and $-\overline{u'v'}$, $\Pi_{i,k} = \Phi_{i,k}$. All budgets have been normalized by w_*^3/z_i. The averaging periods for the budgets are slightly different than those used for the statistics presented thus far. For the budgets only, 50 realizations over $tw_*/z_i = 2.01$ were used for Case B1 and 45 realizations over $tw_*/z_i = 1.37$ were used for Case B2.

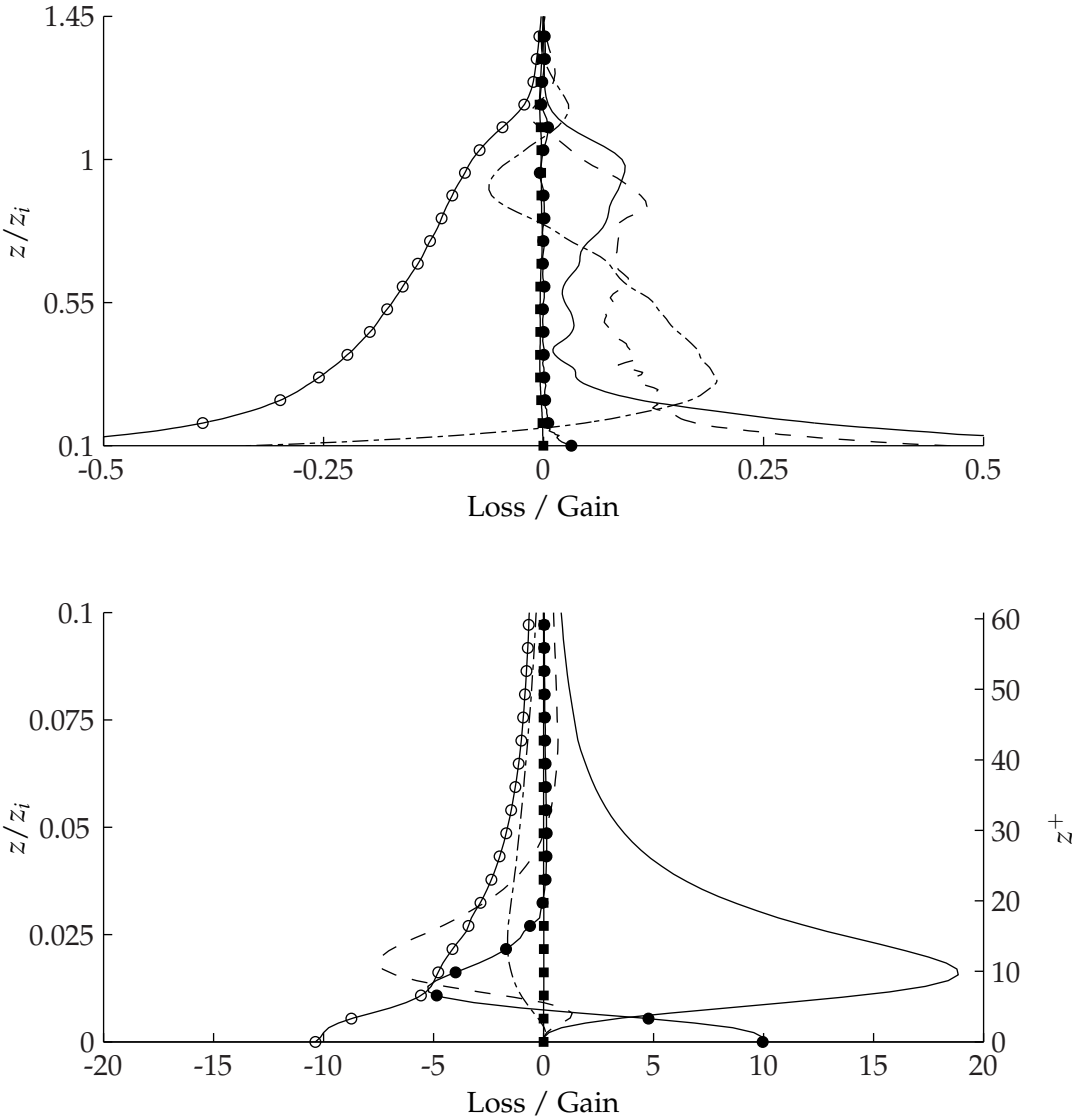

Figure 5.15: Case B1 turbulent kinetic energy budget for $\overline{u'u'}$ component. Production, solid; turbulent diffusion, dashed; pressure transport, dot-dash; molecular diffusion, solid circle; viscous dissipation, open circle; Coriolis redistribution, solid square. All terms have been normalized by w_*^3/z_i.

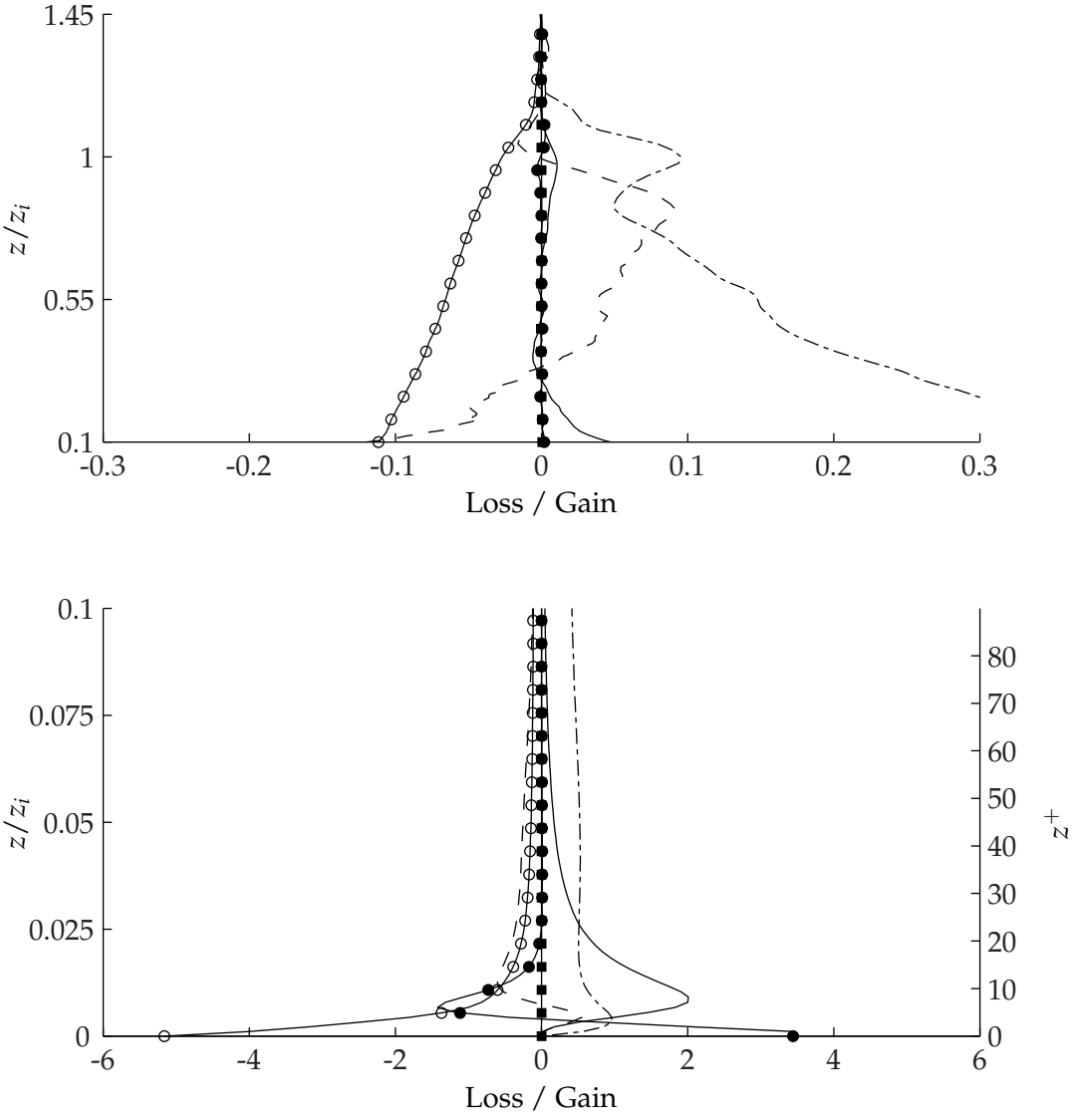

Figure 5.16: Same as Fig. 5.15 but for Case B2.

5.3.1 Variance Budgets

The budgets for $\overline{u'u'}$ in Case B1 and B2 are given in Fig. 5.15 and 5.16. Near the wall the neutrally stratified (Fig. 4.17) and weakly unstable cases are similar to each other qualitatively. The major source of energy is production by mean shear; molecular and turbulent diffusion transport this energy to other parts of the flow: $T_{1,1}$ to the farfield and $D_{1,1}$ towards the wall. A clear difference between Case A and B1 concerns the pressure transport (pressure strain to be precise). The amount of energy lost by $\overline{u'u'}$ due to pressure transport appears to decrease with the presence of thermal stratification. Figure 5.16 shows that pressure transport actually supplies energy to $\overline{u'u'}$. Increasing the stratification increases the role of buoyant forcing such that $\overline{w'w'}$ is now the dominant Reynolds stress. This term then supplies energy to the in-plane Reynolds stresses through the return-to-isotropy transport term. With moderate stratification turbulent diffusion and production by mean shear both supply energy to $\overline{u'u'}$. Likewise, pressure strain acts as a source throughout the mixed layer except for a small region of loss immediately below z_i where the streamwise term supplies energy to other terms through $\Pi_{1,1}$. For vigorous heating, the role of production is diminished at z_i and pressure strain is the primary source of energy along with turbulent diffusion.

As with $\overline{u'u'}$, the $\overline{v'v'}$ budgets for Case B1 (Fig. 5.17) and Case A (Fig. 4.18) are quite similar near the wall. Case B1 shows a slight decrease in the role of $P_{2,2}$ relative to the pressure transport. Increasing the stratification level further decreases production by mean shear such that the spanwise production term is negligible (Fig. 5.18). In Case B2, the sole source of energy is pressure strain which supplies energy to the spanwise term from $\overline{w'w'}$. Comparing Fig. 5.16 and 5.18 demonstrates that the in-plane budgets are essentially identical except when $z^+ < 40$ where streamwise shear production plays a role in supplying energy.

For a vigorously heated field (Case B2), the streamwise and spanwise energy transport are equivalent outside of a small layer near the wall. Likewise,the normal Reynolds stresses in Fig. 5.7 are also similar to each other away from the wall. With a further increase in the convective

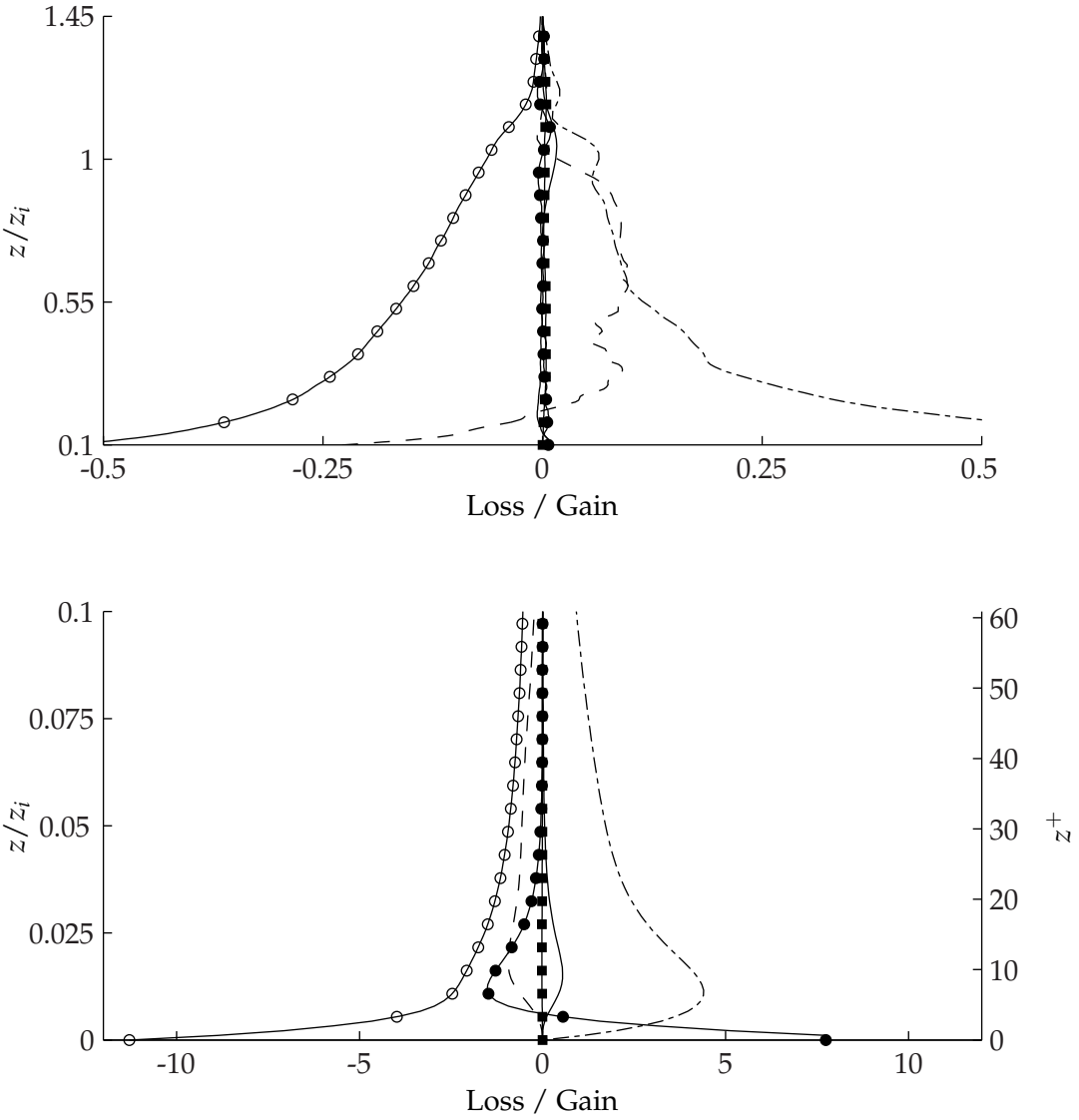

Figure 5.17: Case B1 turbulent kinetic energy budget for $\overline{v'v'}$ component. Production, solid; turbulent diffusion, dashed; pressure transport, dot-dash; molecular diffusion, solid circle; viscous dissipation, open circle; Coriolis redistribution, solid square. All terms have been normalized by w_*^3/z_i.

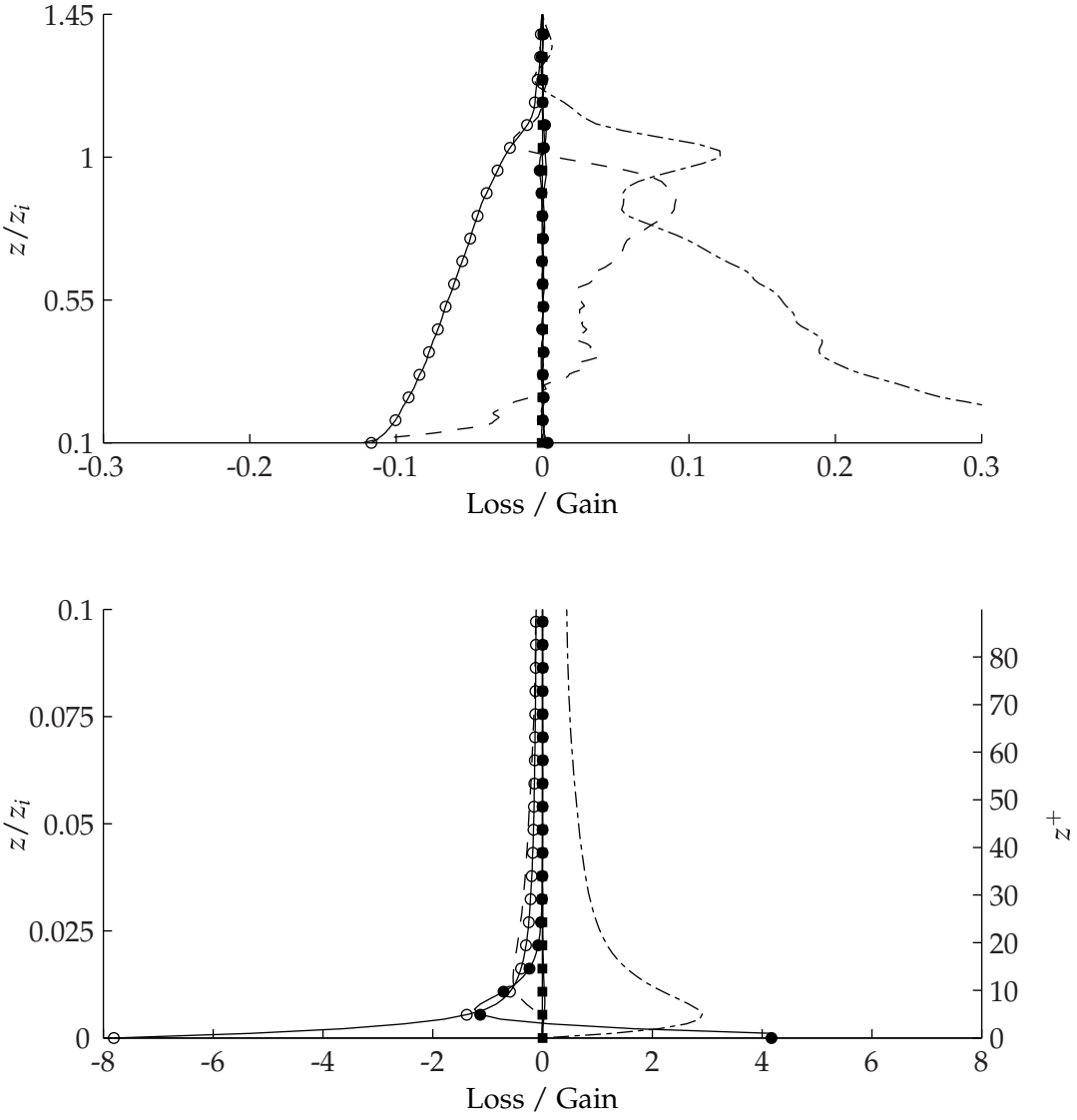

Figure 5.18: Same as Fig. 5.17 but for Case B2.

Reynolds number Re_c, this layer is likely to shrink and the small role of shear production in $\overline{u'u'}$ will decrease further.

The $\overline{w'w'}$ budget shown in Fig. 5.19 and 5.20 for Case B1 and B2 respectively are significantly different from the corresponding Case A budget in Fig. 4.17. Buoyant production energizes $\overline{w'w'}$ such that this term now supplies energy to the in-plane components. In Fig. 4.20(c) the total pressure transport $\Pi_{3,3}$ is a gain over the entire boundary layer. With stratification, pressure transport drains energy from the vertical Reynolds stress to energize the other components. Although $\beta_{1,1} = \beta_{2,2} = 0$ in Eq. 4.3.1, the effects of buoyancy are still felt by the horizontal stresses through the return-to-isotropy term. Turbulent diffusion plays a significant role in the $\overline{w'w'}$ budget as it transports energy from the bottom half of the mixed layer (where buoyant production is largest) to the top half where buoyant forcing is small. The role of viscous dissipation $\varepsilon_{3,3}$ is decreased with increased stratification.

5.3.2 Turbulent Kinetic Energy Balance

As with the neutrally stratified simulations, the total energy production and dissipation of energy are defined by

$$P = 0.5P_{i,i} \tag{5.3.1a}$$

$$\varepsilon = 0.5\varepsilon_{i,i} \tag{5.3.1b}$$

$$\beta = 0.5\beta_{i,i} \tag{5.3.1c}$$

with a summation over the repeated index. Out of the entire budget, these three terms are responsible for all energy creation or destruction. The budgets for k are given in Fig. 5.21 and 5.22 for Case B1 and B2 respectively. For both cases the production by buoyant forcing β has an amplitude near the wall of $\beta z_i / w_*^3 \approx 1$. For moderate heating the flow is still dominated by production by mean shear near the wall. The increased stratification in Case B2 drastically decreases the relative impact of P and ε when compared to β. If the flow were in equilibrium (which is not the case for

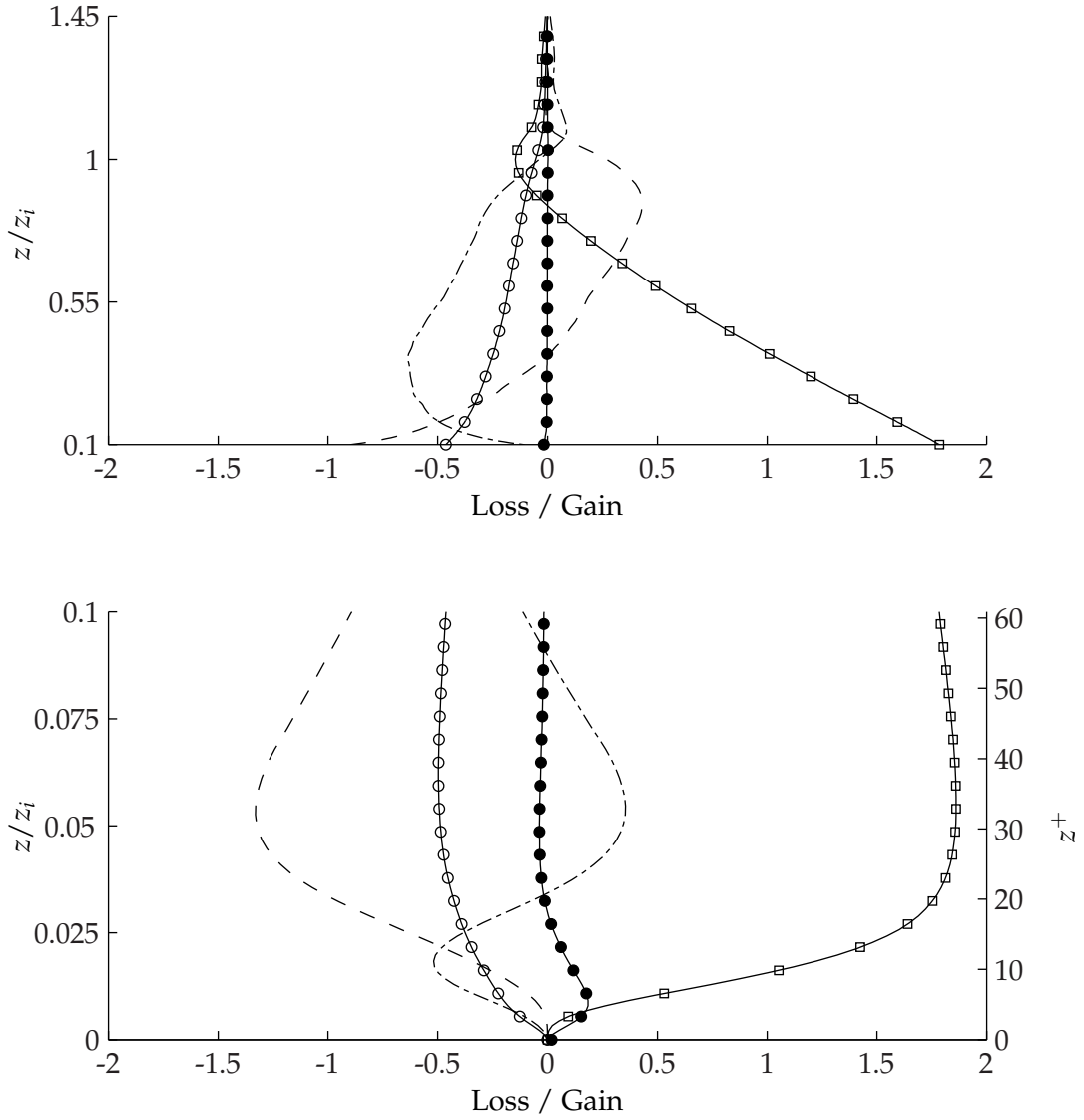

Figure 5.19: Case B1 turbulent kinetic energy budget for $\overline{w'w'}$ component. Turbulent diffusion, dashed; pressure transport, dot-dash; molecular diffusion, solid circle; viscous dissipation, open circle; buoyant production, open square. All terms have been normalized by w_*^3/z_i.

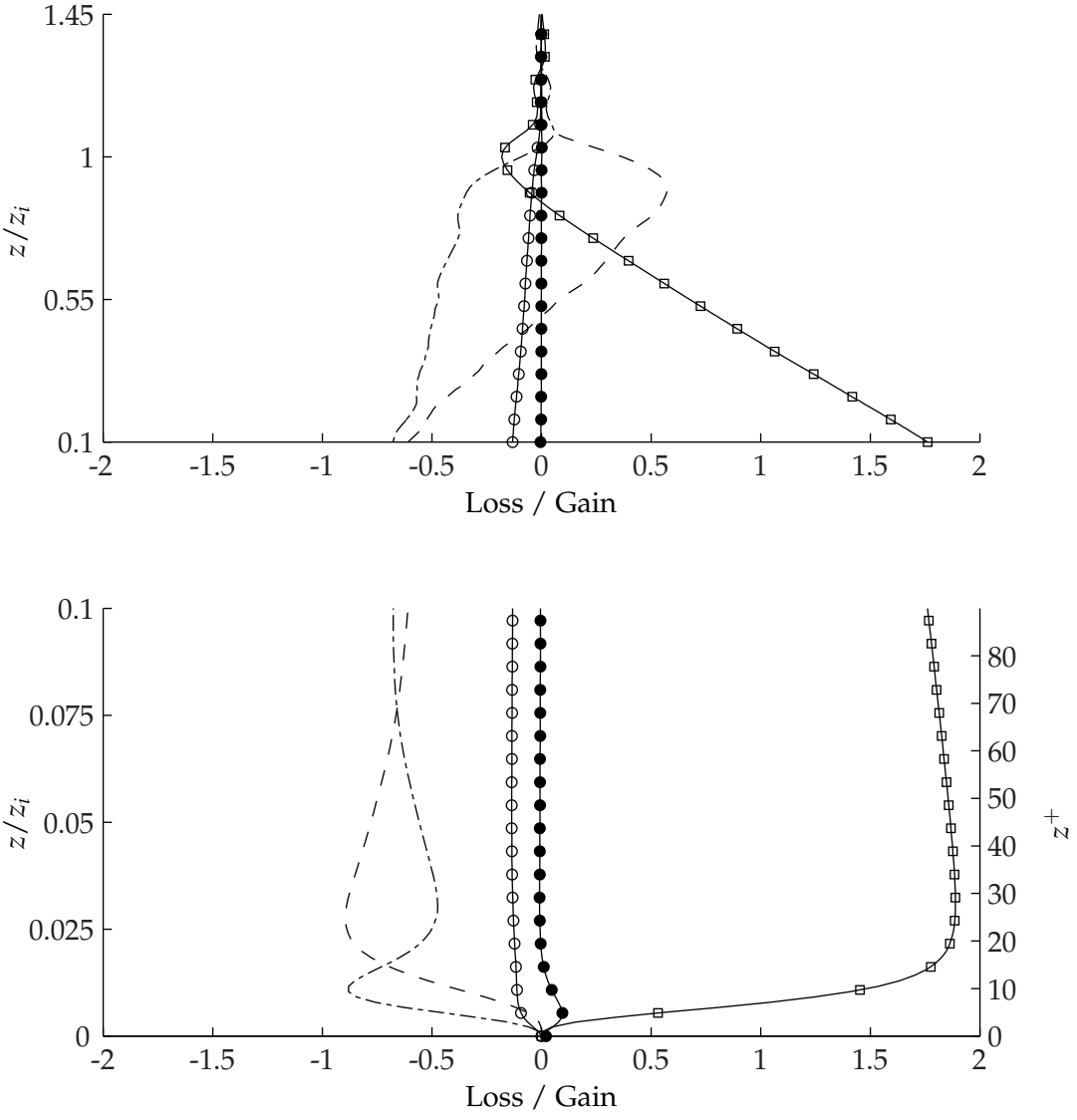

Figure 5.20: Same as Fig. 5.19 but for Case B2.

unstable stratification), the total energy produced in the domain would be balanced by the energy dissipated. The following expression is defined as a measure of the balance of production and dissipation:

$$\frac{\int_0^\infty P\,\mathrm{d}z + \int_0^\infty \beta\,\mathrm{d}z + \int_0^\infty \varepsilon\,\mathrm{d}z}{\int_0^\infty P\,\mathrm{d}z + \int_0^\infty \beta\,\mathrm{d}z} = \text{ TKE balance} \tag{5.3.2}$$

The value of the above expression is 0.269 for Case B1 and 0.653 for Case B2. The positive values indicate that more energy is being produced than dissipated for both cases. Consequently, excess production will results in a slight increase of kinetic energy over the integration period. Coleman and Ferziger (1994) demonstrate such an increase in kinetic energy (their Fig. 3(b)) for the convective boundary layer. The imbalance of energy is a consequence of two factors:

(1) The assumption that Case B1 and B2 are stationary with time (i.e. term 0 in Eq. 4.3.1 is zero) is incorrect. The flow slowly adapts as heat from the wall and temperature inversion is added to the mixed region. The increased stratification associated with Case B2 results in more of a contribution from the time rate of change of the Reynolds stress.

(2) For a case that is stationary in time (such as Case A), production and destruction will be in balance if the statistics are fully converged. Since Case A was only within 9.3% of equilibrium, it is expected that similar results would occur in the convective boundary layers.

5.3.3 Covariance Budgets

As with the neutrally stratified simulation, primary Reynolds shear stresses are responsible for the production of kinetic energy through mean shear. While effects of buoyancy do not directly appear in the $\overline{u'u'}$ or $\overline{v'v'}$ budgets, it has already been shown that energy is transfered to these components through pressure transport (return-to-isotropy) as $\overline{w'\theta'}$ directly feeds into the $\overline{w'w'}$ budget. It will be shown here that buoyancy effects also manifest themselves in the shear production term for the in-plane kinetic energy components.

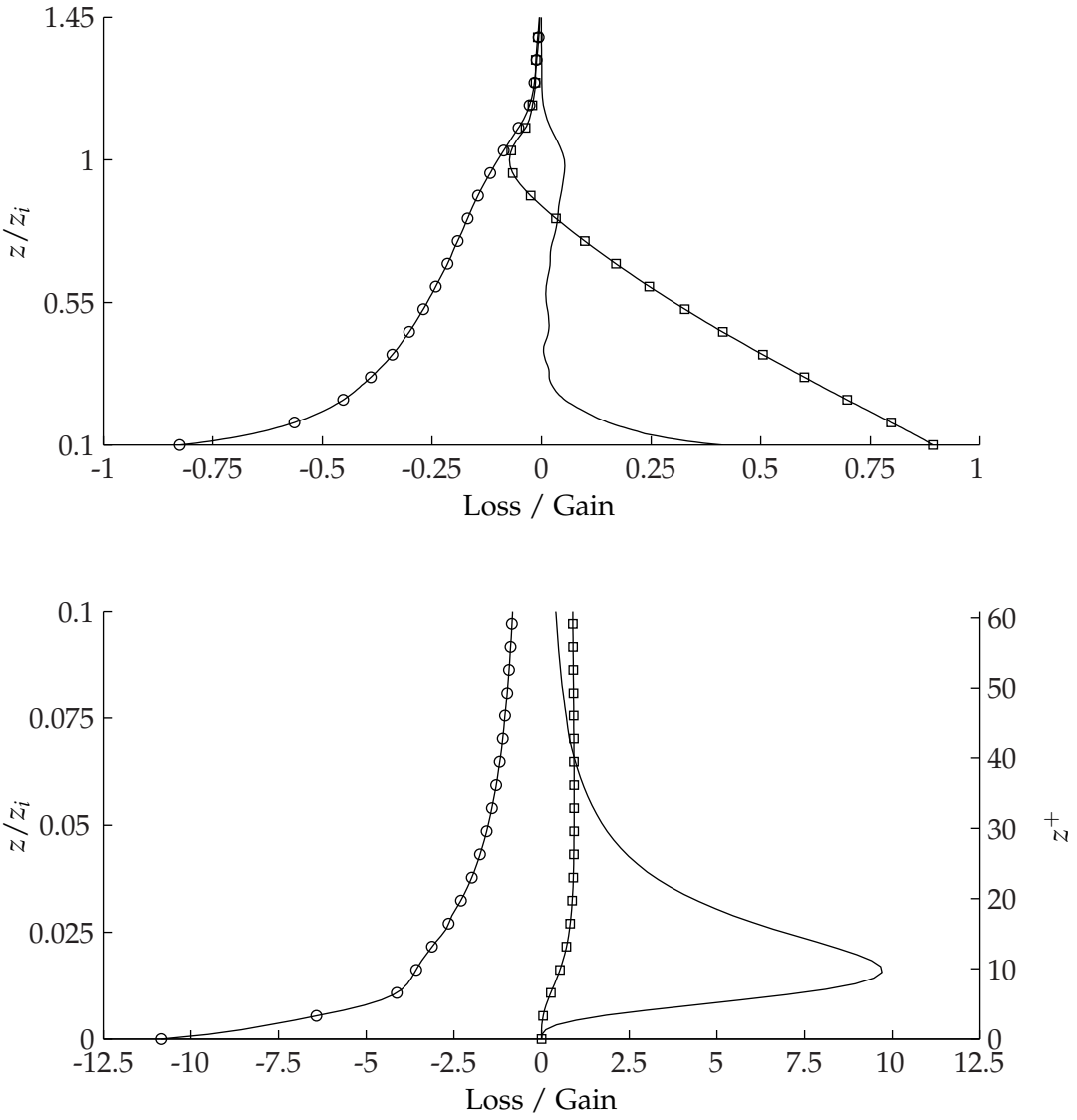

Figure 5.21: Case B1 turbulent kinetic energy balance. Production, solid; viscous dissipation, open circle; buoyant production; open square. All terms have been normalized by w_*^3/z_i.

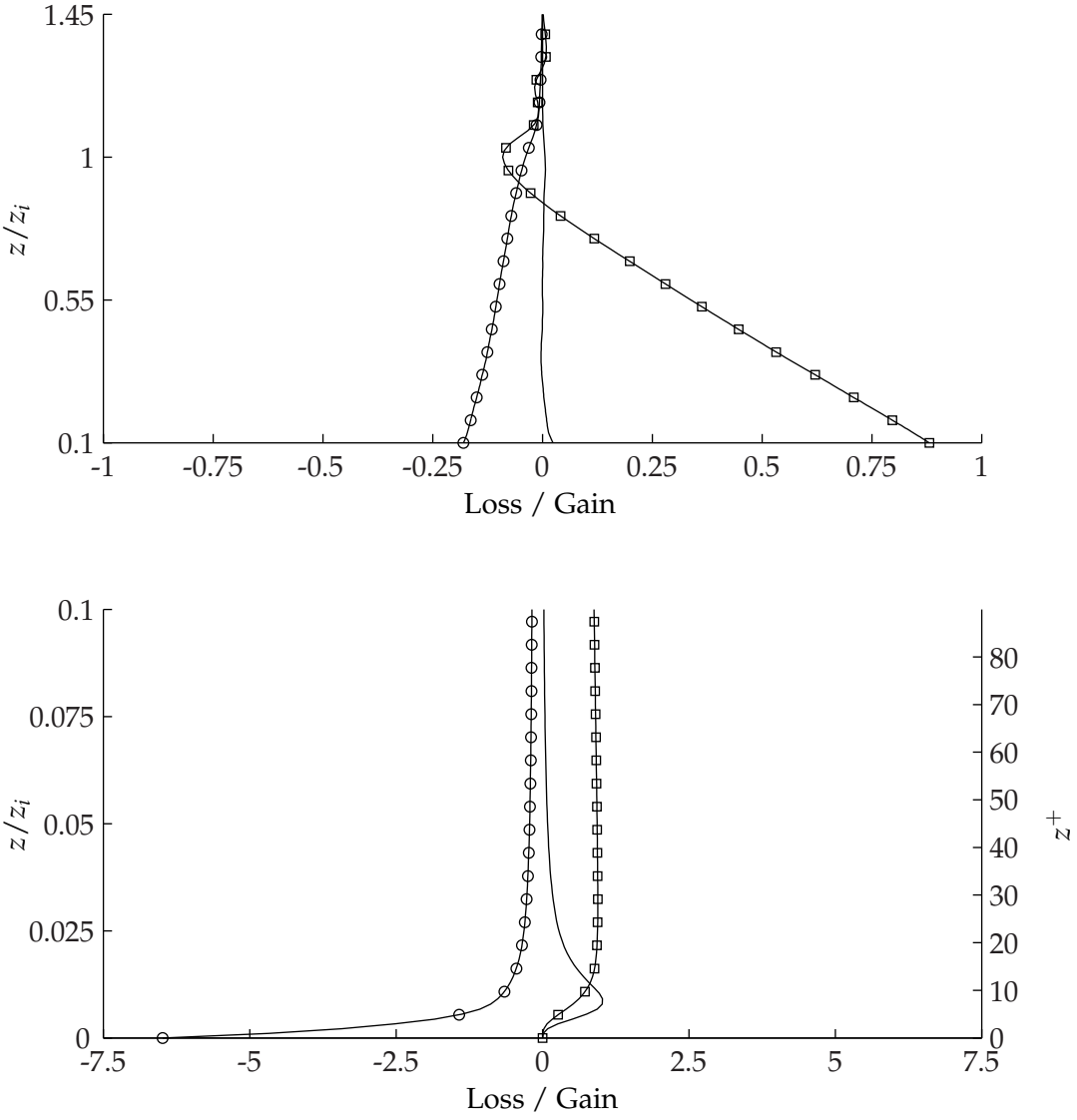

Figure 5.22: Same as Fig. 5.21 but for Case B2.

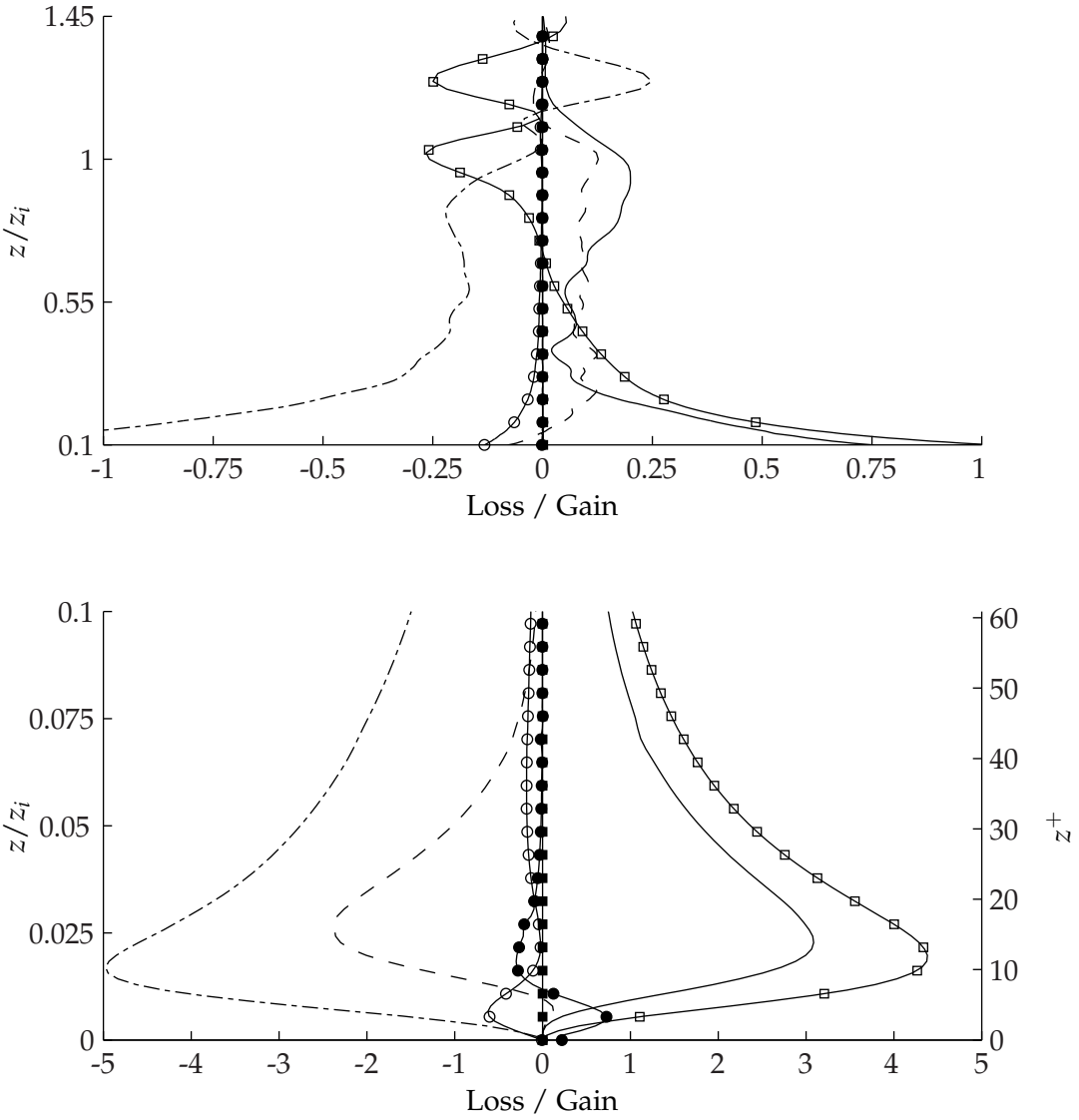

Figure 5.23: Case B1 turbulent kinetic energy budget for $-\overline{u'w'}$ component. Production, solid; turbulent diffusion, dashed; pressure transport, dot-dash; molecular diffusion, solid circle; viscous dissipation, open circle; Coriolis redistribution, solid square; buoyant production, open square. All terms have been normalized by w_*^3/z_i.

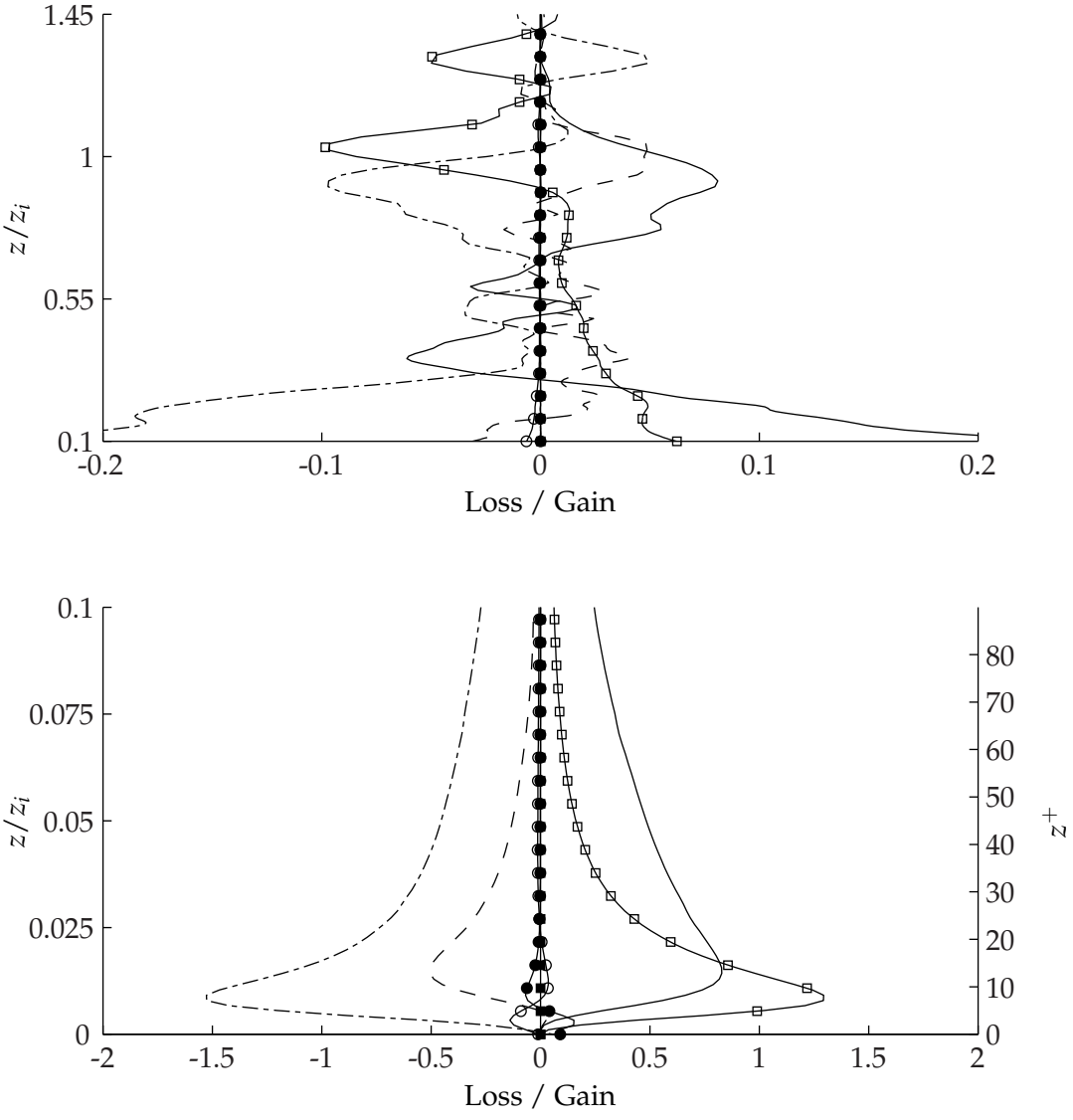

Figure 5.24: Same as Fig. 5.23 but for Case B2.

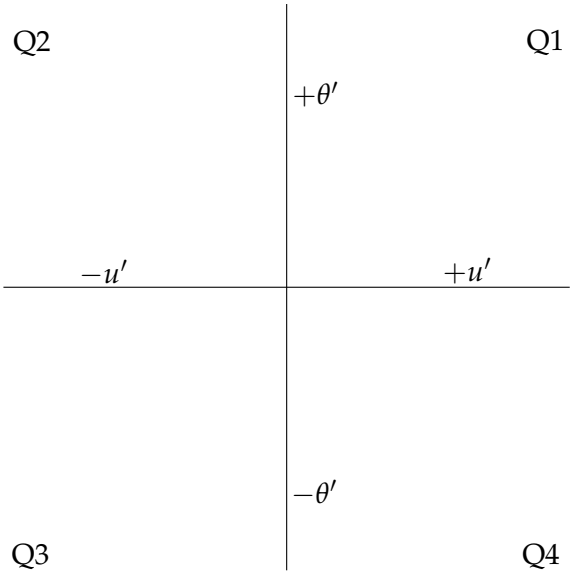

Figure 5.25: Quadrant analysis of temperature and velocity fluctuations.

The budgets for $-\overline{u'w'}$ are shown in Fig. 5.23 and 5.24 for Case B1 and B2 respectively. For the neutrally stratified simulation, the energy gain for this term was primarily (almost exclusively) supplied by mean shear production. For the moderately heated case, Fig. 5.23 demonstrates that $\beta_{1,3}$ is the primary source of energy in the budget near the wall. From Eq. 4.3.1 for $-\overline{u'w'}$, buoyancy will result in production of energy if $-\overline{u'\theta'} > 0$ and destruction if $-\overline{u'\theta'} < 0$. For the quadrants shown in Fig. 5.25, energy is produced in Q2 and Q4 and lost in Q1 and Q3. A Q2 event corresponds to low momentum fluid that is being forced upwards due to the positive temperature fluctuation. Conversely, a Q4 event tends to pull high momentum fluid towards the wall given that $\theta' < 0$. These two events directly impact the shear stress by encouraging (or as is shown near the temperature inversion, discouraging) sweeps and ejections. Surprisingly, the vigorously heated case does not show a large relative increase in buoyant production in comparison to shear production. Although the $\beta_{1,3}$ is more influential near the wall, production by shear becomes the primary source of energy for Case B2 at $z^+ \approx 12.5$. $P_{1,3}$ remains the primary energy source until $z/z_i > 0.27$ where buoyancy again takes over.

Near the inversion both Case B1 and B2 demonstrate similar behavior: (a) a peak in buoyant destruction at $z \approx z_i$ which is balanced by mean shear production and turbulent diffusion and (b) a second local minima in $\beta_{1,3}$ near $z/z_i \approx 1.3$ which is balanced by pressure transport.

Statistics through the mixed layer for the covariance terms show large oscillations. Deducing concrete observations from this region would require an increase in the averaging window which may adversely affect the velocity variance budgets because the flow is not stationary. As shown in Fig. 5.9, the Reynolds shear stresses scale better with u_* rather than w_*; this indicates a longer integration time might be required given that $z_i/u_* > z_i/w_*$. Furthermore, the deviation between these two time scales grows with an increase in $-z_i/L$ (see Table 5.2). This helps to explain why Case B1 shows better statistical convergence than Case B2 in the mixed layer.

$-\overline{v'w'}$ budgets in Fig. 5.26 and 5.27 show similar behavior to the primary streamwise velocity covariance near the wall. The majority of energy is supplied by buoyant and mean shear production. The budget shown in Fig. 5.23 shows buoyant destruction and shear production near $z = z_i$. However, the spanwise covariance demonstrates a gain from buoyancy throughout the boundary layer and a change in the sign of production at $z/z_i \approx 0.13$. The sign change in $P_{2,3}$ corresponds with the change in sign of $\partial V/\partial z$. Two peaks are evident in buoyant production and pressure transport above the inversion height; this is similar to the $-\overline{u'w'}$ budget but the roles have been reversed. The location of the local minima between the two peaks corresponds to the location of the largest gradient in the temperature inversion.

The switched roles of $\beta_{1,3}$ and $\beta_{2,3}$ at z_i is intriguing. At the temperature inversion, $\partial U/\partial z > 0$ while $\partial V/\partial z < 0$. This causes the roles of buoyant production to be reversed. For $\overline{u'w'}$, buoyant destruction at the inversion – coupled with the positive velocity gradient – results in a net loss of turbulent energy. In the case of the spanwise production term, $\beta_{2,3}$ appears to be a gain, but, since the mean velocity gradient in in the spanwise direction is negative, the total effect is that production acts as a sink. Therefore, at the inversion, both primary covariances tend to suppress turbulence.

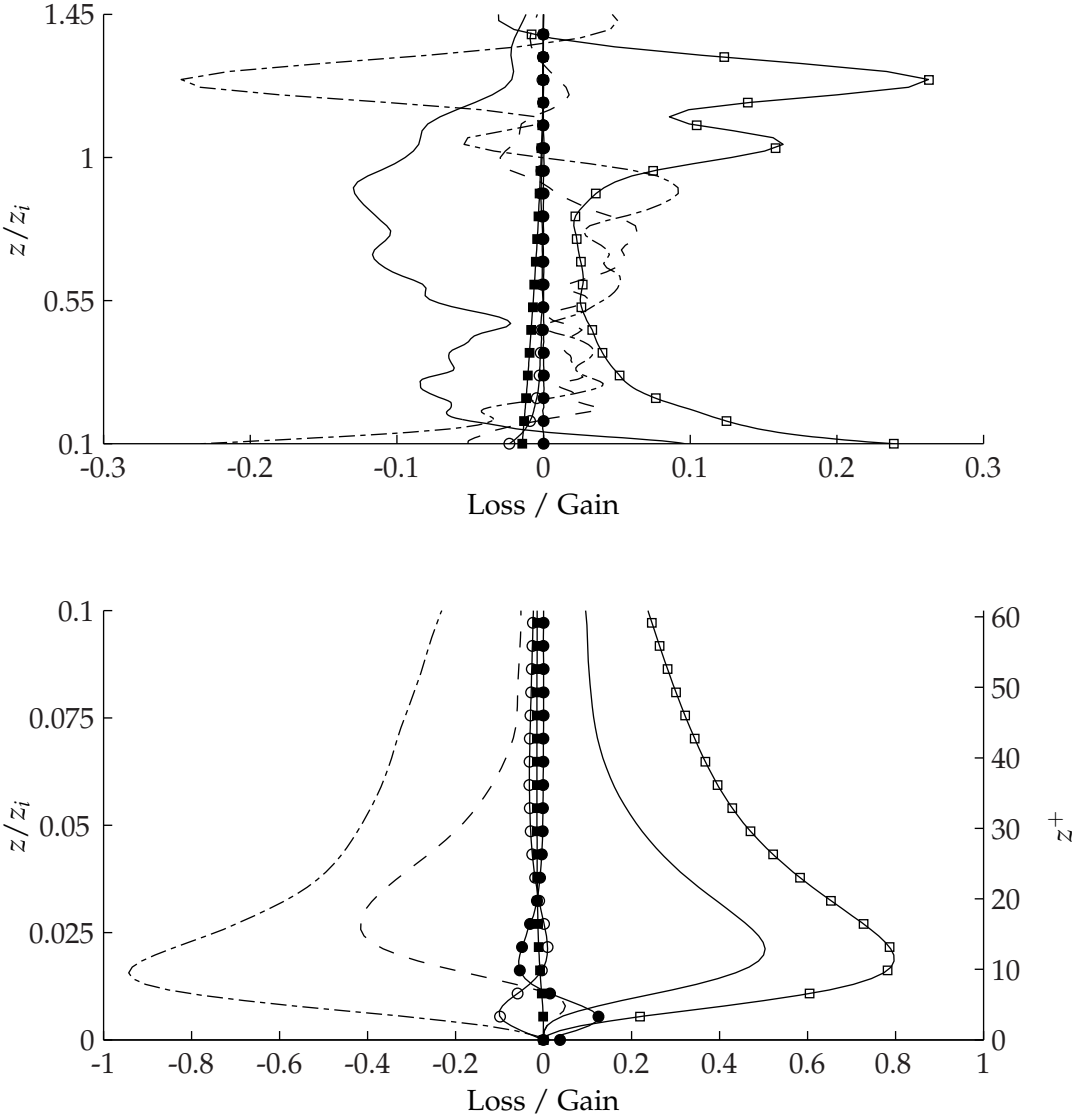

Figure 5.26: Case B1 turbulent kinetic energy budget for $-\overline{v'w'}$ component. Production, solid; turbulent diffusion, dashed; pressure transport, dot-dash; molecular diffusion, solid circle; viscous dissipation, open circle; Coriolis redistribution, solid square; buoyant production, open square. All terms have been normalized by w_*^3/z_i.

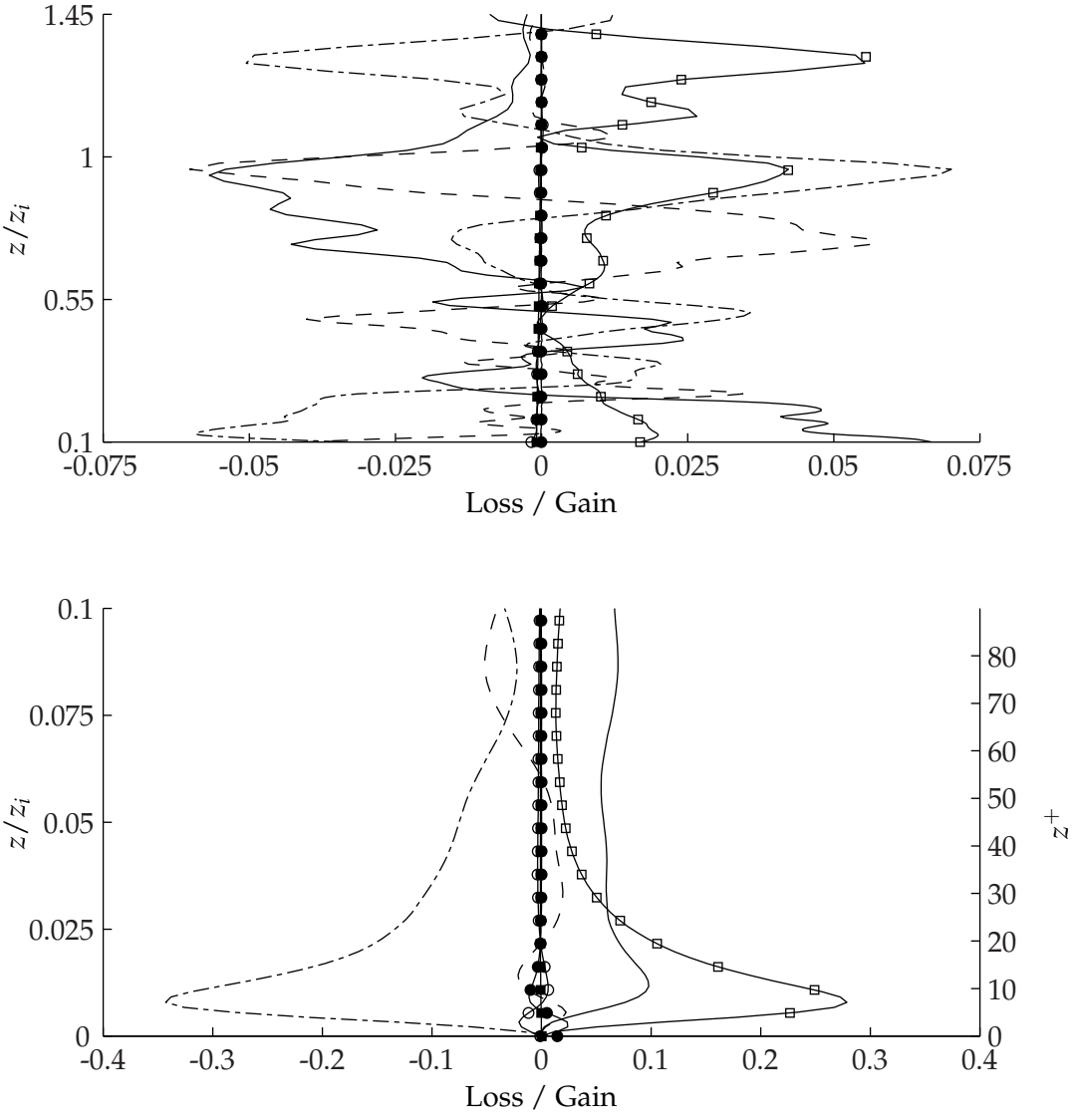

Figure 5.27: Same as Fig. 5.26 but for Case B2.

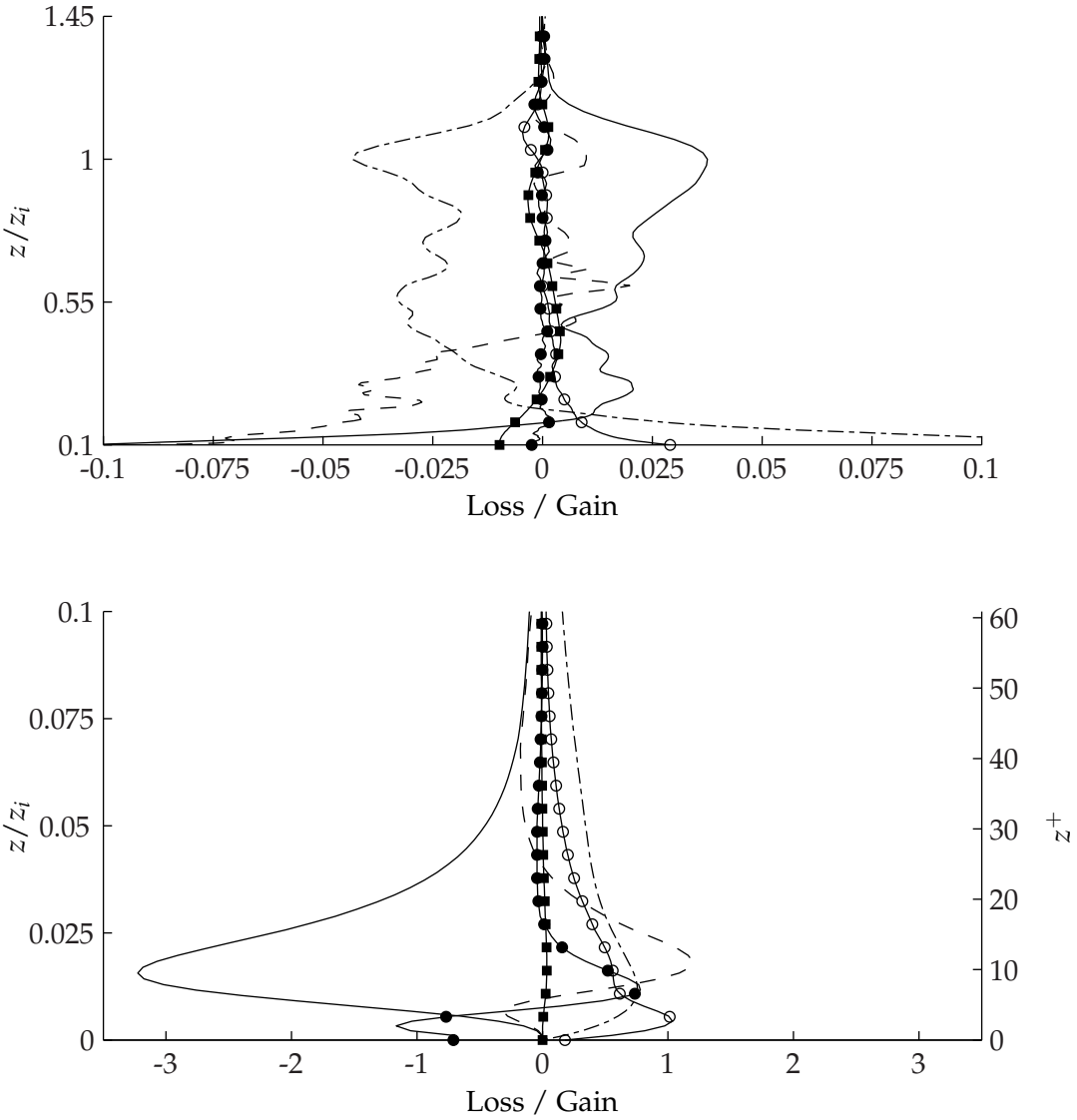

Figure 5.28: Case B1 turbulent kinetic energy budget for $-\overline{u'v'}$ component. Production, solid; turbulent diffusion, dashed; pressure transport, dot-dash; molecular diffusion, solid circle; viscous dissipation, open circle; Coriolis redistribution, solid square. All terms have been normalized by w_*^3/z_i.

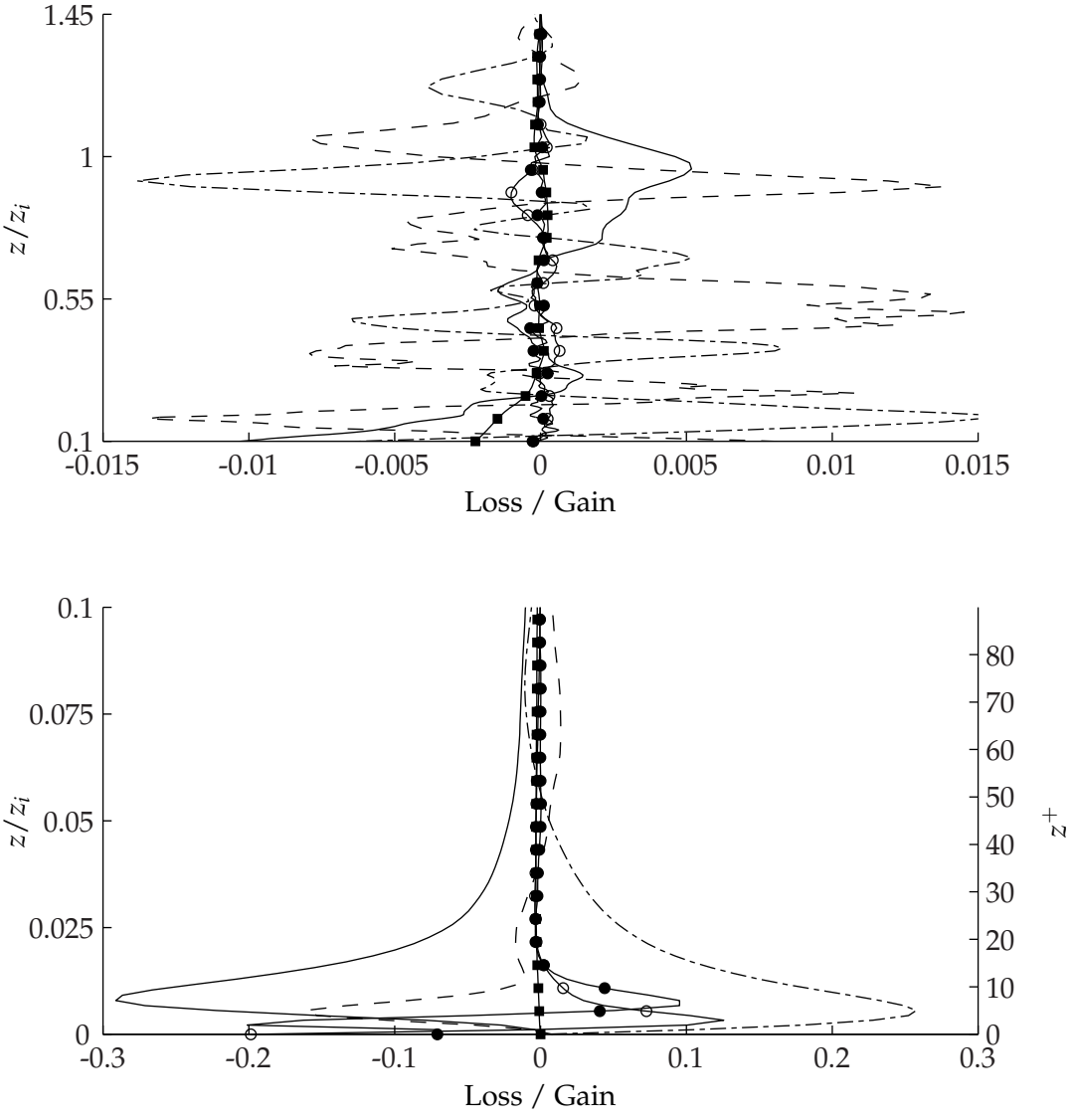

Figure 5.29: Same as Fig. 5.28 but for Case B2.

For the unstably stratified cases, Coriolis redistribution is insignificant in the transport of energy (see Figs. 5.15 through 5.27). Nevertheless, the secondary covariance budget is shown in Figs. 5.28 and 5.29 for Case B1 and B2 respectively. For the moderately stratified case, the budget closely resembles the neutrally stratified budget near the wall (Fig. 4.17). Away from the wall, production and pressure transport are in balance. The vigorously heated case demonstrates that, apart from the near wall region, the integration time is not sufficient to statistically average the results.

5.4 Evaluation of Closure Model: Third and Fourth Moments

In §4.5 the $k-\varepsilon$ model was compared against the neutrally stratified Ekman layer. It represented a variant of a second-order closure; instead of solving for the six Reynolds stresses individually, an equation for the kinetic energy and dissipation rate were solved instead.

Under thermal stratification, additional velocity-temperature correlations require closure. Here the DNS data will be used to evaluate a closure which parameterizes the third and fourth-order moments as functions of the heat flux ($\overline{w'\theta'}$), vertical velocity variance ($\sigma_w^2 = \overline{w'w'}$), temperature variance ($\sigma_\theta^2 = \overline{\theta'\theta'}$), and the velocity and temperature skewness (S_w and S_θ). A simple set of third and fourth-order closures are given by

$$\overline{w'^2\theta'} = S_w \sigma_w \overline{w'\theta'} \tag{5.4.1a}$$

$$\overline{w'\theta'^2} = S_\theta \sigma_\theta \overline{w'\theta'} \tag{5.4.1b}$$

$$\overline{w'^4} = \left(1 + S_w^2\right) \sigma_w^4 \tag{5.4.1c}$$

$$\overline{\theta'^4} = \left(1 + S_\theta^2\right) \sigma_\theta^4 \tag{5.4.1d}$$

$$\overline{w'^3\theta'} = \left(1 + S_w^2\right) \sigma_w^2 \overline{w'\theta'} \tag{5.4.1e}$$

$$\overline{w'\theta'^3} = \left(1 + S_\theta^2\right) \sigma_\theta^2 \overline{w'\theta'} \tag{5.4.1f}$$

The parameterizations of Eq. 5.4.1a and 5.4.1b were suggested by Abdella and McFarlane (1997).

The closure given by Eq. 5.4.1e was discussed by Abdella and McFarlane (1999). Remaining fourth-order closures are explicitly given by Gryanik and Hartmann (2002).

For zero skewness turbulence, $\overline{w'\theta'^2}$ (flux of temperature variance) and $\overline{w'^2\theta'}$ (flux of heat flux) in Eq. 5.4.1 will both be zero. Furthermore, zero skewness implies that all fourth-order moments are function of only the second-order moments σ_w^2, σ_θ^2, and $\overline{w'\theta'}$. Kraichnan (1957) argues that relating the fourth-order velocity moments to second-order moments – as is done in a Gaussian distribution where skewness is, by definition, zero – results in a violation of conservation of energy. Thus, the parameterization $\overline{w'^4} \approx \overline{w'^2}^2$ is fundamentally flawed.

A generalized modification to Eq. 5.4.1 is given by (Gryanik and Hartmann, 2002, Zilitinkevich et al., 1999)

$$\overline{w'^2\theta'} = a_1 S_w \sigma_w \overline{w'\theta'} - K_1 \frac{\partial \overline{w'\theta'}}{\partial z} \tag{5.4.2a}$$

$$\overline{w'\theta'^2} = a_2 S_\theta \sigma_\theta \overline{w'\theta'} - K_2 \frac{\partial \overline{\theta'^2}}{\partial z} \tag{5.4.2b}$$

$$\overline{w'^4} = a_3 \left(1 + d_3 S_w^2\right) \sigma_w^4 \tag{5.4.2c}$$

$$\overline{\theta'^4} = a_4 \left(1 + d_4 S_\theta^2\right) \sigma_\theta^4 \tag{5.4.2d}$$

$$\overline{w'^3\theta'} = a_5 \left(1 + d_5 S_w^2\right) \sigma_w^2 \, \overline{w'\theta'} \tag{5.4.2e}$$

$$\overline{w'\theta'^3} = a_6 \left(1 + d_6 S_\theta^2\right) \sigma_\theta^2 \, \overline{w'\theta'} \tag{5.4.2f}$$

The third-order moments include a form of down-gradient diffusion of second-order moments. Zilitinkevich et al. (1999) proposed

$$a_1 = 1 \tag{5.4.3a}$$

$$a_2 = 1 \tag{5.4.3b}$$

$$K_1 = C_k K_{w\theta} \tag{5.4.3c}$$

$$K_2 = 0 \tag{5.4.3d}$$

where $C_k = 0.1$ and $K_{w\theta} = 0.2\tau_Z \sigma_w^2$. The characteristic time τ_Z was parameterized as $\tau_Z = k/\varepsilon$.

Gryanik and Hartmann (2002) instead related the diffusivities to the kinetic energy by

$$K_i = d_i \sqrt{k} z_i \tag{5.4.4}$$

for $i = 1, 2$ (note that z_i still refers to the inversion height).

Gryanik and Hartmann (2002) argue that, in the limit that skewness goes to zero, the fourth-order statistics should approach Gaussian behavior. This implies $a_i = 3$ for $i = 3 - 6$. For turbulence with large skewness, the coefficient $a_i d_i$ should approach 1. So, $d_i = 1/3$ all fourth-order moments.

To assess the ability of the above closures to correctly parameterize high-order moments, Gryanik and Hartmann (2002) use the explained variance to quantify the difference between the modeled moment and the actual moment:

$$\sigma_f^2 = 1 - \frac{\overline{(y_i - f(x_i))^2}}{\overline{(y_i - \overline{y})^2}} \tag{5.4.5}$$

Actual measurements are given by y_i while the parameterization is given by $f(x_i)$. The overbar denotes an averaged quantity. To account for the clustering of mesh points in the near-wall region, the explained variance is redefined for this work as an integral over the boundary layer:

$$\sigma_f^2 \equiv 1 - \frac{\int_0^{L_z} (y_i - f(x_i))^2 \, \mathrm{d}z}{\int_0^{L_z} (y_i - \overline{y})^2 \, \mathrm{d}z} \tag{5.4.6}$$

where y_i are values from the DNS and $f(x_i)$ are, once again, the corresponding model predictions. The mean $\overline{y}$ is computed by

$$\overline{y} = \frac{1}{L_z} \int_0^{L_z} y_i \, \mathrm{d}z \tag{5.4.7}$$

The definition in Eq. 5.4.6 eliminates the bias associated with the clustering of meshpoints at the lower boundary.

5.4.1 Third-order Moments

The third-order closures in Eq. 5.4.2 were compared with data from Case B1 and B2. Optimum values of a_i and d_i were found by sampling data with different combinations of the two

parameters and locating the largest explained variance (which correlates with a better model). The contour plots in Fig. 5.30(a) and (b) show the explained variance of Case B1 for $\overline{w'^2\theta'}$ and $\overline{w'\theta'^2}$ respectively. The filled circles correspond to the values of a_i and d_i which maximize the explained variance using the DNS data; the open circles give the values proposed by Gryanik and Hartmann (2002) and the open square corresponds to the diffusivities recommended by Zilitinkevich et al. (1999). For a_1, the value which matches our DNS is larger (24-44%) than both recommended values. The range of recommended values for a_2 is relatively small.

The diffusion coefficient d_1 and d_2, however, show large variations. Relating the two definitions of K_1 in Eq. 5.4.3c and 5.4.4 requires that

$$0.2C_k\frac{k}{\varepsilon}\sigma_w^2 = d_1\sqrt{k}z_i$$

or

$$d_1 = \frac{0.2C_k\sqrt{k}\sigma_w^2}{\varepsilon z_i} \tag{5.4.8}$$

where $C_k = 0.1$. This gives the parameter d_1 proposed by Gryanik and Hartmann (2002) in terms of the diffusivity definition given by Zilitinkevich et al. (1999). Since the kinetic energy, dissipation, and vertical velocity variance change over the boundary layer, the mean value of d_1 in Eq. 5.4.8 is computed using Eq. 5.4.7. For the present DNS, the values of d_1 and d_2 proposed by Gryanik and Hartmann (2002) speculated an increased role of down-gradient diffusion in the third-order moments. However, these values of d_i would result in a negative explained variance indicating an over-emphasis of the diffusion of the second-order moment. The values of d_1 and d_2 which maximize σ_f^2 are close to the parameterizations of Zilitinkevich et al. (1999). In fact, based on the DNS results, the down-gradient diffusion term in the third-order closures of Eq. 5.4.2 could be eliminated entirely ($d_1 = d_2 = 0$) with little loss in the accuracy of the model.

A comparison of Case B1 data and the models for $\overline{w'^2\theta'}$ and $\overline{w'\theta'^2}$ are given in Fig. 5.31(a) and (b) respectively where the model uses values for a_i and d_i which maximize σ_f^2 (as shown in Fig. 5.30). The general trend of $\overline{w'^2\theta'}$ is captured by the model although some large differences between

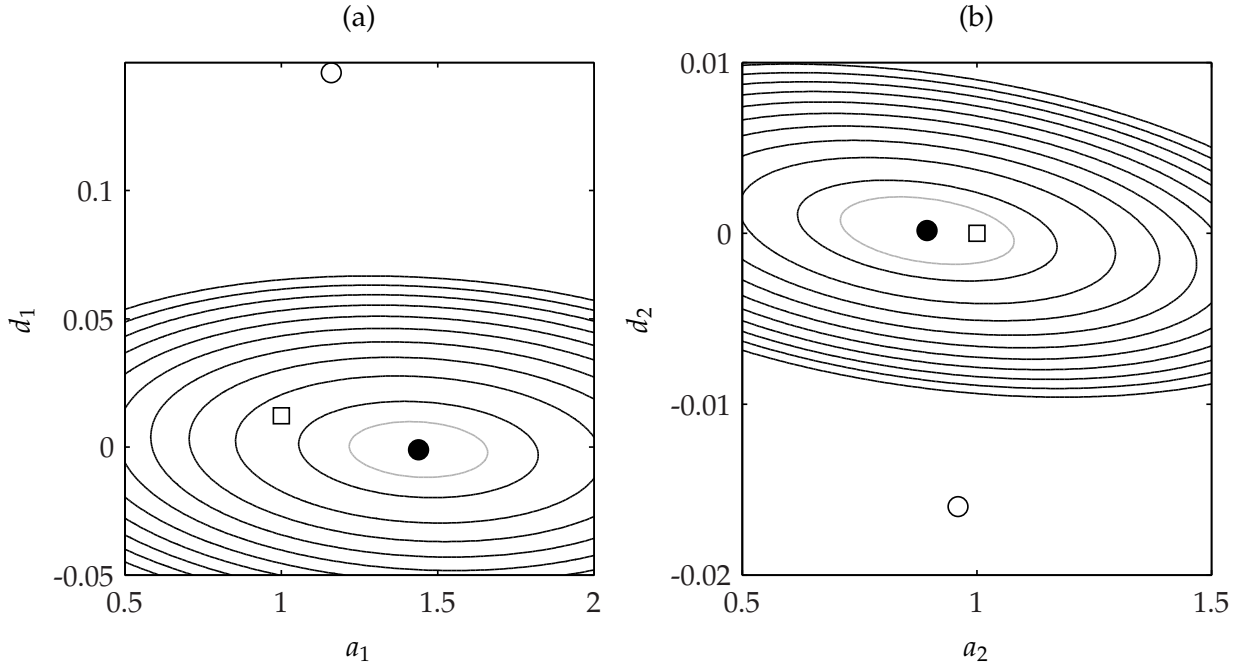

Figure 5.30: Calculation of empirical constants for third-order moments. Contours give explained variance as calculated by Eq. 5.4.6. (a) $\overline{w'^2\theta'}$, (b) $\overline{w'\theta'^2}$. Contour interval is $\Delta = 0.1$ for the black contours; gray contour gives $\sigma_f^2 = 0.95$. Open circles, Gryanik and Hartmann (2002); open squares, Zilitinkevich et al. (1999); closed circles, Case B1.

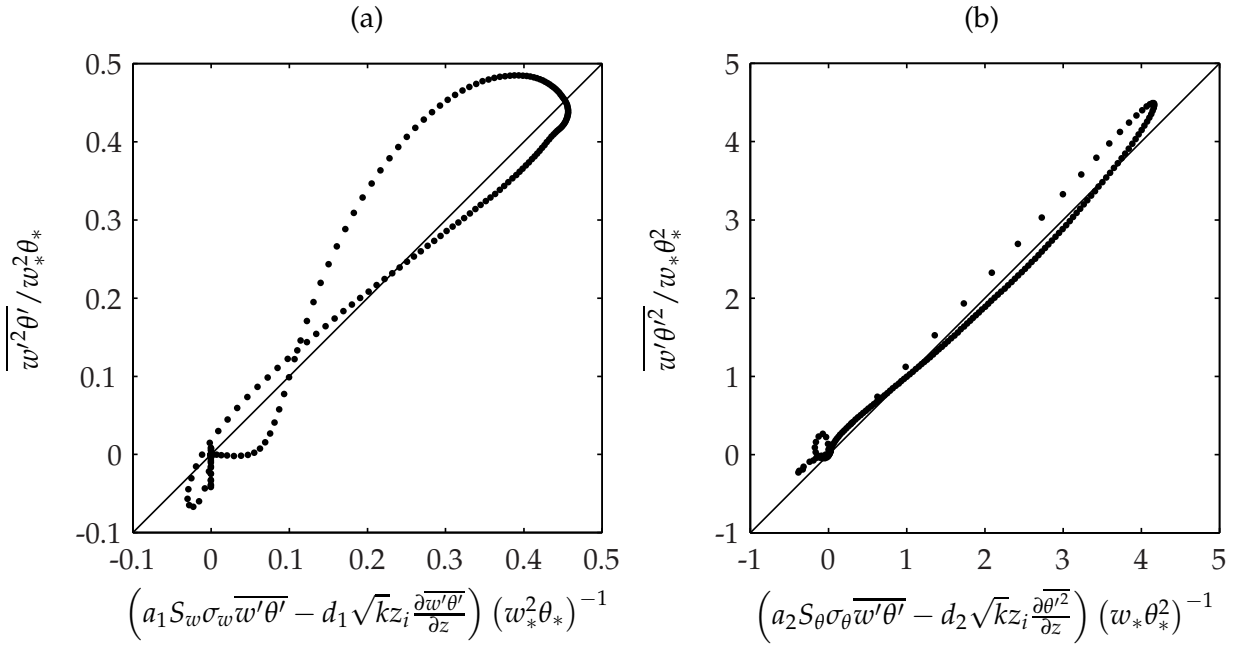

Figure 5.31: Third-order moments: (a) $\overline{w'^2\theta'}$, $a_1 = 1.44$, $d_1 = -1.17 \times 10^{-3}$; (b) $\overline{w'\theta'^2}$, $a_2 = 0.894$, $d_2 = 1.67 \times 10^{-4}$. Dots are Case B1 data and the line is unity.

the DNS data and the model exist. The model does well for $\overline{w'\theta'^2}$ throughout the boundary layer as shown in subplot (b).

5.4.2 Fourth-order Moments

As with the third-order closures, a sensitivity analysis was performed to demonstrate how variations in a_i and d_i affect the modeling abilities of Eq. 5.4.2. The coefficients a_i and d_i for $i = 1, 2$ effectively controlled the strength of the two modeling terms. In order to shut off the role of down-gradient diffusion, d_i was set to zero. This action has no direct impact on the coefficient a_i.

However, for the fourth order moments, the coefficients a_i and d_i for $i = 3 - 6$ are coupled. Rewriting the closure for the fourth moment of vertical velocity (Eq. 5.4.2c) yields

$$a_3 \left(1 + d_3 S_w^2\right) \sigma_w^4 = a_3 \sigma_w^4 + a_3 d_3 S_w^2 \sigma_w^4$$

Although the first term on the right-hand-side of the above expression only depends on a_3, the second term is a function of the product $a_3 d_3$. The fourth-order closures, as will be demonstrated shortly, have an array of coefficients a_i and d_i which satisfy the fourth-moments of Eq. 5.4.2c–f.

For Case B1, Fig. 5.32 shows σ_f^2 as a function of a_i and d_i for the fourth-order moments. As speculated, a band of values for a_i and d_i will achieve sufficient accuracy of the model. With the exception of $\overline{w'\theta'^3}$, the theoretical prediction of $a_i = 3$ and $d_i = 1/3$ given by Gryanik and Hartmann (2002) perform better than the coefficients obtained from atmospheric data. This supports the theoretical arguments which led to $a_i = 3$ and $d_i = 1/3$ for fourth-order closures. Without the ability to fine-tune the coefficients, these recommended values appear to be strong.

The closure for $\overline{\theta'^4}$ demonstrates the poorest performance with a maximum explained variance of 0.986. Figure 5.33(b) shows a large spike in the temperature moment which is not accurately captured. This peak in $\overline{\theta'^4}$ occurs in the very near wall region with a second peak at the inversion (much like the variance of θ, see Fig. 5.13). These two extrema dominate the parameter-

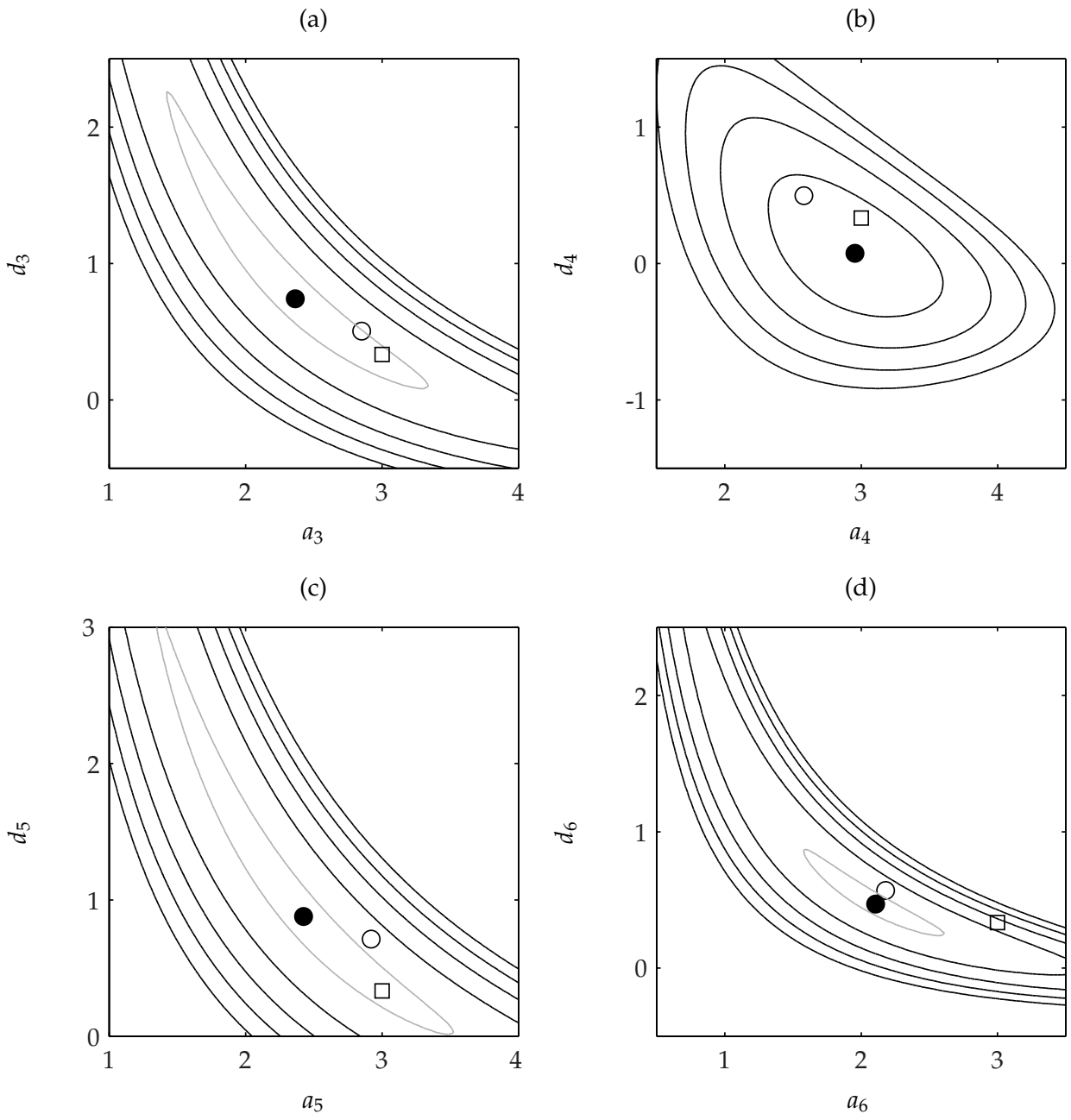

Figure 5.32: Calculation of empirical constants for fourth-order moments. Contours give explained variance as calculated by Eq. 5.4.6. (a) $\overline{w'^4}$, (b) $\overline{\theta'^4}$, (c) $\overline{w'^3\theta'}$, (d) $\overline{w'\theta'^3}$. Contour interval is $\Delta = 0.05$ for the black contours (minimum of $\sigma_f^2 = 0.8$); gray contour gives $\sigma_f^2 = 0.99$. Open circles, Gryanik and Hartmann (2002); open squares, Zilitinkevich et al. (1999); closed circles, Case B1.

ization of a_4 and d_4 such that the mixed layer – where the magnitude of $\overline{\theta'^4}$ is almost 3 orders of magnitude smaller – is insignificant when computing Eq. 5.4.6.

As seen in Fig. 5.33(a), (c), and (d), the optimum coefficients a_i and d_i found in Fig. 5.32 do a good job at modeling the DNS results. Note the exceptional performance of the model for $\overline{w'\theta'^3}$. The coefficients computed for a_6 and d_6 are close to the values recommended by Gryanik and Hartmann (2002), both of which deviate significantly from theoretically expected values.

5.4.3 Recommended Coefficients

A summary of the findings is given in Table 5.3. Contour plots showing σ_f^2 as a function of a_i and d_i for Case B2 are given in Appendix C. The values listed for Case B2 are based on these results. Note that d_1 changes sign between Case B1 and B2 and that both coefficients are an order of magnitude smaller than the recommended value (REC). It is likely that d_1 is a function of the strength of stratification. With how small the amplitudes are, simply letting $d_1 = 0$ would remove the uncertainty associated with this term with only a small decrease in model accuracy.

The two values of d_2 for Case B1 and B2 were found to be identical to three significant digits. Although small, it appears this coefficient is optimal for the current DNS data.

Only small changes in the coefficients a_i and d_i are seen for the comparison between Case B1 and B2 with the exception of d_4. The value of the coefficient computed for Case B2 is much closer to the predicted value of Gryanik and Hartmann (2002). Since their atmospheric measurements were such that $10 < -z_i/L < 20$, it seems d_4 is a function of the level of stratification: stronger heating results in an increase in role of skewness when parameterizing the fourth-moment of temperature.

5.5 Top-down / Bottup-up Diffusion

In the unstably stratified atmospheric boundary layer (ABL), mean velocity and potential temperature are well mixed below the capping inversion. To account for nonzero gradients in the

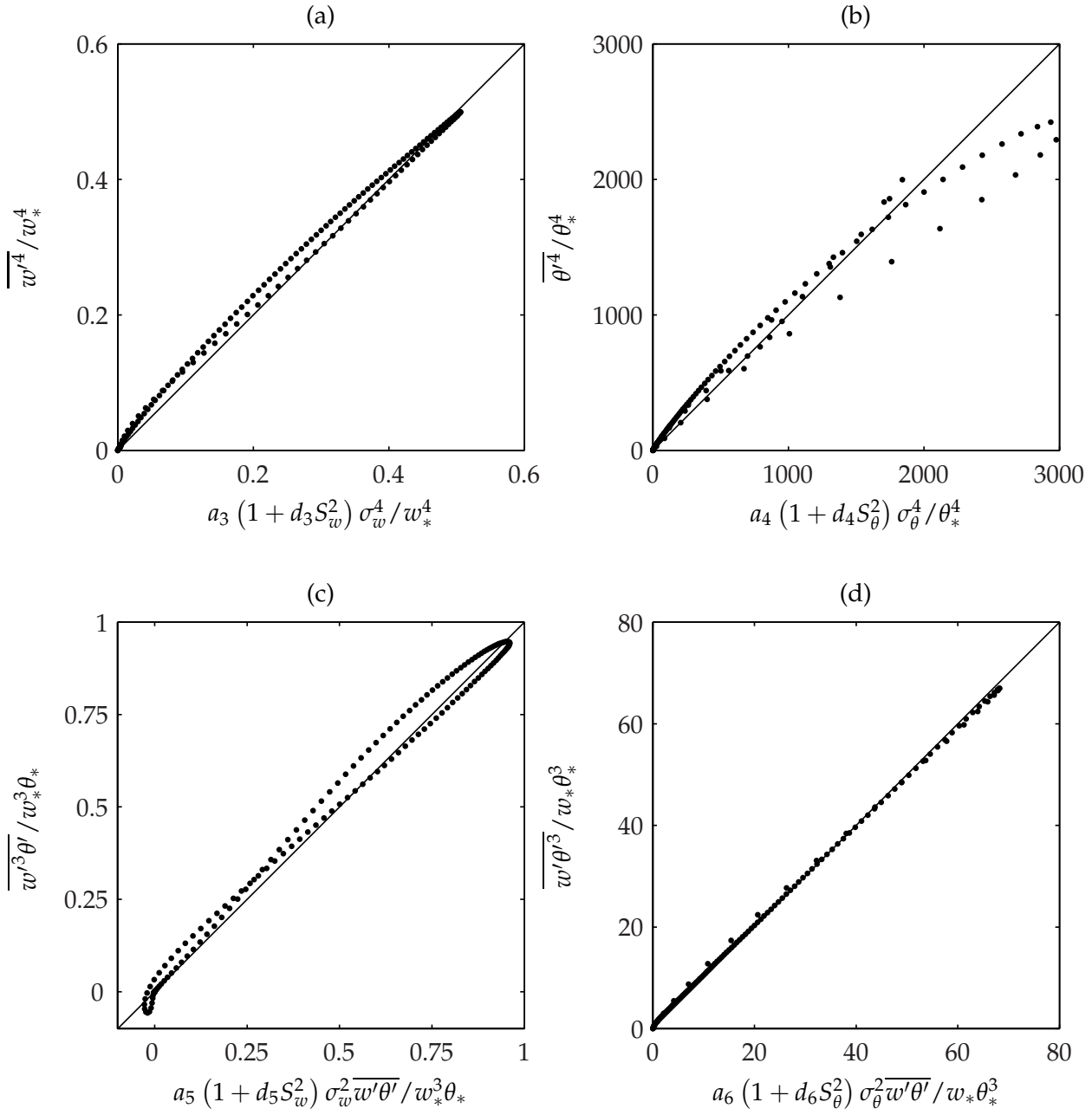

Figure 5.33: Fourth-order moments: (a) $\overline{w'^4}$, $a_3 = 2.36$, $d_3 = 0.742$, $\sigma_f^2 = 0.998$; (b) $\overline{\theta'^4}$ $a_4 = 2.95$, $d_4 = -7.58 \times 10^{-2}$, $\sigma_f^2 = 0.986$; (c) $\overline{w'^3\theta'}$, $a_5 = 2.42$, $d_5 = 0.879$, $\sigma_f^2 = 0.996$; (d) $\overline{w'^3\theta'^2}$, $a_6 = 2.11$, $d_6 = 0.470$, $\sigma_f^2 = 0.995$. Dots are Case B1 data and the line is unity.

Table 5.3: Coefficients for third and fourth-order moment closures, Case B: Recommended values (REC) for $i = 1, 2$ by Zilitinkevich et al. (1999) and $i = 3 - 6$ by Gryanik and Hartmann (2002). Best-fit for atmospheric measurements (GH) given by Gryanik and Hartmann (2002). Left and right d_1 coefficients calculated by Eq. 5.4.8 for Case B1 and B2 respectively.

a_i, d_i	REC	GH	B1	B2	$\sigma_f^2\big\|_{\mathrm{B1}}$	$\sigma_f^2\big\|_{\mathrm{B2}}$
a_1	1.00	1.16	1.44	1.65	0.975	0.986
d_1	0.0122 / 0.0162	0.146	-0.00117	0.000836		
a_2	1.00	0.96	0.894	0.854	0.991	0.994
d_2	0.00	-0.016	0.000167	0.000167		
a_3	3.00	2.85	2.36	2.15	0.998	0.998
d_3	0.33	0.146	0.742	0.803		
a_4	3.00	2.58	2.95	2.50	0.986	0.972
d_4	0.33	0.497	0.0758	0.348		
a_5	3.00	2.926	2.42	2.48	0.996	0.996
d_5	0.33	0.713	0.879	0.970		
a_6	3.00	2.18	2.11	2.17	0.995	0.996
d_6	0.33	0.570	0.470	0.439		

mixed layer for specific humidity, Wyngaard and Brost (1984) proposed the concept of top-down and bottom-up diffusion. Given a scalar concentration q, Wyngaard describes the total scalar flux as a linear combination of the surface flux (subscript b) and entrainment-zone flux (subscript t):

$$\overline{w'q'} = \overline{w'q'}_b + \overline{w'q'}_t \tag{5.5.1}$$

By means of large-eddy simulation (LES), Wyngaard and Brost (1984) parameterized the eddy diffusivity for both top-down and bottom-up passive scalars by treating the processes as symmetric. Their results show good agreement between LES and their proposed closure approximation. Moeng and Wyngaard (1984) built upon this analysis by constructing functions to parameterize scalar covariances and compute the flux budgets for both top-down and bottom-up scalars. Patton et al. (2003) and Wang et al. (2007) proposed revisions to the gradient functions proposed by Wyngaard and Brost (1984) for a convective boundary layer over a forested site where the canopy acts to increase surface roughness.

The purpose of this work is to simulate passive scalars as bottom-up and top-down pro-

cesses over a smooth surface while resolving flow features through the viscous sublayer and down to the wall via direct numerical simulation (DNS). This allows a fundamental study of the two diffusion processes in the absence of a rough wall and avoids assumptions concerning near-wall temperature and scalar fluxes. Comparison between DNS results and previous LES simulations provides insight into the effect of surface roughness on scalar flux.

5.5.1 Simulation Specifications

Starting from the end of the Case B2 simulation, two scalars were initialized in the domain with small amplitude random fluctuations. The new case is denoted as Case B2s (s for 'scalars'). The first passive scalar q_b was initialized with a constant value through most of the boundary layer and with a steep gradient near the wall. A constant scalar value ($q_b = 1$) condition was imposed at the wall with $\partial q_b/\partial z = 0$ at $z_{\max}$. The top-down scalar q_t was initialized using a step function and allowed to evolve with a zero gradient condition at the wall. The height of the initial step function for q_t was chosen to align with the temperature inversion height (though z_i grows with time). With the newly introduced passive scalars q_b and q_t, the field was advanced forward in time until a quasi-steady state was reached. Field variables were then averaged using 50 data realizations. The mean profiles of q_b and q_t are shown with their corresponding initial distribution in Fig. 5.34(a) and (b) respectively. Since Case B2s has evolved from Case B2, the temperature field and surface heat flux change slightly. Over the time-averaging period used for Case B2s, the mean surface Richardson number decreases to $\mathrm{Ri}_0 = -14.02$ (slightly lower than that of Case B2).

The data for this Case B2s were averaged over a sampling window of $t/\mathcal{T} \approx 1.4$, i.e. an entire large eddy turnover time was captured. This corresponds to an averaging window of $tf \approx 0.05$ in terms of the Coriolis parameter. For Case B2s, $z_i/L = -49.1$. The strength of stratification is slightly lower than that of Case B2 since the flow has evolved longer.

The total temperature flux is composed of both turbulent and viscous flux components:

$$Q_\theta = \overline{w'\theta'} - \frac{1}{\mathrm{Pr}\,\mathrm{Re}}\frac{\partial \theta}{\partial z} \tag{5.5.2}$$

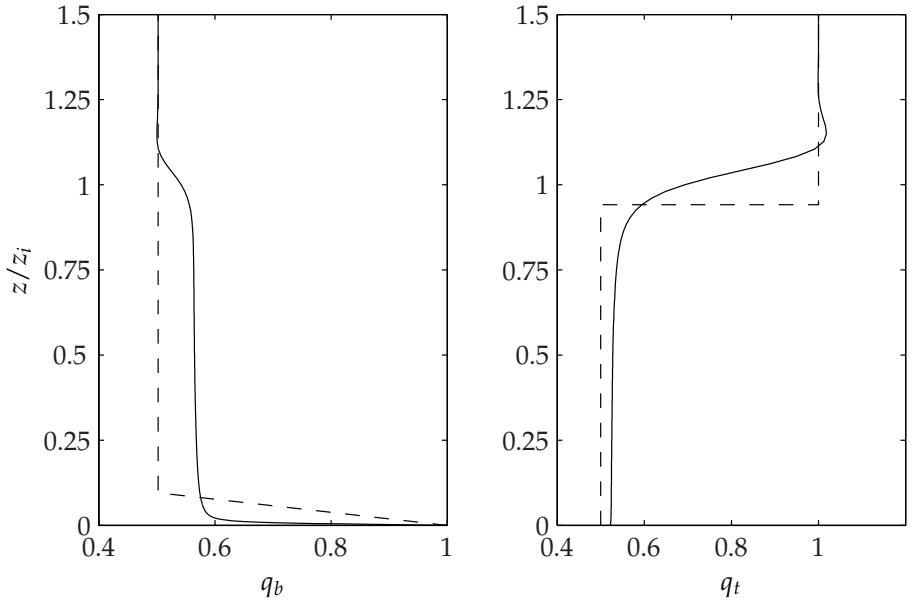

Figure 5.34: Mean scalar profiles for q_b (left) and q_t (right). Dashed lines indicates initial conditions while solid lines show time-averaged profiles.

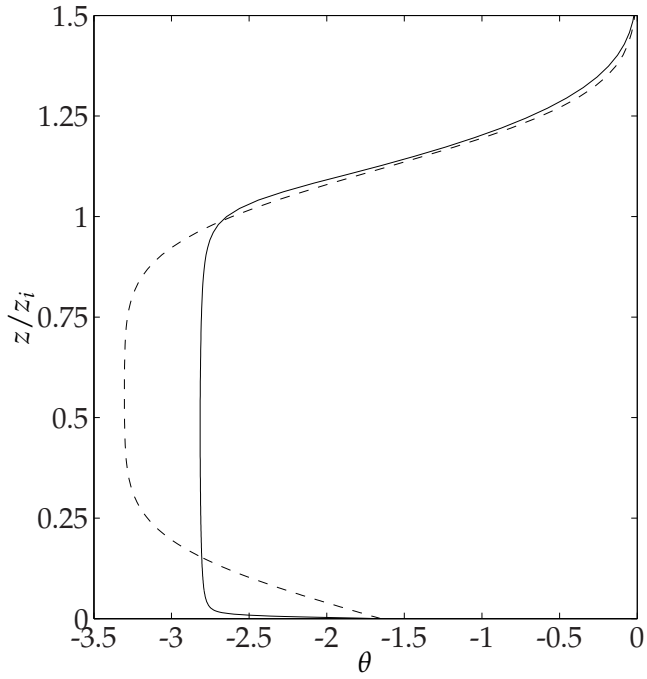

Figure 5.35: Mean temperature profile: solid, time-averaged θ; dashed, initial condition.

The contributions of each term are shown in Fig. 5.36. Note that viscous effects only are prevalent in the very near wall region and when $z \geq z_i$. Furthermore, it is clear that the heat flux maintains a linear shape for $0 \leq z/z_i \leq 1$. The minimum heat flux at $z = z_i$, which gives an indication of the strength of top-down diffusion to bottom-up diffusion and also entrainment, has a value of $Q_\theta/Q_{\theta,0} = -0.153$. Sorbjan (2004) simulated the unstable ABL under various conditions with $-4.17 \leq z_i/L \leq -1.95$ using LES. In Sorbjan's LES, the ratio between the total heat flux at the top and bottom of the mixed layer varied between approximately -0.17 and -0.3. Our results indicate slightly less entrainment influences at the top of the mixed layer relative to the bottom when stronger stratification is present (Jonker et al., 2010).

In the same fashion as Eq. 5.1.2, a surface flux parameter is defined for the bottom-up scalar q_b:

$$\frac{Q_{q_b,0}}{U_g} = -\frac{1}{\mathrm{Sc}\,\mathrm{Re}} \left.\frac{\partial q_b}{\partial z}\right|_{z_0} \tag{5.5.3}$$

Note that q_b is a dimensionless scalar concentration so $Q_{q_b,0}/U_g$ is likewise a dimensionless flux. The total, turbulent, and viscous fluxes for q_b are shown in Fig. 5.37(a). The near-wall region is once again dominated by viscous flux as the no slip condition enforces zero turbulent flux. However, for $z/z_i > 0.04$, the viscous term is less than 1% of $Q_{q_b,0}$ where $\overline{w'\theta'}$ is the primary transport mechanism. At the inversion, $Q_{q_b,0}/U_g = 0.06$ indicating very weak scalar flux.

While it is convenient to normalize θ and q_b by the surface value of the viscous flux, such an operation is not possible for q_t since both the turbulent and viscous fluxes at $z = 0$ are zero. Instead, the total flux

$$Q_{q_t} = \overline{w'q_t'} - \frac{1}{\mathrm{Sc}\,\mathrm{Re}} \frac{\partial q_t}{\partial z} \tag{5.5.4}$$

is normalized by $Q_{q_t,1}$ where

$$Q_{q_t,1} = \min\left(Q_{q_t}\right) \tag{5.5.5}$$

Note that, for the distribution of q_t shown in Fig. 5.34, both the turbulent and viscous fluxes will be negative over the entire mixed layer as the scalar is transported downward towards the wall. The maximum of $Q_{q_t}/Q_{q_t,1}$ is found to occur at $z/z_i = 0.87$ which correlates very well with the

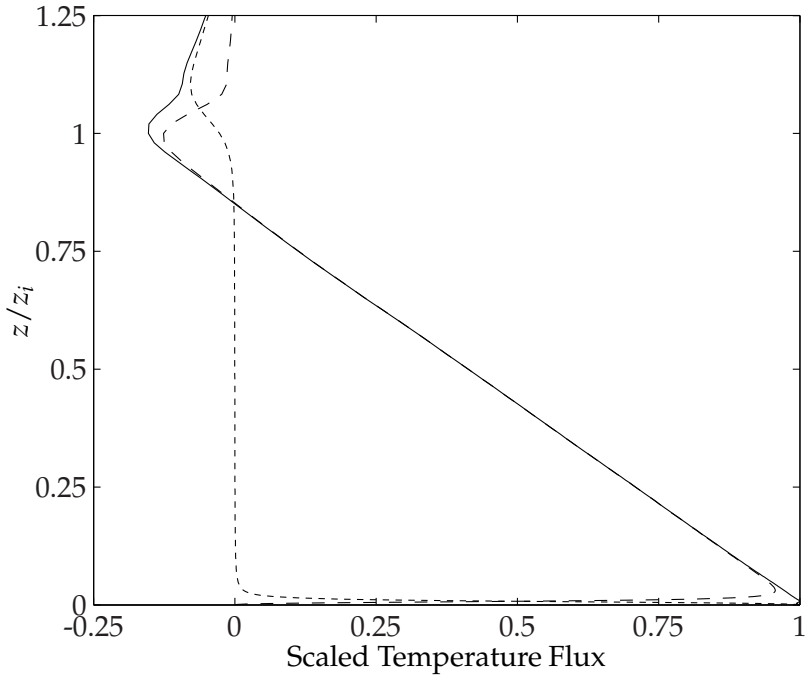

Figure 5.36: Vertical temperature flux: solid, total temperature flux; dashed, turbulent flux; dotted, viscous flux. All terms have been normalized by $Q_{\theta,0}$ (Eq. 5.1.3).

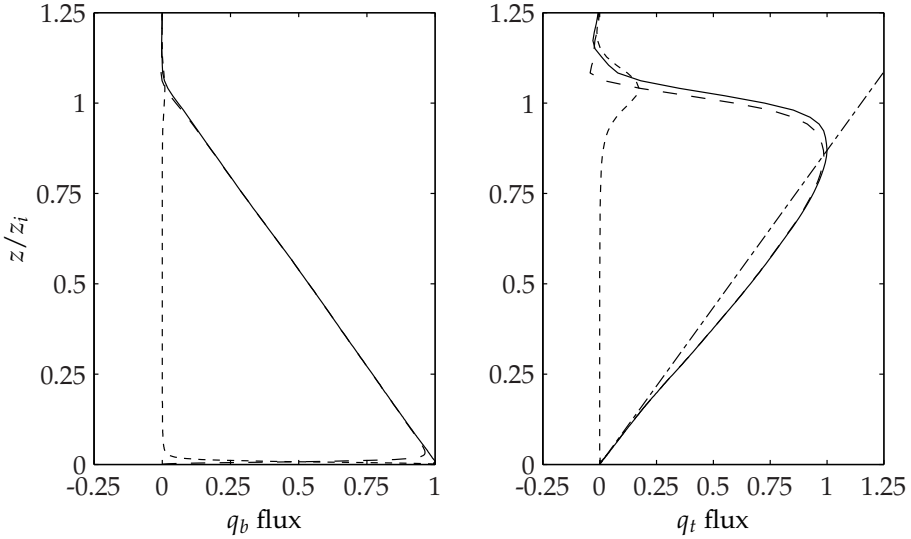

Figure 5.37: Vertical scalar flux for q_b (left) and q_t (right). Solid, total scalar flux; dashed, turbulent flux; dotted, viscous flux. Dash-dot indicates linear relationship between zero flux wall and maximum top-down flux.

Table 5.4: Case B2s Simulation Parameters. Type codes: SW = smooth wall, WT = water tank experiment, RW = rough wall LES, and C = canopy LES.

	Type	Re_c	u_*/w_*	Ri	$-z_i/L$
DNS (Present work)	SW	4473	0.203	55.5	49.1
Patton et al. (2003)	RW	$--$	0.252	$--$	24.9
Patton et al. (2003)	C	$--$	0.282	$--$	17.8
Piper et al. (1995)	WT	1000-2000	$--$	29	$--$
Moeng and Wyngaard (1984)	RW	$--$	0.350	54	10
Wyngaard and Brost (1984)	RW	$--$	0.184	$--$	64

crossover point where Q_θ goes from positive to negative flux. Unlike Q_θ or Q_{q_b}, the flux profile of a top-down process is not linear. Wyngaard and Brost (1984) attributed this to deepening of the ABL with time. The peak in viscous flux occurs just above the inversion ($z/z_i \approx 1.04$). At this point the turbulent and viscous fluxes are nearly equal in amplitude and greater than 17% of $Q_{q_t,1}$. Whereas viscous effects are relevant only in a very thin layer at the wall for bottom-up diffusion, both viscous and turbulent fluxes play an important role at the temperature inversion for the top-down processes given the low Reynolds number of the simulation.

A comparison between the current DNS and other LES are provided in Table 5.4. The Reynolds number based on convective scales is defined as $\mathrm{Re}_c = w_* z_i/\nu$ and the Richardson number is

$$\mathrm{Ri} = \frac{z_i/\delta_E}{\left(w_*/U_g\right)^2}\Delta\theta \tag{5.5.6}$$

in terms of dimensionless quantities. Note that $\Delta\theta$ is the jump in potential temperature across the entrainment layer. Despite the fact that our DNS is at a substantially lower Reynolds number in comparison with atmospheric LES studies, all other flow parameters are comparable to rough wall LES conditions. In terms of the convective Reynolds number, the DNS is close to the water dye experiments of Piper et al. (1995).

5.5.2 Top-down Diffusion

In order for a scalar to exhibit pure top-down diffusion, the scalar gradient at $z = 0$ must be identically zero to ensure both turbulent and viscous flux vanish at the wall. This is accomplished by imposing a zero gradient boundary condition on the top-down scalar q_t. Consequently, the steepest gradients in q_t occur near the inversion and decay as $z \to 0$.

A simple mixing length hypothesis for the scalar flux of q_t can be constructed as follows:

$$Q_{q_t} = -K_t \frac{\partial q_t}{\partial z} \tag{5.5.7}$$

where K_t is the eddy diffusivity for a top-down scalar. Solving for K_t yields

$$K_t = -\frac{Q_{q_t}}{\partial q_t / \partial z} \tag{5.5.8}$$

A dimensionless scalar gradient can be defined as

$$g_t = -\frac{z_i}{q_{t*}} \frac{\partial q_t}{\partial z} \tag{5.5.9}$$

where q_{t*} is a characteristic scalar value defined as

$$q_{t*} = \frac{Q_{q_t,1}}{w_*} \tag{5.5.10}$$

The dimensionless mean scalar gradient g_t obtained from the present DNS is shown in Fig. 5.38 and is compared with the best fit curve of Moeng and Wyngaard (1984) defined as

$$g_t \approx C_t (1 - z/z_i)^{-2} \tag{5.5.11}$$

with $C_t = 1$; Moeng and Wyngaard (1984) chose $C_t = 0.7$ as a fit to their LES data. The data show good agreement between their approximation and the DNS data for $0.1 < z/z_i < 0.95$. Approaching the wall, the gradient function demonstrates a deviation from Eq. 5.5.11 as g_t increases. Similar near-wall behavior for a top-down scalar is noted by Piper et al. (1995). In their work, Patton et al. (2003) demonstrated that adding a tree canopy to their LES had little effect on g_t. Our results validate their findings: the top-down diffusion of a scalar is not a function of surface roughness. As shown in Fig. 5.38, only a slight increase in the gradient function throughout the mixed

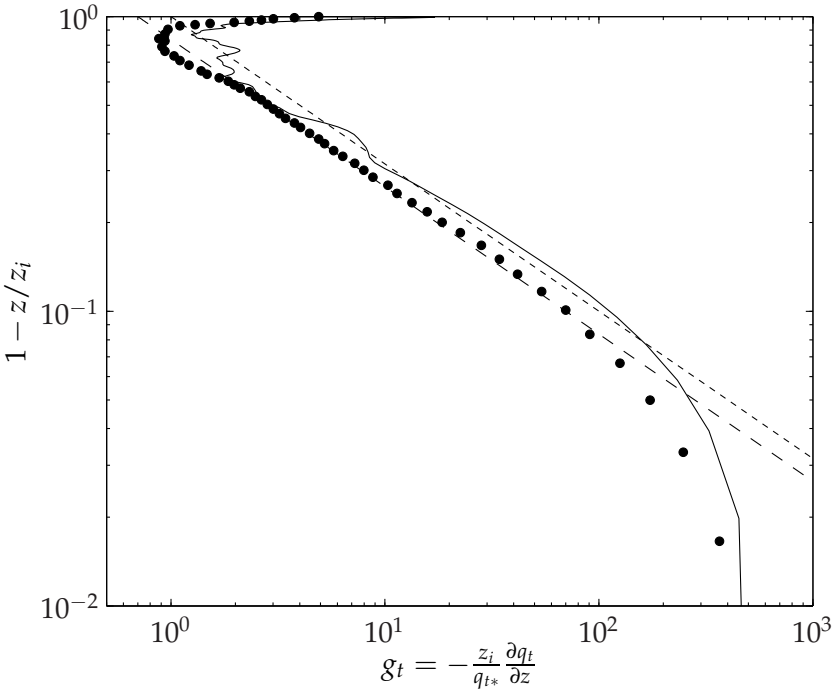

Figure 5.38: Gradient of mean top-down scalar distribution. Solid line, DNS; dashed line, Eq. 5.5.11 $C_t = 0.7$; dotted line, Eq. 5.5.11 $C_t = 1$; closed circles, LES with canopy (see Patton et al., 2003).

layer is noted for the low Reynolds number DNS. This increase in g_t indicates a small decrease in mixing efficiency. The difference in the amplitude of g_t is likely a consequence of the Reynolds number as opposed to the surface roughness given the consistency of the offset throughout the mixed layer. Nevertheless, the similarity between the smooth-wall, low Reynolds number DNS with rough-wall, atmospheric LES suggests that in the mixed layer, g_t is only weakly influenced by surface roughness, large variations in the Reynolds number, or the strength of stratification.

If a linear relationship between the scalar flux and height in the mixed layer is assumed such that the maximum flux occurs at the temperature inversion, then

$$\frac{Q_{q_t}}{Q_{q_t,1}} \approx \frac{z}{z_i} \tag{5.5.12}$$

Combining Eq. 5.5.8-5.5.12 with $C_t = 1$, the predicted eddy diffusivity based on a linear flux profile is given by

$$\frac{K_t}{w_* z_i} \approx \left(\frac{z}{z_i}\right)\left(1 - \frac{z}{z_i}\right)^2 \tag{5.5.13}$$

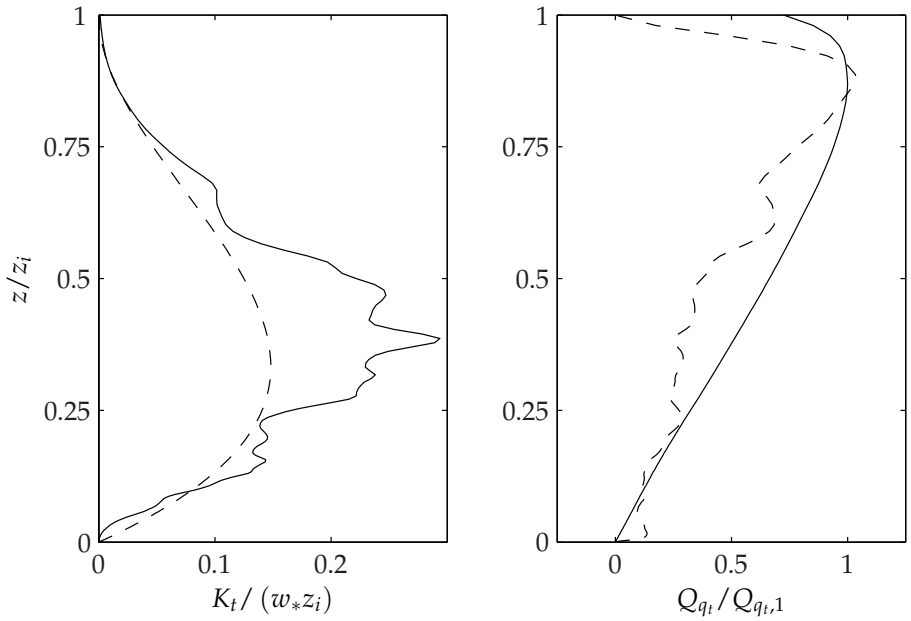

Figure 5.39: Eddy diffusivity (left) and scalar flux (right) for top-down scalar. Solid line, DNS; dashed line, Eq. 5.5.13.

Figure 5.39 compares this cubic polynomial approximation along with our DNS results for the eddy diffusivity and scalar flux and indicates that Eq. 5.5.13 and the DNS results are in relatively good agreement. K_t is slightly underpredicted through the mixed layer and overpredicted in the very near-wall region. From Fig. 5.38 it is clear the the near-wall deviation is caused by an under-estimation of the velocity gradient at the lower boundary (top of figure). As shown in Fig. 5.39(b), the location of the maximum scalar flux, which is computed via Eq. 5.5.7 and 5.5.13, is correctly captured ($z/z_i \approx 0.88$) and the magnitude of the flux is only off by approximately 3.5%. For $0.25 < z/z_i < 0.85$, the total top-down flux is marginally underpredicted. This is partially a consequence of assuming the flux is linear with a maximum flux at the inversion (Eq. 5.5.12). A small improvement through the mixed layer is obtained by fitting a linear trend between the wall (zero flux) and the height at which $Q_{q_t}/Q_{q_t,1} = 1$. However, the height at which this occurs ($z/z_i = 0.869$ for this case) may not be universal and could demonstrate dependence on Reynolds number or the strength of stratification. Finally, the parameterization of g_t by Eq. 5.5.11 dictates that the eddy diffusivity is zero at $z = z_i$. In actuality, both the turbulent and viscous fluxes are

substantial at the inversion. The total scalar flux from the DNS reaches zero at approximately $z/z_i = 1.13$.

5.5.3 Bottom-up Diffusion

Since a top-down diffusion process exhibits zero flux at the wall, a true bottom-up process should exhibit zero flux near the temperature inversion. Wyngaard and Brost (1984) explicitly enforced a zero flux condition at the top of the mixed layer (as determined by the maximum amplitude of their top-down scalar flux). Moeng and Wyngaard (1984) and Piper et al. (1995) extract the bottom-up scalar gradient using the top-down scalar and a scalar (or temperature) which exhibits both top-down and bottom-up diffusion. Although results from the DNS (see Fig. 5.37) show Q_{q_b} is small at z_i indicating only a small contribution from top-down diffusion, the effect of top-down diffusion on the bottom-up scalar has been removed so a pure bottom-up process is captured.

As with the top-down scalar, the eddy diffusivity for a bottom-up process is given by

$$K_b = -\frac{Q_{q_b}}{\partial q_b / \partial z} \tag{5.5.14}$$

and a dimensionless scalar gradient is defined as

$$g_b = -\frac{z_i}{q_{b*}} \frac{\partial q_b}{\partial z} \tag{5.5.15}$$

where

$$q_{b*} = \frac{Q_{q_b,0}}{w_*} \tag{5.5.16}$$

Top-down diffusion effects are removed using the assumption that the gradient of an arbitrary scalar has both top and bottom diffusion effects:

$$\frac{\partial c}{\partial z} = \frac{\partial c_b}{\partial z} + \frac{\partial c_t}{\partial z} \tag{5.5.17}$$

The gradient of c_t has already been parameterized in Fig. 5.38, so g_b (minus top-down effects) is

given by

$$g_b = -\frac{z_i w_*}{Q_{q_b,0}} \frac{\partial q_b}{\partial z} - \frac{Q_{q_b,1}}{Q_{q_b,0}} g_t \tag{5.5.18}$$

The height at which $Q_{q_b,1}$ was taken corresponds to the point where $Q_{q_t}/Q_{q_t,1} = 1$. The gradient profile g_b is shown in Fig. 5.40. The model

$$g_b \approx C_b \left(\frac{z}{z_i} \right)^{-3/2} \tag{5.5.19}$$

of Wyngaard and Brost (1984) fits the scalar q_b data very well for $0.08 < z/z_i < 0.4$. For $z/z_i > 0.4$, the gradient function changes sign and Eq. 5.5.19 no longer holds. Interestingly, if top-down effects are not removed (i.e. $g_b = -\left(z_i w_*/Q_{q_b,0}\right) \partial q_b/\partial z$), agreement between the model and DNS show agreement up until $z/z_i \approx 0.7$ (gray curve in Fig. 5.40). The constant $C_b = 0.23$ used to fit our data is close to the value $C_b = 0.4$ used by Wyngaard and Brost (1984) for their LES data. Patton et al. (2003) notice enhanced mixing efficiency (a decrease in g_b) for flow with canopy in comparison to flow without. It is expected, then, that the smooth-wall DNS would also show an increase in g_b near the wall as mixing from surface roughness is eliminated. However, the gradient function g_b closely aligns with their no-canopy results for $z/z_i > 0.02$. Thus, differences between bottom-up diffusion for a smooth and rough wall are limited to a very thin layer near the wall. Below $z/z_i = 0.02$, the smooth-wall results show a considerable increase in g_b through the viscous sublayer (note that $z/z_i = 0.01$ corresponds with $z^+ \approx 9.1$). For the Reynolds number of the DNS, the viscous sublayer is considerably thicker than that of rough wall LES.

Both Moeng and Wyngaard (1984) and Piper et al. (1995) show $g_b \approx 0$ at $z/z_i \approx 0.5 - 0.6$ when g_b is deduced from other flow variables; this crossover point is well captured by our DNS results. The gradient function in the bottom half of the mixed layer appears to be well represented by Eq. 5.5.19 as shown in Fig. 5.40. However, above $z/z_i > 0.6$ the gradient function model does not capture the sign change associated with pure bottom-up diffusion.

Combining Eq. 5.5.14, 5.5.19 and the approximation that $Q_{q_b}/Q_{q_b,0} \approx 1 - z/z_i$ yields the

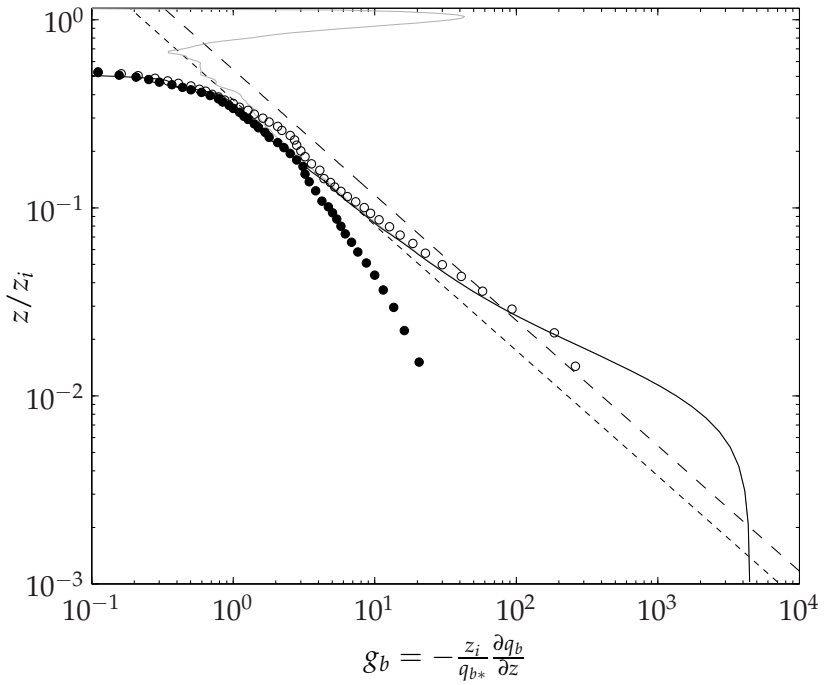

Figure 5.40: Gradient of mean bottom-up scalar distribution. Gray line, DNS Eq. 5.5.15; black line, DNS Eq. 5.5.18; dashed line, Eq. 5.5.19 w/ $C_b = 0.4$; dotted line, Eq. 5.5.19 w/ $C_b = 0.23$; open circles, LES without canopy; closed circles, LES with canopy (see Patton et al., 2003).

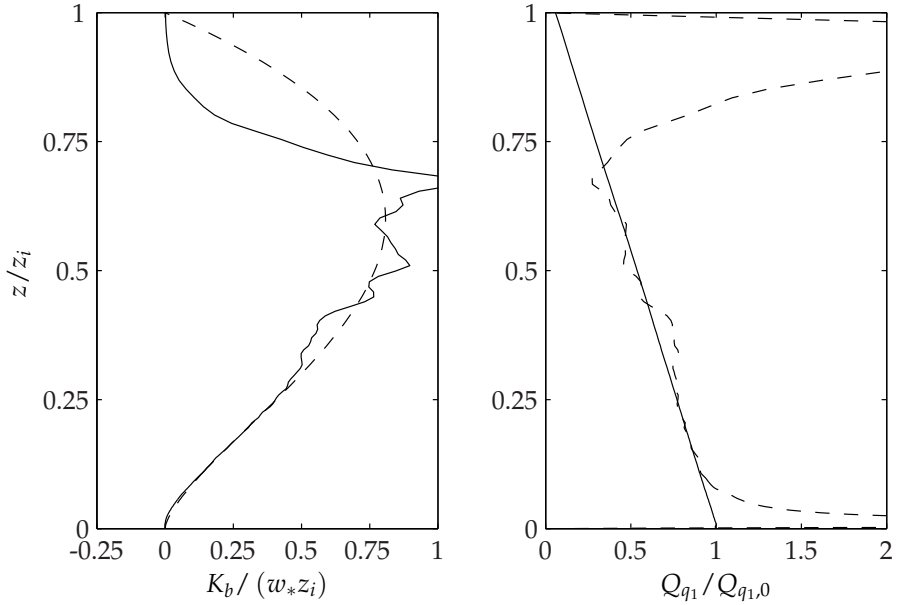

Figure 5.41: Eddy diffusivity (left) and scalar flux (right) for bottom-up scalar. Solid line, DNS; dashed line, Eq. 5.5.20

following model for the eddy diffusivity of a bottom-up scalar:

$$\frac{K_b}{w_* z_i} = \left(\frac{1}{0.23}\right)\left(1 - \frac{z}{z_i}\right)\left(\frac{z}{z_i}\right)^{3/2} \tag{5.5.20}$$

Figure 5.41 compares the DNS and model eddy diffusivities (a) and resulting total scalar flux (b). Note that the turbulent flux $\overline{w'q'_b}$ has not had top-down effects removed. Once again, the model does well except for close to the inversion and near the wall where the viscous sublayer is approached. It is expected that the model will perform better in the near-wall region as the Reynolds number increases. The over-prediction over the total flux near the inversion is likely a consequence of the presence of top-down diffusion in $\overline{w'q'_b}$ and not, necessarily, a Reynolds number effect.

5.5.4 Variance and Covariance Functions

The gradient functions for top-down and bottom-up processes are useful in determining the vertical flux of a scalar in the mixed layer. While Eq. 5.5.1 relates the flux of a scalar to contributions from both top-down and bottom-up diffusion, the variance of a scalar c is a function of top-down diffusion, bottom-up diffusion, and a cross-correlation between the two processes (Moeng and Wyngaard, 1989):

$$\overline{c'c'} = \overline{c'_t c'_t} + 2\overline{c'_t c'_b} + \overline{c'_b c'_b} \tag{5.5.21}$$

In an attempt to parameterize $\overline{c'c'}$, variance functions – denoted f_t, f_b, and f_{tb} for top, bottom, and mixed diffusion – can be formed for each term as follows:

$$\overline{c'_t c'_t} = q_{t*}^2 f_t \tag{5.5.22a}$$

$$\overline{c'_t c'_b} = q_{t*} q_{b*} f_{tb} \tag{5.5.22b}$$

$$\overline{c'_b c'_b} = q_{b*}^2 f_b \tag{5.5.22c}$$

If the above variance functions are universal (independent of Reynolds number or the strength of stratification), then the variance of some arbitrary scalar could be determined if the strength of

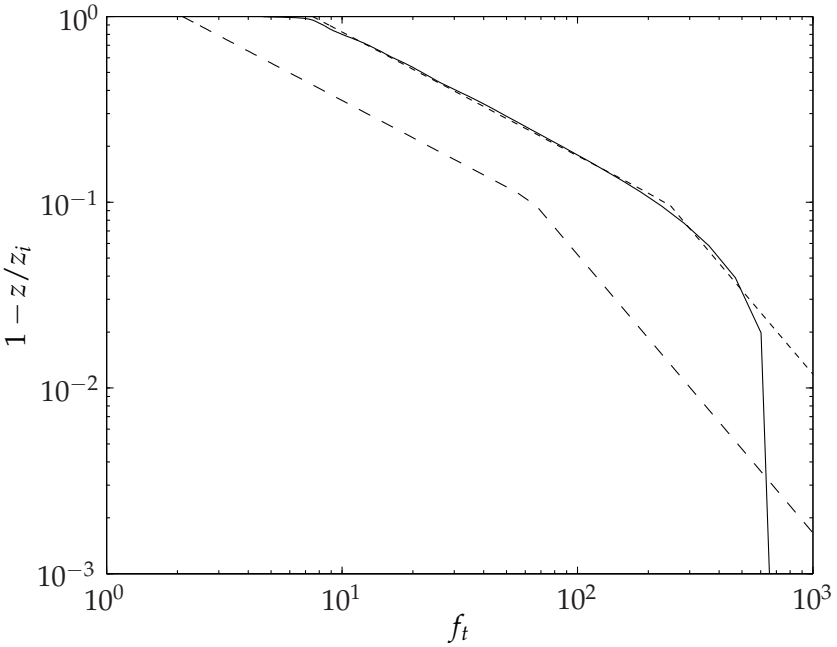

Figure 5.42: Scalar variance for top-down diffusion: Solid line, DNS; dashed line, Eq. 5.5.24 ($a_1 = 2.1$ and $a_2 = 14$); dotted line, Eq. 5.5.24 ($a_1 = 7.5$ and $a_2 = 52$).

top-down diffusion relative to bottom-up diffusion is known. Letting $R = Q_{c,1}/Q_{c,0}$ be the ratio of the entrainment flux to surface flux, the variance for an arbitrary scalar c can be approximated as

$$\frac{\overline{c'c'}}{c_*^2} = R^2 f_t + 2R f_{tb} + f_b \tag{5.5.23}$$

where $c_* = Q_{c,0}/w_*$, the total surface flux divided by the convective velocity.

Variance of the top-down scalar for the present DNS is shown in Fig. 5.42. Moeng and Wyngaard (1984) fit their LES data with empirical functions

$$f_t = a_1 \left(1 - \frac{z}{z_i}\right)^{-3/2}, \qquad z/z_i < 0.9 \tag{5.5.24a}$$

$$f_t = a_2 \left(1 - \frac{z}{z_i}\right)^{-2/3}, \qquad z/z_i > 0.9 \tag{5.5.24b}$$

and specified $a_1 = 2.1$ and $a_2 = 14$ to fit their data. While the $-3/2$ relation in the mixed layer appears qualitatively correct, a large increase in a_1 is required to fit our smooth wall results. Because of coarse resolution in their LES near the inversion, the fit Moeng and Wyngaard (1984) propose

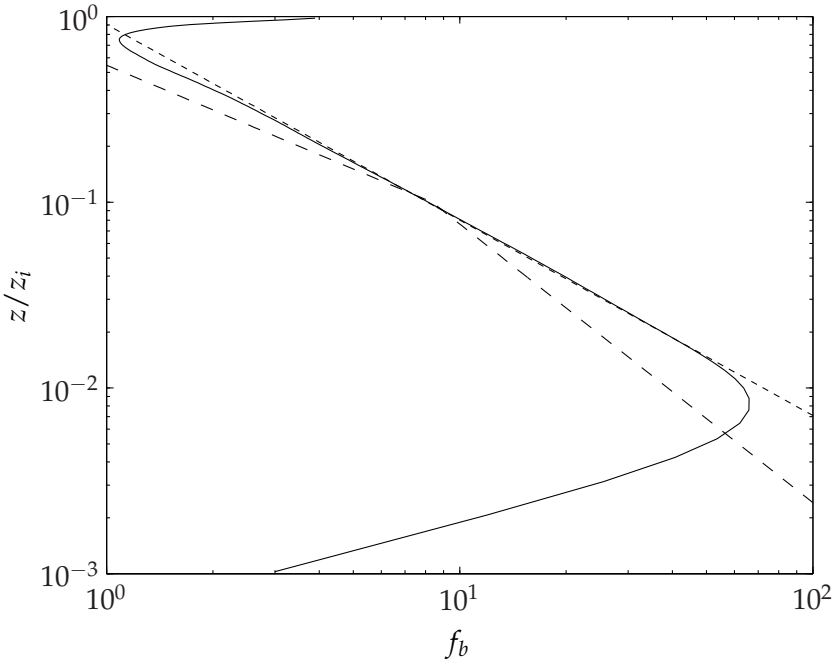

Figure 5.43: Scalar variance for bottom-up diffusion: Solid line, DNS; dashed line, $b_1 = 1.8$ and $b_2 = 0.47$; dotted line, $f_t \approx 0.91\,(z/z_i)^{-0.95}$.

for $z/z_i > 0.9$ is relatively uncertain. Our DNS also has a coarse resolution near the inversion (in comparison to the near-wall region), but mesh points closer to the inversion were captured allowing for a better approximation of f_t near z_i. The $-2/3$ relation does reasonably well at capturing scalar variance near the inversion. However, Eq. 5.5.24 assumes that $\overline{q_t' q_t'} \to \infty$ as $z/z_i \to 1$ and will perform poorly near the inversion as the scalar variance is bounded.

The bottom up scalar q_b and temperature θ were used to solve for f_b and f_{tb}. Since f_t is known, a two equation system for f_b and f_{tb} is formed from Eq. 5.5.23 and solved using variances $\overline{q_b' q_b'}$ and $\overline{\theta'\theta'}$ (see Moeng and Wyngaard, 1984). The scalar variances for a bottom-up process are approximated by Moeng and Wyngaard (1984) as

$$f_b = b_1 \left(\frac{z}{z_i}\right)^{-2/3}, \qquad z/z_i < 0.9 \tag{5.5.25a}$$

$$f_b = b_2 \left(\frac{z}{z_i}\right)^{-5/4}, \qquad z/z_i > 0.9 \tag{5.5.25b}$$

The constants are given by $b_1 = 1.8$ and $b_2 = 0.47$. Moeng and Wyngaard (1989) adjust this model

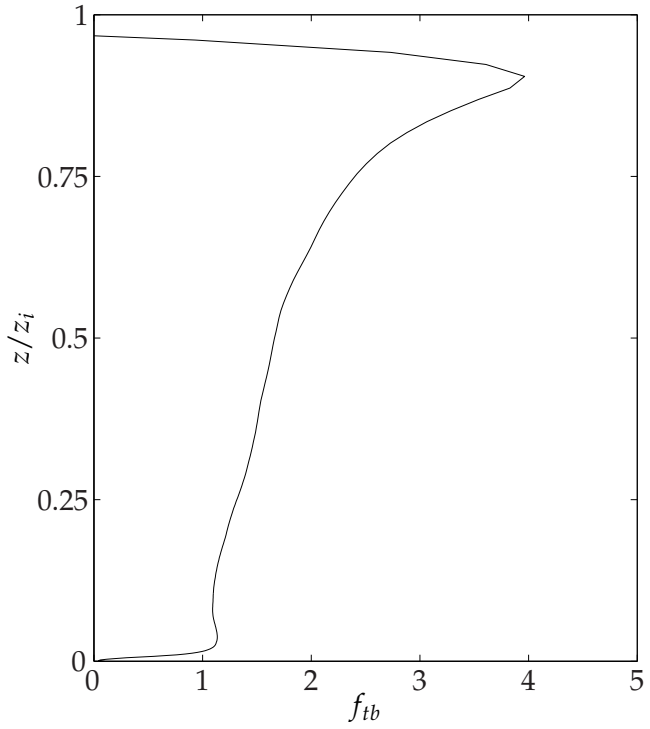

Figure 5.44: Scalar covariance: Solid line, DNS.

by changing the exponent of Eq. 5.5.25a to be -0.9. Figure 5.43 demonstrates that the piecewise function given by Eq. 5.5.25 does not correlate well with the DNS results. Instead of a two-step function, it appears that the variance is better approximated by a single relationship:

$$f_b \approx 0.91 \left(\frac{z}{z_i} \right)^{-0.95} \tag{5.5.26}$$

The exponent -0.95 is close to the modified exponent of Moeng and Wyngaard (1989) though they still employ a piecewise function to model the variance near the wall ($z/z_i < 0.1$). Not only does Eq. 5.5.26 fit our DNS for the majority of the mixed layer, there is very good agreement for $z/z_i < 0.1$ up until $z/z_i < 0.01$ where viscous effects start to dominate ($z^+ \approx 9.1$).

The covariance between the top-down and bottom-up scalars is shown in Fig. 5.44. Given the small amplitude of f_{tb} relative to the variance functions, the covariance is commonly modeled as a constant. Moeng and Wyngaard (1989) demonstrate an increase in the magnitude of f_{tb} with an increase in LES resolution. As their calculation of f_{tb} does not account for subgrid effects,

correlation is lost in subgrid scales without a fine resolution. Patton et al. (2003) utilized a nested grid LES to better resolve the wall region and found a maximum covariance of $f_{tb} \approx 4.5$ with a tree canopy and $f_{tb} \approx 4.0$ without. Our DNS results give a maximum covariance of $f_{tb} \approx 3.96$ at $z/z_i \approx 0.9$. Therefore, the smooth-wall results of this DNS, the rough-wall LES of Patton et al. (2003), Moeng and Wyngaard (1989), and Moeng and Wyngaard (1984), and the canopy results of Patton et al. (2003) show the scalar covariance may vary little with surface roughness and that small scale effects play a substantial role in f_{tb}.

5.6 Summary

Two unstably stratified simulations of the convective ABL were carried out. Case B1 was moderately heated ($-z_i/L = 5.90$) while Case B2 was initialized with much more vigorous surface heating ($-z_i/L = 50.54$). After integrating the two cases forward in time, both simulations developed a mixed layer where temperature and velocity were nearly constant.

The normal Reynolds stress scale well with the convective velocity w_*^2. Scaling of the horizontal components display a slight effect concerning the strength of stratification. The vertical Reynolds stress, however, scales well with w_*^2. Shear Reynolds stresses do not scale properly with w_*^2, and an improvement is obtained by scaling them with the friction velocity u_*^2 (especially for the streamwise shear stress $\overline{u'w'}$).

Turbulent energy budgets were computed for the velocity variance and covariance terms. For the moderately heated case, the primary source of turbulent energy near the wall is production by mean shear. Away from the wall, energy is supplied to both horizontal components via the return-to-isotropy pressure strain term. For vigorous heating, both production by mean shear and pressure strain supply energy to the streamwise energy component near the surface. Production in the spanwise direction is negligible under vigorous heating conditions. The major changes in the budgets, in comparison to those of Case A, is the production by buoyant forces that appears in

the $\overline{w'w'}$ budget. When the vertical velocity is energized in this manner, it can now act to supply energy to the horizontal components rather than simply acting as a sink (as in Case A).

A high-order closure model for the third and fourth moments of the vertical velocity and temperature was discussed. Results show that, in general, the predicted values of a_i and d_i perform sufficiently. For the third-order closures, the down-gradient diffusion term was shown to be almost negligible for the low Reynolds number cases that were analyzed. Sensitivity analyses were performed for each modeled term to determine the range of values for the constants a_i and d_i that will provide sufficient accuracy. It was found that the optimum values computed for the fourth-order moments were (in most cases) close to those predicted by Gryanik and Hartmann (2002) and Zilitinkevich et al. (1999).

Finally, two scalars were introduced into the Case B2 simulation to model top-down and bottom-up diffusion processes. The scalar q_t is a function of top-down diffusion only as a zero-gradient boundary condition is imposed at the surface. Like Wyngaard and Brost's (1984) results, the total flux of q_t is not linear but exhibits a slight curvature (which has been attributed to the deepening of the ABL). As the temperature inversion is approached, viscous flux increases and is not negligible (as it is through the mixed layer) for the low Reynolds number case presented here. The gradient function of q_t is well represented by the model of Moeng and Wyngaard (1984) except at the inversion (where the model is expected to perform poorly) and at the wall. Though resigned to a thin region, a large increase in the scalar gradient occurs as $z \rightarrow 0$. Since a pure bottom-up diffusion scalar could not be replicated, top-down effects were removed from q_b by means of the potential temperature (Moeng and Wyngaard, 1984, Piper et al., 1995). The model of Wyngaard and Brost (1984) represents the gradient for approximately the bottom half of the mixed layer (apart from the very near-wall region). The gradient function switches sign for $z/z_i > 0.6$ and is therefore not represented by the empirical fit proposed by Wyngaard and Brost (1984). If the small effects of top-down diffusion on q_b are not removed, agreement with Wyngaard and Brost's (1984) is extended to $z/z_i \approx 0.7$. The bottom-up gradient function was found to correlate very

closely with the rough-wall LES of Patton et al. (2003) without a tree canopy. Differences (notably, an increase in g_b) are resigned to a very thin layer at the lower boundary. Both the top-down and mixed scalar variances (f_t and f_{tb} respectively) show little surface roughness or Reynolds number effects in comparison with the results of Patton et al. (2003). However, a new model for the pure bottom-up scalar variance ($f_b \propto (z/z_i)^{-0.95}$) is proposed. The exponent -0.95 is close to the model of Moeng and Wyngaard (1989) who use a constant of -0.9. Here two piecewise functions of Moeng and Wyngaard (1984, 1989) are replaced with a single expression. With the new model, the variance is accurately captured from the top of the viscous sublayer to $z/z_i \approx 0.9$.

CHAPTER 6

TURBINE EFFECTS IN THE ATMOSPHERIC BOUNDARY LAYER

In this section, an analysis of the environmental effects of an array of wind turbines on nearby farmland is presented. Since the purpose of a wind turbine is to extract energy from the atmosphere, it seems logical that the flow will dramatically change as it passes through the rotor blades. This is an important realization since typically an array of turbines is employed rather than a single machine. Not only is it important to design wind farms such that the most power can be extracted from the field, turbulence that occurs as a result of passing through the turbine can increase loading on turbines downstream.

In considering the dynamics of a wind turbine wake, there are several important issues to consider. Vermeer et al. (2003) provide a great overview of both near and far wake characteristics.

(1) Extracting energy from the flow results in a velocity deficit downstream of the turbine (Chamorro and Porté-Agel, 2009). This is important since the flow must recover before interacting with the next turbine in the wind farm. Consequently, the rate at which the wake is able to re-energize directly impacts the optimal spacing between turbine hubs. Additionally, the change in mean velocity directly impacts turbulent energy production and can increase fatigue loading on structures downstream.

(2) In addition to an axial (aligned with the hub) velocity deficit, the turbine imparts an azimuthal velocity component into the wake region. Medici and Alfredsson (2006) took hot wire measurements of a scaled down wind turbine in a wind tunnel. Their results indicate

that the azimuthal velocity component can be as large as 25% of the free stream velocity. The azimuthal velocity can increase the production of turbulence causing large velocity fluctuations downstream.

(3) Tip vortices (see Fig. J-2 in Hand et al., 2001) develop at the end of each turbine blade. The spiraling vortices are propagated downstream by the mean flow and tend to increase turbulence levels as they break down (Hahm and Wußow, 2006).

Recent studies have addressed how wind farms may affect their surroundings. Keith et al. (2004) simulates how large wind farms (significant land coverage) might impact global climate. This is accomplished using two global circulation models and altering the surface drag coefficient (through either an increase in surface roughness or an explicit drag term). To determine the implications of very large scale wind power generation, Keith et al. (2004) varied wind farm coverage between 2.5% of all land surface and an extreme case where all land except Antarctica was utilized. Keith et al.'s (2004) results indicate that large scale wind farms may have an impact on global temperatures.

In a more local sense, Roy and Pacala (2004) looks at how a wind farm might affect meteorology in the immediate area. Their results show that, through generating turbulence, vertical mixing is enhanced and surface heating and drying can occur. Since the ABL is a constantly evolving system, these effects vary based on time of day.

The drying effect associated with an increase in humidity transport away from the wall is of particular interest in this study. Calaf et al. (2011) performed an LES study of a fully developed wind turbine array. For the neutrally stratified boundary layer, their results indicated an increase in surface scalar flux of a passive scalar by approximately 10–15%.

The goal of this work is to study the evolution of the wind turbine wake with an emphasis on heat and scalar transport at the surface. Using the results presented in Chap. 4 and 5 as a reference point, the present work aims to:

- Section 6.1 – introduce a new method for modeling the idealized wake of a wind farm.
- Section 6.2 – determine the extent to which DNS can be used in modeling wind farm dynamics.
- Section 6.3 – quantify the increase (or decrease) in scalar and thermal flux at the surface under neutral and unstable stratification.
- Section 6.4 – identify the mechanism(s) through which turbulence is developed in the wake and transported to other parts of the flow field.
- Section 6.5 – evaluate whether closure models which were effective in the absence of a wake will still correctly capture turbulence dynamics.

6.1 Wake Model for Wind Turbine

The flow past a wind turbine is an exceedingly difficult problem to model when all of its details are considered. To accurately capture flow and separation dynamics past each blade requires substantial meshing and resolution. Accounting for the rotation of turbine blades and the mechanical resistance of doing so requires even more sophisticated meshing routines and fluid-structure interaction models. The range of scales required to fully resolve the characteristic scales of the atmospheric boundary layer and flow over a turbine blade is outside of current computational capabilities.

While it is (currently) impossible to simulate all facets of the turbine in the ABL, the current research applies simplifications to the problem which ease the computational cost. This work will focus on two aspects of the wind turbine wake: the velocity deficit and azimuthal velocity component. Porté-Agel et al. (2010) demonstrate that LES turbine models which introduce rotation perform better than non-rotating models. The simulation will analyze the wake region only and does not directly model flow through the turbine.

Conceptually, the introduction of the wake into the flow field is quite simple. Energy is taken out of the flow as it passes through a turbine causing a momentum deficit and axial vorticity in the wake region. For the wake model used, the turbine itself will not directly impart any turbulent fluctuations onto the flow. Instead, only the mean flow feels the impact of the turbine. In mathematical terms, the velocity field immediately downstream of the rotor blades can be written as

$$u_i = U_i + u_i' + U_{i,\mathrm{t}} \tag{6.1.1}$$

where $U_{i,\mathrm{t}}$ is the velocity deficit that results from passing through the turbine. The turbulent fluctuation u' immediately downstream of the rotor are the same as the fluctuations immediately upstream.

The wake of a wind turbine is inherently three-dimensional. The cartoons shown in Fig. 6.1 demonstrate how a velocity deficit might appear from a top-down perspective. The velocity profiles are immediately downstream of a series of wind turbines that are positioned parallel to one another. Conceptually, as you place more turbines in the flow, the wakes begin to overlap until a nearly constant wake (see Fig. 6.1(d)) develops. The simulations presented here model this theoretical constant wake by enforcing periodicity across the region of velocity deficit. For a given distance from the wall, the velocity deficit $U_{i,\mathrm{t}}$ will be applied across the entire domain in the x/y plane. Consequently, the velocity deficit will be aligned with the velocity direction and be a function of z only. A limitation of this method is that the spanwise (with respect to the turbine) momentum transfer from ambient flow to the wake can not occur. This may result in a slower re-energizing of the velocity deficit.

Chamorro and Porté-Agel (2009) demonstrates that downstream of the wind turbine, the change in velocity takes on a nearly Gaussian shape. Denoting the axial component of velocity that results from the turbine as U_{ax}, the velocity deficit from the turbine is approximated as

$$U_{ax} = -\gamma_{ax} \exp\left[-\frac{(z - z_h)^2}{2\sigma^2}\right] \tag{6.1.2}$$

where γ_{ax} is the strength of the wake (given as a fraction of the geostrophic velocity U_g), z_h is

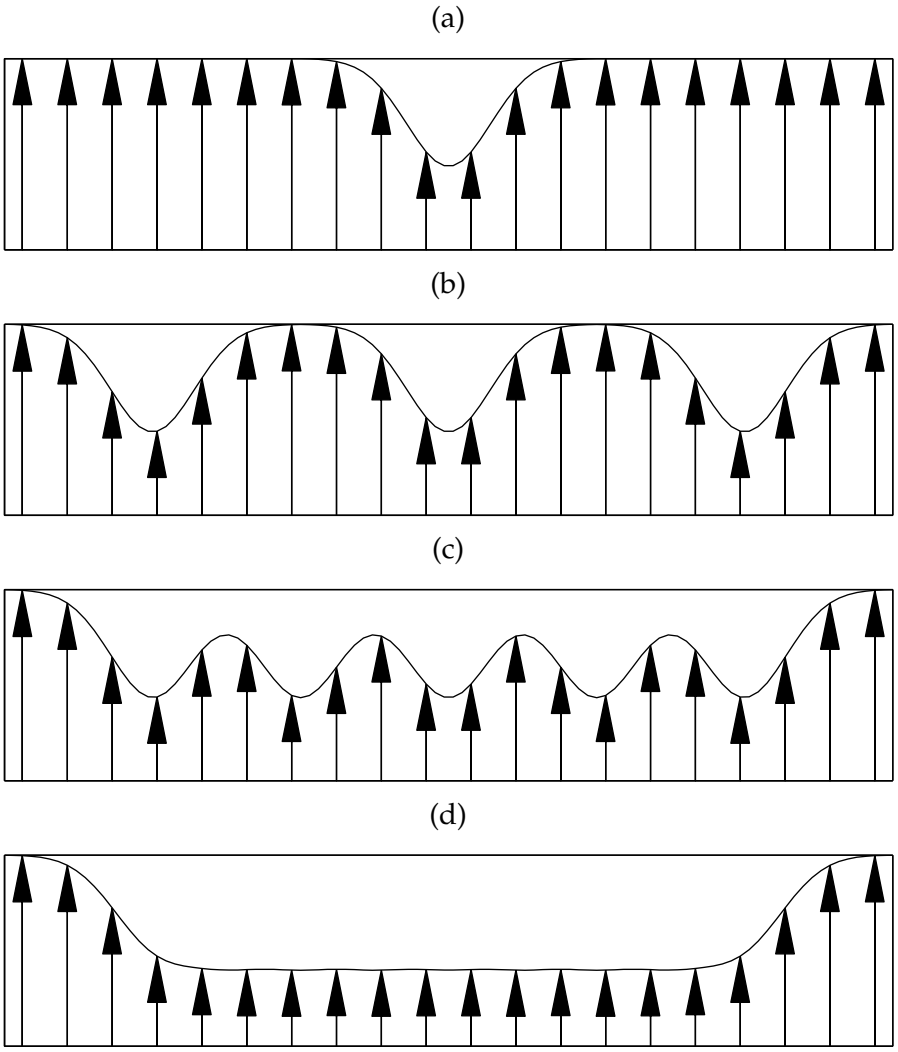

Figure 6.1: Top-down view of interacting wakes velocity field: (a) 1 wake, (b) 3 wakes, (c) 5 wakes, (d) 7 wakes.

the height of the turbine hub, and σ^2 controls the thickness of the wake. It is assumed that the velocity deficit is aligned with the mean velocity. However, this direction changes with height in the turbulent Ekman layer so the deficit is aligned with the mean velocity direction β_t. Note that the mean flow direction β_t and the shear direction β at a given distance from the wall are not coincident.

In the same manner that velocity deficit is applied over the entire domain, an azimuthal velocity component is added to mimic the rotational element of the turbine wake. The velocity distribution used for the azimuthal component (U_{az}) is given by Vatistas (2006):

$$U_{az} = \gamma_{az}\xi \left(\frac{\alpha_v + 1}{\alpha_v + \xi^4} \right)^m \tag{6.1.3}$$

where

$$\xi = \frac{z - z_h}{r_{\max}} \tag{6.1.4}$$

is the dimensionless radial coordinate and

$$m = \frac{\alpha_v + 1}{4} \tag{6.1.5}$$

The strength of the azimuthal component is controlled by γ_{az} and α_v controls the level of turbulence in the vortex core where $\alpha_v = 1$ gives a laminar profile. Vatistas (2006) shows $\alpha_v \approx 0.75$ while Maalouf et al. (2009) shows a slightly lower value ($\alpha_v \approx 0.65$) for tip vortices in a wind turbine. The radius of the vortex $r_{\max}$, controls the location at which the peak velocity occurs. Although Eq. 6.1.3 was designed for use with tip vortices, this model will be used to impose the azimuthal velocity component across the domain to mimic the rotational velocity component that occurs as flow passes through a turbine. As with U_{ax}, U_{az} will be rotated to align with the velocity direction corresponding to z_h.

Figure 6.2 demonstrates the two velocity components centered about the hub height z_h. To completely define the wake profile for this study, seven parameters must be set. In addition to the five shown in Fig. 6.2 (z_h, σ, γ_{ax}, $r_{\max}$, and γ_{az}), the turbulent parameter α_v and angle of velocity

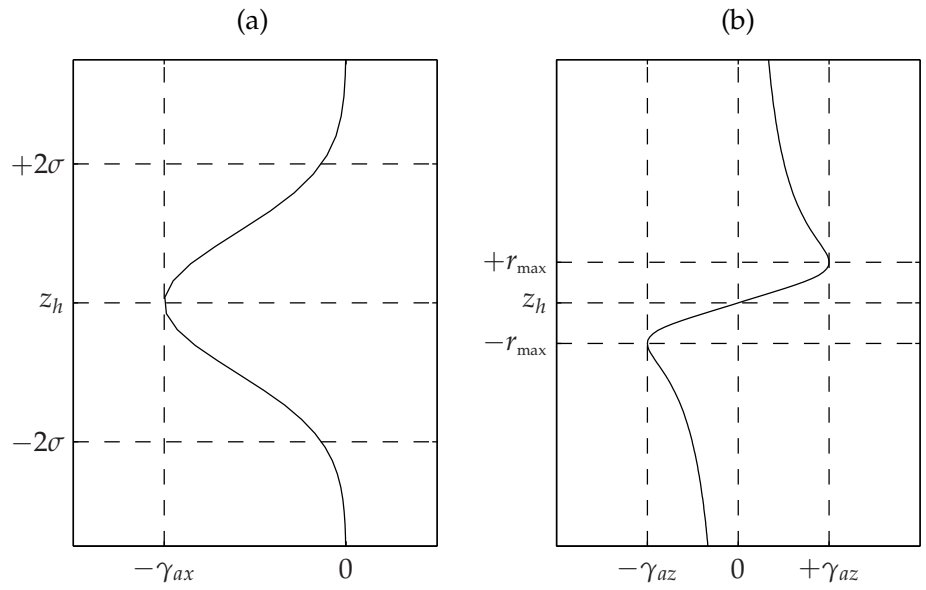

Figure 6.2: Examples of turbine velocity: (a) U_{ax}, (b) U_{az}.

rotation β_t must be specified. The rotated velocity contributions from the turbine are simply

$$u_t = U_{ax} \cos \beta_t - U_{az} \sin \beta_t \tag{6.1.6a}$$

$$v_t = U_{ax} \sin \beta_t + U_{az} \cos \beta_t \tag{6.1.6b}$$

The diameter of the turbine is taken to be

$$D = 4\sigma \tag{6.1.7}$$

Two cases will be presented with a turbine wake superimposed on the mean velocity profile. Case CN will denote the neutrally stratified boundary layer with a wake, and CH indicates the wake with surface heating. Case parameters for the each simulation are given in Table 6.1. In order to gain an insight into how stratification alone affects the results, all parameters are the same except for β_t (which is dependent upon the velocity field). Starting from a fully converged solution, the wake profile is introduced into the mean velocity field – the fluctuating velocity component is unchanged – and then allowed to evolve in time. Since the flow field is periodic, no spatial evolution will occur. Instead, the field will evolve with time as the velocity deficit is grad-

Table 6.1: Case CN & CH Simulation Parameters

Case	Init. Cond.	Re	Sc	z_h	β_t	U_{ax}	U_{az}	$r_{\max}$	α	σ
CN	A	1000	0.7336	δ_E	13.3	0.5	0.25	0.05	0.75	0.2
CH	B1	1000	0.7336	δ_E	11.0	0.5	0.25	0.05	0.75	0.2

ually recovered. Moreover, turbulence characteristics, as will be shown shortly, will drastically change because of the changes introduced to the mean velocity gradient.

From this temporal simulation it is possible to extract spatial statistics by assuming that the entire field is advected downstream at a velocity of U_g (the geostrophic velocity). Integrating the solution forward by Δt, the entire field would then be displaced a distance of

$$\Delta x = \Delta t U_g \tag{6.1.8}$$

through Taylor's hypothesis (see Pope, 1993). By performing a spatial average over the x/y plane (the angle brackets $\langle \cdot \rangle$ are used to emphasize this) at each time realization that is saved, the evolution of turbulent statistics in the geostrophic direction can be determined. Similar methods have been used in studying the effect of surface roughness on a neutral boundary layer (Lin et al., 1997), modeling the flow of warm air over cool water (Skyllingstad et al., 2005), and determining the effect of sea-surface temperature variation on surface fluxes in the marine ABL (Skyllingstad et al., 2007).

6.1.1 Overview of Case CN

The neutrally stratified wake simulation was started from the Case A simulation. A passive scalar q was initialized in the field with a Dirichlet condition $q_0 = 0.01$ at the wall. The outer boundary condition has a zero gradient (i.e. $\partial q/\partial z = 0$) with an initial value of $q = 0.001$. These initial values for the scalar flux were chosen as they are close to values of specific humidity that would be encountered in the atmospheric boundary layer (Mahrt, 1976).

As with the unstably stratified simulations presented in Chap. 5, a steady-state will not be

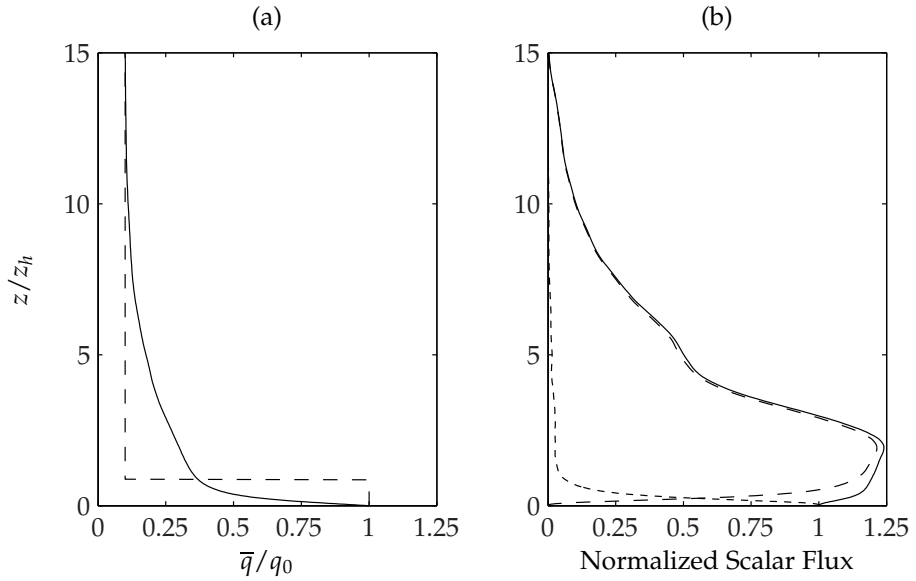

Figure 6.3: Case CN Mean distribution of q (a): solid, DNS; dashed, initial condition. Normalized turbulent and viscous flux (b): solid, total flux; dashed, turbulent flux; dotted, viscous flux.

reached for the passive scalar. Instead, the flow was integrated until initial transients in the scalar flux profile are eliminated. The distribution of $\overline{q}$ after integrating forward in time (as well as the initial profile) is shown for Case CN in Fig. 6.3(a). An averaged scalar flux profile (after allowing initial transients to die out) for Case CN is shown in Fig. 6.3(b). Note that the contribution from both the viscous and turbulent fluxes are shown and have been normalized by the surface flux. Both figures use an averaging window of $tf = 0.02$ using 10 iterations. In general, time averaging periods for the results presented in this chapter will be short due to the transient nature of the problem.

In Fig. 6.3 the vertical axis has been normalized by z_h, the height at which turbine wake will be centered. In both cases, z_h is set to be $z_h = \delta_E$. In comparison to the total depth of the atmospheric boundary layer, the height of the wind farm is small. Since q is a passive scalar for Case CN, the introduction of q into the flow field will not change the characteristics of turbulence. Therefore, the results from Chap. 4 can be used as a baseline for determining wind farm effects.

Based on the last iteration of Case A, the wake is rotated $\beta_t = 13.3^\circ$ with respect to the geostrophic velocity. This will align U_{ax} with the local mean velocity direction at z_h.

6.1.2 Overview of Case CH

Case CH is restarted from Case B1, the unstably-stratified simulation presented in Chap. 5. The initial distribution and boundary conditions of the scalar q are identical to the neutrally stratified case. However, in Case CH, q is an active scalar and is incorporated into the vertical momentum equation by Eq. 2.4.1e. Given the small amplitude of q in comparison to θ in Case B1, the effects of specific humidity will be small in comparison to those of potential temperature. Since Sc and Pr change between Case B1 and Case CH, the simulation was integrated forward until transients had died out before initializing the wake profile.

As with Case CN, the unstably stratified wake simulation has $z_h = \delta_E$. This leads to a ratio of $z_i/z_h \approx 8.59$. Typically the ABL is $1-2$ kilometers in height while the hub of a wind turbine can be as high as 100 meters. Thus, actual wind turbines in the convective ABL have a ratio of $z_i/z_h \approx 10-20$. The ratio from the DNS is close to these values of actual atmospheric conditions though on the low side. The angle which U_{ax} and U_{az} are rotated changes slightly between Case CN and CH. For the unstably stratified case, $\beta_t = 11^\circ$.

Despite the change in the magnitude of the scalar concentration, the distribution of $\overline{q}$ with z is nearly identical in shape to the bottom-up scalars presented in §5.5.2. Figure 6.4(a) shows the initial scalar distribution and an average result immediately before initializing the wake (computed using only 8 time realizations). The normalized scalar flux shown in Fig. 6.4(b) displays a kink near $z/z_h \approx 4$ which is not seen in the earlier results from Case B1 (Fig. 5.37). This is likely a result of the short integration time used.

The temperature profile was restarted from Case B1 and is nearly identical to Fig. 5.4. Since the field has been integrated longer, the mixed layer is slightly warmer.

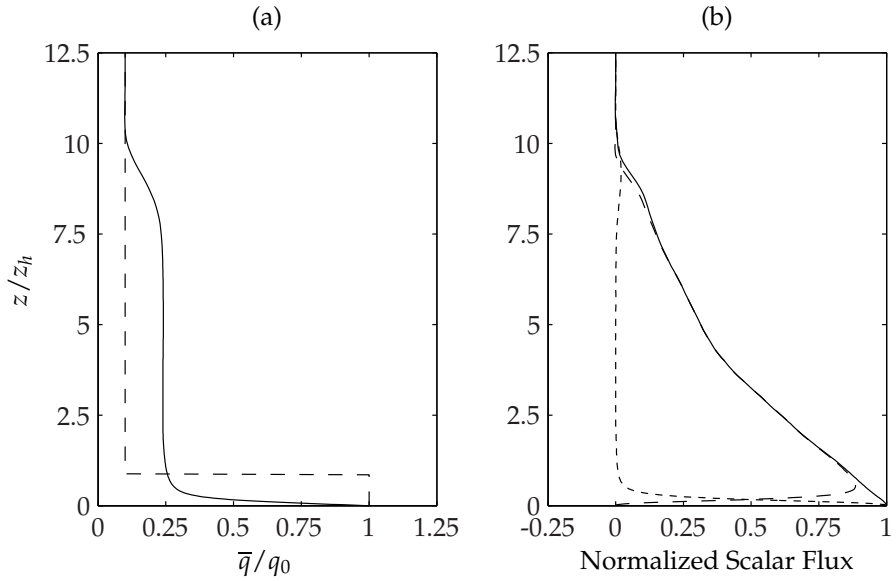

Figure 6.4: Case CH Mean distribution of q (a): solid, DNS; dashed, initial condition. Normalized turbulent and viscous flux (b): solid, total flux; dashed, turbulent flux; dotted, viscous flux.

6.2 Comparison between DNS and other results

Here the results from the DNS are compared against other wind tunnel and simulation data. This will assist in validating the method of modeling a wind farm in the manner described in the previous section.

To determine the exact influence of the wake, both cases were continued from their initial starting condition without introducing the wake. Direct effects of the wake profile are then assumed to be additive:

$$\text{effects of wake} = \text{data with wake} - \text{data without wake} \tag{6.2.1}$$

This simple relationship can be applied to all statistics including mean velocity components, scalar flux profiles, and kinetic energy budgets. To differentiate between data with a wake, without a wake, and the difference between the two, the subscripts 'ww' (with wake), 'nw' (no wake), and 'Δ' (difference) will be used in this chapter. As an example, for some arbitrary variable a, Eq. 6.2.1 can be written as $a_\Delta = a_{ww} - a_{nw}$.

Case CN

The streamwise and spanwise velocity profiles for 4 locations downstream are shown in Fig. 6.5 for Case CN. Comparison of the streamwise velocity distributions in Fig. 6.5(a) with the neutrally-stratified wind tunnel measurements of Wu and Porté-Agel (2011) shows qualitative agreement. As the flow progresses downstream (or, with time in the DNS), the wake spreads as momentum is transferred towards the region of maximum deficit. The spanwise component is dominated by the azimuthal velocity component. The sharpest velocity gradient occurs at z_h and is heavily suppressed as the flow travels downstream. Moreover, the local minimum in $\langle v \rangle_{ww}$ is moved closer to the wall and the maximum is transfered upwards. While the location of the velocity deficit in $\langle u \rangle_{ww}$ does not move, the peaks in velocity in $\langle v \rangle_{ww}$ are translated away from the hub. The distance from z_h at which the maximum in the azimuthal velocity occurs is found to be slightly smaller than the wind tunnel data of Medici and Alfredsson (2006). Moreover, at $\Delta x/D = 1$ their results show a sharper drop-off of the azimuthal velocity outside of $z_h \pm D/2$.

Another means of visualizing the data presented in Fig. 6.5 is demonstrated in Fig. 6.6. In this figure, subplot (a) refers to the streamwise component $\langle u \rangle_{ww}$ while (b) gives the spanwise velocity $\langle v \rangle_{ww}$. Negative values of x/D indicate flow upstream of the imposed wind farm wake. Since β_t is small (see Table 6.1), the velocity deficit is primarily seen in $\langle u \rangle_{ww}$. These results, then, are comparable to the wind tunnel experiments of Chamorro and Porté-Agel (2010) and show that high momentum fluid does not start being transported back towards the wall immediately. Instead, after about 5 turbine diameters, the velocity deficit tends to angle downwards as momentum is transported towards the wall. The center of the vertex in the spanwise direction starts at $z = z_h$. As flow progresses, the vortex center appears to be transported away from the wall.

In Fig. 6.7 the mean velocity profile without the wake profile is subtracted from the simulation with a wake. The largest initial changes occur in the $\langle v \rangle_{\Delta}$ component as the peaks in the azimuthal velocity are quickly suppressed. The streamwise deficit remains nearly Gaussian as the wake develops. This matches the results of Chamorro and Porté-Agel (2009) where it is demon-

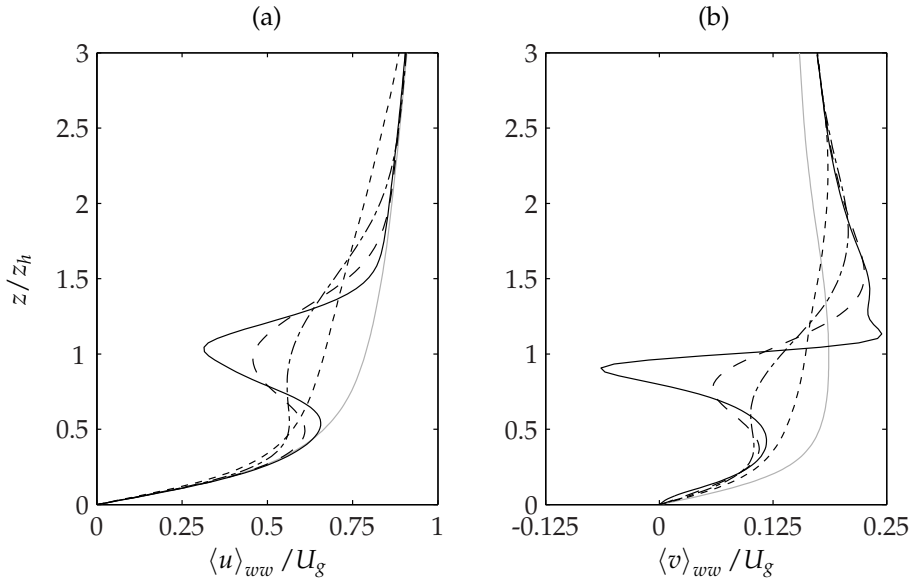

Figure 6.5: Case CN velocity distribution: (a) $\langle u \rangle_{ww}$, (b) $\langle v \rangle_{ww}$. Gray, initial condition without wake; solid, $\Delta x/D = 1.25$; dashed, $\Delta x/D = 6.25$; dash-dot, $\Delta x/D = 12.5$; dotted, $\Delta x/D = 31.25$.

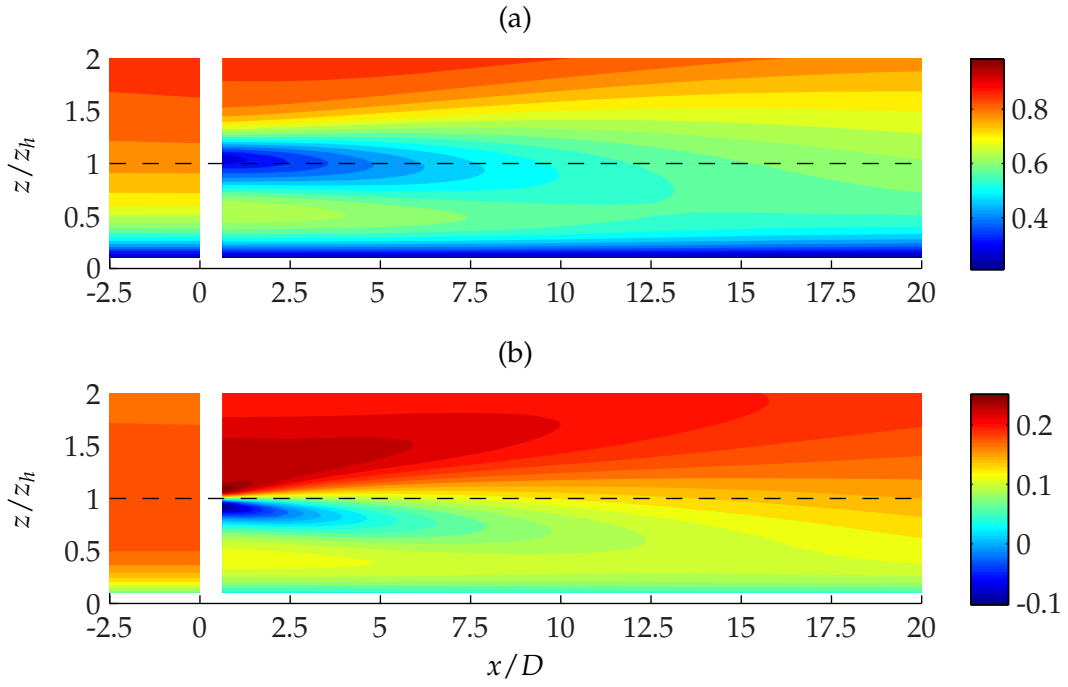

Figure 6.6: Case CN velocity contours downstream of wind farm: (a) $\langle u \rangle_{ww}$, (b) $\langle v \rangle_{ww}$. Dashed line indicates $z = z_h$. Colorbar is in units of U_g^{-1}.

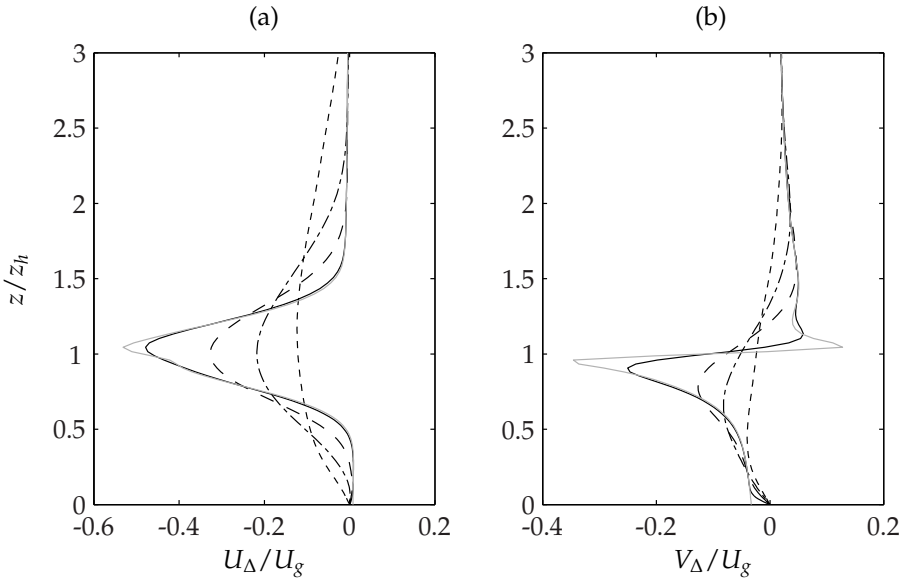

Figure 6.7: Evolution of mean turbine wake velocity: (a) $\langle u \rangle_\Delta$, (b) $\langle v \rangle_\Delta$. Gray, initial wake distribution; solid, $\Delta x/D = 1.25$; dashed, $\Delta x/D = 6.25$; dash-dot, $\Delta x/D = 12.5$; dotted, $\Delta x/D = 31.25$.

strated that the Gaussian profile is maintained until $5D$ downstream of the turbine. After this, the distribution is skewed such that the velocity deficit is not symmetric about the turbine axis. Instead, the data in Fig. 6.7(a) and data of Chamorro and Porté-Agel (2009) both show more gradual return to the unperturbed solution above the turbine hub.

Reynolds stresses are shown in Fig. 6.8. The streamwise stress component in Fig. 6.8(a) shows an increase in energy for $z > z_h$ and a decrease when $z < z_h$. This agrees with the wind tunnel tests of Chamorro and Porté-Agel (2010). However, the position downstream at which the flow begins to recover is greater in Case CN than in the wind tunnel tests. This is likely a consequence of the 'slab' wake that is being modeled in the current simulation. Momentum and energy transport are limited to the vertical direction in the current DNS, whereas energy transport in the wind tunnel is three-dimensional. The minimum in energy located at $z/z_h \approx 0.5$ occurs at $x/D \approx 18$. Chamorro and Porté-Agel (2010) shows a similar feature at $x/D \approx 7$. Although the distance downstream of the events is off by over a factor of 2, the qualitative agreement in the results is promising. Since the specification of $D = 4\sigma$ is somewhat arbitrary, it is

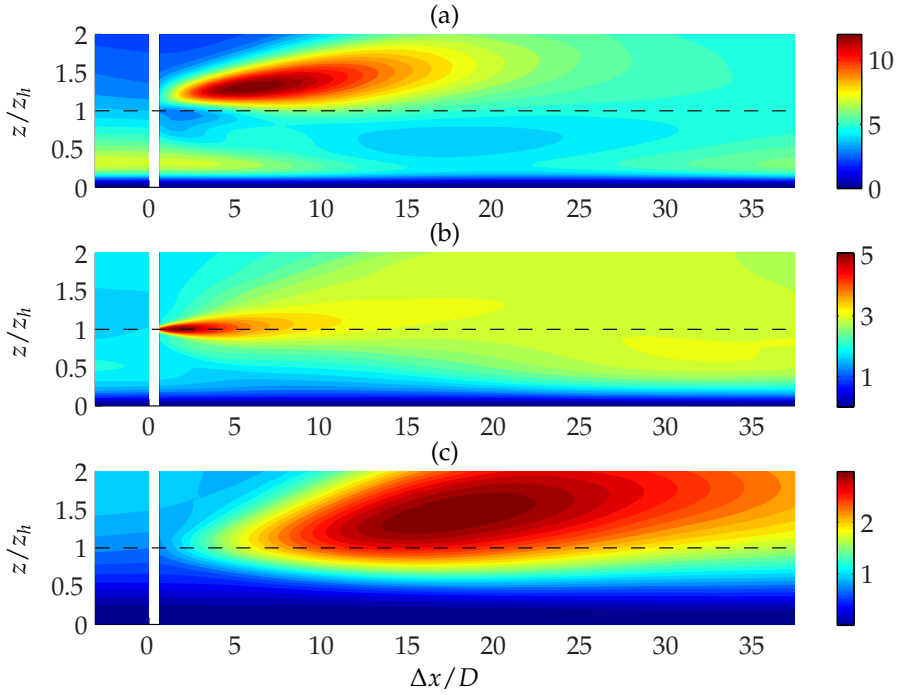

Figure 6.8: Normal Reynolds stresses for Case CN: (a) $\langle u'u' \rangle_{ww}$, (b) $\langle v'v' \rangle_{ww}$, (c) $\langle w'w' \rangle_{ww}$. Dashed line indicates $z = z_h$. Colorbar is in units of u_*^{-2} (see Case A data in Table 4.2).

possible that choosing $D = 8\sigma$ would give better scaling between wind tunnel tests and the DNS data. Regardless, the qualitative agreement between the simulation and experiment is good. The spanwise Reynolds stress (subplot (b)) quickly picks up energy due to the sharp gradient in the wake profile. As the gradient is attenuated, turbulent energy rapidly drops off and is transported to other regions of the domain.

The contours of $\langle w'w' \rangle_{ww}$ in Fig. 6.8(c) are different from the in-plane components. The energy in the x and y directions grows as a direct consequence of the change in production that results from modifying the mean flow (see §6.4). The vertical Reynolds stress, however, shows a growth in energy where the peak occurs much further downstream (at $x/D \approx 17$). Furthermore, even though the primary stress $\langle u'u' \rangle_{ww}$ has a local minimum between $15 < x/D < 20$, the maximum in the vertical stress occurs at the same location and no reduction in magnitude is evident throughout the domain.

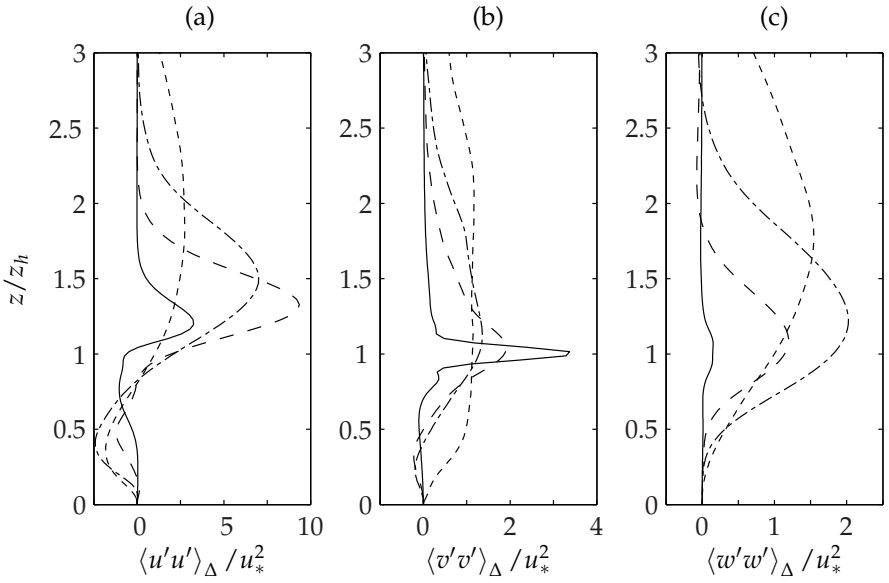

Figure 6.9: Change in normal Reynolds stresses for Case CN: (a) $\langle u'u' \rangle_\Delta$, (b) $\langle v'v' \rangle_\Delta$, (c) $\langle w'w' \rangle_\Delta$. Solid, $\Delta x/D = 1.25$; dashed, $\Delta x/D = 6.25$; dash-dot, $\Delta x/D = 12.5$; dotted, $\Delta x/D = 31.25$. All terms have been normalized by u_*^2 given for Case A in Table 4.2.

Changes resulting from the wake are clearly seen in Fig. 6.9 where the difference between the wake and no-wake simulations is shown. The decrease in the streamwise energy component is clearly indicated below z_h. The sharp increase in $\langle v'v' \rangle_\Delta$ at $\Delta x/D = 1.25$ is quickly spread across the boundary layer. Far downstream, the spanwise Reynolds stress is well mixed for $0.5 \leq z/z_h \leq 2.25$. In Fig. 6.9(c) the delay in the accumulation of energy in the vertical direction is clearly evident. Only after the two horizontal components are established does $\langle w'w' \rangle_\Delta$ pick up energy. The peak in energy (which begins at a height of z_h) is slowly transported away from the wall.

Reynolds shear stresses are shown in Fig. 6.10. The stress $-\langle u'w' \rangle_{ww}$ clearly shows a negative region below z_h and a positive region above. This indicates high momentum fluid is being transported towards z_h to re-energize the velocity deficit. However, the region where $-\langle u'w' \rangle_{ww} < 0$ ends at $z/z_h \approx 12.5$. After this, the covariance is positive everywhere indicating high momentum fluid is transported downwards from above the wake. This is an important realization: in the case where the wake is two-dimensional and wall-bounded, the velocity deficit is

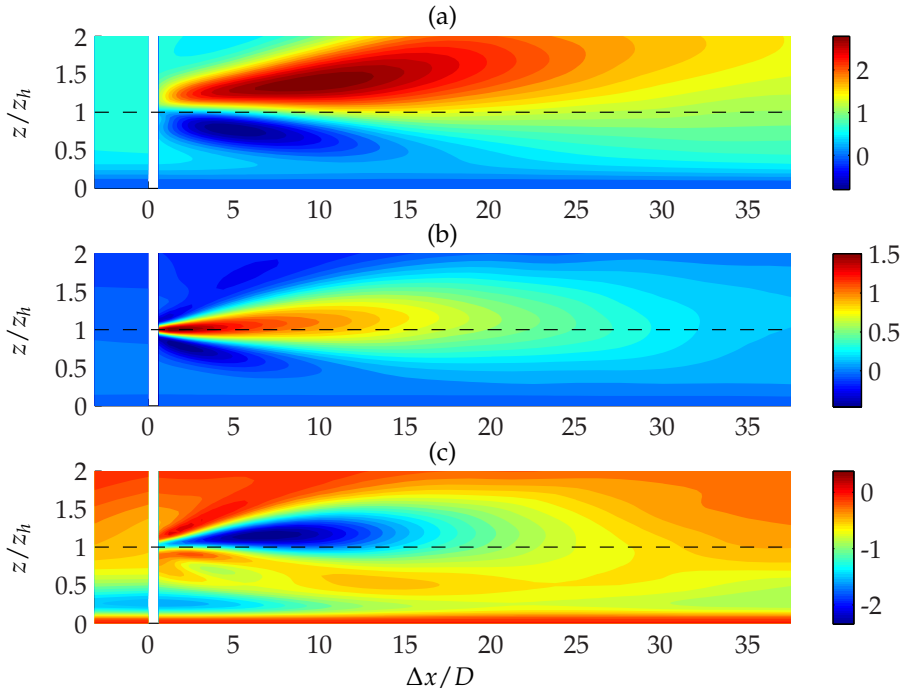

Figure 6.10: Shear Reynolds stresses for Case CN: (a) $-\langle u'w'\rangle_{ww}$, (b) $-\langle v'w'\rangle_{ww}$, (c) $-\langle u'v'\rangle_{ww}$. Dashed line indicates $z = z_h$. Colorbar is in units of u_*^{-2} (see Case A data in Table 4.2).

re-energized by the transport of momentum from the free-stream towards the wall. Similar behavior is seen by Chamorro and Porté-Agel (2009, 2010). The term $-\langle v'w'\rangle_{ww}$ is also heavily modified because of the wake. A region where $-\langle v'w'\rangle_{ww} > 0$ starts as a narrow band at z_h and expands downstream. For $x/D > 20$, the positive region appears to remain nearly constant in height and gradually decreases in magnitude.

The difference in shear stress plotted in Fig. 6.11 confirms the above findings except that the location of at which $-\langle u'w'\rangle_{\Delta} > 0$ for all z is further downstream than is evident in Fig. 6.10. Additionally, Fig 6.11(c) shows that the wake does have a noticeable effect on $-\langle u'v'\rangle_{\Delta}$. This shear component increases for $z/z_h < 1$ and tends to decrease above the hub height. Referring to Eq. 4.3.1, an increase in $-\langle u'v'\rangle_{\Delta}$ promotes transport from $\overline{u'u'}$ to $\overline{v'v'}$. A decrease in $-\langle u'v'\rangle_{\Delta}$ encourages energy to be transferred the other direction.

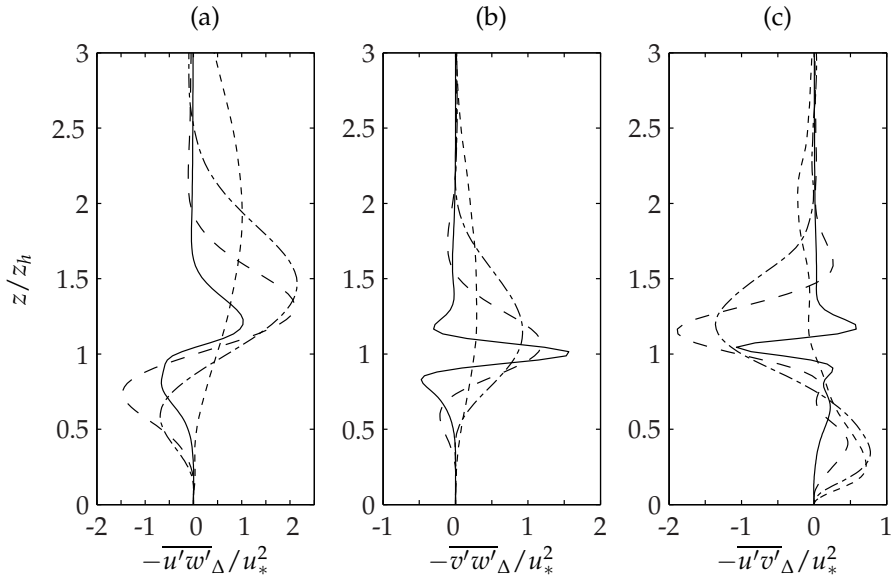

Figure 6.11: Change in shear Reynolds stresses for Case CN: (a) $-\langle u'w'\rangle_\Delta$, (b) $-\langle v'w'\rangle_\Delta$, (c) $-\langle u'v'\rangle_\Delta$. Solid, $\Delta x/D = 1.25$; dashed, $\Delta x/D = 6.25$; dash-dot, $\Delta x/D = 12.5$; dotted, $\Delta x/D = 31.25$. All terms have been normalized by u_*^2 given for Case A in Table 4.2.

Case CH

In contrast to the neutrally stratified wake simulation, Case CH incorporates surface heating which generates a mixed layer. The velocity profiles for the Case CH simulation are shown in Fig. 6.12. In comparison with the neutral results in Fig. 6.5, the heated case tends to re-energize the wake (or spread) at a faster rate than the neutral results. This is a direct consequence of the heating. Buoyant plumes already tend to mix the velocity prior to introducing the wake.

Viewing the velocity as a contour map (Fig. 6.13) shows the same results: the velocity deficit recovers quicker with surface heating. Additionally, Fig. 6.13(a) shows that the maximum deficit in $\langle u\rangle_{ww}$ tends to get transfered towards the wall much earlier than Case CN.

The horizontally averaged Reynolds stresses are shown in Fig. 6.14 as the simulation progresses through time (space). In several aspects the results from Case CH share characteristics of those from Case CN. Streamwise energy is produced for $z > z_h$ and destroyed when $z < z_h$. However, the peak in turbulence occurs much earlier at $x/D \approx 2.5$ ($x/D \approx 5$ for Case CN). The

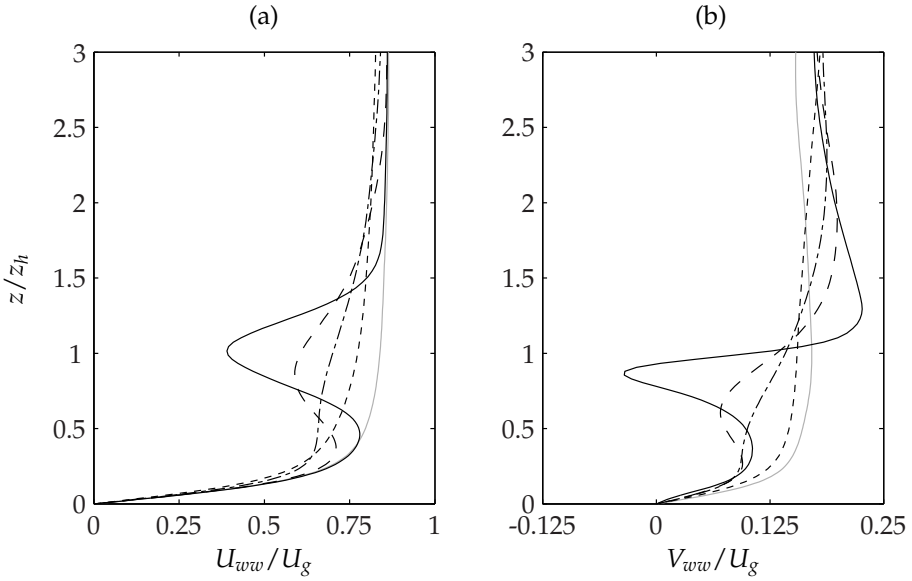

Figure 6.12: Case CH velocity distribution: (a) $\langle u \rangle_{ww}$, (b) $\langle v \rangle_{ww}$. Gray, initial condition without wake; solid, $\Delta x/D = 1.25$; dashed, $\Delta x/D = 6.25$; dash-dot, $\Delta x/D = 12.5$; dotted, $\Delta x/D = 31.25$.

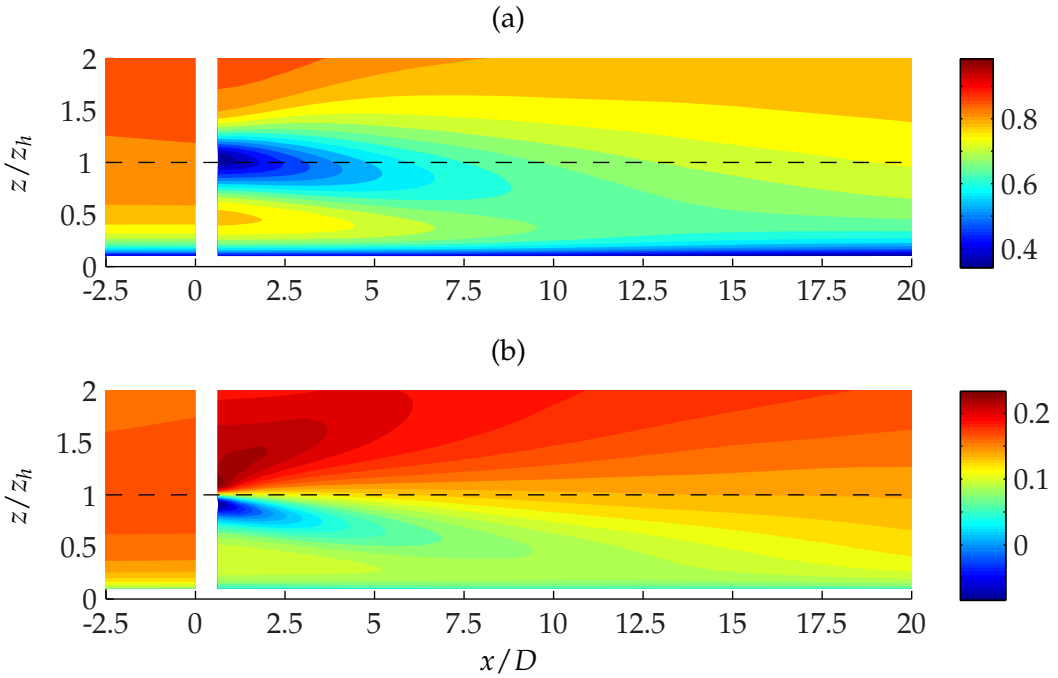

Figure 6.13: Case CH velocity contours downstream of wind farm: (a) $\langle u \rangle_{ww}$, (b) $\langle v \rangle_{ww}$. Dashed line indicates $z = z_h$. Colorbar is in units of U_g^{-1}.

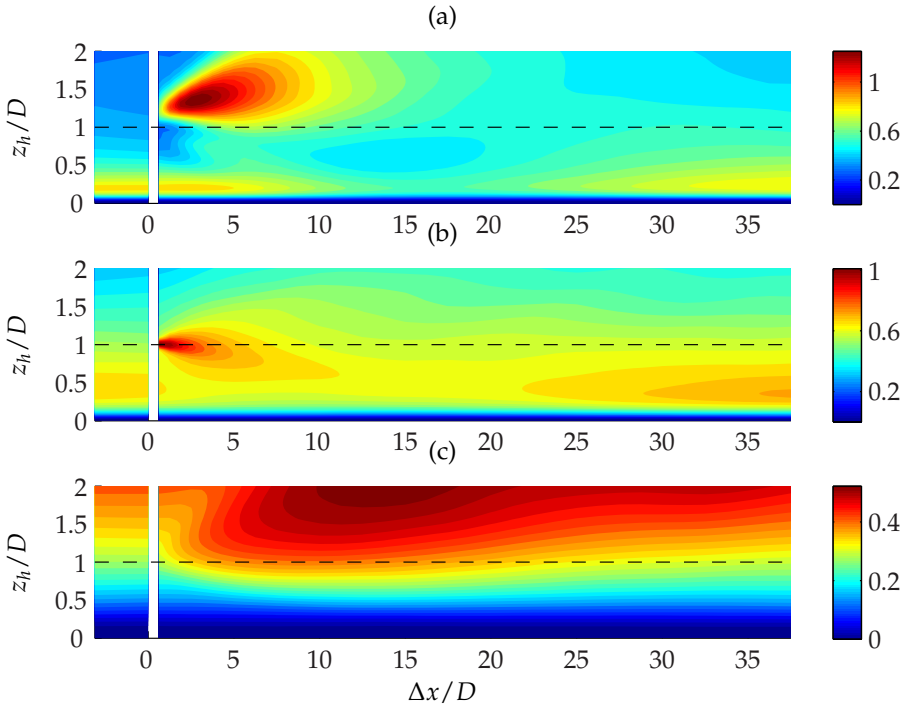

Figure 6.14: Normal Reynolds stresses for Case CH: (a) $\langle u'u' \rangle_{ww}$, (b) $\langle v'v' \rangle_{ww}$, (c) $\langle w'w' \rangle_{ww}$. Dashed line indicates $z = z_h$. Colorbar is in units of w_*^{-2} (see Case B1 data in Table 5.2).

spanwise Reynolds stress grows quickly behind the turbine but is then transported towards the wall as seen in subplot (b). The results from Case CN show a different result; in the neutrally stratified case the maximum in the spanwise Reynolds stress is carried away from the wall up until $x/D \approx 20$. The upstream values of $\langle w'w' \rangle_{ww}$ are much larger in Case CH than those of Case CN. Thus, the increase in the vertical energy component is less dramatic for the results in Fig. 6.14(c) than those in 6.8(c). Moreover, the maximum in the neutral case is closer to the wall than in the unstable case.

Looking at the difference in Reynolds stress between the wake and no-wake results shows similar characteristics of the neutrally stratified case. In Fig. 6.15(a) there is quicker growth of the Reynolds stress for $z > z_h$. The relative increase in $-\overline{u'w'}$ for the unstable case in comparison to the neutral simulation is likely responsible (see Fig. 4.11 and 5.9). The minimum of $\langle u'u' \rangle_\Delta$ is about the same magnitude for both cases, though the extrema occurs closer to the wall for the

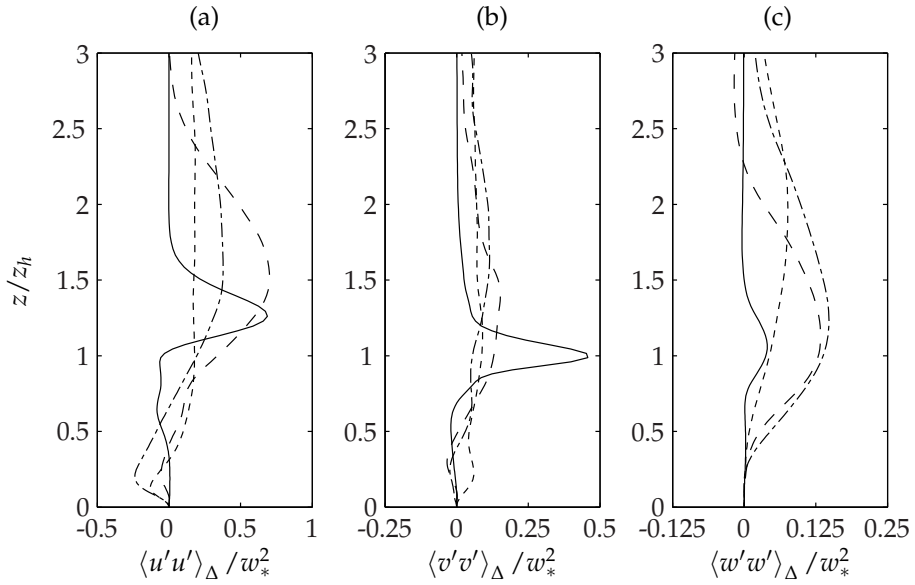

Figure 6.15: Change in normal Reynolds stresses for Case CH: (a) $\langle u'u' \rangle_\Delta$, (b) $\langle v'v' \rangle_\Delta$, (c) $\langle w'w' \rangle_\Delta$. Solid, $\Delta x/D = 1.25$; dashed, $\Delta x/D = 6.25$; dash-dot, $\Delta x/D = 12.5$; dotted, $\Delta x/D = 31.25$. All terms have been normalized by w_*^2 given for Case B1 in Table 5.2.

unstable case. Far downstream (dotted line in Fig. 6.15(a)), the excess in Reynolds stress becomes well mixed for $z/z_h > 0.5$.

The spanwise Reynolds stress increases rapidly immediately after the turbine is imposed; at $\Delta x/D = 1.25$, the magnitude of the stress in Fig. 6.15 is greater than the corresponding Case CN results. However, the energy is quickly distributed vertically and a uniform increase in $\langle v'v' \rangle_\Delta$ is apparent between $0.2 < z/z_h < 3$.

The results shown in Fig. 6.14(c) are somewhat misleading. It appears that the largest increase in $\langle w'w' \rangle_{ww}$ occurs well above z_h. Because of the large magnitude of the stress upstream of the turbine due to surface heating, however, the relative increase in the vertical energy is more difficult to visualize. Figure 6.15 clearly shows that the point where $\langle w'w' \rangle_\Delta$ is a maximum occurs just above z_h. As the flow evolves the maximum slowly translates upwards at a slow rate. Comparing the unstable and neutral results, the magnitude of change in vertical energy between the two cases are comparable. Energy is transferred to the vertical component quicker due to a faster growth rate in the horizontal energy components.

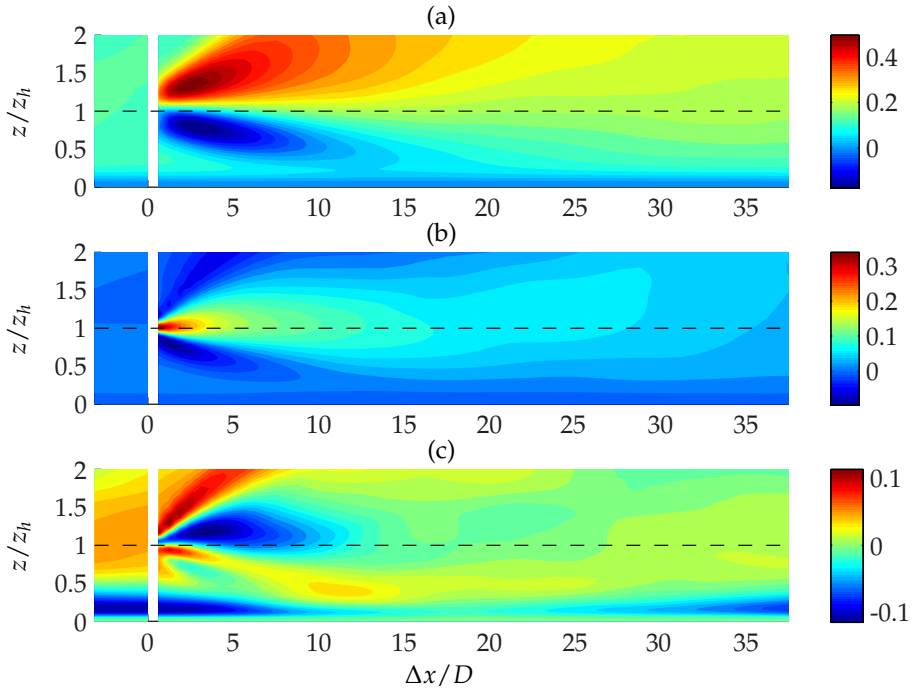

Figure 6.16: Shear Reynolds stresses for Case CH: (a) $-\langle u'w'\rangle_{ww}$, (b) $-\langle v'w'\rangle_{ww}$, (c) $-\langle u'v'\rangle_{ww}$. Dashed line indicates $z = z_h$. Colorbar in units of w_*^{-2} (see Case B1 data in Table 5.2).

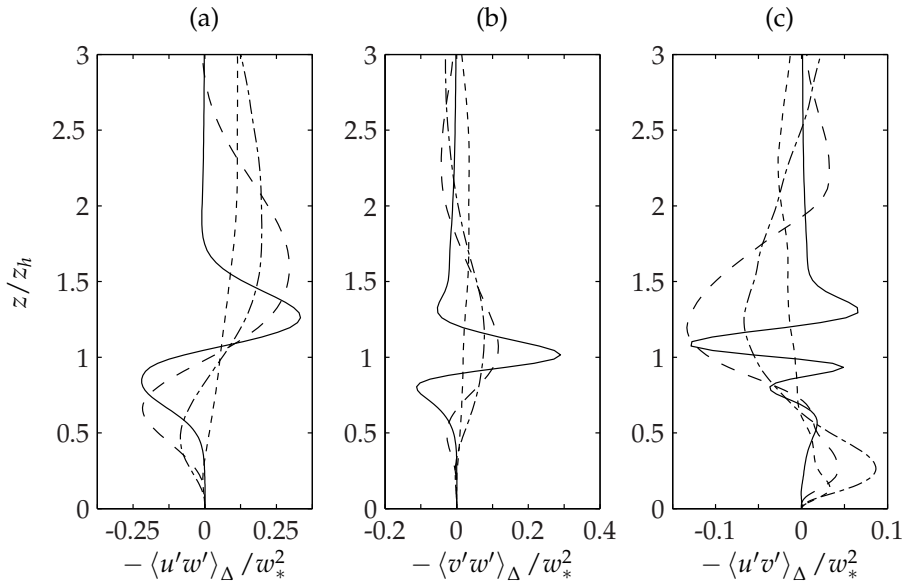

Figure 6.17: Change in shear Reynolds stresses for Case CH: (a) $-\langle u'w'\rangle_\Delta$, (b) $-\langle v'w'\rangle_\Delta$, (c) $-\langle u'v'\rangle_\Delta$. Solid, $\Delta x/D = 1.25$; dashed, $\Delta x/D = 6.25$; dash-dot, $\Delta x/D = 12.5$; dotted, $\Delta x/D = 31.25$. All terms have been normalized by w_*^2 given for Case B1 in Table 5.2.

Figure 6.16 shows the evolution of the shear Reynolds stresses in the turbulent wake. The unstable results mimic the behavior of the neutrally stratified case quite closely for all three components. The most notable difference is the speed in which the simulation returns to its natural (no wake) state. Under neutral stratification (Fig. 6.10) the flow features are stretched much further downstream than the corresponding unstable data. Since the turbulent time scale is shorter under unstable stratification, the time it takes for mixing to occur should be smaller. This is plainly seen in Fig. 6.17. Although the behavior of the Reynolds shear stresses is qualitatively the same, results from the heated case show enhanced mixing as sharp features are blended in the vertical direction.

The neutral case takes a longer time to spread the wake than the unstable case. This is due, in part, to the fact that Case CH already has enhanced vertical mixing because of the hot surface. The mixing necessary to spread the wake in Case CN must rely on the less vigorous turbulence found in the neutral Ekman layer, and turbulence that is generated by the wake itself. Since turbulence is not immediately generated, a delayed response occurs as turbulent fluctuations are enhanced.

6.3 Effect of Wake on Thermal and Scalar Flux

In §6.2 it was demonstrated that spatially averaged results from the DNS show qualitative agreement with wind tunnel results in the wake of a single turbine. With this in mind, attention is now turned towards scalar and thermal flux in the vicinity of the wake.

Case CN

The concentration of scalar q changes with time in the neutrally stratified turbulent Ekman layer. As time progresses, the scalar becomes more mixed and the concentration will increase throughout the boundary layer. In order to determine the effect of adding the wind farm wake into the simulation, the difference between the unperturbed solution and the wake field (the Δ variables) will be focused on.

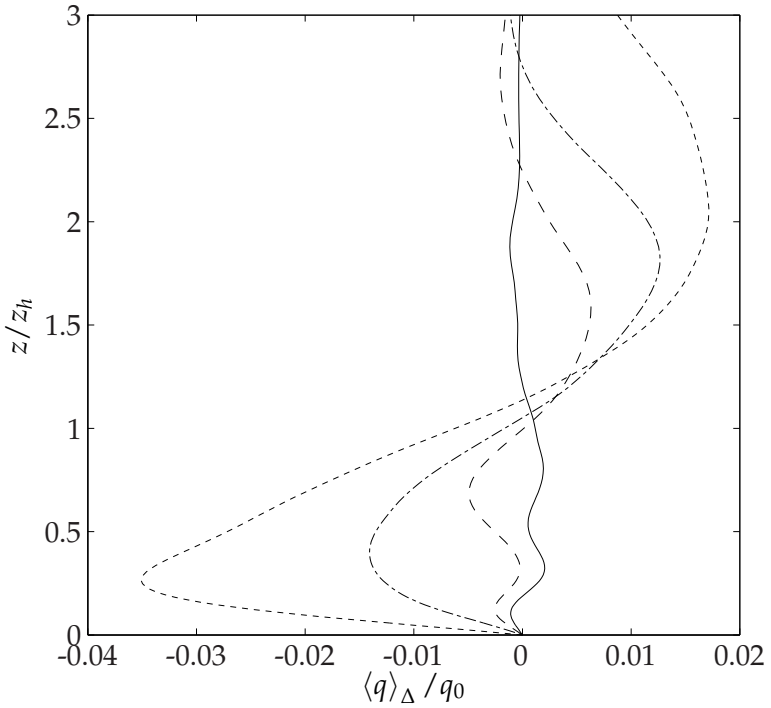

Figure 6.18: Change in scalar concentration for Case CN. Solid, $\Delta x/D = 6.25$; dashed, $\Delta x/D = 12.5$; dash-dot, $\Delta x/D = 18.75$; dotted, $\Delta x/D = 31.25$. Results have been normalized by the surface scalar concentration $q_0 = 0.01$.

The change in scalar concentration $\langle q \rangle_\Delta / q_0$ (where q_0 is the surface concentration) is shown in Fig. 6.18. As early as $\Delta x/D = 12.5$ the concentration of $\langle q \rangle_{ww}$ drops below that of $\langle q \rangle_{nw}$ for $z < z_h$ (i.e. negative value of $\langle q \rangle_\Delta$). Increasing $\Delta x/D$ further decreases the concentration of the scalar below the hub. It appears that q is transported upwards given the surplus of $\langle q \rangle_\Delta$ that is evident when $z > z_h$. The scalar concentration can significantly change (a few percentage points of the surface value) below z_h as a direct consequence of the wind farm wake.

Given the presence of a scalar deficit below z_h and a surplus above, it is likely that the scalar flux profile will show an increase over the majority of the wake region. This will be indicative of the transport of high scalar concentrations upwards and low concentrations towards the wall. The changes in viscous and turbulent flux downstream of the turbine are shown in Fig. 6.19(a) and (b) respectively. In both plots, the flux has been normalized by the surface scalar flux without a wake: $Q_{q,0,nw}$. If the scalar flux were to not deviate from the no-wake simulation, the data should

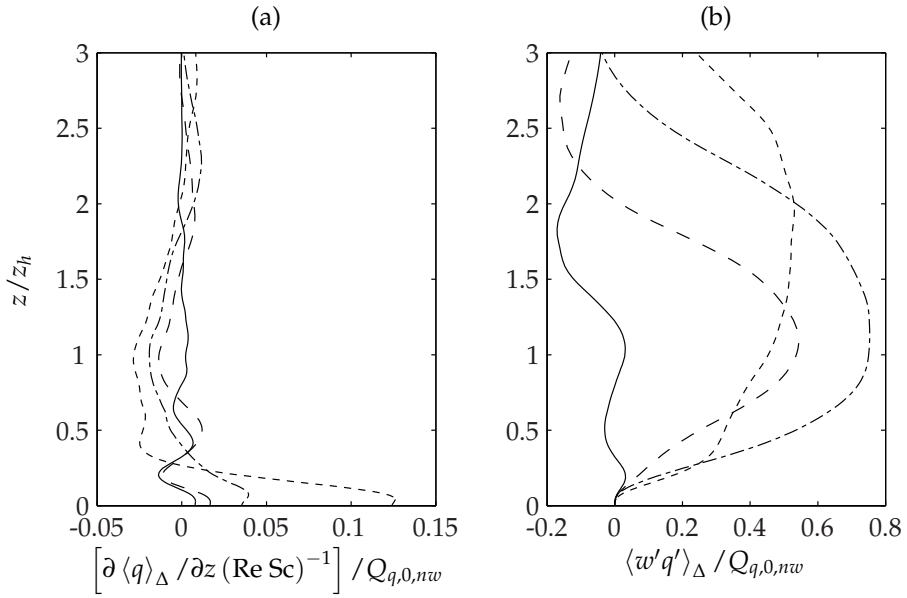

Figure 6.19: Change in scalar flux for Case CN: (a) viscous flux, (b) turbulent flux. Solid, $\Delta x/D = 6.25$; dashed, $\Delta x/D = 12.5$; dash-dot, $\Delta x/D = 18.75$; dotted, $\Delta x/D = 31.25$. Results have been normalized by the surface viscous flux of the no wake simulation at the corresponding integration time (or $\Delta x/D$).

be zero for all z. However, the results show an increase of over 10% in the viscous flux at the wall and almost 80% in the turbulent flux near the hub height. Calaf et al. (2011) perform an LES of a wind turbine array and also show significant increases in the vertical scalar transport. The findings shown in Fig. 6.19 confirm their results and offer insight into how scalar transport might evolve as a wake is spreading behind a wind turbine.

The viscous scalar flux at the wall is shown as a function of $\Delta x/D$ in Fig. 6.20. The flux at the wall gradually increases until approximately $15 < \Delta x/D < 20$ where the transfer of q increases drastically. This location corresponds to the minimum that occurs in the streamwise energy term and the maximum in the vertical stress component (see Fig. 6.8(a) and (c) respectively). Increasing $\langle w'w' \rangle$ causes q to be transported away from the wall by enhancing mixing the z direction. This, in turn, decreases the concentration of q near the surface (see Fig. 6.18) resulting in an increase in the gradient of the mean scalar. Since the viscous flux of a scalar is a direct function of the mean gradient (Eq. 5.5.3), the viscous flux will necessarily change as well.

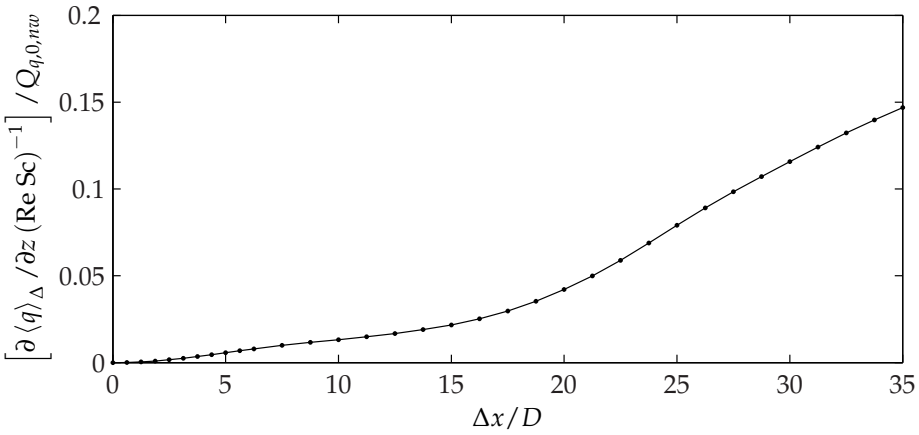

Figure 6.20: Change in surface viscous flux for Case CN. Results have been normalized by the surface viscous flux of the no wake simulation at the corresponding integration time (or $\Delta x/D$).

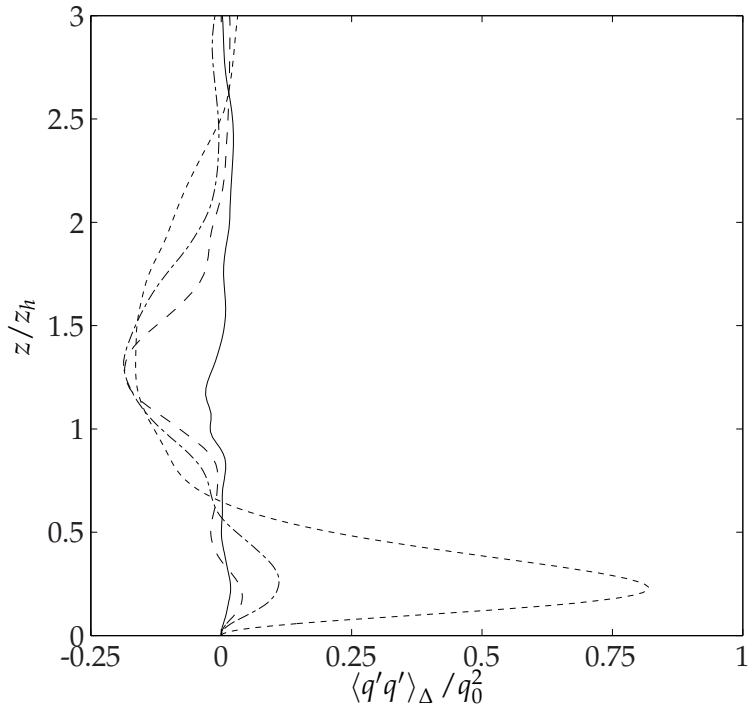

Figure 6.21: Change in $\langle q'q' \rangle_\Delta$ for Case CN: solid, $\Delta x/D = 6.25$; dashed, $\Delta x/D = 12.5$; dash-dot, $\Delta x/D = 18.75$; dotted, $\Delta x/D = 31.25$. Results have been normalized by the surface scalar concentration $q_0 = 0.01$.

While the imposed velocity field tends to transport the scalar away from the wall, the fluctuations in concentration also increase below z_h. Figure 6.21 shows the normalized scalar concentration at four locations downstream of the wind farm. A clear increase in seen in the scalar variance below the hub while a decrease in the magnitude of the fluctuations occurs above. The strength of the oscillations downstream tend to increase with distance below z_h. This is likely a consequence of $\langle w'w' \rangle_{ww}$ gaining energy from the two other energy components. Above z_h, however, the relative change in the variance of the scalar tends to remain constant in both magnitude and the location of the minimum.

Case CH

The change in scalar concentration for the unstably stratified simulation is presented in Fig. 6.22. Like the neutral case, scalar concentration near the surface decreases. Away from the wall, a small increase in $\langle q \rangle$ is evident. Three unique characteristics distinguish the results in Fig. 6.18 and 6.22:

(1) The height at which $\langle q \rangle_\Delta \approx 0$ is close to $z/z_h = 1$ for the neutral case. With surface heating, this crossover is much closer to the wall ($z/z_h < 0.5$).

(2) Above the zero crossover, the scalar concentration is fairly well mixed as is expected in the mixed layer of the convective boundary layer. The neutral case shows a clear peak in the scalar concentration indicating a decreased level of mixing.

(3) At corresponding distances downstream, the ratio of $\langle q \rangle_\Delta$ for the neutral to unstable case is greater than three. This indicates a much larger decrease in the concentration near the wall for the neutral case. Likely, this is a consequence of the relative difference in initial turbulent intensities before the wake is initialized.

The change in scalar flux for the unstably-stratified simulation is presented in Fig. 6.23. As a consequence of adding the wake, the flux at the surface increases by approximately 3.5%

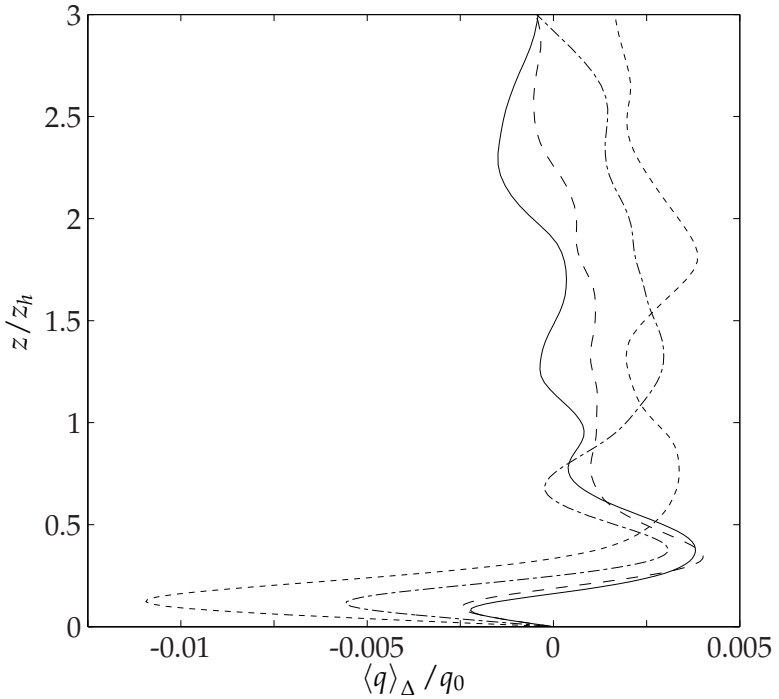

Figure 6.22: Change in scalar concentration for Case CH. Solid, $\Delta x/D = 6.25$; dashed, $\Delta x/D = 12.5$; dash-dot, $\Delta x/D = 18.75$; dotted, $\Delta x/D = 31.25$. Results have been normalized by the surface scalar concentration $q_0 = 0.01$.

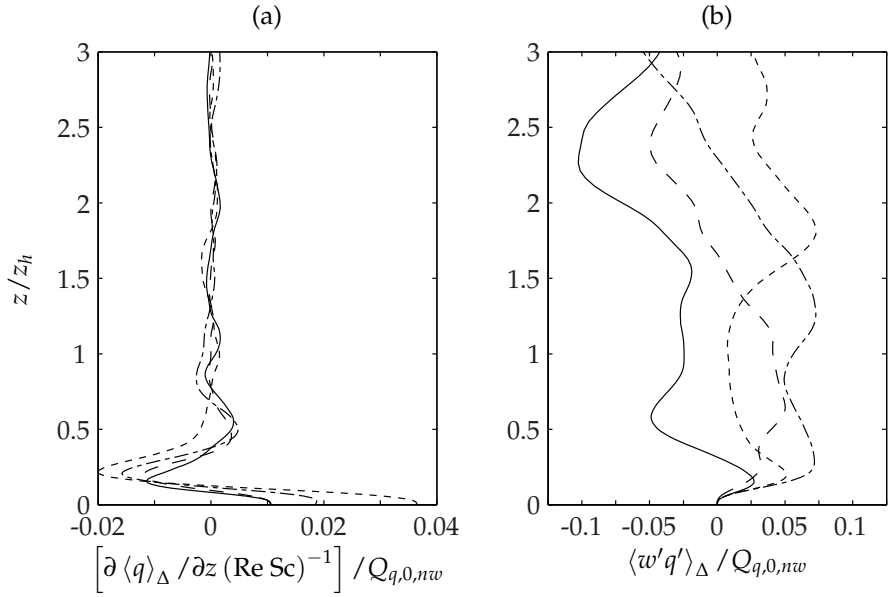

Figure 6.23: Change in scalar flux for Case CH: (a) viscous flux, (b) turbulent flux. Solid, $\Delta x/D = 6.25$; dashed, $\Delta x/D = 12.5$; dash-dot, $\Delta x/D = 18.75$; dotted, $\Delta x/D = 31.25$. Results have been normalized by the surface viscous flux of the no wake simulation at the corresponding integration time (or $\Delta x/D$).

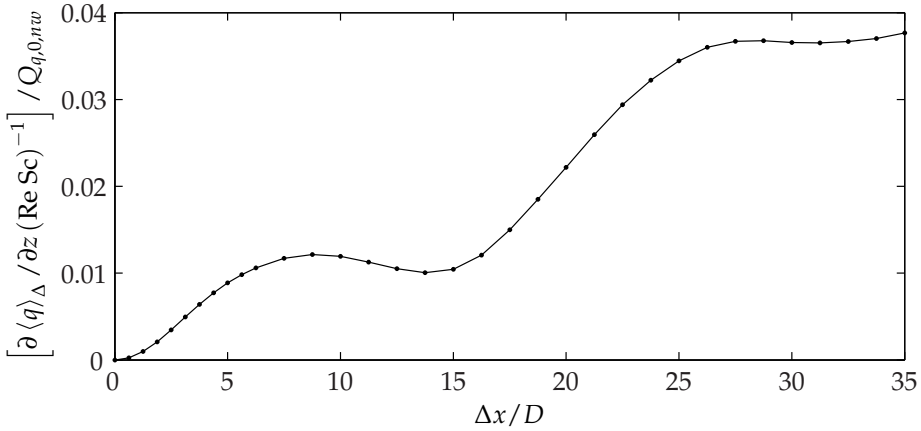

Figure 6.24: Change in surface viscous flux for Case CH. Results have been normalized by the surface viscous flux of the no wake simulation at the corresponding integration time (or $\Delta x/D$).

at $\Delta x/D = 31.25$. This is a significant decrease from the neutral case where adding the wake increased surface flux by over 10% of $Q_{q,0,nw}$. Figure 6.24 clearly shows that surface flux increases by $< 4\%$ when the wake is added. For the turbulent flux shown in Fig. 6.23(b), $\langle w'q' \rangle_\Delta$ tends to be negative immediately after introducing the velocity deficit. A small region of increased flux is evident close to the wall. As the wake evolves, the scalar flux increases until two local maxima are evident: one close to the wall and one above the wake. Far downstream of the turbine, the scalar flux increases relative to the no-wake simulation. However, values of $\langle w'q' \rangle_\Delta$ are small signaling that changes in scalar flux are minor.

While $\langle q'q' \rangle_\Delta$ is on the same order of magnitude as q_0^2 for Case CN, the scalar variance changes much less for Case CH. Figure 6.25 shows the change in scalar variance is about two order of magnitudes smaller than the neutral case. Once again, the unstable case is already well mixed so the wake has less of an influence on q than the neutral simulation.

In addition to the scalar q, the introduction of the wake has a small effect on the temperature of the fluid as mixing is increased. Like q, the temperature decreases near the wall as thermal energy is transported upwards (see Fig. 6.26). Consequently, temperature increases away from the wall. Comparing the change in humidity and temperature for Case CN (Figs. 6.22 and 6.26

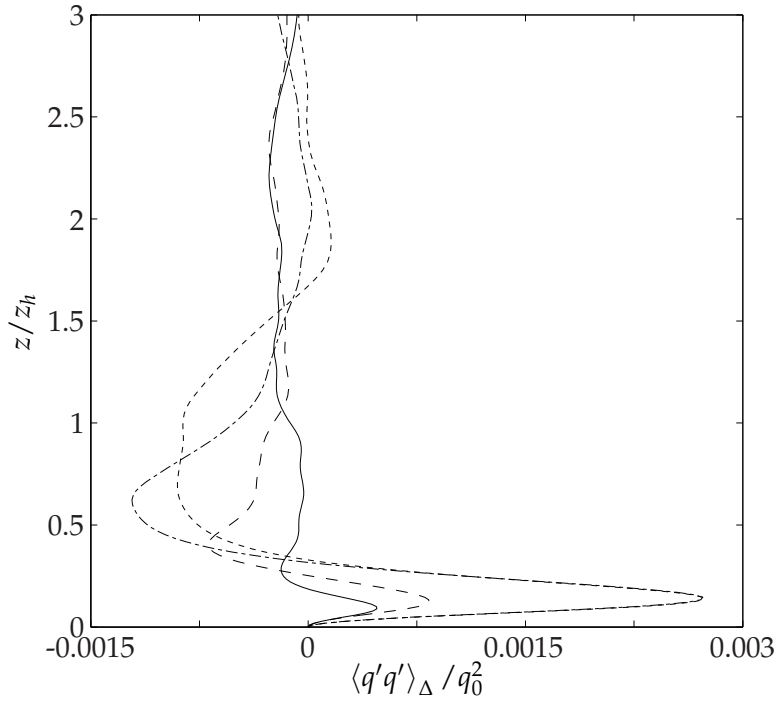

Figure 6.25: Change in $\langle q'q' \rangle_\Delta$ for Case CH: solid, $\Delta x/D = 6.25$; dashed, $\Delta x/D = 12.5$; dash-dot, $\Delta x/D = 18.75$; dotted, $\Delta x/D = 31.25$. Results have been normalized by the surface scalar concentration $q_0 = 0.01$.

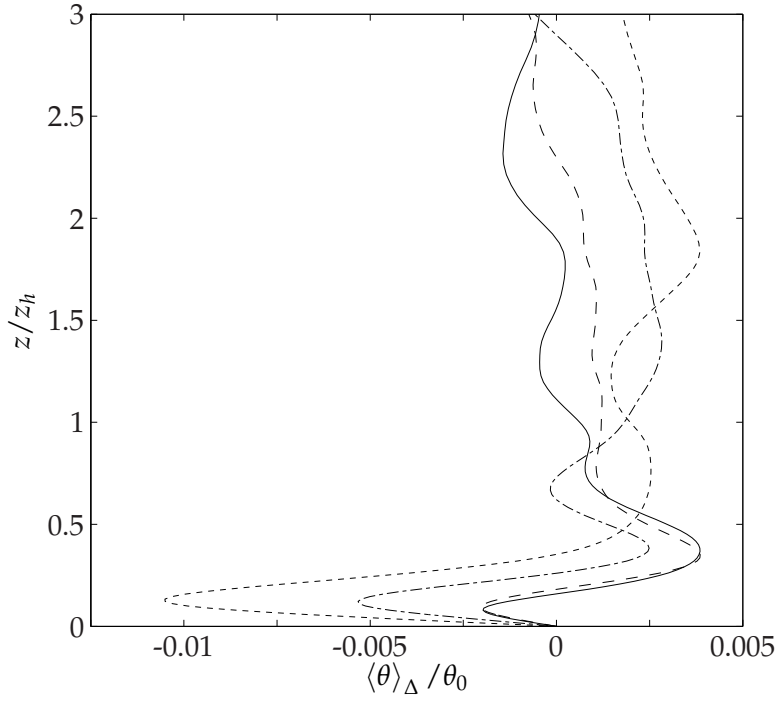

Figure 6.26: Change in $\langle \theta \rangle_\Delta$ for Case CH: solid, $\Delta x/D = 6.25$; dashed, $\Delta x/D = 12.5$; dash-dot, $\Delta x/D = 18.75$; dotted, $\Delta x/D = 31.25$. Results have been normalized by the surface temperature θ_0.

respectively), the results are nearly identical when both are scaled by their corresponding surface value. As both are active scalars for Case CH, similar behavior is expected. Additional statistics for the temperature including the heat flux and fluctuating temperature variance are nearly identical to the scalar statistics and are, consequently, not necessary to show.

6.4 Turbulent Budgets

Budgets for the turbulent kinetic energy ($\overline{u_i' u_k'}$) and the humidity flux ($\overline{u_i' q'}$) help uncover the mechanism which causes the increase/decrease in turbulent energy once the wind turbine wake has been introduced into the flow. To capture the 'average' effect of the wake, budgets have been averaged over $0 < \Delta x/D < 37.5$ using 30 equally spaced flow realizations. Although the flow evolves with time, the results give a general feel for how energy is redistributed downstream of a turbine.

6.4.1 Kinetic Energy Budgets

Kinetic energy budgets were computed from Eq. 4.3.1 for the six variance and covariance terms. A direct comparison between the with-wake and no-wake results is made to highlight the effect of the wake on the various budget terms. Note that insignificant terms (e.g. Coriolis redistribution) might not be shown in the following plots.

Case CN

For the neutrally stratified wake profile there is no buoyant forcing; therefore, term II in Eq. 4.3.1 is zero. Additionally, it was shown in §4.3 that Coriolis redistribution plays only a minor role in the transport of energy. Results indicated that the same conclusion was true in the wake profile, and differences between the with-wake and no-wake results were small with regards to $C_{i,k}$. For this reason, $C_{i,k}$ is not considered here.

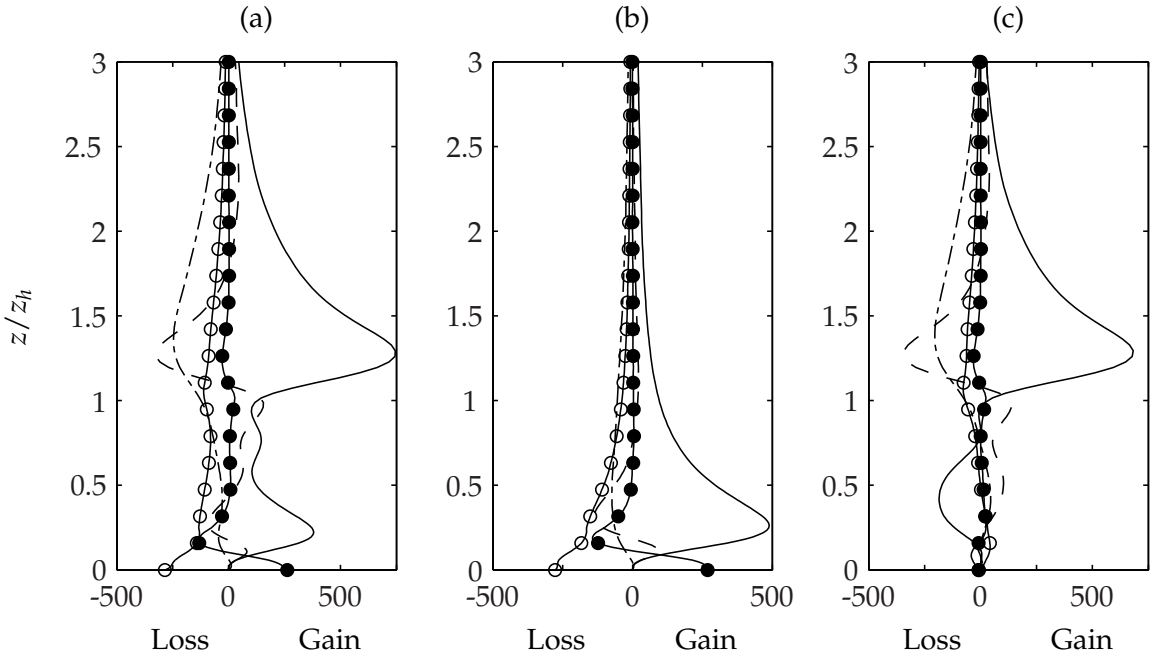

Figure 6.27: Case CN, budget for $\overline{u'u'}$: (a) with wake, (b) no wake, (c) difference. Solid, production; dashed, turbulent diffusion; dot-dash, pressure strain; solid circle, molecular diffusion; open circle, viscous dissipation. All terms have been normalized by u_*^3/δ from Case A.

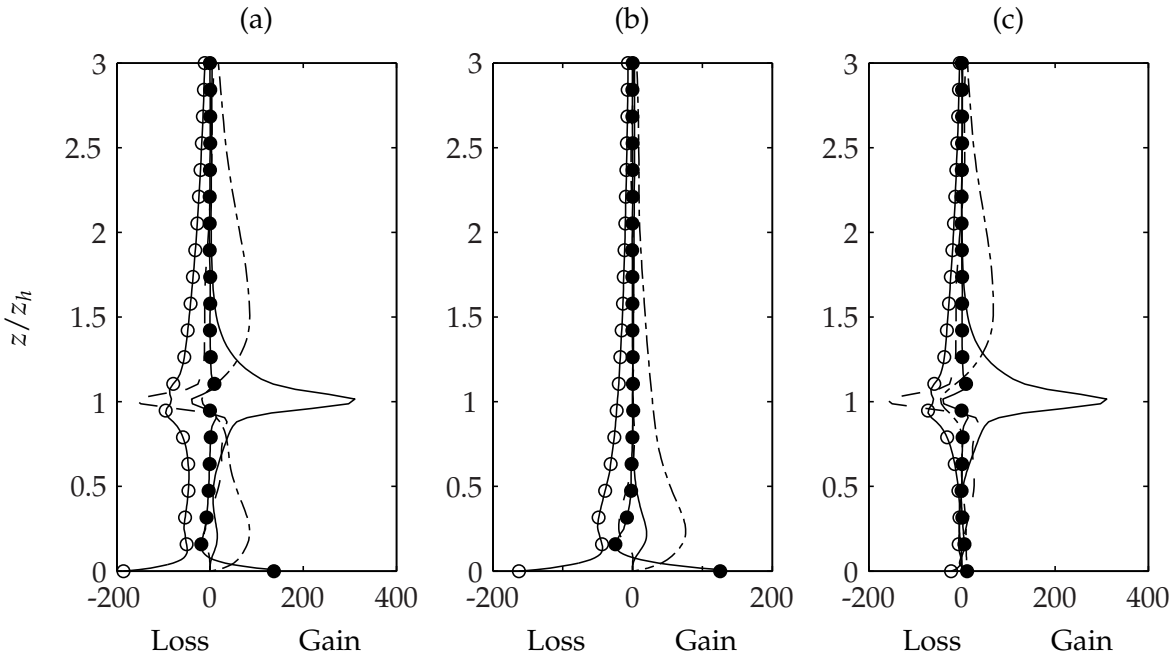

Figure 6.28: Case CN, budget for $\overline{v'v'}$: (a) with wake, (b) no wake, (c) difference. Solid, production; dashed, turbulent diffusion; dot-dash, pressure strain; solid circle, molecular diffusion; open circle, viscous dissipation. All terms have been normalized by u_*^3/δ from Case A.

In the neutrally stratified Ekman layer, production in the $\overline{u'u'}$ budget was the primary source of kinetic energy. The same holds true for the wake simulation shown in Fig. 6.27. In each budget figure, subplot (a) shows the with-wake results, (b) the no-wake results, and (c) the difference (Δ) between the two. The results have been normalized by u_*^3/δ as reported in Table 4.2. The most notable feature is the drastic increase production for $z > z_h$. The large positive mean velocity gradient (see Fig. 6.5) coupled with an increase in $-\langle u'w' \rangle$ yields a sizable increase in $P_{1,1}$. Consequentially, production near the wall is no longer the primary source of kinetic energy. While the increase in the gradient of u yields an increase in production over z_h, the opposite holds true below the hub height. A slight decrease in production is seen near $z/z_h \approx 0.4$. Although energy production displays major increases, energy destruction by viscous dissipation is affected much less. A slight decrease in $\varepsilon_{1,1}$ (i.e. a larger loss or more dissipation of energy) is seen throughout the wake region. The maximum difference of $\varepsilon_{1,1_\Delta} \approx -77.2$ occurs just above $z = z_h$. Looking at Fig. 6.27(c), the gain by production above z_h is not balanced by the production lost below z_h and the dissipation. Consequently, a net increase in $\overline{u'u'}$ occurs. Molecular diffusion is mostly unchanged, but turbulent diffusion acts to transport momentum from the region of maximum production towards the wall. Between $0.5 < z/z_h < 1$ production remains the primary source of energy, but turbulent diffusion acts as a secondary source that is not negligible in this region. Pressure strain remains unchanged below the hub and acts as a sink above z_h. As will be shown shortly, energy is redistributed from $\overline{u'u'}$ to the other two Reynolds normal stresses.

In Fig. 6.28, the most notable differences occur very close to the hub. The gradient of the mean spanwise velocity is increased quite drastically due to the imposition of the planar vortex onto the field. Hence, production at z_h is on the same scale as production in the streamwise direction. Dissipation at the hub is increased such that more energy is lost by $\varepsilon_{2,2}$ when compared with the no-wake simulation. The change in viscous dissipation is comparable in magnitude for both horizontal stress components. Turbulent diffusion balances the peak in production and pressure-strain for the no-wake simulation as shown in Fig. 6.28(b). Introducing the wake causes turbulent

diffusion to act as a major sink while transporting energy downwards. The study shown in Fig. 4.18 indicates that $T_{2,2}$ is mostly responsible for transporting energy away from the wall. Therefore, the role of turbulent diffusion is the same: transport energy from high production regions to regions where turbulent energy is not produced. Finally, above $z/z_h \approx 1.25$ the primary source of energy is the return-to-isotropy term. Energy from $\overline{u'u'}$ is transfered to $\overline{v'v'}$ in a manner such that pressure strain is the primary source of energy outside of the small region where production by mean shear dominates. Should the vortex not be introduced into the field, pressure strain would likely be nearly constant across $0.25 < z/z_h < 2$ as the spike in production would no longer be evident.

Since $\overline{w'w'}$ does not have any direct production through mean shear or buoyancy (in the neutral case), all differences in the budget are a direct consequence of energy that is transfered to the term via pressure strain. Unlike the horizontal energy components where the with-wake simulation retains some of the characteristics of the no-wake case, the budget of the vertical energy component (Fig. 6.29) is completely dominated by the introduction of the wake into the mean velocity. The primary source of energy with the wake is via pressure strain as the vertical component is energized by $\overline{u'u'}$. Figure 6.29(b) shows that the total pressure transport term is a gain throughout the boundary layer when no wake is present. After introducing the wake, pressure transport acts as a sink when $z/z_h < 0.6$. Turbulent diffusion takes energy from above $z/z_h \approx 0.75$ and transports it towards the wall. Pressure strain then redistributes this energy to $\overline{v'v'}$. The spanwise budget actually has three sources of energy near the wall: production by mean shear and an inter-component energy transfer from both $\overline{u'u'}$ and $\overline{w'w'}$. Vertical dissipation acts as a larger sink (approximately three times stronger) when the wake is present while molecular diffusion is essentially unchanged with the introduction of the wake.

Figure 6.30 gives the energy budget for $-\overline{u'w'}$ in Case CN. Production increases above z_h while decreasing below the hub height. Consider an element of fluid with streamwise velocity u_1. The fluctuating velocity at some point 1 is given by $u'_1 = u_1 - U_1$. If the fluid element remains at a

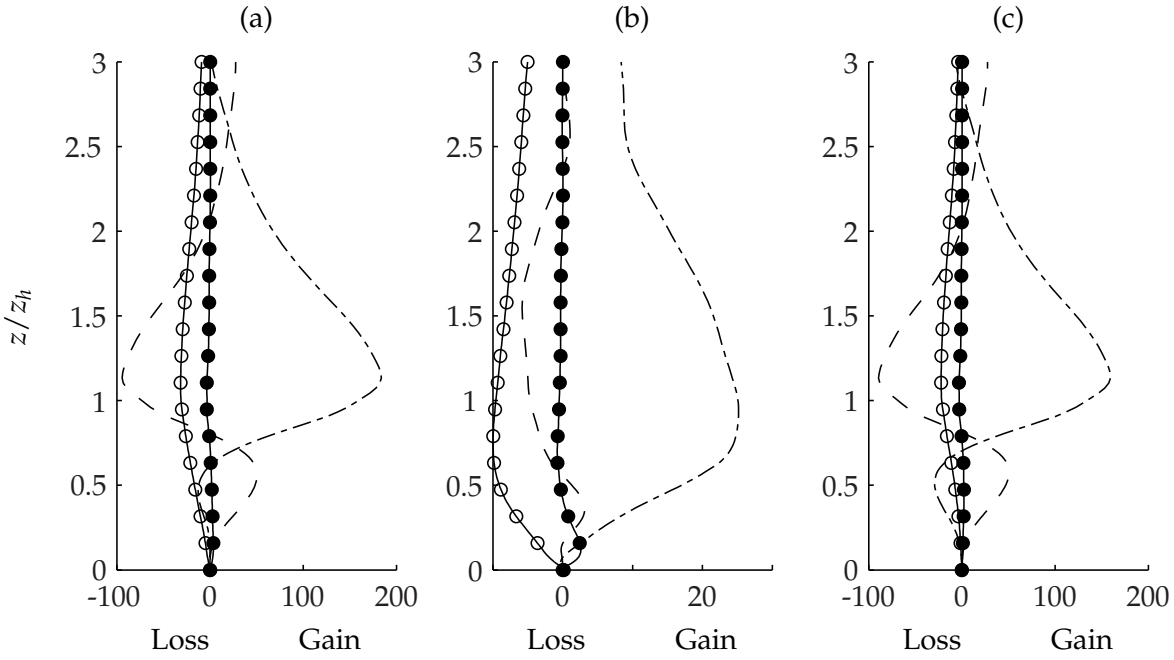

Figure 6.29: Case CN, budget for $\overline{w'w'}$: (a) with wake, (b) no wake, (c) difference. Solid, production; dashed, turbulent diffusion; dot-dash, total pressure transport; solid circle, molecular diffusion; open circle, viscous dissipation. All terms have been normalized by u_*^3/δ from Case A.

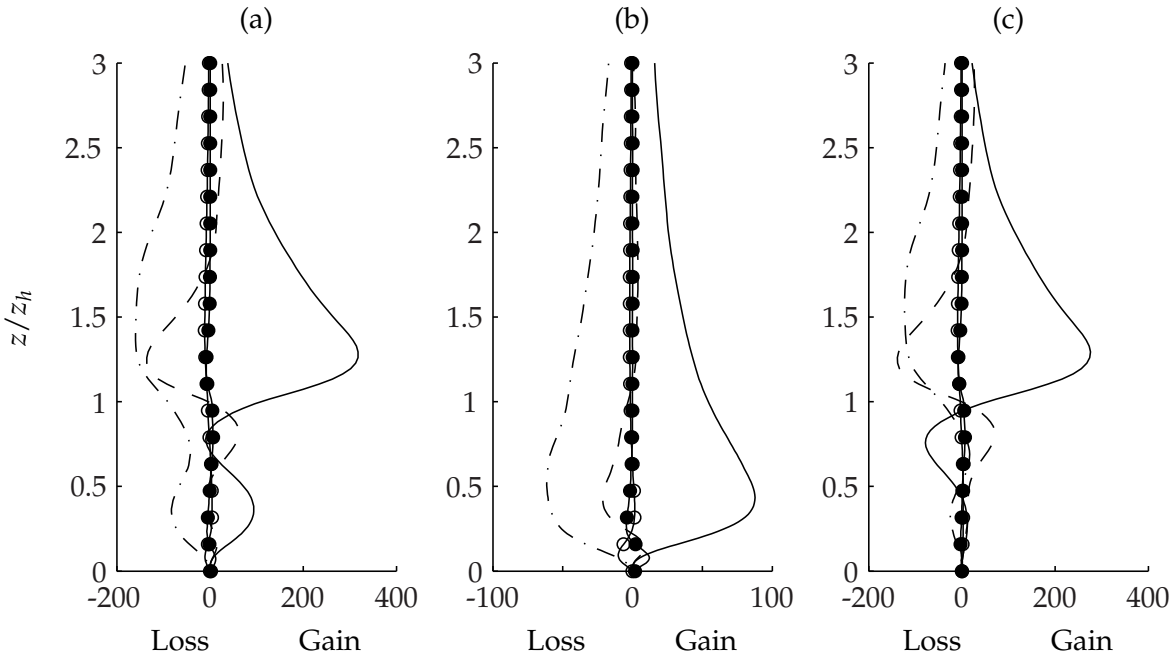

Figure 6.30: Case CN, budget for $-\overline{u'w'}$: (a) with wake, (b) no wake, (c) difference. Solid, production; dashed, turbulent diffusion; dot-dash, total pressure transport; solid circle, molecular diffusion; open circle, viscous dissipation. All terms have been normalized by u_*^3/δ from Case A.

constant velocity and is transported upwards ($+w'$) to a new level 2, the new fluctuating velocity is given by $u'_2 = u_2 - U_2$. If the streamwise velocity of the element does not change ($u_2 = u_1$) but the mean velocity increases ($U_2 > U_1$), then $u'_2 < u'_1$. This results in an increase in $-\overline{u'w'}$ if the vertical velocity is unchanged. Therefore, changing the mean velocity profile will have major effects on the Reynolds shear stresses.

Pressure transport acts as a sink for the streamwise shear stress with an increase in strength occurring above $z \approx z_h$. Both viscous dissipation and molecular diffusion remain mostly unchanged.

The budget of $-\overline{v'w'}$ is dominated by wake effects. A peak in production at $z \approx z_h$ occurs and is counteracted by pressure transport. The pressure term is responsible for the diffusion of energy to other regions of the boundary layer – notice the positive region above $z/z_h > 2$ in Fig. 6.31(a) – and also redistribution to other energy terms. It appears energy is transported into the $-\overline{u'v'}$ term. Little change occurs with either viscous term ($\varepsilon_{2,3}$ or $D_{2,3}$).

Like the budget shown in Fig. 4.23, the kinetic energy budget for $-\overline{u'v'}$ shown in Fig. 6.32 shows a reversal of the role of the components. Above $z/z_h \approx 1$, production by mean shear acts as a significant sink. An increase in the total pressure transport occurs and is likely an acquisition of energy from both $-\overline{u'w'}$ and $-\overline{v'w'}$. Changes in the budget of $-\overline{u'v'}$ are limited to $z/z_h < 2$; above this, little change to any term occurs.

Case CH

Budgets for Case CH share many of the same characteristics of the budgets from Case CN. As with Case B1 and B2, Coriolis redistribution plays a very minor role in redistributing energy. Results from Case CH indicate that the change in $C_{i,k}$ that results from adding the wake is small. For this reason, Coriolis redistribution is not included in the following budget results even though this term is nonzero.

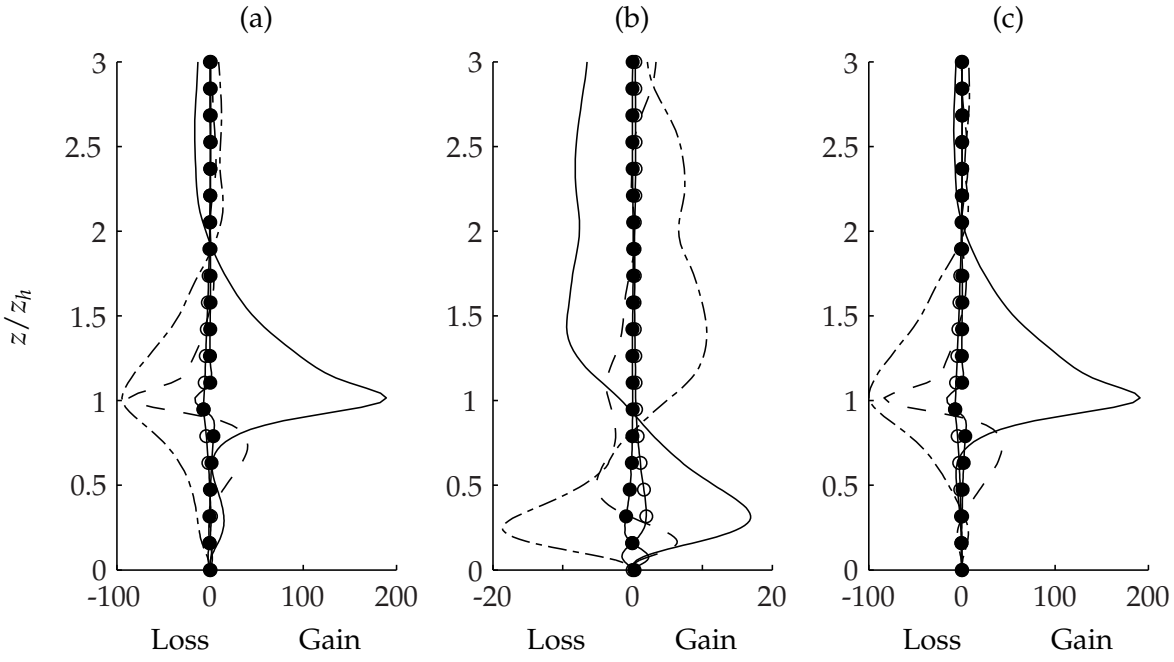

Figure 6.31: Case CN, budget for $-\overline{v'w'}$: (a) with wake, (b) no wake, (c) difference. Solid, production; dashed, turbulent diffusion; dot-dash, total pressure transport; solid circle, molecular diffusion; open circle, viscous dissipation. All terms have been normalized by u_*^3/δ from Case A.

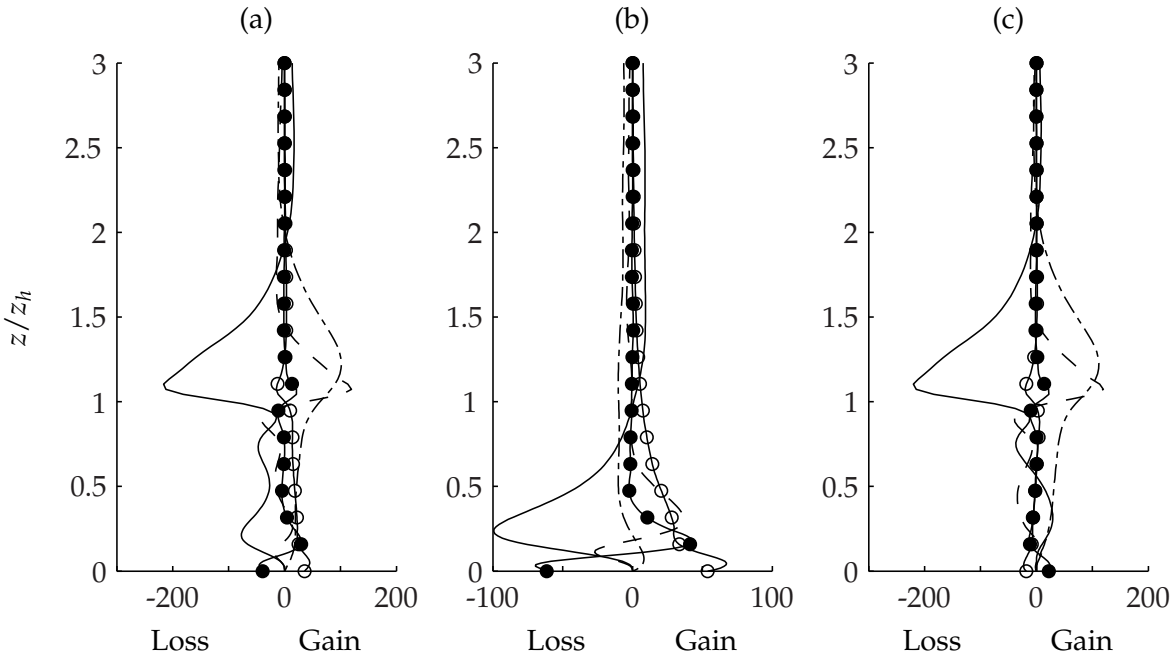

Figure 6.32: Case CN, budget for $-\overline{u'v'}$: (a) with wake, (b) no wake, (c) difference. Solid, production; dashed, turbulent diffusion; dot-dash, total pressure transport; solid circle, molecular diffusion; open circle, viscous dissipation. All terms have been normalized by u_*^3/δ from Case A.

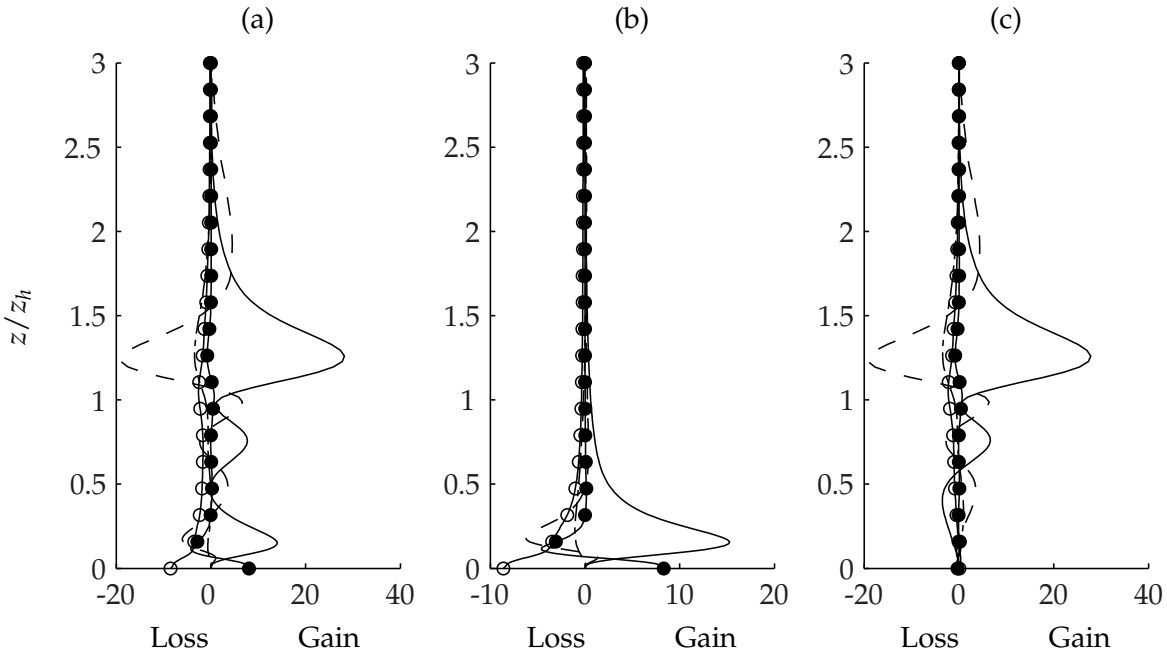

Figure 6.33: Case CH, budget for $\overline{u'u'}$: (a) with wake, (b) no wake, (c) difference. Solid, production; dashed, turbulent diffusion; dot-dash, pressure strain; solid circle, molecular diffusion; open circle, viscous dissipation. All terms have been normalized by w_*^3/z_i from Case B1.

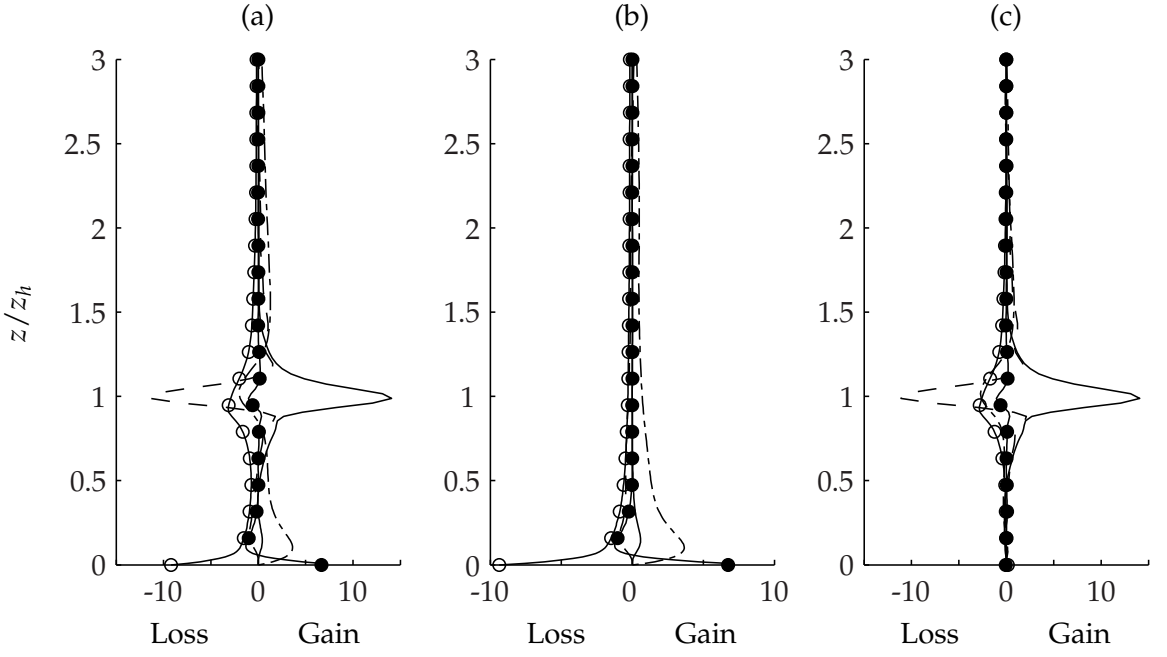

Figure 6.34: Case CH, budget for $\overline{v'v'}$: (a) with wake, (b) no wake, (c) difference. Solid, production; dashed, turbulent diffusion; dot-dash, pressure strain; solid circle, molecular diffusion; open circle, viscous dissipation. All terms have been normalized by w_*^3/z_i from Case B1.

In Fig. 6.33(c) it is clear that production by mean shear is increased when $z/z_h > 1$. A third local maximum in the production curve in seen in Fig. 6.33(a) which is not evident in the Case CN results (see Fig. 6.27). A weakening of production still occurs for the unstably-stratified case, but to less of an extent than the neutral simulation. The second notable change in the energy budget is the increase in turbulent diffusion just above the hub height. However, the large pressure strain sink term that was evident for Case CN is not present with stratification. Since production in the $\overline{u'u'}$ budget is no longer the sole source of energy (buoyant production), the return-to-isotropy term takes less energy from the streamwise component.

Figure 6.34 gives the energy budget for the spanwise velocity variance. Changes in the budget balance only occur at the hub height. The increase in production is balanced by turbulent diffusion as the energy is redistributed throughout the boundary layer. Pressure strain acts as a second sink as energy is redistributed to the vertical component. Finally, viscous dissipation increases slightly at z_h.

The most notable change in the vertical energy budget occurs with the pressure transport term (see Fig. 6.35). Without the wake, the vertical component is energized by buoyant forcing. Recall that q is an active scalar in Case CH. Therefore, the buoyancy term $\beta_{3,3}$ includes contributions from temperature and humidity:

$$\overline{w'\theta'_v} = \overline{w'\theta'} + 0.61\overline{w'q'} \tag{6.4.1}$$

Given the small magnitude of the scalar concentration relative to θ, the contribution to buoyant forcing by humidity content is over an order of magnitude smaller than the contribution by the potential temperature. The increase in pressure transport (mostly pressure-strain) at z_h draws energy from the horizontal energy components. The sharp mean velocity gradients and enhanced vertical mixing from buoyancy injects energy at the hub height. The energy is then transfered to $\overline{w'w'}$ through return-to-isotropy and then transported throughout the boundary layer by an increased role of turbulent diffusion.

The primary shear stress budgets for $-\overline{u'w'}$ and $-\overline{v'w'}$ are presented in Fig. 6.36 and 6.37

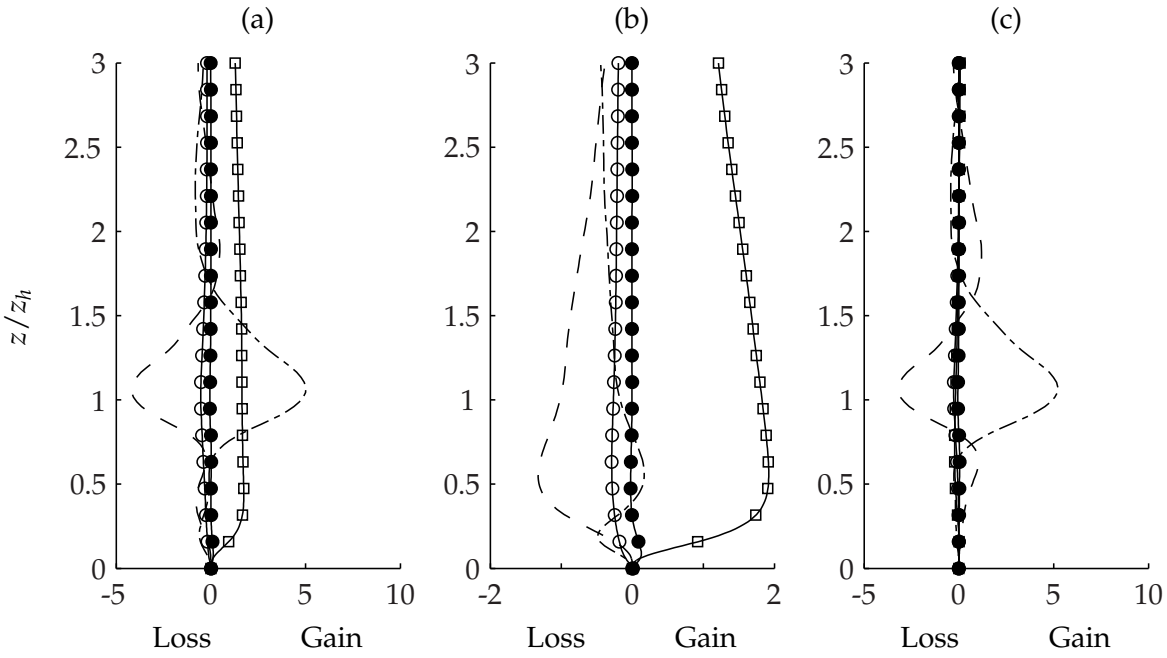

Figure 6.35: Case CH, budget for $\overline{w'w'}$: (a) with wake, (b) no wake, (c) difference. Dashed, turbulent diffusion; dot-dash, total pressure transport; diamond, pressure diffusion; solid circle, molecular diffusion; open circle, viscous dissipation; square, buoyant production. All terms have been normalized by w_*^3/z_i from Case B1.

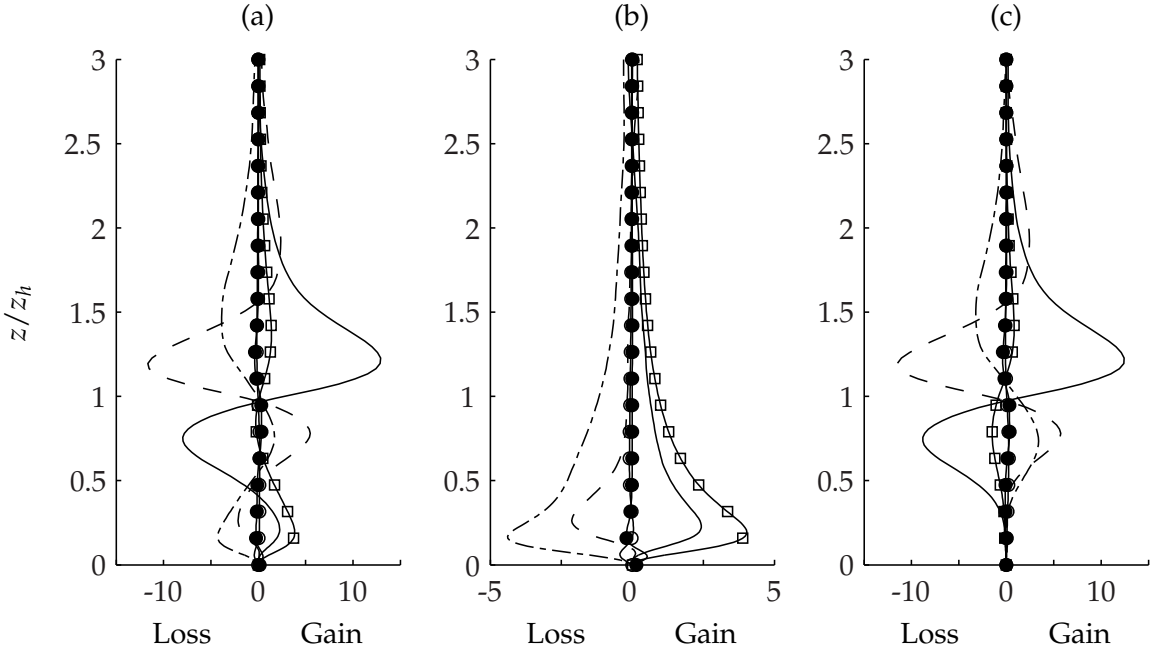

Figure 6.36: Case CH, budget for $-\overline{u'w'}$: (a) with wake, (b) no wake, (c) difference. Solid, production; dashed, turbulent diffusion; dot-dash, total pressure transport; solid circle, molecular diffusion; open circle, viscous dissipation; square, buoyant production. All terms have been normalized by w_*^3/z_i from Case B1.

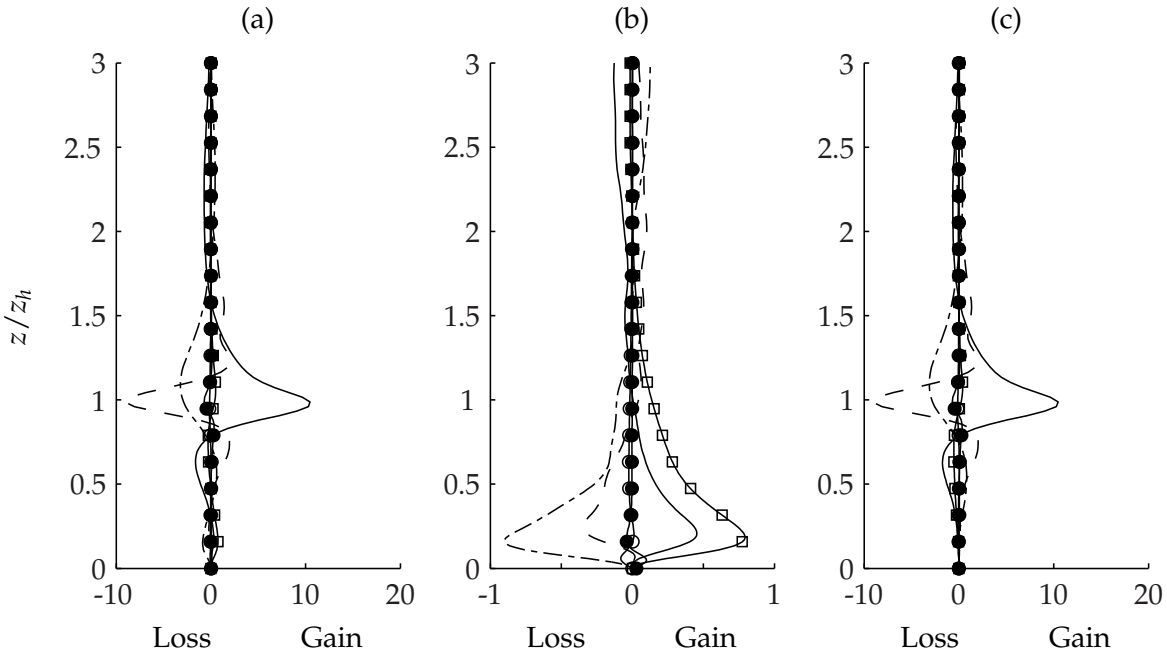

Figure 6.37: Case CH, budget for $-\overline{v'w'}$: (a) with wake, (b) no wake, (c) difference. Solid, production; dashed, turbulent diffusion; dot-dash, total pressure transport; solid circle, molecular diffusion; open circle, viscous dissipation; square, buoyant production. All terms have been normalized by w_*^3/z_i from Case B1.

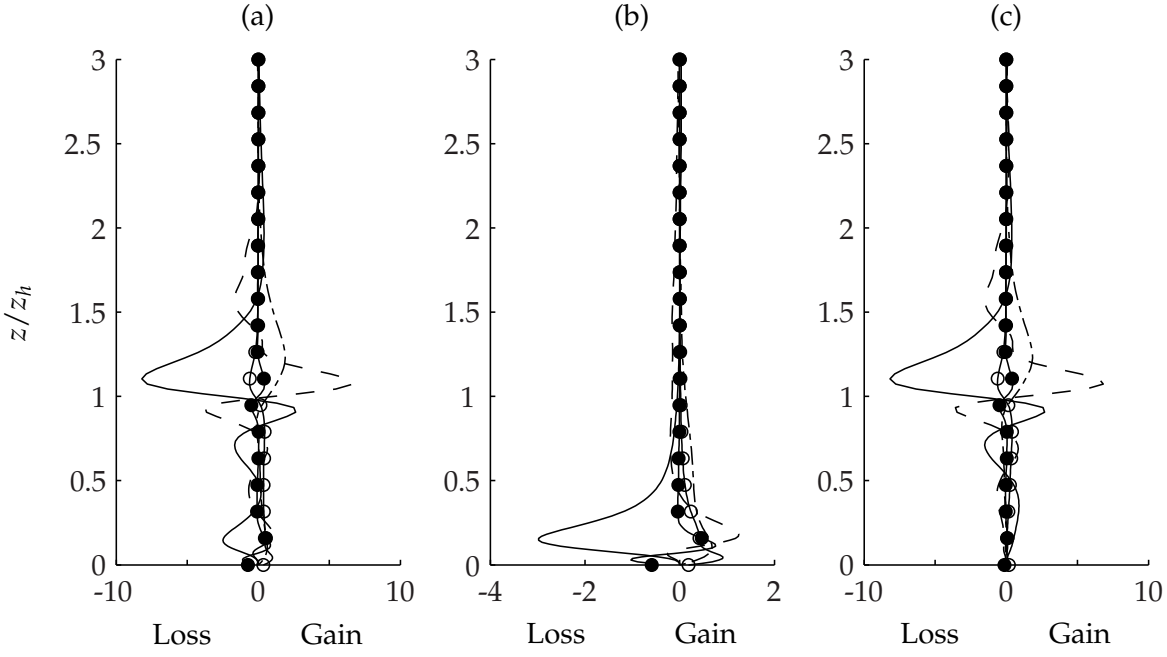

Figure 6.38: Case CH, budget for $-\overline{u'v'}$: (a) with wake, (b) no wake, (c) difference. Solid, production; dashed, turbulent diffusion; dot-dash, pressure strain; solid circle, molecular diffusion; open circle, viscous dissipation. All terms have been normalized by w_*^3/z_i from Case B1.

respectively. Buoyant production acts as a source throughout the boundary both with and without the wake present. Below the hub, the gain from buoyancy is reduced while it is slightly increased above the hub. The other terms behave in a similar fashion to the Case CN results presented in Fig. 6.30 and 6.31. In the streamwise direction, pressure transport displays a small increase below the hub that is not evident without temperature stratification. For $-\overline{v'w'}$, less of a change in pressure transport is seen with stratification with thermal forcing.

The horizontal shear stress (Fig. 6.38) displays an increase in production over z_h and is balanced by an increase in the energy lost to pressure strain and turbulent diffusion. Apart from a rather narrow region ($0.75 < z/z_h < 2$), no changes to the budget of $-\overline{u'v'}$ are evident.

6.4.2 Scalar Transport Budgets

The scalar transport budget for term $\overline{u_i'q'}$ is developed in Appendix B. Like the kinetic energy budget, it is derived by substituting mean and fluctuating components for velocity and scalar concentration into the governing equations of momentum and scalar transport. Analyzing the scalar transport budget reveals important characteristics of the mechanisms responsible for increasing the transport of humidity in the wake of a turbine. In its full form, the budget is given by

$$\underbrace{\frac{\partial \overline{u_i'q'}}{\partial t}}_{0} = \underbrace{-U_j\frac{\partial \overline{u_i'q'}}{\partial x_j}}_{\text{I}} \underbrace{+\overline{q'\theta_v'}\delta_{k3}}_{\text{II}} \underbrace{-\overline{u_i'u_j'}\frac{\partial \overline{q}}{\partial x_j} - \overline{q'u_j'}\frac{\partial U_i}{\partial x_j}}_{\text{III}} \underbrace{-\frac{\partial \overline{u_i'u_j'q'}}{\partial x_j}}_{\text{IV}}$$

$$\underbrace{-\left(\frac{2}{\mathrm{Re}}+\frac{2}{\mathrm{Re\,Sc}}\right)\overline{\frac{\partial u_i'}{\partial x_j}\frac{\partial q'}{\partial x_j}}}_{\text{V}} \underbrace{+\left(\frac{1}{\mathrm{Re}}+\frac{1}{\mathrm{Re\,Sc}}\right)\frac{\partial^2 \overline{u_i'q'}}{\partial x_j\partial x_j}}_{\text{VI}} \underbrace{+\overline{p'\frac{\partial q'}{\partial x_i}}}_{\text{VII}} \tag{6.4.2}$$

$$\underbrace{-\frac{\partial \overline{q'p'}}{\partial x_i}}_{\text{VIII}} \underbrace{+\frac{1}{\mathrm{Ro}}\varepsilon_{ij3}\overline{q'u_j'}}_{\text{IX}} \underbrace{-\frac{1}{\mathrm{Re}}\overline{u_i'\frac{\partial^2 q'}{\partial x_j\partial x_j}} - \frac{1}{\mathrm{Re\,Sc}}\overline{q'\frac{\partial^2 u_i'}{\partial x_j\partial x_j}}}_{\text{X}}$$

Many of the above terms are analogous to the kinetic energy equations of Eq. 4.3.1. Term 0 is the time rate of change of the scalar flux $\overline{u_i' q'}$ and I is advection by mean shear (or A_i); together these form the substantial derivative of the scalar flux. Term II is buoyant production by the virtual potential temperature β_i, III gives production by mean shear (P_i), and IV is the turbulent diffusion term T_i. Viscous dissipation is given by term V (ε_i) and molecular diffusion by term VI (D_i). Pressure fluctuations manifest themselves in pressure strain (term VII, Φ_i) and pressure diffusion (term VIII, Θ_i). Coriolis redistribution is given by IX and is denoted C_i. Finally, an extra viscous term appears with leftover viscous terms and is given by X. This extra term will be denoted as X_i.

The time rate of change of the flux term is not explicitly calculated. However, based on the energy balance of the remaining terms it is possible to infer whether the flux term is growing or not. Given that $W = 0$, the advection term is identically zero.

The energy budget terms are normalized by $u_* q_0^2 / \delta$ where both u_* and δ are taken from Case A results. As before, q_0 is the scalar concentration at $z = 0$.

Case CN

Under neutral stratification, $\beta_i = 0$ for all values of i. The primary transport term of interest is $\overline{w'q'}$. This term is responsible for the vertical transport of humidity towards and away from the wall. The following analysis will start with this important velocity and scalar product as given in Fig. 6.39. Production by mean shear is nonzero given the nonzero gradient in $\overline{q}$. Without the wake, P_3 is the primary source of flux throughout the boundary layer. Although not shown, molecular diffusion provides a small gain region in the very near wall region. The pressure transport terms for the no-wake simulation in Fig. 6.39(b) act as a sink throughout the region shown. Pressure transport nearly balances production. Turbulent diffusion predictably acts to move energy from regions of high production both towards the wall and into the farfield.

After introducing the wake, the $\overline{w'q'}$ budget in Fig. 6.39(a) demonstrates a doubling of the magnitude of production by mean shear. Figure 6.18 clearly shows that q is transported away

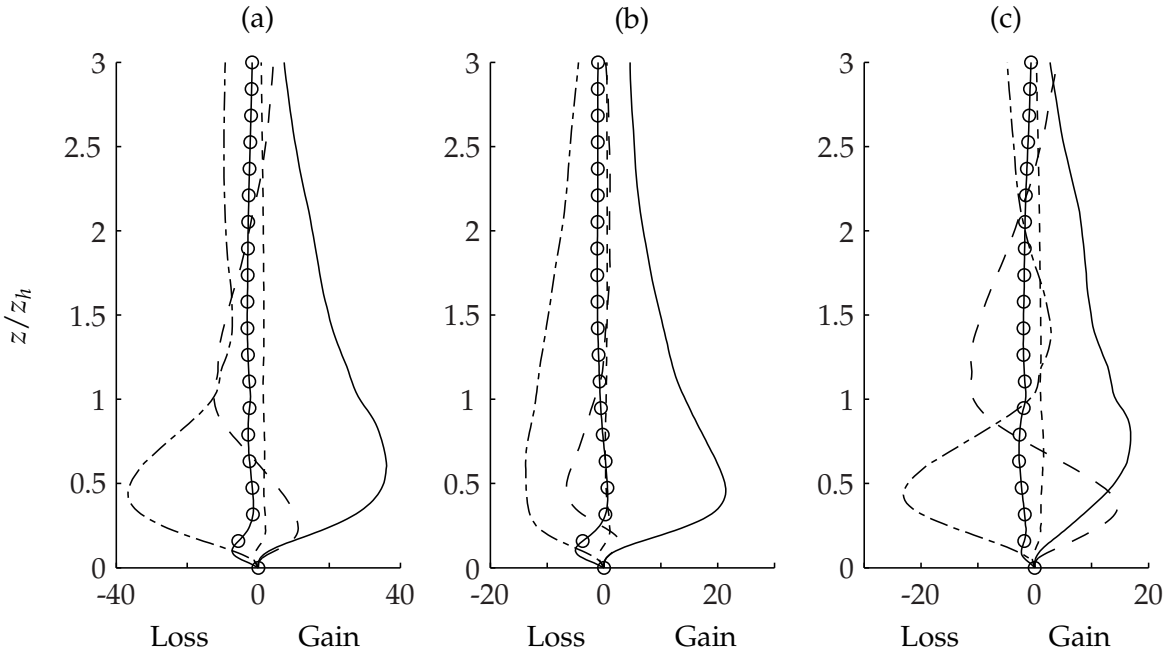

Figure 6.39: Case CN, budget for $\overline{w'q'}$: (a) with wake, (b) no wake, (c) difference. Solid, production; dashed, turbulent diffusion; dot-dash, total pressure transport; open circle, viscous dissipation; dotted, extra viscous terms. All terms have been normalized by $u_* q_0^2/\delta$ (u_* and δ from Case A).

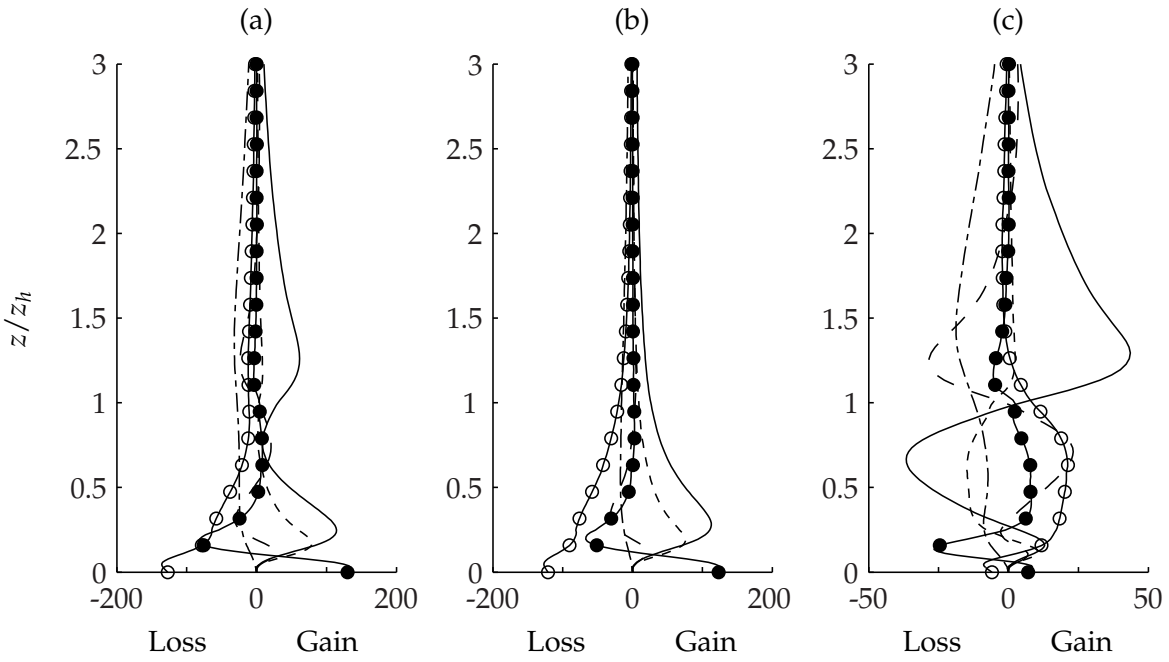

Figure 6.40: Case CN, budget for $-\overline{u'q'}$: (a) with wake, (b) no wake, (c) difference. Solid, production; dashed, turbulent diffusion; dot-dash, pressure strain; open circle, viscous dissipation; closed circle, molecular diffusion; dotted, extra viscous terms. All terms have been normalized by $u_* q_0^2/\delta$ (u_* and δ from Case A).

from the wall. This causes a decrease in $\partial\overline{q}/\partial z$ (or an increase in P_3). The increase in production of $\overline{w'q'}$ is not limited to the region in close proximity of the hub height, rather, the increased production is seen for $0 < z/z_h < 3$. Pressure transport acts to balance the increased production below z_h, but slightly decreases in amplitude when $z/z_h > 1$. With the wake present, vertical transport by turbulent diffusion is increased and likely is responsible for reducing the role of pressure transport. By adding the wake, the magnitude of dissipation increases slightly as more flux is removed. The extra viscous terms (X_3) are very small in comparison to other budget terms.

Figure 6.19(b) shows an increase in turbulent flux both below and above the hub height. The increase in production is primarily responsible for the increase in $\overline{w'q'}$. Immediately behind the wake, production would be identical to the no-wake simulation. Only as time progresses and the vertical turbulent energy grows through pressure strain would production pick up. As the gradient of $\overline{q}$ changes (humidity transported away from the wall), production of scalar flux further increases. Consequently, the catalyst for the increase in the vertical flux of a scalar is the transfer of energy from the horizontal components to the vertical.

The budget of $-\overline{u'q'}$ is shown in Fig. 6.40. Note that the negative sign is required in order to get the sign such that terms act as expected (i.e. production is a gain, viscous dissipation is a loss). This is a reversal of the dynamics associated with $\overline{w'q'}$. With no-wake present, the budget in Fig. 6.40(b) looks qualitatively comparable to the streamwise velocity variance budget shown in Fig. 6.27: a maximum in production close to the wall that is balanced by a large loss by dissipation. Molecular diffusion acts to transport scalar flux towards the wall while turbulent fluctuations transport flux towards the farfield. The significant contribution from X_1 (the extra viscous terms) near the wall is surprising given their small amplitude for the $\overline{w'q'}$ budget. Likely, the difference is the amplitude of u' relative to w' explains the order of magnitude difference between the two terms. Upon adding the wake, streamwise scalar flux shows an increase in production above the hub height, a reduction in the strength of dissipation below the hub, and a decrease in production below z_h. Pressure strain is exaggerated when the wake is introduced and acts as a sink for $0 <$

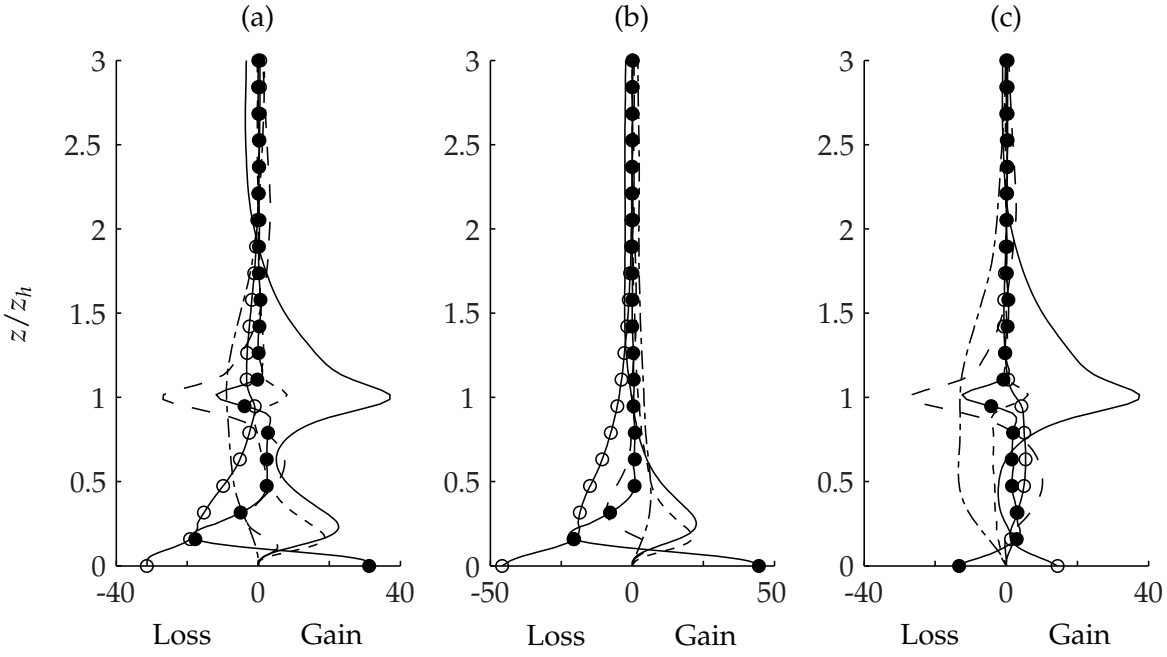

Figure 6.41: Case CN, budget for $-\overline{v'q'}$: (a) with wake, (b) no wake, (c) difference. Solid, production; dashed, turbulent diffusion; dot-dash, pressure strain; open circle, viscous dissipation; closed circle, molecular diffusion; dotted, extra viscous terms. All terms have been normalized by $u_* q_0^2/\delta$ (u_* and δ from Case A).

$z/z_h < 3$. The role of the extra viscous terms is diminished below z_h. Likely, this is a byproduct of the reduction in the $\overline{u'u'}$ energy term behind the wake.

The no-wake scalar flux in the spanwise direction is qualitatively similar to the no-wake streamwise scalar flux. Comparing Fig. 6.41(b) with Fig. 6.40(b) it is clear that the primary difference between the two budgets is simply the magnitude of each term. In the streamwise budget, the no-wake results are approximately a factor of 4 larger than the corresponding spanwise profiles. The addition of the wake causes a sharp increase in spanwise flux production (due to the increase in the gradient of V) and an increase in the energy lost to pressure strain. At the wall, the energy lost to viscous dissipation is decreased as is the energy gained from molecular diffusion. Consequently, both terms are still nearly in balance when the wake is applied to the field.

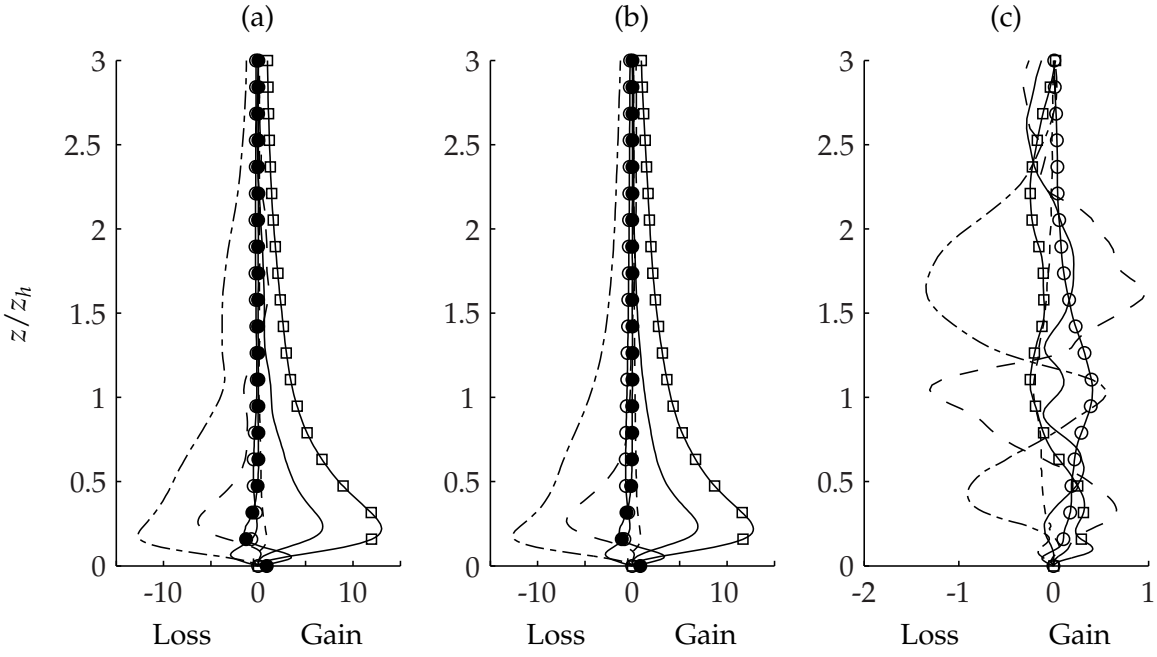

Figure 6.42: Case CH, budget for $\overline{w'q'}$: (a) with wake, (b) no wake, (c) difference. Solid, production; dashed, turbulent diffusion; dot-dash, total pressure transport; closed circle, molecular diffusion; open circle, viscous dissipation; dotted, extra viscous terms; open square, buoyant production. All terms have been normalized by $w_* q_0^2 / z_i$ (w_* and z_i from Case B1).

Case CH

Figure 6.42 gives the scalar flux budget for Case CH with (a) and without (b) a wake. Changes to the flux budget for the neutrally stratified case were on the same order as the magnitude of the terms in the wake free boundary layer. After modifying the mean velocity profile, the flux budget is dominated by a gain via production, a loss through pressure transport, and turbulent diffusion. The budget difference between the wake and no-wake simulation in Fig. 6.42(c) clearly indicates that the wake has less of an effect on vertical flux when unstable stratification is present. Without the wake, buoyant production replaces shear production as the largest gain in $\overline{w'q'}$. Buoyant production already causes enhanced vertical transport such that the increase due to the addition of a wake is small. If the strength of stratification were further increased (e.g. Case B2 from Chap. 5), it is expected that vertical transport from turbine effects would be even smaller

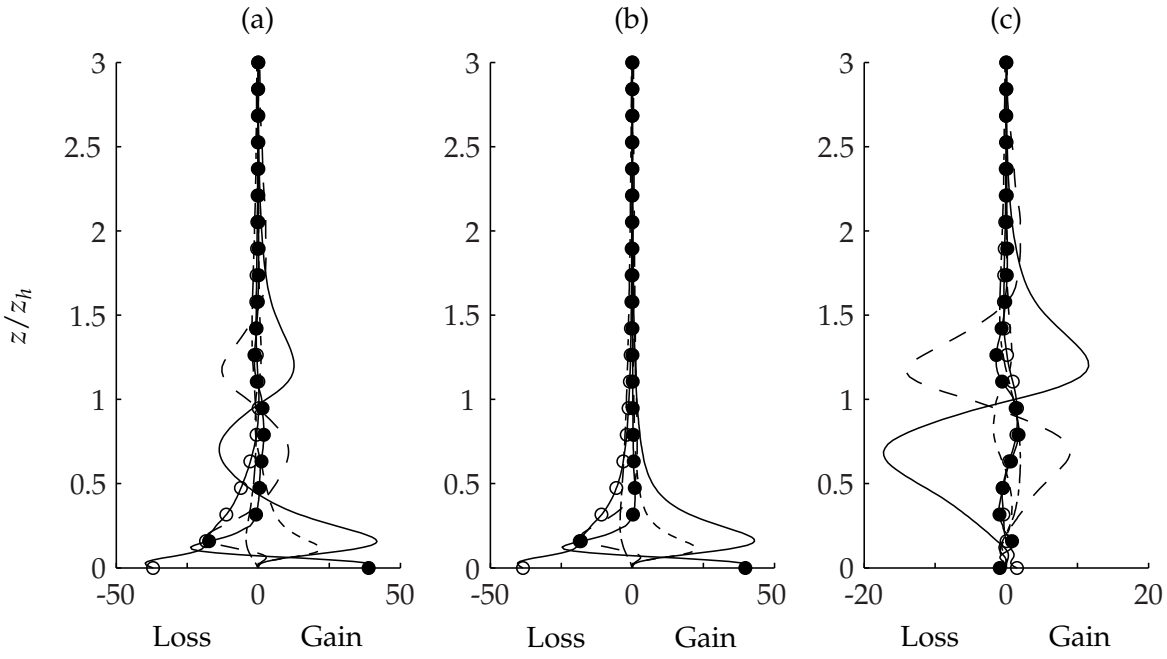

Figure 6.43: Case CH, budget for $-\overline{u'q'}$: (a) with wake, (b) no wake, (c) difference. Solid, production; dashed, turbulent diffusion; dot-dash, pressure strain; open circle, viscous dissipation; closed circle, molecular diffusion; dotted, extra viscous terms. All terms have been normalized by $w_* q_0^2 / z_i$ (w_* and z_i from Case B1).

relative to transport that results from the unstable temperature gradient. Pressure transport is the largest sink term and approximately balances buoyant production. Small increases in the magnitude of pressure transport is seen above and below z_h. However, differences between the wake and no-wake budget is an order of magnitude smaller than the largest budget terms.

Unlike $\overline{w'q'}$, the streamwise scalar flux term is not directly influenced by buoyant production. In fact, the budgets for the neutrally-stratified no-wake simulation in Fig. 6.40(b) and the unstably-stratified no-wake simulation in Fig. 6.43(b) are nearly identical apart from the difference in the scale of the terms. Introducing the wake when a thermal gradient is present causes a reduction in $-\overline{u'q'}$ below the inversion and an increase above. Turbulent diffusion plays a role in transporting flux from regions where production is a source to those regions of the domain where production acts as a sink (see Fig. 6.43(a)). The remaining terms (i.e. viscous terms and pressure strain) are largely unaffected by the introduction of the wake.

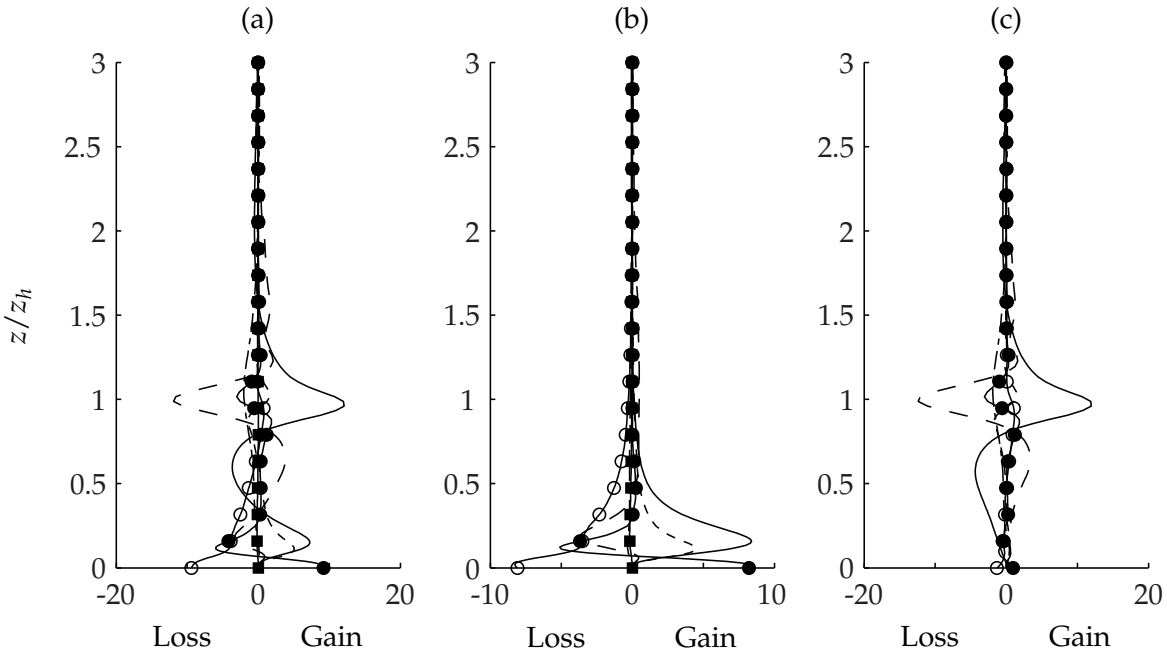

Figure 6.44: Case CH, budget for $-\overline{v'q'}$: (a) with wake, (b) no wake, (c) difference. Solid, production; dashed, turbulent diffusion; dot-dash, pressure strain; open circle, viscous dissipation; closed circle, molecular diffusion; dotted, extra viscous terms. All terms have been normalized by $w_* q_0^2 / z_i$ (w_* and z_i from Case B1).

Finally, the scalar flux budget for $-\overline{v'q'}$ is given in Fig. 6.44. The budget is modified quite substantially by introducing the wake. Downstream of the wake, (subplot (a)), production acts as a sink between $0.35 < z/z_h 0.8$ and adds a second peak in production that reaches a maximum at $z \approx z_h$. Once again, turbulent diffusion is increased to transport flux from regions of high production to other areas of the flow field.

6.5 Turbulent Closure Evaluation

In earlier chapters, different closure models for approximating second, third, and fourth order moments were discussed. Here three models are revisited to understand how adding the wake profile to the mean velocity will affect correlation between the modeled terms and DNS. Since the profiles evolve steadily with time, results have been averaged in the same fashion as the budgets presented in §6.4: 30 equally spaced flow snapshots over $0 < \Delta x/D < 37.5$.

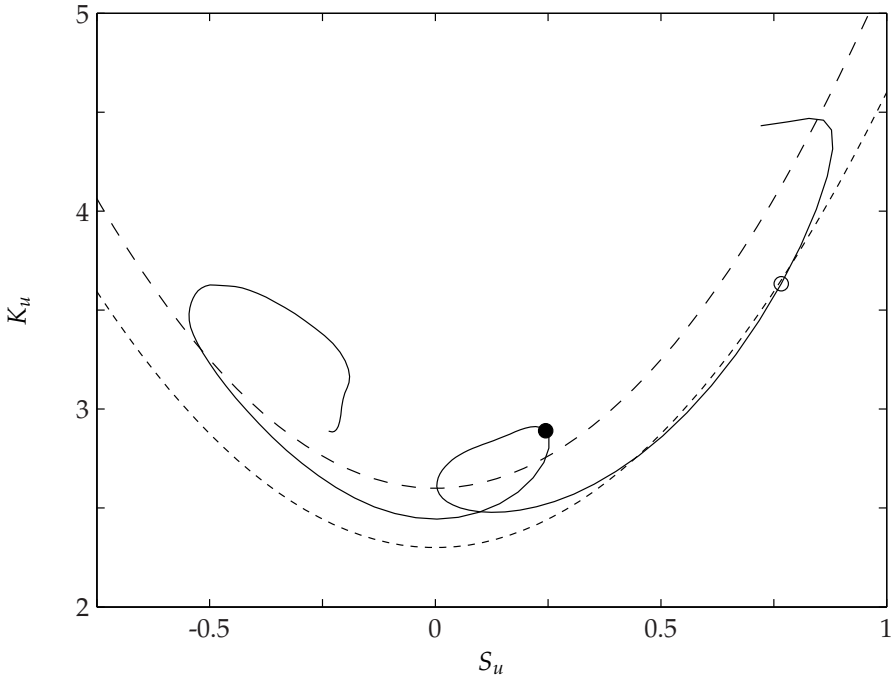

Figure 6.45: Case CN, K_u versus S_u: Solid, Case CN; dashed, $\alpha = 2.6$; dotted, $\alpha = 2.3$. Open circle, $z/z_h = 0.1$; filled circle, $z/z_h \approx 1$.

6.5.1 Kurtosis vs. Skewness under Neutral Stratification

Section 4.2.3 discussed the model first proposed by Mole and Clarke (1995). It was found that the parabolic relationship $K_{u_i}^2 = \alpha \left(S_{u_i}^2 + 1\right)$ performed well as a model of the streamwise kurtosis under neutral stratification. The spanwise and vertical components showed less agreement.

In Fig. 6.45, K_u is shown as a function of S_u for Case CN when $0 < z/z_h < 5$. Like the results shown in Fig. 4.14, the model performs well near the wall with a coefficient of $\alpha = 2.3$. Away from the wall, $\alpha = 2.6$ performs better. The height of the turbine hub is noted by the filled circle. This point is characterized by a local maximum in the both the skewness and kurtosis. Apart from the region in the immediate vicinity of the hub and the very far field (where turbulent fluctuations are small), the parabolic relationship between skewness and kurtosis appears to be unaffected by the presence of the wake.

Figure 6.46 shows the relationship between spanwise skewness and kurtosis. The y compo-

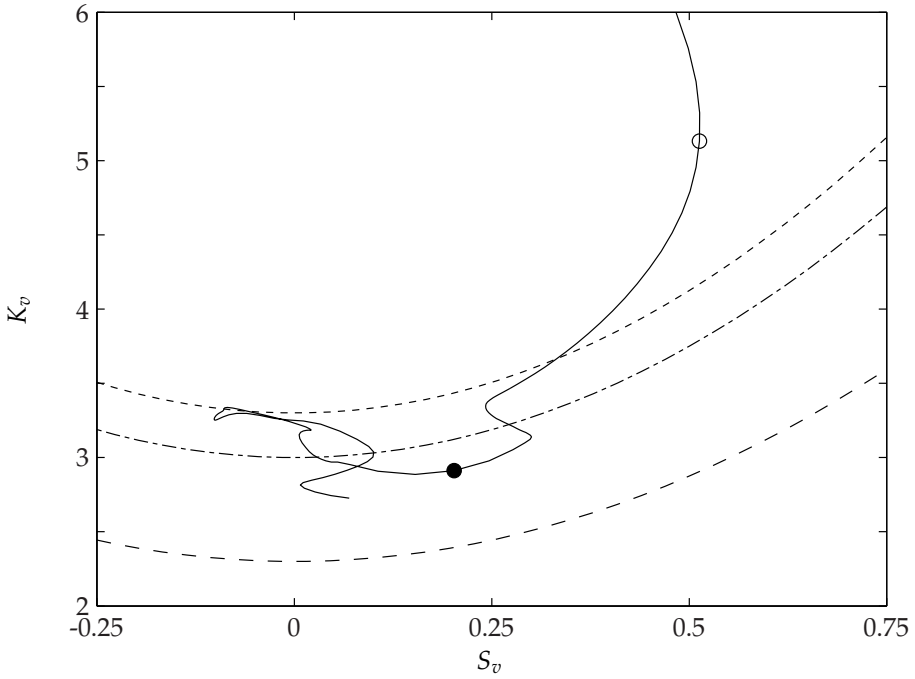

Figure 6.46: Case CN, K_v versus S_v: Solid, Case CN; dashed, $\alpha = 2.3$; dash-dot, $\alpha = 3$; dotted, $\alpha = 3.3$. Open circle, $z/z_h = 0.1$; filled circle, $z/z_h \approx 1$.

nent of velocity does not show significant changes in either high order correlation near the hub height. K_v appears to be fluctuating around $K_v \approx 3$ which suggests that fluctuations are distributed in a Gaussian manner. When $z < z_h$, a slight positive skewness is present. Above the hub height, however, the skewness appears to be centered about $S_v = 0$. It appears from Fig. 6.46 that $\alpha = 3$ is a good approximation of the model constant, but the component does not show the large changes in the magnitude of skewness or kurtosis that are evident in the streamwise direction.

In the vertical direction, a parabolic relationship between skewness and kurtosis did not appear to be evident for Case A (see Fig. 4.16). However, Fig. 6.47 shows a clear parabolic relationship around z_h. The near wall region still demonstrates large kurtosis values that were evident in Case A, but the increase in vertical energy appears to lock the vertical skewness and kurtosis together. This allows a better approximation of α to be made for the vertical component. It appears $\alpha = 2.9$ is a more suitable approximation for the vertical velocity relationship.

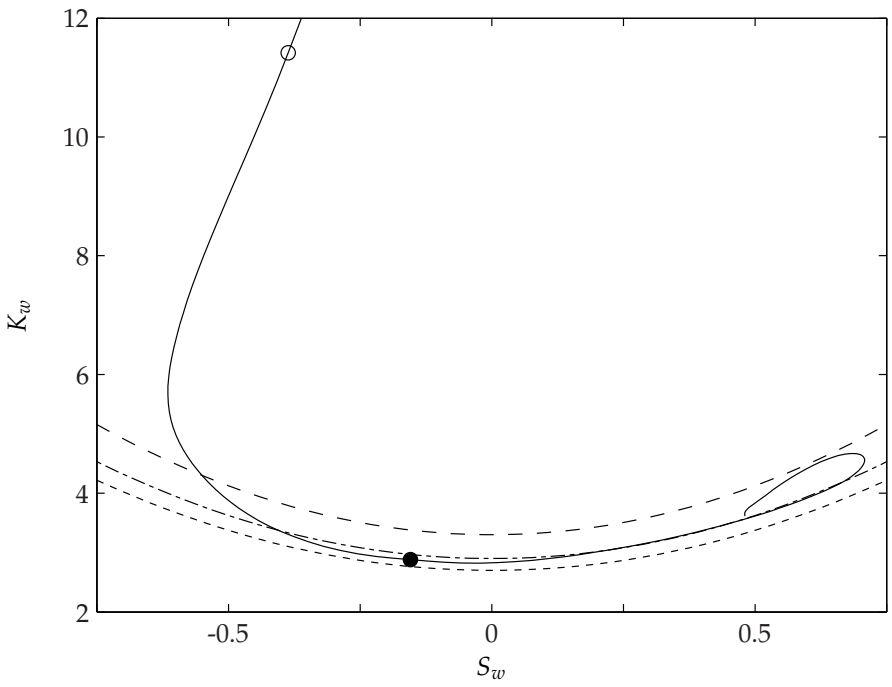

Figure 6.47: Case CN, K_w versus S_w: Solid, Case CN; dashed, $\alpha = 2.7$; dash-dot, $\alpha = 2.9$; dotted, $\alpha = 3.3$. Open circle, $z/z_h = 0.1$; filled circle, $z/z_h \approx 1$.

6.5.2 $k - \varepsilon$ Model in Turbine Wake

Here the $k - \varepsilon$ model that was discussed in §4.5 is revisited. The model equations given by Eq. 4.5.2 through 4.5.6 are reprinted here for convenience. The eddy diffusivity incorporates both horizontal directions since the mean velocity has components in both coordinate directions:

$$\sqrt{\overline{u'w'}^2 + \overline{v'w'}^2} = -K_m \sqrt{\left(\frac{\partial U}{\partial z}\right)^2 + \left(\frac{\partial V}{\partial z}\right)^2}$$

The governing equations for the kinetic energy k and the dissipation ε are given by

$$\frac{Dk}{Dt} = -\overline{u'w'}\frac{dU}{dz} - \overline{v'w'}\frac{dV}{dz} - \frac{d\left(\overline{w'p'} + \overline{w'k'}\right)}{dz} - \varepsilon$$

and

$$\frac{D\varepsilon}{Dt} = C_{\varepsilon 1}\left(\frac{\varepsilon}{k}\right)\left[-\overline{u'w'}\frac{dU}{dz} - \overline{v'w'}\frac{dV}{dz}\right] - \frac{d\overline{w'\varepsilon'}}{dz} - C_{\varepsilon 2}\left(\frac{\varepsilon^2}{k}\right)$$

The modeled eddy diffusivity is given by

$$K_m = \frac{(\alpha_m k)^2}{\varepsilon}$$

Pressure transport and turbulent diffusion is modeled as a down-gradient transport of kinetic energy:

$$\overline{w'p'} + \overline{w'k'} = -K_m \frac{dk}{dz}$$

The turbulent transport of dissipation uses the same methodology:

$$\overline{w'\varepsilon'} = -\frac{K_m}{C_{\varepsilon 3}} \frac{d\varepsilon}{dz}$$

The constant $C_{\varepsilon 3} = 1.30$ as before. Three values of α_m in the definition of the eddy diffusivity are used: (1) $\alpha_m = 0.3$, (2) $\alpha_m = 0.18$, and (3) a variable diffusivity based on the turbulent Reynolds number $\mathrm{Re}_T = \mathrm{Re}(k^2/\varepsilon)$:

$$\alpha_m = \left[0.09 \exp\left(\frac{-2.5}{1 + \mathrm{Re}_T/50} \right) \right]^{1/2}$$

Finally, the production is computed using

$$-\overline{u'w'}\frac{dU}{dz} - \overline{v'w'}\frac{dV}{dz} \approx K_m \left[\left(\frac{dU}{dz} \right)^2 + \left(\frac{dV}{dz} \right)^2 \right]$$

Figure 6.48 shows the averaged eddy diffusivity from Case CN alongside the values of K_m computed using various values of α_m. Near the wall, all three model curves over estimate the eddy diffusivity. Around the height of the turbine hub, K_m from the DNS becomes somewhat erratic with two large peaks immediately below $z/z_h = 1$. Apart from these two anomalies, it appears that $\alpha_m = 0.18$ gives the closest results as both other models overestimate K_m.

The resulting distribution of the Reynolds shear stress is shown in Fig. 6.49. Between $0.5 < z/z_h < 1$ all models do a decent job at approximating the shear stresses. Below $z/z_h \approx 0.5$, all three models overestimate the magnitude of the stress (though $\alpha_m = 0.18$ is off by the least). Above $z/z_h \approx 1$, the model with $\alpha_m = 0.18$ is, again, closest to the actual Reynolds shear stresses found in the DNS.

Like the results of Case A shown in Fig. 4.50, the production near the wall is overestimated for Case CN (Fig. 6.50). Above the hub where an increase in production occurs, however, the $k-\varepsilon$ model with $\alpha_m = 0.18$ performs exceptionally well. This is deviation from the results of Case A

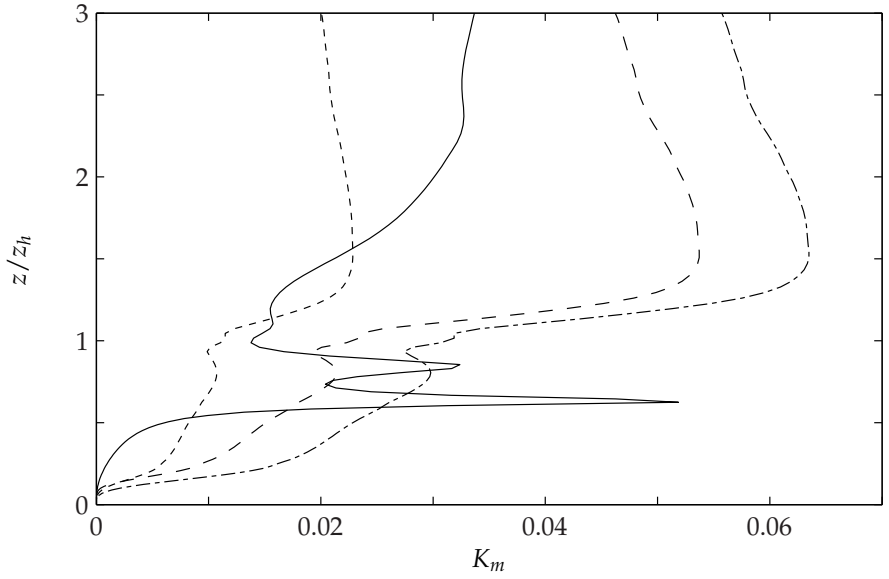

Figure 6.48: $k-\varepsilon$ model, eddy diffusivity: Solid, Case CN; dashed, $\alpha_m = f(\mathrm{Re}_T)$; dotted, $\alpha_m = 0.18$; dot-dash, $\alpha_m = 0.3$.

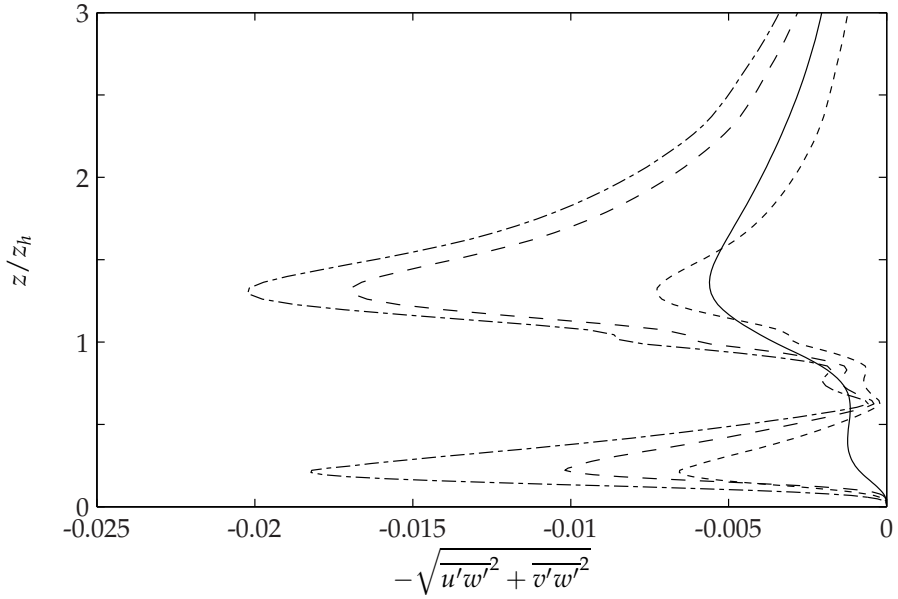

Figure 6.49: $k-\varepsilon$ model, Reynolds shear stress: Solid, Case CN; dashed, $\alpha_m = f(\mathrm{Re}_T)$; dotted, $\alpha_m = 0.18$; dot-dash, $\alpha_m = 0.3$.

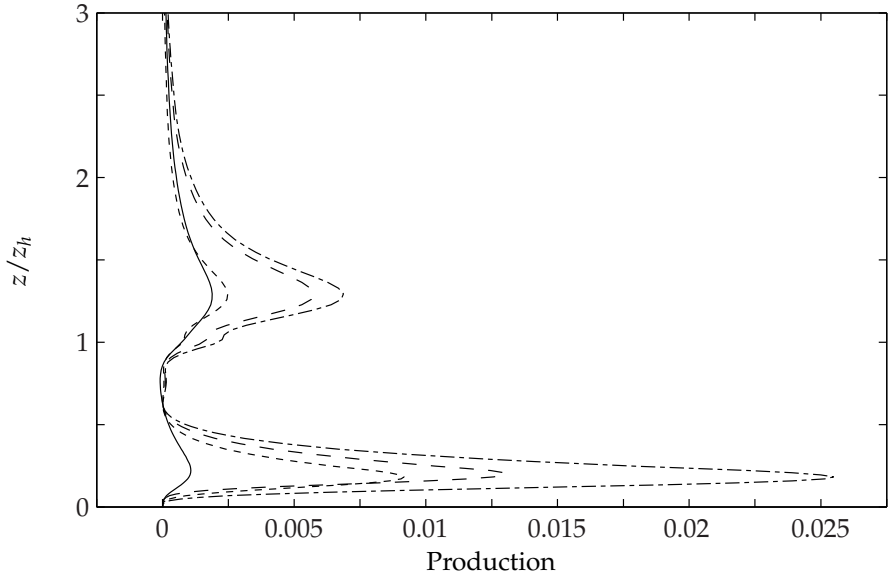

Figure 6.50: $k-\varepsilon$ model, production: Solid, Case CN; dashed, $\alpha_m = f(\mathrm{Re}_T)$; dotted, $\alpha_m = 0.18$; dot-dash, $\alpha_m = 0.3$.

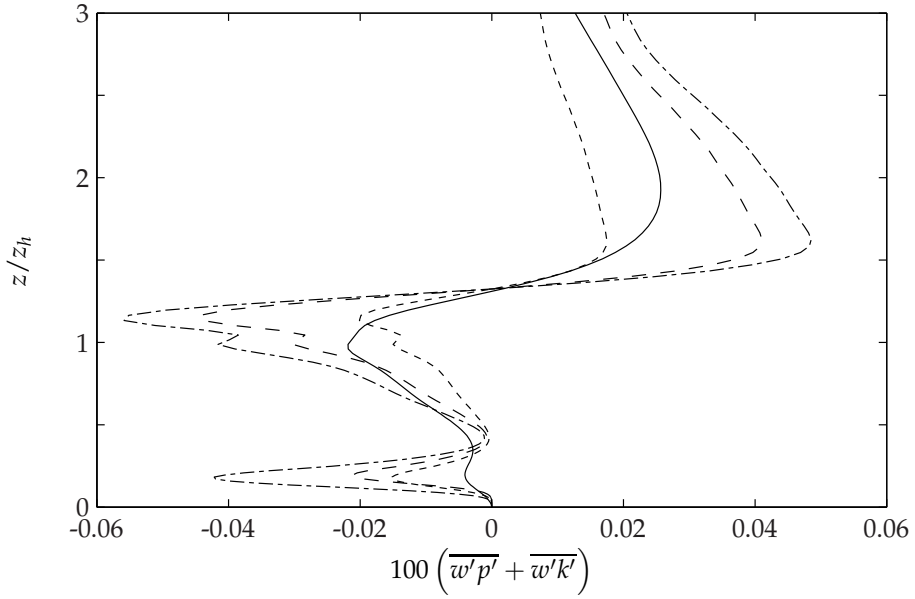

Figure 6.51: $k-\varepsilon$ model, transport terms: Solid, Case CN; dashed, $\alpha_m = f(\mathrm{Re}_T)$; dotted, $\alpha_m = 0.18$; dot-dash, $\alpha_m = 0.3$.

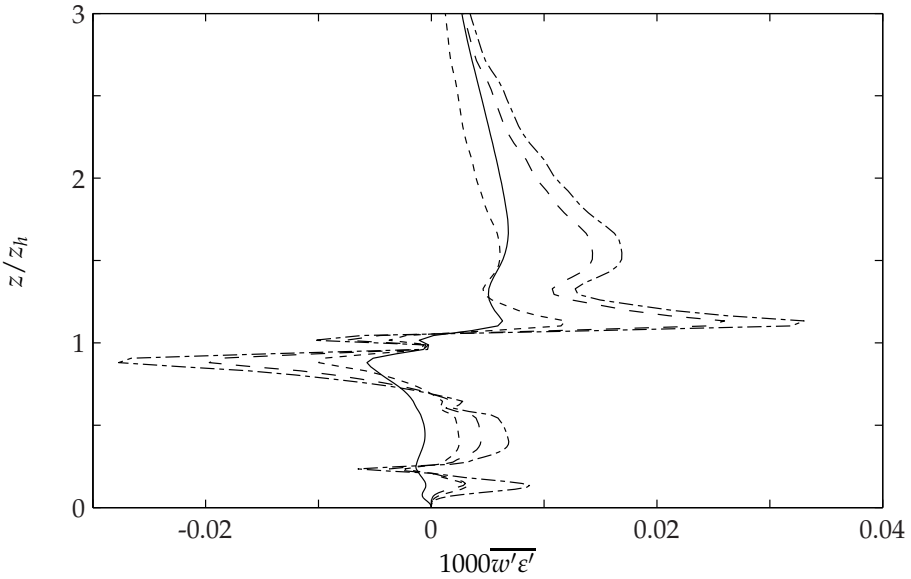

Figure 6.52: $k-\varepsilon$ model, dissipation transport: Solid, Case CN; dashed, $\alpha_m = f(\mathrm{Re}_T)$; dotted, $\alpha_m = 0.18$; dot-dash, $\alpha_m = 0.3$.

where the non-constant α_m performed best. The models with $\alpha_m = f(\mathrm{Re}_T)$ and $\alpha_m = 0.3$ both overestimated the production when $z/z_h > 1$ by over a factor of 3 (though both correctly capture the location of the maximum production). Peak production as modeled by $\alpha_m = 0.18$ is by only 12% at the peak near $z/z_h \approx 1.25$.

Turbulent transport – which considers both pressure transport and turbulent diffusion – shows inconsistencies between the model and DNS results. In Fig. 6.51, the transport is overestimated below $z/z_h < 0.5$. When $\alpha_m = 0.18$ the model does a decent job of capturing dynamics when $0.5 < z/z_h < 1.1$. Additionally, the crossover point at which transport becomes a source rather than a sink is well captured at $z/z_h \approx 1.04$. Above this, the modeled transport terms do not fall in line with the DNS results, though the actual transport is bounded by the $\alpha_m = 0.18$ and $\alpha_m = f(\mathrm{Re}_T)$ models.

The transport of dissipation for Case CN is shown in Fig. 6.52. When $z/z_h < 0.75$, the three transport terms are incorrect. $\overline{w'\varepsilon'}$ acts as a sink in the DNS while the $k-\varepsilon$ closure model shows a net gain in dissipation near the wall. At $z/z_h \approx 1$ there is a change in sign of the dissipation

transport. The location is accurately captured and the $\alpha_m = 0.18$ model is close to the capturing the magnitude of the transport term.

To summarize, many of the deficiencies in the $k - \varepsilon$ model that were noted in §4.5 are still evident in the neutrally-stratified turbine wake simulation. However, agreement is further depreciated outside of the near-wall region because of changes that were made to the mean velocity in imposing the wake. The coefficient $\alpha_m = 0.18$ appears to perform the best in predicting the turbine wake results. Especially strong agreement in turbulent energy production near $z \approx z_h$ is evident.

6.5.3 Third and Fourth Moments of Temperature and Velocity Closure

For the wake simulation under unstable stratification, the high-order closure presented for Case B1 and B2 in §5.4 is analyzed again. The previous section indicates that the third and fourth moments of vertical velocity (skewness and kurtosis) are altered when the wake is introduced into the flow. As such, it is expected that the constants controlling the third and fourth-order closures of velocity and temperature might be changed. Recall that the closure equations are given by Eq. 5.4.2.

Figure 6.53 shows the calculation of the constants a_i and d_i for $i = 1, 2$. The optimal values computed are close to those found for Case B1 (refer to Table 5.3). As with the Case B1 simulation, d_1 and d_2 are nearly zero and could easily be approximated as such with little (or no) loss in accuracy. Both $a_1 = 1.53$ and $a_2 = 0.924$ are within 7% of the values computed for Case B1. Although changes to the intensity of $\overline{w'w'}$ are occurring (as well as the skewness of the vertical velocity component), the model remains sound and the constants do not need to be altered to account for the presence of a wake. Using the optimal values shown in Fig. 6.53, the computed moments are compared with results of the DNS in Fig. 6.53. Note that w_* and θ_* are taken to be the values computed for Case B1.

As with the third-order moments, the fourth-order moments show little deviation from the Case B1 results. The small deviations in a_i and d_i are of little significance. The largest change

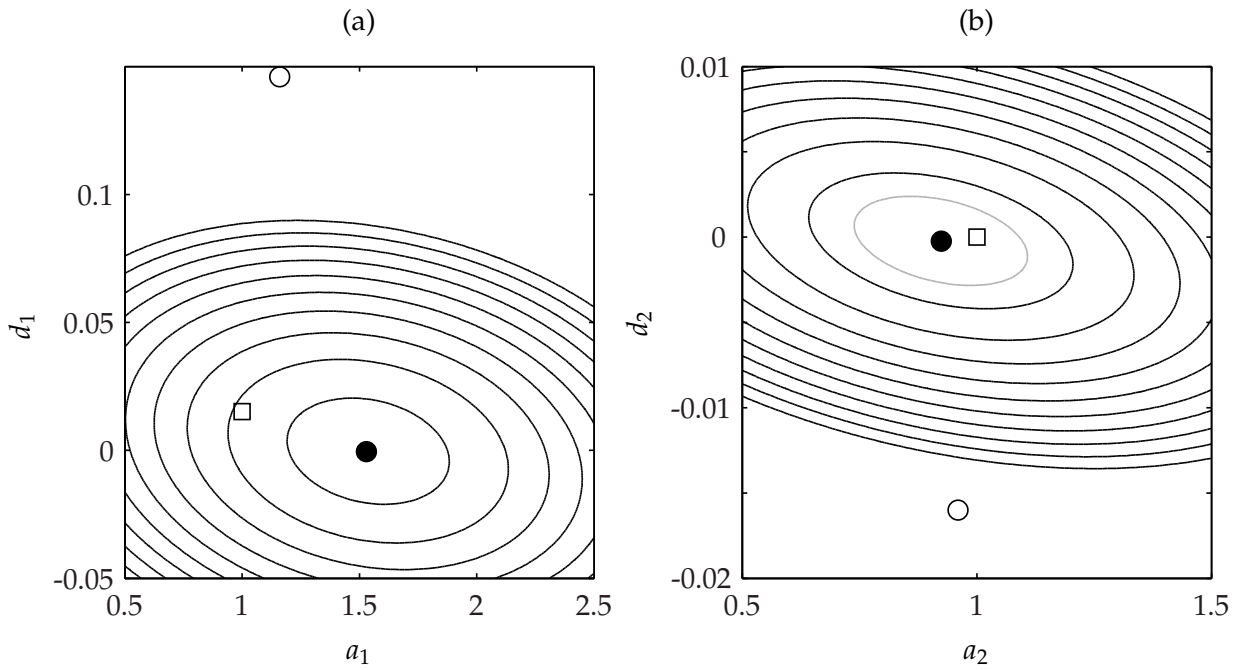

Figure 6.53: Calculation of empirical constants for third-order moments. Contours give explained variance as calculated by Eq. 5.4.6. (a) $\overline{w'^2\theta'}$, (b) $\overline{w'\theta'^2}$. Contour interval is $\Delta = 0.1$ for the black contours; gray contour gives $\sigma_f^2 = 0.95$. Open circles, Gryanik and Hartmann (2002); open squares, Zilitinkevich et al. (1999); closed circles, Case CH.

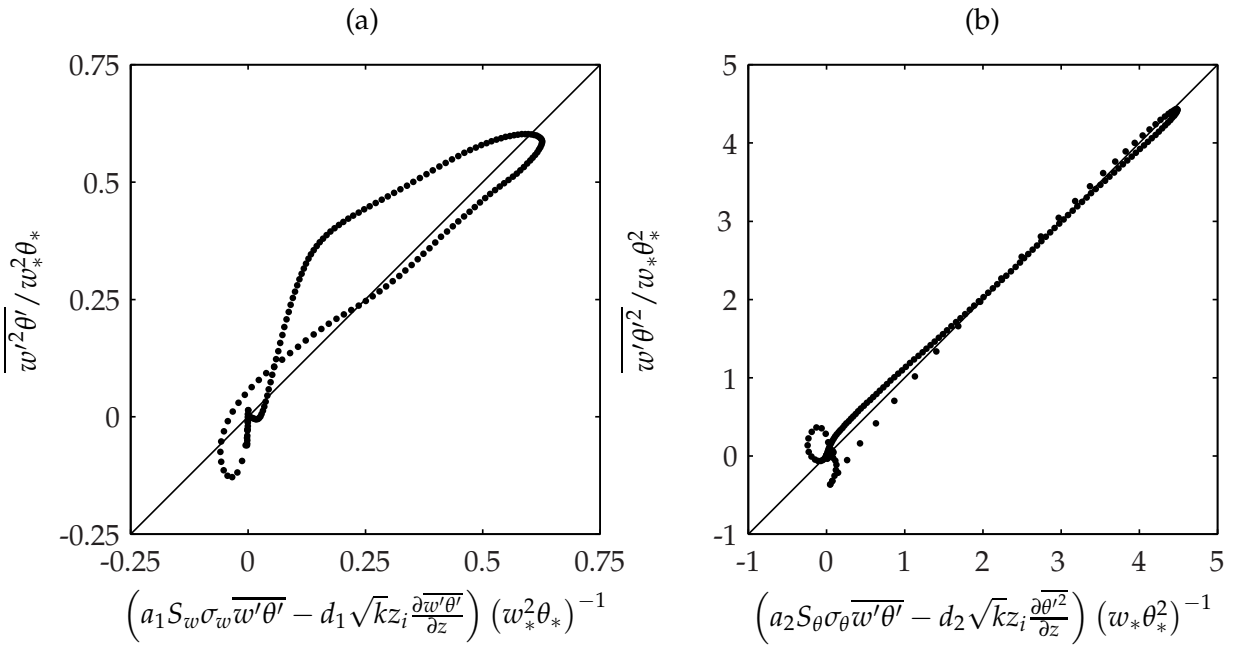

Figure 6.54: Third-order moments: (a) $\overline{w'^2\theta'}$, $a_1 = 1.53$, $d_1 = -5.02 \times 10^{-4}$; (b) $\overline{w'\theta'^2}$, $a_2 = 0.924$, $d_2 = -2.34 \times 10^{-4}$. Dots are Case B1 data and the line is unity. θ_* and w_* are taken to from Case B1.

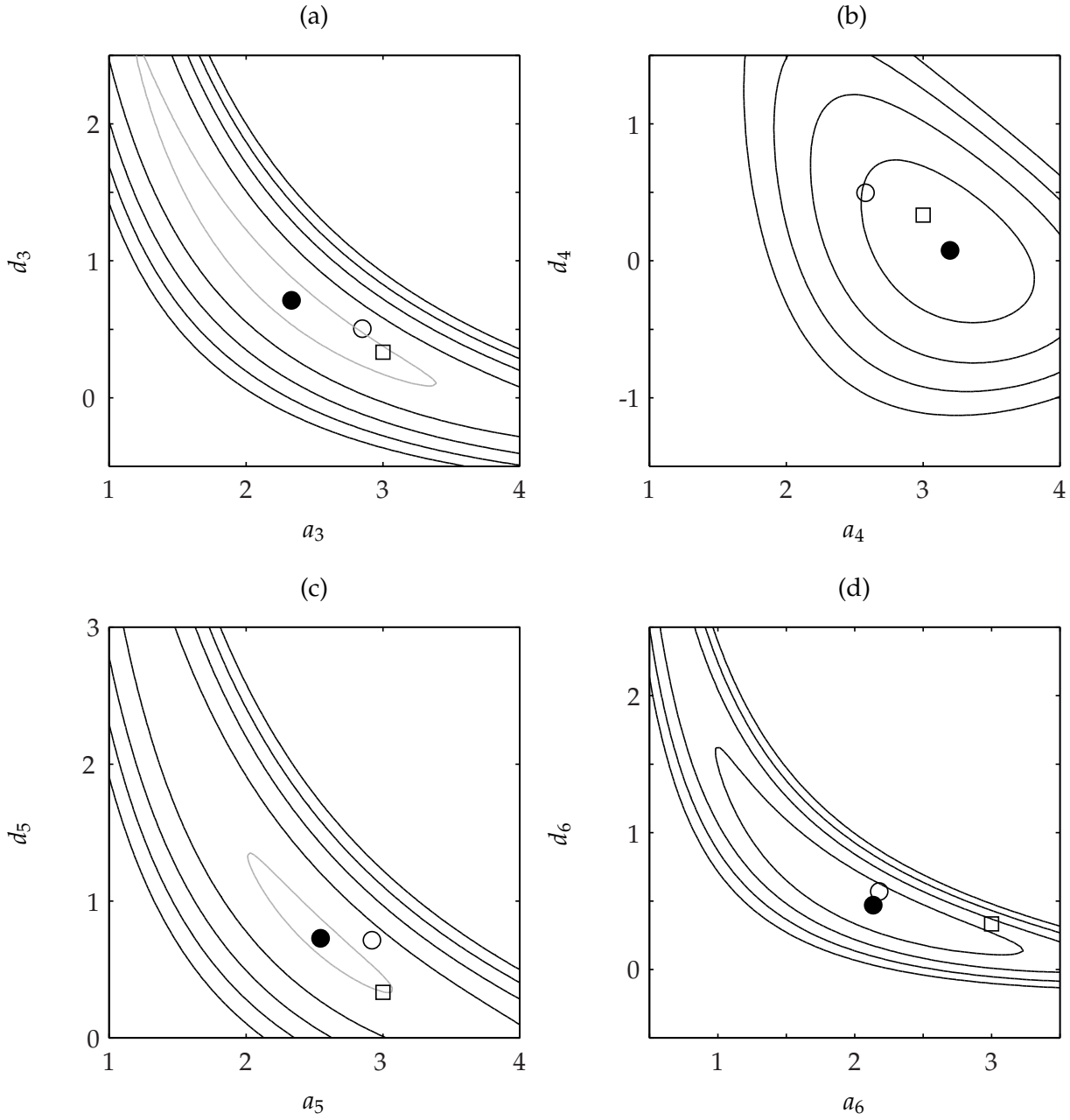

Figure 6.55: Calculation of empirical constants for fourth-order moments. Contours give explained variance as calculated by Eq. 5.4.6. (a) $\overline{w'^4}$, (b) $\overline{\theta'^4}$, (c) $\overline{w'^3\theta'}$, (d) $\overline{w'\theta'^3}$. Contour interval is $\Delta = 0.05$ for the black contours (minimum of $\sigma_f^2 = 0.8$); gray contour gives $\sigma_f^2 = 0.99$. Open circles, Gryanik and Hartmann (2002); open squares, Zilitinkevich et al. (1999); closed circles, Case CH.

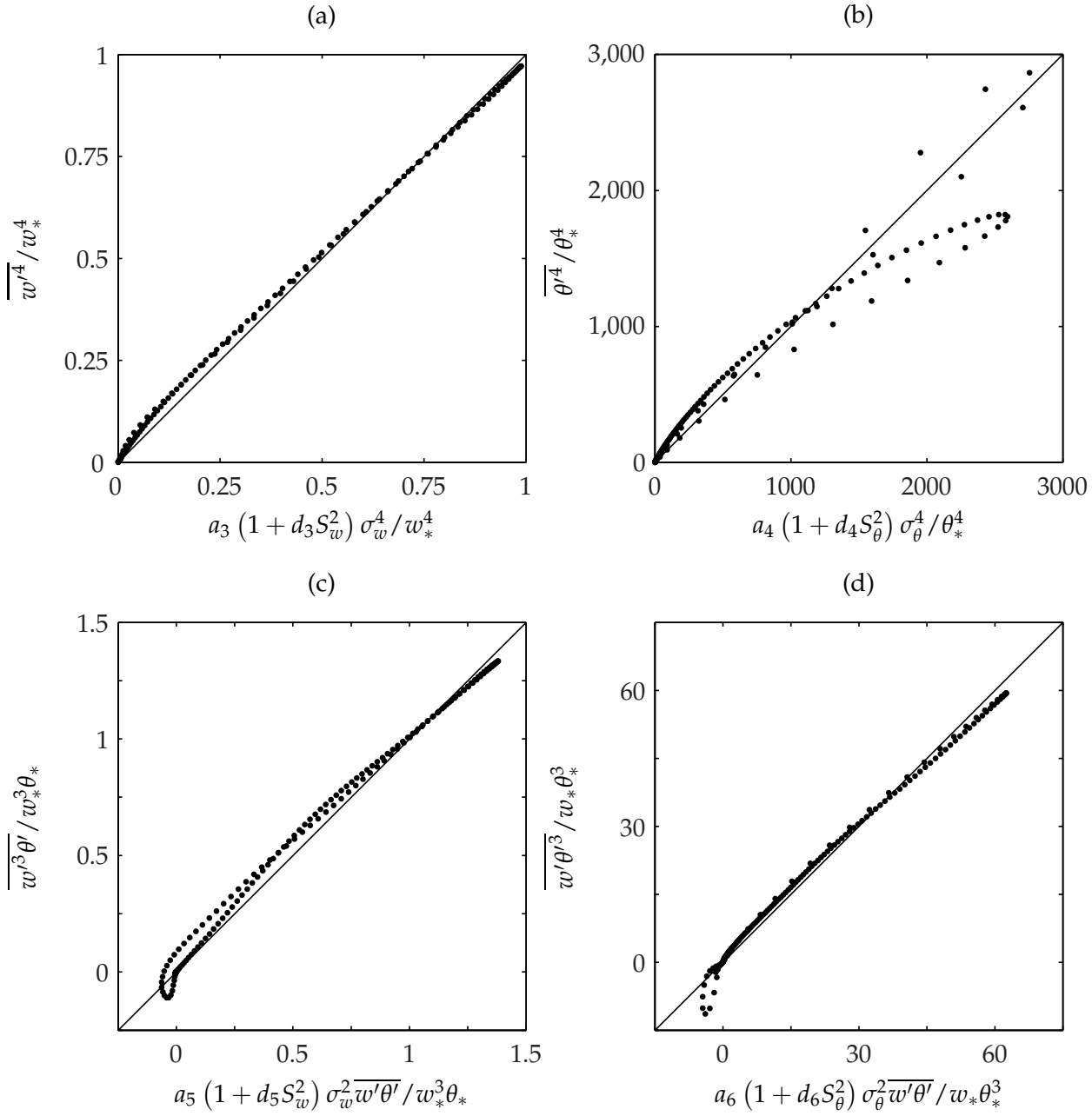

Figure 6.56: Fourth-order moments: (a) $\overline{w'^4}$, $a_3 = 2.33$, $d_3 = 0.712$; (b) $\overline{\theta'^4}$ $a_4 = 3.20$, $d_4 = -7.58 \times 10^{-2}$; (c) $\overline{w'^3\theta'}$, $a_5 = 2.55$, $d_5 = 0.727$; (d) $\overline{w'^3\theta'^2}$, $a_6 = 2.14$, $d_6 = 0.470$. Dots are Case CH data and the line is unity. θ_* and w_* are taken to from Case B1.

comes in the $\overline{\theta'^4}$ closure in Fig. 6.56(b). The new value of $a_4 = 3.20$ is approximately 8.5% off from the value found in Case B1 ($a_4 = 2.95$). Nevertheless, adding the wake to the mean profile does little to affect the capabilities of the model. Thus, the values reported in Table 5.3 should be sufficient from unstably-stratified turbine flow calculations.

6.6 Summary

Two simulations were carried out to model the influence of turbines on turbulent transport in the ABL. A velocity deficit was imposed on the mean velocity field to mimic the energy removed from the flow by the turbine. Secondly, an azimuthal component of velocity was imposed in the form of a vortex plane. Porté-Agel et al. (2010) demonstrated that turbine models with rotation more closely represented wind tunnel measure of turbine wakes.

Both the neutrally-stratified and unstably-stratified simulations were integrated forward in time after initializing the wake. Furthermore, a control case was performed for each simulation. The same initial condition without the wake was integrated forward so a proper comparison of the data could be made. Spatial evolution of the wake was determined by averaging the periodic domain over the lateral directions at various simulation times. The amount the averaged field advanced spatially was simply determined by $\Delta x = U_g \Delta t$.

Basic spatially evolving turbulence statistics show agreement with previous wind tunnel experiments. The mean velocity deficit is recovered by a spreading of the wake in the vertical direction. Once the wake impacts the wall, all momentum must be transported from above the wake to re-energize the field. While both horizontal energy components are directly impacted by an increase in energy production by mean shear, the vertical component is energized through the return-to-isotropy term which balances the energy among the three coordinate directions. Given the increased mixing due to buoyant forces, the heated case displays less of an influence from the wake in comparison to the neutrally stratified simulation.

Humidity transport throughout the boundary layer increases for both Case CN and CH. The increase in turbulent energy in the vertical direction causes an increase in turbulent diffusion in the wall-normal direction. Consequently, humidity flux at the wall under neutral stratification increases by over 10% compared to the no-wake simulation. Scalar flux for Case CH also increased but by a lesser degree. Budgets indicate that the largest increase in vertical flux is a consequence of production by mean shear. As the vertical turbulent energy increases through the return-to-isotropy term in the kinetic energy budget, additional flux is generated. Turbulent diffusion then transports the flux down to the wall.

Three of the turbulence models presented earlier were analyzed to determine if the presence of a wake would detract from the model's capabilities. Agreement with the $k-\varepsilon$ model is decreased when the wake is present. It was found that the variable model coefficient $\alpha_m = f(\mathrm{Re}_T)$ performed best for Case A. The results presented in this chapter show that $\alpha_m = 0.18$ performs best when the mean flow has been modified. The high-order closures for velocity and temperature variances and covariances showed only slight changes when a wake was imposed. In general, the coefficients found for Case CH aligned well with those of Cases B1 and B2.

CHAPTER 7

CONCLUSIONS AND RECOMMENDATIONS

This dissertation has focused on aspects of the atmospheric boundary layer under various thermal conditions. The primary objective, of which, was to better understand if – and how – humidity is transported in the wake of wind farms as previous research has suggested. Through a series of increasingly complex numerical simulations, an in depth analysis of the ABL and humidity transport was completed.

Modeling the ABL was accomplished by means of direct simulation. Although the Reynolds number of the field is substantially lower than actual atmospheric conditions, many of the results were found to agree with and complement both experimental data as well as higher Reynolds number large-eddy simulations.

This chapter has been divided into three sections: an overview of the research completed (§7.1), a summary of the significant contributions from this dissertation (§7.2), and suggestions for future research that would benefit the scientific community (§7.3).

7.1 Overview

The atmospheric boundary layer over an infinite flat plate was modeled by solving conservation equations of an incompressible fluid. System rotation effects were included to incorporate the unique dynamics associated with the spin of the Earth. Conservation of thermal energy was

Table 7.1: Overview of Cases Presented

Case	Stratification	Strength of Heating	Wake?
A	Neutral	$--$	No
B1	Unstable	Moderate	No
B2	Unstable	Vigorous	No
CN	Neutral	$--$	Yes
CH	Unstable	Moderate	Yes

solved and coupled to the vertical conservation of momentum equation via the Boussinesq approximation. Humidity and passive scalars are modeled using advection-diffusion scalar transport equations.

The conservation equations are simulated on a stretched Cartesian mesh using fourth-order accurate finite differences and a semi-implicit time advancement scheme that is second-order accurate in time. The Reynolds number of all simulations was set to $\mathrm{Re} = 1000$ where the Reynolds number is defined in terms of the inertial scales. The resolution required for such a simulation is beyond the capabilities of single-processor codes. Therefore, a parallelized numerical algorithm was developed for performing the simulations. The code functions well over a wide range of resolutions such that it is efficient for large or small size problems. As of its latest revision, the most computationally expensive subroutine of the code involves solving for the elliptic pseudo-pressure at each time step.

Since the flow geometry does not change (pressure driven boundary layer over a flat plat with Coriolis rotation), the primary difference between the various simulations is the strength of thermal stratification. A secondary effect is introduced by imposing a wake profile onto the velocity field to approximate the downstream region of a wind turbine. A total of five cases were analyzed in Chap. 4 through 6 as outlined in Table 7.1. Stable stratification (surface cooling) was not simulated in this collection of results.

Despite the fact that pure neutral stratification rarely occurs in atmospheric turbulence, a number of previous studies (Coleman, 1999, Miyashita et al., 2006, Spalart et al., 2008) have stud-

ied the neutrally stratified Ekman layer at similar Reynolds numbers to those presented in this dissertation. Results from Case A were in agreement with these previous studies. In addition to traditional turbulent statistics (mean velocity profiles, second-order velocity moments, etc.), a selection of unique analyses were completed. These include the calculation of complete energy budgets (e.g. Marlatt et al., 2012), the evaluation of two closure models used to approximate high-order moments, and visualization of turbulent structures through the calculation of velocity and pressure autocorrelations.

In general, the atmospheric boundary layer exhibits either unstable (daytime) or stable (nighttime) stratification. Chapter 5 discusses results from two simulations of the unstably-stratified Ekman layer. Given the presence of thermal stratification, the characteristic scales associated with the field change such that the inertial scales relevant in the neutrally-stratified Ekman layer are no longer applicable. Instead, the field is characterized by both shorter length and time scales. Though the strengths of the stratification applied in Cases B1 and B2 differ by an order of magnitude (see Table 5.2), both are within the range of stratifications that occur in the ABL. When a hot surface and temperature inversion are present, a mixed layer develops in both the mean velocity and temperature distributions. Like Case A, turbulent energy budgets are computed so as to understand the transfer of energy between the three Reynolds stresses. While the vigorously-heated case is dominated by the production of turbulence due to buoyancy, Case B1 (moderate heating) results show that both shear and buoyant production contribute significantly to the generation of turbulence. In simulating stratified turbulence at high Reynolds numbers, it is necessary to apply closures to high-order covariances between w' and θ'. Accurate approximation of these third (e.g. the flux of heat flux) and fourth (e.g. the flux of the flux of heat flux) moments is crucial for an accurate representation of convective dynamics. An involved analysis of a closure (see Gryanik and Hartmann, 2002) was completed to determine how model parameters change under varying levels of stratification when the Reynolds number of the turbulence is low. In general, the model performed quite well as discussed in §5.4. Finally, an analysis of top-down (nonzero entrainment,

zero wall flux) and bottom-up (zero entrainment, nonzero wall flux) diffusion processes (Wyngaard and Brost, 1984) was completed for Case B2. Two passive scalars were initialized such that both processes could be separated and analyzed individually. Slight modifications to various various models are proposed and a discussion concerning the effect of surface roughness is presented. Comparing the DNS results with rough-wall simulations, it is evident that surface roughness has little effect on top-down diffusion processes; however, roughness promotes mixing in the near-wall region for the bottom-up process.

Using the results from Case A and B1 as a reference, Chap. 6 simulates humidity transport in the wake of a wind turbine. To accomplish this, the deficit in the mean velocity field that is seen immediately downstream of a turbine was directly imposed onto the mean velocity field. Furthermore, an azimuthal velocity component was imposed in the direction perpendicular to the mean velocity direction to capture the rotational component of velocity that is imparted onto the fluid as it passes through a turbine. Turbulent fluctuations were not directly modified in any way. Using the modified initial condition, the field was integrated forward in time to approximate the spatial evolution of the wake downstream of the turbine. Mean velocity and second-order statistics demonstrated qualitative agreement between the neutrally stratified simulation and the wind tunnel experiments of Wu and Porté-Agel (2011). The streamwise energy component is increased above the hub height and decreased below. This is a direct consequence of the production term in the energy budget; the change in sign of the streamwise mean velocity below z_h causes a reduction in energy production. The vertical energy component demonstrates an increase in amplitude for both the neutrally and unstably-stratified wake simulations. However, the heated case already exhibits an amplification of vertical velocity fluctuations given the buoyant forcing. Consequently, the increase in kinetic energy is much more dramatic in the neutral case in comparison to the same simulation without a wake imposed on the initial condition.

The primary goal of this research was to understand how humidity (or other scalars) respond in the wake of a turbine. Scalars were monitored in both Case CN and CH to address this

question. For Case CN (neutral stratification), humidity flux out of the surface was drastically increased. Below the hub height there is a clear reduction in the mean concentration of the scalar $\langle q \rangle$. Above z_h, the concentration of the scalar increases. The turbulent flux of humidity in the vertical direction $\langle w'q' \rangle$ demonstrates an increase by as much as 60% of the surface scalar flux when no wake is present. For both Case CN and CH, the concentration of the scalar q at the wall was held constant ($q = q_0$). Though this prohibits the concentration of q to change on the wall, the viscous flux at the wall is allowed to vary with time. In comparison to the simulation without a wake, the flux at the wall increased by over 10% far downstream of the turbine. This would represent a drying effect at the wall and humidity (water) content in the surface would likely decrease downstream of the turbine.

The heated wake simulation (Case CH) also showed a decrease in the concentration of $\langle q \rangle$ near the wall. However, the layer which shows a decrease in the humidity content is much thinner when thermal stratification is present. The excess humidity that is transported upwards is immediately mixed. Buoyant forcing excites the vertical direction in a manner such that the turbine has a much smaller effect on the vertical transport of humidity. Flux at the wall increases by almost 4% when the wake is present under stratified conditions. Thus, introducing the turbine into the velocity field under thermal stratification still produces an increase in the vertical transport of humidity. However, as the strength of stratification increases, the extent to which the turbine affects the turbulent flux will likely be reduced as the flow dynamics are overwhelmed by buoyant forces.

7.2 Significant Contributions

- A fully parallelized direct simulation code was developed to solve the Ekman layer flow geometry with thermal stratification and two (passive or active) scalars. Verification of the numerical algorithm was accomplished by monitoring the growth of perturbations in a channel flow and comparing them with growth rates derived from the Orr-Sommerfeld equation.

- The neutrally-stratified Ekman layer at Re $= 1000$ was simulated in a periodic domain. Temporally and spatially-averaged turbulent statistics agree with similar simulations.

- The parabolic relationship $K_u = \alpha\left(S_u^2 + 1\right)$ was critiqued for all three velocity components under neutral stratification. It was found that the streamwise kurtosis is accurately captured by the parabolic relationship in the near-wall region when $\alpha = 2.3$ and in the logarithmic region of the velocity field when $\alpha = 2.6$. The other two components demonstrated less agreement with the model.

- The full kinetic energy budgets were analyzed under neutral and unstable stratification (at two levels of heating). As Reynolds number increases, the role of Coriolis redistribution is reduced. With vigorous heating, both horizontal energy components behave in a similar fashion except in the near wall region where shear production occurs in the streamwise direction. Under moderate heating, the near-wall region resembles the neutrally stratified budgets. Moving away from the wall, buoyancy plays a significant role in energizing the vertical energy component (which is then transfered through pressure strain to both horizontal components.

- Characteristic turbulent structures in the neutral Ekman layer were computed by means of velocity and pressure autocorrelations. Structures near the wall tend to align with the surface shear direction. Away from the wall, velocity autocorrelations tend to align between the local shear direction and the coordinate direction of the velocity component. The spanwise velocity autocorrelation shows significant lifting downstream of the structure center suggesting that turbulence generated near the wall is transported upwards as it progresses downstream. The spanwise tilt of the streamwise autocorrelation is a direct results of system rotation.

- The $k-\varepsilon$ turbulence model was evaluated for the neutrally-stratified Ekman layer. Results indicate that the model does a good job of calculating the eddy diffusivity when $\alpha_m =$

$f(\mathrm{Re}_T)$. The closure assumes that all three energy components are equal and the inter-component transport of energy is ignored. Given the anisotropy of the field, ignoring energy redistribution may contribute to model inaccuracies.

- Under unstable stratification, a model of the third and fourth-order vertical velocity and temperature correlations was shown to perform well. The optimal coefficients computed from the DNS results change only slightly with large changes in $-z_i/L$. In most cases, the optimal coefficient is close to the theoretical value of the constant. Likely because of the low Reynolds number, down-gradient diffusion of $\overline{w'\theta'}$ and $\overline{\theta'^2}$ contributes very little to the closure of $\overline{w'^2\theta'}$ and $\overline{w'\theta'^2}$ respectively. The extra diffusion terms can be ignored ($d_1 = d_2 = 0$) with little loss to the accuracy of the model.

- Top-down diffusion processes are not affected by surface roughness. However, the gradient function g_b increases near the wall when a smooth surface is present. This indicates that mixing is decreased near the wall for bottom-up diffusion. The flow region where smooth and rough-wall simulations diverge is confined to a narrow region at the wall (as the viscous sublayer is approached). A modification to the model for the bottom-up scalar variance is proposed: the piecewise model of Moeng and Wyngaard (1984) is replaced by a single function which improves accuracy in the mixed layer and better approximates the near-wall region of the smooth-wall low Reynolds number flow.

- A means of approximating the wake of a wind turbine via a periodic domain is introduced. Mean velocity statistics and second-order correlations indicate the method qualitatively reproduces the region downstream of a single turbine (along the centerline of the turbine).

- DNS results indicate that the increase in vertical turbulent energy downstream of the turbine tends to increase the transport of humidity away from the wall when the surface has a humidity concentration that is greater than the edge of the boundary layer. Under neutral stratification, surface humidity flux increases by more than 10% relative to the same sim-

ulation without introducing a wake. Though an increase in humidity flux is still evident when surface heating is present, the turbine has less influence on the transport dynamics since buoyant forcing already increases vertical mixing (hence the existence of the mixed layer).

- Vertical turbulent flux is increased primarily through production by mean shear of the mean humidity gradient. Immediately downstream of the turbine, however, the scalar gradient is identical with and without the wake (since humidity is not modified by adding a wake). Consequently, initial changes in the humidity flux occur when pressure strain redirects energy from the horizontal turbulent energy components (where energy increases directly through a change in production by mean shear) to the vertical energy component. This increase in energy directly increases the production of vertical scalar flux. Turbulent diffusion then transports the increase in flux down to the wall.

7.3 Recommendations for Future Work

A number of interesting (and challenging) research subjects can be pursued to build upon the work previously discussed. A few of the most interesting and beneficial are outlined below.

- The topic of the stably-stratified atmospheric boundary layer should be pursued. During nighttime hours, the atmosphere can exhibit a low-level jet of high velocity air. Given its relatively low turbulent intensity, this excess momentum is ideal for wind farming applications. However, it is not fully understood why the jet forms and what conditions lead to its development. A DNS of the low Reynolds number stably-stratified could give light to a number of interesting topics concerning the jets formation: (1) What specific stratification conditions lead to the formation of the jet? (2) Do daytime convective boundary layer conditions impact the development and strength of the jet? (3) Do turbulence closures correctly handle subgrid scales in the jet (large velocity gradient but low turbulent

intensity)?

- In the unstably-stratified boundary layer simulations that were performed, the temperature inversion that was imposed was chosen based on previous work. It is expected that the strength of the inversion could have an impact on how strong top-down diffusion processes evolve. A series of DNS simulations with variations in the lapse rate of the temperature at the top of the mixed layer will be useful to parameterize the entrainment process at the top of the convective boundary layer.

- The $k - \varepsilon$ model has a number of improvements and modifications that have been developed to address specific flow geometries. Evaluating these model revisions would show if a modification to the $k - \varepsilon$ model might improve its capabilities when system rotation is present and the mean velocity is three dimensional.

- The closures used for LES were not addressed in this work. Like RANS simulations, LES requires that unresolved scales be modeled. The DNS data provide an excellent opportunity to determine the limitations of these models with respect to low Reynolds number flow with Coriolis acceleration.

- The turbine wake results presented here represent an attempt to address the problem of environmental impacts by wind turbine wakes. While some work has been completed by the scientific community on the impact of 'infinite wind farms,' it would be interesting to use DNS to model the spatially evolving flow past a model turbine (possibly using a drag-disk approximation). This case would require careful handling of the periodic boundary conditions. A possible solution would be to remove the Coriolis acceleration so that the mean flow is two-dimensional. This would allow the domain to be elongated in the streamwise direction and contracted in the spanning direction. Periodicity could be enforced as long as the flow completely recovers before reaching the end of the domain. This could be encouraged by a buffer region which helps damp out the turbulent signal

associated with the turbine.

- The assumption that the bottom boundary had a constant humidity concentration was sufficient for this work. An interesting alternative would be to run a large-eddy simulation at atmospheric conditions and develop a surface model to mimic the change in water content in the soil. This would give an indication of how quickly moisture is transported upwards from the Earth's surface.

- All cases in this study were performed with flow over a flat wall. Given that typical atmospheric flows rarely occur over perfectly flat terrain, it would be interesting to introduce topographic features into the field. Two prominent cases come to mind: (1) Modeling flow over an infinite series of hills. The case can be run using the present code in its current periodic configuration. The hills can be added be either mapping the lower boundary onto a smooth two-dimensional contour and adjusting the difference operators as needed (difficult), or by introducing an additional forcing function which creates an immersed boundary in the field (easier). The former is beneficial in that no grid resolution is lost underneath the hill, while the latter could need less programming effort. (2) The second case with flow over a hill can be approximated by the simple case of flow over a forward facing (smooth) step. Accurate predictions of separation turbulence dynamics could benefit wind farm design in regions with topographic features.

- Little work was performed on time dependent flow visualization. The turbine wake simulations present a unique opportunity to visualize the evolution of turbulence as the mean velocity undergoes drastic changes. Flow visualization might help uncover how eddies change in shape and strength when the flow is forced away from its equilibrium state. The conclusions of such a study could potentially be applied to any flow where the turbulent fluctuations remain relatively unchanged but the mean flow is drastically modified in a nearly instantaneous manner.

REFERENCES

K. Abdella and N. McFarlane. A New Second-Order Turbulence Closure Scheme for the Planetary Boundary Layer. J. of Atm. Sci., 54:1850–1867, 1997.

K. Abdella and N. McFarlane. Reply. J. of Atm. Sci., 56:3482–3483, 1999.

F. Akerblom. Recherches sur les courants les plus bas de l'atmosphère au-dessus de Paris. Nova Acta Reg. Soc. Sci., 2:1–45, 1908.

S. Alberghi, A. Maurizi, and F. Tampieri. Relationship between the Vertical Velocity Skewness and Kurtosis Observed during Sea-Breeze Convection. J. of Applied Meteorology, 4:885–889, 2002.

D. A. Anderson, J. C. Tannehill, and R. H. Pletcher. Computational Fluid Mechanics and Heat Transfer. Hemisphere Publishing Corporation, New York, NY, 1984.

K. E. Atkinson. An Introduction to Numerical Analysis, 2^{nd} Ed. John Wiley & Sons, 1989.

C. W. V. Atta and J. C. Wyngaard. On higher-order spectra of turbulence. J. Fluid Mech., 72: 673–694, 1975.

S. Balay, W. D. Gropp, L. C. McInnes, and B. F. Smith. Efficient management of parallelism in object oriented numerical software libraries. In E. Arge, A. M. Bruaset, and H. P. Langtangen, editors, Modern Software Tools in Scientific Computing, pages 163–202. Birkhäuser Press, 1997.

S. Balay, J. Brown, , K. Buschelman, V. Eijkhout, W. D. Gropp, D. Kaushik, M. G. Knepley, L. C. McInnes, B. F. Smith, and H. Zhang. PETSc users manual. Technical Report ANL-95/11 - Revision 3.1, Argonne National Laboratory, 2010.

S. Balay, J. Brown, K. Buschelman, W. D. Gropp, D. Kaushik, M. G. Knepley, L. C. McInnes, B. F. Smith, and H. Zhang. PETSc Web page, 2011. http://www.mcs.anl.gov/petsc.

B. B. Balsley, R. G. Frehlich, M. L. Jensen, and Y. Meillier. Extreme Gradients in the Nocturnal Boundary Layer: Structure, Evolution, and Potential Causes. J. of the Atm. Sci., 60:2496–2508, 2003.

R. M. Banta. Stable-boundary-layer regimes from the perspective of the low-level jet. Acta Geophysica, 56:58–87, 2008.

R. J. Beare, M. K. Macvean, A. A. M. Holtslag, J. Cuxart, I. Esau, J.-C. Golaz, M. A. Jimenez, M. Khairoutdinov, B. Kosovic, D. Lewellen, T. S. Lund, J. K. Lundquist, A. McCabe, A. F. Moene, Y. Noh, S. Raasch, and P. Sullivan. An Intercomparison of Large-Eddy Simulations of the Stable Boundary Layer. Boundary-Layer Meteorol, 118:247–272, 2006.

A. C. M. Beljaars, J. L. Walmsley, and P. A. Taylor. A mixed spectral finite-difference model for neutrally stratified boundary layer flow over roughness changes and topography. Bound. Layer Meteor., 38:273–303, 1987.

A. K. Blackadar and H. Tennekes. Asymptotic similarity in neutral barotropic planetary boundary layers. J. Atm. Sci., 25:1015–1020, 1968.

A. Brandenburg and A. Nordlund. Astrophysical turbulence modeling. Rept. Prog. Phys., 74: 046901, 2011.

M. Calaf, C. Meneveau, and J. Meyers. Large eddy simulation study of fully developed wind-turbine array boundary layers. Phys. Fluids, 22, 2010.

M. Calaf, M. B. Parlange, and C. Meneveau. Large eddy simulation study of scalar transport in fully developed wind-turbine array boundary layers. Phys. Fluids, 23, 2011.

D. R. Caldwell and C. W. V. Atta. Characteristics of Ekman boundary layer instabilities. J. Fluid Mech., 44:79–95, 1970.

D. R. Caldwell, C. W. V. Atta, and K. N. Helland. A laboratory study of the turbulent Ekman layer. Geophys. Fluid Dyn., 3:125–160, 1972.

L. P. Chamorro and F. Porté-Agel. A Wind-Tunnel Investigation of Wind-Turbine Wakes: Boundary-Layer Turbulence Effects. Bound. Layer Meteor., 132:129–149, 2009.

L. P. Chamorro and F. Porté-Agel. Effects of Thermal Stability and Incoming Boundary-Layer Flow Characteristics on Wind-Turbine Wakes: A Wind-Tunnel Study. Bound. Layer Meteor., 136:515–533, 2010.

W. Cheney and D. Kincaid. Numerical Mathematics and Computing, 5^{th} Ed. Brooks/Cole-Thomson Learning, Belmont, CA, 2004.

G. N. Coleman. Similarity Statistics from a Direct Numerical Simulation of the Neutrally Stratified Planetary Boundary Layer. J. of Atm. Sci., 56:891–900, 1999.

G. N. Coleman and J. H. Ferziger. A Numerical Study of the Convective Boundary Layer. Boundary-Layer Meteorol, 70:247–272, 1994.

G. N. Coleman and J. H. Ferziger. Direct numerical simulation of a vigorously heated low Reynolds number convective boundary layer. Dyn. of Atm. and Oceans, 24:85–94, 1996.

G. N. Coleman, J. H. Ferziger, and P. R. Spalart. A numerical study of the Ekman layer. J. Fluid Mech., 213:313–348, 1990.

G. N. Coleman, J. H. Ferziger, and P. R. Spalart. Direct simulation of the stably stratified turbulent Ekman layer. J. Fluid Mech., 244:677–712, 1992.

J. Crank and P. Nicolson. A Practical Method for Numerical Evaluation of Solutions of Partial Differential Equations of the Heat-Conduction Type. Proc. Cambridge Philos. Soc., 43:50–67, 1947.

G. T. Csanady. On the "Resistance Law" of a Turbulent Ekman Layer. J. of Atm. Sci., 24:467–471, 1967.

J. W. Deardorff. Numerical Investigation of Neutral and Unstable Planetary Boundary Layers. J. of Atm. Sci., 29:91–115, 1972.

J. W. Deardorff and G. E. Willis. Further Results from a Laboratory Model of the Convective Planetary Boundary Layer. Bound. Layer Meteor., 32:205–236, 1985.

V. W. Ekman. On the Influence of the Earth's Rotation on Ocean-Currents. Arch. Math. Astron. Phys., 2:1–52, 1905.

D. Etling and R. A. Brown. Roll Vortices in the Planetary Boundary Layer: A Review. Boundary-Layer Meteorology, 65:215–248, 1993.

J. H. Ferziger and M. Perić. Computational Methods for Fluid Dynamics, 3^{rd} rev. ed. Springer, New York, NY, 2002.

R. P. Feynman, R. B. Leighton, and M. L. Sands. The Feynman Lectures on Physics. Addison-Wesley Publishing Co., Reading, MA, 1963.

J. J. Finnigan and S. E. Belcher. Flow over a hill covered with a plant canopy. Quart. J. R. Met. Soc., 130:1–29, 2004.

R. Frehlich, Y. Meillier, M. L. Jensen, and B. Balsley. A Statistical Description of Small-Scale Turbulence in the Low-Level Nocturnal Jet. J. of Atm. Sci., 61:1079–1085, 2004.

V. M. Gryanik and J. Hartmann. A Turbulence Closure for the Convective Boundary Layer Based on a Two-Scale Mass-Flux Approach. J. of Atm. Sci., 59:2729–2744, 2002.

T. Hahm and S. Wußow. Turbulent Wakes in Wind Farm Configuration. In European Wind Energy Conference and Exhibition, Athens, Greece, 27 February – 2 March 2006.

M. Hand, D. Simms, L. Fingersh, D. Jager, J. Cotrell, S. Schreck, and S. Larwood. Unsteady aerodynamics experiment phase vi: Wind tunnel test configurations and available data campaigns. Technical report NREL/TP-500-29955, NREL, December 2001.

D. M. Hargreaves and N. G. Wright. On the use of the $k-\varepsilon$ model in commercial CFD software to model the neutral atmospheric boundary layer. J. Wind Eng. Ind. Aerodyn., 95:355–369, 2007.

J. R. Holton. An Introduction to Dynamic Meteorology, Fourth Edition, pages 28–54,115–138. Elsevier Press, Burlington, MA, 2004.

J. C. R. Hunt, G. J. Shutts, and S. H. Derbyshire. Stably stratified flows in meteorology. Dyn. of Atm. and Oceans, 23:63–79, 1996.

J. J. Ernest Wilkins. A Note on Skewness and Kurtosis. Ann. Math. Stat., 15:133–135, 1944.

R. Johnstone and G. N. Coleman. The turbulent Ekman boundary layer over an infinite wind-turbine array. J. Wind Eng. Ind. Aerodyn., 100:46–57, 2012.

W. P. Jones and B. E. Launder. The prediction of laminarization with a two-equation model of turbulence. Intern. J. Heat Mass Transf., 15:301–314, 1972.

W. P. Jones and B. E. Launder. The calculation of low reynolds number phenomena with a two-equation model of turbulence. Intern. J. Heat Mass Transf., 16:1119–1130, 1973.

H. J. J. Jonker, P. P. Sullivan, E. G. Patton, and M. van Reeuwijk. Direct Numerical Simulation of Entrainment in Dry Convective Boundary Layers. In 19th Symposium on Boundary Layers and Turbulence, Keystone, CO, August 2010.

J. C. Kaimal and J. J. Finnigan. Atmospheric Boundary Layer Flows, Their Structure and Measurement. Oxford University Press, New York, NY, 1994.

D. W. Keith, J. F. DeCarolis, D. C. Denkenberger, D. H. Lenschow, S. L. Malyshev, S. Pacala, and P. J. Rasch. The influence of large-scale wind power on global climate. PNAS, 101:16115–16120, 2004.

L. V. Keller and A. A. Friedmann. Differentialgleichung für die turbulente Bewegung einer Kompressiblen Flüssigkeit. Proc. First Intern. Congr. Appl. Mech., Delft, pages 394–405, 1924.

M. L. Khandekar. Effect of Moisture on the Potential Temperature. Arch. Met. Geoph. Biokl., 26: 31–38, 1977.

J. Kim, P. Moin, and R. Moser. Turbulence statistics in fully developed channel flow at low reynolds number. J. Fluid Mech., 177:133–166, 1987.

J.-J. Kim and J.-J. Baik. A numerical study of the effects of ambient wind direction on flow and dispersion in urban street canyons using the RNG $k - \varepsilon$ turbulence model. Atmospheric Environment, 38:3039–3048, 2004.

A. N. Kolmogorov. Dissipation of energy in the locally isotropic turbulence. Proc. R. Soc. Lond., 434:15–17, 1991.

B. Kosović and J. A. Curry. A Large Eddy Simulation Study of a Quasi-Steady, Stably Stratified Atmospheric Boundary Layer. J. of the Atm. Sci., 57:1052–1068, 2000.

R. H. Kraichnan. Relation of Fourth-Order to Second-Order Moments in Stationary Isotropic Turbulence. Physical Review, 107:1485–1490, 1957.

P. K. Kundu and I. M. Cohen. Fluid Mechanics, Third Edition. Elsevier Academic Press, San Diego, CA, 2004.

C.-L. Lappen, D. Randall, and T. Yamaguchi. A Higher-Order Closure Model with an Eplicit PBL Top. J. of Atm. Sci., 67:834–850, 2010.

A.-T. Le, G. Coleman, and J. Kim. Near-wall turbulence structures in three-dimensional boundary layers. J. of Heat and Fluid Flow, 21:480–488, 2000.

M. A. LeMone. Some Observations of Vertical Velocity Skewness in the Convective Boundary Layer. J. of Atm. Sci., 47:1163–1169, 1990.

D. H. Lenschow, J. Mann, and L. Kristensen. How Long Is Long Enough When Measuring Fluxes and Other Turbulence Statistics? J. of Atmospheric and Oceanic Technology, 11:661–673, 1994.

D. H. Lenschow, V. Wulfmeyer, and C. Senff. Measuring Second- through Fourth-Order Moments in Noisy Data. J. of Atmospheric and Oceanic Technology, 17:1330–1347, 2000.

L. Liang, L. Xiaofeng, L. Borong, and Z. Yingxin. Improved $k - \varepsilon$ two-equation turbulence model for canopy flow. Atmospheric Environment, 40:762–770, 2006.

C.-L. Lin, C.-H. Moeng, P. P. Sullivan, and J. C. McWilliams. The effect of surface roughness on flow structures in a neutrally stratified planetary boundary layer flow. Phys. Fluids, 9:3235–3249, 1997.

B. Maalouf, I. Dobrev, and F. Massouh. Vortex structure in the wake of a wind turbine rotor. In 19$^{\text{ème}}$ Congrès Francais de Mécanique, August 2009.

L. Mahrt. Mixed Layer Moisture Structure. Monthly Weather Review, 104:1403–1407, 1976.

N. M. Mansour, J. Kim, and P. Moin. Reynolds-stress and dissipation-rate budgets in a turbulent channel flow. J. Fluid Mech., 194:15–44, 1988.

S. Marlatt, S. Waggy, and S. Biringen. Direct Numerical Simulation of the Turbulent Ekman Layer: Turbulent Energy Budgets. J. of Thermophysics and Heat Transfer, 24:544–555, 2010.

S. Marlatt, S. Waggy, and S. Biringen. Direct Numerical Simulation of the Turbulent Ekman Layer: Evaluation of Closure Models. J. Atm. Sci., 69:1106–1117, 2012.

S. W. Marlatt. Direct Numerical Simulation of Ekman Layer Transition and Turbulence. PhD thesis, University of Colorado, Boulder, 1994.

I. Marusic and G. J. Kunkel. Streamwise turbulence intensity formulation for flat-plate boundary layers. Phys. Fluids, 15(8):2461–2464, 2003.

P. J. Mason. Large-Eddy Simulation of the Convective Atmospheric Boundary Layer. J. of Atm. Sci., 46(11):1492–1516, 1989.

P. J. Mason and R. I. Sykes. A Two-Dimensional Numerical Study of Horizontal Roll Vortices in the Neutral Atmospheric Boundary Layer. Q. J. R. Meteorol. Soc., 106:351–366, 1980.

P. J. Mason and R. I. Sykes. A Two-Dimensional Numerical Study of Horizontal Roll Vortices in an Inversion Capped Planetary Boundary Layer. Q. J. R. Meteorol. Soc., 108:801–823, 1982.

W. J. Massman. A review of the molecular diffusivites of H_2O, CO_2, CH_4, CO, O_3, SO_2, NH_3, N_2O, NO, and NO_2 in air, O_2 and N_2 near STP. Atmospheric Environment, 32(6):1111–1127, 1998.

D. Medici and P. H. Alfredsson. Measurements on a Wind Turbine Wake: 3D Effects and Bluff Body Vortex Shedding. Wind Energy, 9:219–236, 2006.

A. Melling, S. Noppenberger, M. Still, and H. Venzke. Interpolation Correlations for Fluid Properties of Humid Air in the Temperature range 100 °C to 200 °C. J. Phys. Che. Ref. Data, 26(4): 1111–1123, 1997.

D. V. Mironov, V. M. Gryanik, C.-H. Moeng, D. J. Olbers, and T. H. Warncke. Vertical turbulence structure and second-moment budgets in convection with rotation: A large-eddy simulation study. Quarterly Journal of the Royal Meteorological Society, 126(563):477–515, 2000.

K. Miyashita, K. Iwamoto, and H. Kawamura. Direct Numerical Simulation of the Neutrally Stratified Turbulent Ekman Boundary Layer. Journal of the Earth Simulator, 6:3–15, 2006.

A. F. Moene, B. I. Michels, and A. A. M. Holtslag. Scaling Variances of Scalars in a Convective Boundary Layer Under Different Entrainment Regimes. Bound. Layer Meteor., 120:257–274, 2006.

C.-H. Moeng and R. Rotunno. Vertical-Velocity Skewness in the Buoyancy-Driven Boundary Layer. J. of Atm. Sci., 47:1149–1162, 1990.

C.-H. Moeng and J. C. Wyngaard. Statistics of Conservative Scalars in the Convective Boundary Layers. J. of Atm. Sci., 41:3161–3169, 1984.

C.-H. Moeng and J. C. Wyngaard. Evaluation of Turbulent Transport and Dissipation Closures in Second-Order Modeling. J. of Atm. Sci., 46:2311–2330, 1989.

P. Moin and J. Kim. Numerical investigation of turbulent channel flow. J. Fluid Mech., 118:341–377, 1982.

N. Mole and E. D. Clarke. Relationships Between Higher Moments of Concentration and of Dose in Turbulent Dispersion. Bound. Layer Meteor., 73:35–52, 1995.

J. F. Morrison, B. J. McKeon, and W. Jiang. Scaling of the streamwise velocity component in turbulent pipe flow. J. Fluid Mech., 508:99–131, 2004.

M. Nelkin. In What Sense Is Turbulence an Unsolved Problem? Science, 255:566–570, 1992.

A. M. Obukhov. Some Specific Features of Atmospheric Turbulence. Journal of Geophysical Research, 67(8):3011–3014, 1962.

A. M. Obukhov. Turbulence in an atmosphere with a non-uniform temperature. Bound. Layer Meteor., 2:7–29, 1971.

T. R. Oke. The energetic basis of the urban heat island. Quart. J. R. Met. Soc., 108:1–24, 1982.

S. A. Orszag and L. C. Kells. Transition to turbulence in plane Poiseuille and plane Couette flow. J. Fluid Mech., 96:159–205, 1980.

H. A. Panofsky and J. A. Dutton. Atmospheric Turbulence: Models and Methods for Engineering Application. John Wiley & Sons, New York, New York, 1984.

E. G. Patton, P. P. Sullivan, and K. J. Davis. The influence of a forest canopy on top-down and bottom-up diffusion in the planetary boundary layer. Q. J. R. Meteorol. Soc., 129:1415–1434, 2003.

U. Piomelli, A. Scotti, and E. Balaras. Large-Eddy Simulations of Turbulent Flows, from Desktop to Supercomputer. In Selected Papers and Invited Talks from the 4th International Conference on Vector and Parallel Processing, VECPAR '00, pages 551–578, London, UK, 2001. Springer-Verlag.

M. Piper, J. C. Wyngaard, W. H. Snyder, and R. E. Lawson, Jr. Top-Down, Bottom-Up Diffusion Experiments in a Water Convection Tank. J. of Atm. Sci., 52:3607–3619, 1995.

S. B. Pope. Turbulent Flows, pages 182–276. Cambridge University Press, Cambridge, United Kingdom, 1993.

F. Porté-Agel, H. Lu, and Y.-T. Wu. A large-eddy simulation framework for wind energy applications. In The Fifth International Symposium on Computational Wind Engineering, May 2010.

G. Poulos, W. Blumen, D. C. Fritts, J. K. Lundquist, J. Sun, S. P. Burns, C. Nappo, R. Banta, R. Newsom, J. Cuxart, E. Terradellas, B. Balsley, and M. Jensen. CASES-99: A comprehensive investigation of the stable nocturnal boundary layer. Bull. Amer. Meteor. Soc., 83:555–581, 2002.

M. M. Rai and P. Moin. Direct Simulations of Turbulent Flow Using Finite-Difference Schemes. J. Comput. Phys., 96:15–53, 1991.

O. Reynolds. An experimental investigation of the circumstances which determine whether the motion of water shall be direct or sinuous and the law of resistance in parallel channels. Phil. Trans. Roy. Soc., 174:935–982, 1883.

S. B. Roy and S. W. Pacala. Can large wind farms affect local meteorology? Journal of Geophysical Research, 109, 2004.

F. Sattin, M. Agostini, R. Cavazzana, G. Serianni, P. Scarin, and N. Vianello. About the parabolic relation existing between the skewness and the kurtosis in time series of experimental data. Physica Scripta, 79(4), 2009.

T. P. Schopflocher and P. J. Sullivan. The relationship between skewness and kurtosis of a diffusing scalar. Bound. Layer Meteor., 115:341–358, 2005.

E. D. Skyllingstad, R. M. Samelson, L. Mahrt, and P. Barbour. A Numerical Modeling Study of Warm Offshore Flow over Cool Water. Monthly Weather Review, 133:345–361, 2005.

E. D. Skyllingstad, D. Vickers, L. Mahrt, and R. Samelson. Effects of mesoscale sea-surface temperature fronts on the marine atmospheric boundary layer. Bound. Layer Meteor., 123:219–237, 2007.

Z. Sorbjan. Large-eddy simulations of the baroclinic mixed layer. Bound. Layer Meteor., 112:57–80, 2004.

P. R. Spalart, G. N. Coleman, and R. Johnstone. Direct numerical simulation of the Ekman layer: A step in Reynolds number, and cautious support for a log law with a shifted origin. Phys. Fluids, 20, 2008.

R. B. Stull. An Introduction to Boundary Layer Meteorology. Kluwer Academic, Dordrecht, Germany, 1988.

P. P. Sullivan, C.-H. Moeng, B. Stevens, D. H. Lenschow, and S. D. Mayor. Stucture of the Entrainment Zone Capping the Convective Atmospheric Boundary Layer. J. of Atm. Sci., 55:3042–3064, 1998.

J. Sun, S. P. Burns, D. H. Lenschow, R. Banta, R. Newsom, R. Coulter, S. Frasier, T. Ince, C. Nappo, J. Cuxart, W. Blumen, X. Lee, and X.-Z. Hu. Intermittent Turbulence Associated with a Density Current Passage in the Stable Boundary Layer. Bound. Layer Meteor., 105:199–219, 2002.

F. Tampieri, A. Maurizi, and S. Alberghi. Lagrangian models of turbulent dispersion in the atmospheric boundary layer. In G. Solari, L. C. Pagnini, , and G. Piccardo, editors, Ingegneria del Vento in Italia 2000, pages 37–50. S.G.E., 2000.

J. R. Taylor and S. Sarkar. Direct and large eddy simulations of a bottom Ekman layer under an external stratification. Int. J. Heat and Fluid Flow, 29:721–732, 2008.

H. Tennekes and J. L. Lumley. A First Course in Turbulence, pages 256–273. The MIT Press, Cambridge, Massachusetts, 1972.

L. N. Trefethen. Spectral Methods in MATLAB, page 151. SIAM, Philadelphia, Pennsylvania, 2000.

L. N. Trefethen and D. Bau. Numerical Linear Algebra, pages 241–320. SIAM, Philadelphia, Pennsylvania, 1997.

L. Umlauf and H. Burchard. Second-order turbulence closure models for geophysical boundary layers: A review of recent work. Continental Shelf Research, 25:795–827, 2005.

G. H. Vatistas. Simple Model for Turbulent Tip Vortices. Journal of Aircraft, 43(5):1577–1579, 2006.

L. J. Vermeer, J. N. Sørensen, and A. Crespo. Wind turbine wake aerodynamics. Prog. in Aerospace Sciences, 39:467–510, 2003.

S. Waggy, S. Marlatt, and S. Biringen. Direct Numerical Simulation of the Turbulent Ekman Layer: Instantaneous Flow Structures. J. of Thermophysics and Heat Transfer, 25:309–318, 2011.

C. Wang and R. G. Prinn. Potential climatic impacts and reliability of very large-scale wind farms. Atmos. Chem. Phys., 10:2053–2061, 2010.

W. Wang, K. J. Davis, C. Yi, E. G. Patton, M. P. Butler, D. M. Ricciuto, and P. S. Bakwin. A note on the top-down and bottom-up gradient functions over a forested site. Bound. Layer Meteor., 124:305–314, 2007.

F. M. White. Viscous Fluid Flow. McGraw-Hill, New York, New York, 1991.

G. E. Willis and J. W. Deardorff. A laboratory model of the unstable planetary boundary layer. J. of Atm. Sci., 31:1297–1307, 1974.

Y.-T. Wu and F. Porté-Agel. Large-Eddy Simulation of Wind-Turbine Wakes: Evaluation of Turbine Parametrisations. Bound. Layer Meteor., 138:345–366, 2011.

J. C. Wyngaard and R. A. Brost. Top-Down and Bottom-Up Diffusion of a Scalar in the Convective Boundary Layer. J. of Atm. Sci., 41:102–112, 1984.

L. Zhou, Y. Tian, S. B. Roy, C. Thorncroft, L. F. Bosart, and Y. Hu. Impacts of wind farms on land surface temperature. Nature Climate Change, 2012. doi: 10.1038/NCLIMATE1505.

S. S. Zilitinkevich, V. M. Gryanik, V. N. Lykossov, and D. V. Mironov. Third-Order Transport and Nonlocal Turbulence Closures for Convective Boundary Layers. J. of Atm. Sci., 56:3463–3477, 1999.

APPENDIX A

REYNOLDS-AVERAGED NAVIER STOKES

A common means of understanding turbulent flows is the decomposition of the flow field into a mean and fluctuating component:

$$u_i = \overline{u_i} + u_i' \tag{A.0.1a}$$

$$\theta = \overline{\theta} + \theta' \tag{A.0.1b}$$

$$q_w = \overline{q_w} + q_w' \tag{A.0.1c}$$

$$p = \overline{p} + p' \tag{A.0.1d}$$

Note that, in this context, the operator $\overline{(\cdot)}$ is used to denote a temporal average such that (Tennekes and Lumley, 1972)

$$\overline{u_i} = \lim_{T\to\infty} \frac{1}{T} \int_{t_0}^{t_0+T} u_i \mathrm{d}t$$

which implies that $d\overline{u_i}/dt = 0$. For homogeneous flow fields (as will be studied here), the overbar can also be used to denote a spatial average. By definition, the average of any fluctuating quantity is zero, i.e. $\overline{u_i'} = 0$. Substitution of Eq. A.0.1 into Eq. 2.4.1 yields a set of equations where contributions by the mean and fluctuating components have been separated.

$$\frac{\partial U_i}{\partial x_i} + \frac{\partial u_i'}{\partial x_i} = 0 \tag{A.0.2a}$$

$$\begin{aligned} \frac{\partial U_i}{\partial t} + \frac{\partial u_i'}{\partial t} + \frac{\partial U_i U_j}{\partial x_j} + \frac{\partial U_i u_j'}{\partial x_j} + \frac{\partial u_i' U_j}{\partial x_j} + \frac{\partial u_i' u_j'}{\partial x_j} + \frac{1}{\mathrm{Ro}}\varepsilon_{3ji} U_j + \frac{1}{\mathrm{Ro}}\varepsilon_{3ji} u_j' \\ = -\frac{\partial \overline{p}}{\partial x_i} - \frac{\partial p'}{\partial x_i} + \frac{1}{\mathrm{Re}}\frac{\partial^2 U_i}{\partial x_j \partial x_j} + \frac{1}{\mathrm{Re}}\frac{\partial^2 u_i'}{\partial x_j \partial x_j} + \overline{\theta_v}\delta_{i3} + \theta_v'\delta_{i3} \end{aligned} \tag{A.0.2b}$$

$$\frac{\partial \overline{\theta}}{\partial t} + \frac{\partial \theta'}{\partial t} + \frac{\partial U_j \overline{\theta}}{\partial x_j} + \frac{\partial u_j' \overline{\theta}}{\partial x_j} + \frac{\partial U_j \theta'}{\partial x_j} + \frac{\partial u_j' \theta'}{\partial x_j} = \frac{1}{\mathrm{Re\,Pr}} \frac{\partial^2 \overline{\theta}}{\partial x_j \partial x_j} + \frac{1}{\mathrm{Re\,Pr}} \frac{\partial^2 \theta'}{\partial x_j \partial x_j} \tag{A.0.2c}$$

$$\frac{\partial \overline{q_w}}{\partial t} + \frac{\partial q_w'}{\partial t} + \frac{\partial U_j \overline{q_w}}{\partial x_j} + \frac{\partial u_j' \overline{q_w}}{\partial x_j} + \frac{\partial U_j q_w'}{\partial x_j} + \frac{\partial u_j' q_w'}{\partial x_j} = \frac{1}{\mathrm{Re\,Sc}} \frac{\partial^2 \overline{q_w}}{\partial x_j \partial x_j} + \frac{1}{\mathrm{Re\,Sc}} \frac{\partial^2 q_w'}{\partial x_j \partial x_j} \tag{A.0.2d}$$

The mean velocity $\overline{u_i}$ has been replaced with U_i to denote a mean velocity field. This notation convention will be used throughout the dissertation. The continuity equation given above implies that both the mean and fluctuating velocity fields must have a zero divergence. Applying the averaging operator $\overline{(\cdot)}$ to each term in Eq. A.0.2 yields the Reynolds-averaged Navier-Stokes (RANS) equations, averaged energy equation, and averaged scalar transport equation:

$$\frac{\partial U_i}{\partial x_i} = 0 \tag{A.0.3a}$$

$$\frac{\partial U_i}{\partial t} + \frac{\partial U_i U_j}{\partial x_j} + \frac{\partial \overline{u_i' u_j'}}{\partial x_j} + \frac{1}{\mathrm{Ro}} \varepsilon_{3ji} U_j = -\frac{\partial \overline{p}}{\partial x_i} + \frac{1}{\mathrm{Re}} \frac{\partial^2 U_i}{\partial x_j \partial x_j} + \overline{\theta_v} \delta_{i3} \tag{A.0.3b}$$

$$\frac{\partial \overline{\theta}}{\partial t} + \frac{\partial U_j \overline{\theta}}{\partial x_j} + \frac{\partial \overline{u_j' \theta'}}{\partial x_j} = \frac{1}{\mathrm{Re\,Pr}} \frac{\partial^2 \overline{\theta}}{\partial x_j \partial x_j} \tag{A.0.3c}$$

$$\frac{\partial \overline{q_w}}{\partial t} + \frac{\partial U_j \overline{q_w}}{\partial x_j} + \frac{\partial \overline{u_j' q_w'}}{\partial x_j} = \frac{1}{\mathrm{Re\,Sc}} \frac{\partial^2 \overline{q_w}}{\partial x_j \partial x_j} \tag{A.0.3d}$$

The only fluctuating components that remain are due to interactions of fluctuating variables via the advective terms. In turbulence research, the products $\overline{u_i' u_j'}$, $\overline{u_j' \theta'}$, and $\overline{u_j' q_w'}$ are the focus of a great deal of attention given that these quantities are responsible for how turbulent fluctuations relate to mean flow characteristics. They will be given their due attention in this work as well.

APPENDIX B

DEVELOPMENT OF BUDGET EQUATIONS

B.1 Turbulent Kinetic Energy Budget

The turbulent kinetic energy budget given in Eq. 4.3.1 are derived from the Navier-Stokes equations of Eq. 2.2.3b. Substituting the total velocity, temperature, and pressure with the corresponding mean and fluctuating components yields the momentum equation in Eq. A.0.2. Performing a time average results in the typical RANS equations (see Eq. A.0.3).

To develop the kinetic energy budget, Eq. A.0.3b is subtracted from Eq. A.0.2b yielding

$$\frac{\partial u_i'}{\partial t} + \frac{\partial U_i u_j'}{\partial x_j} + \frac{\partial u_i' U_j}{\partial x_j} + \frac{\partial u_i' u_j'}{\partial x_j} - \frac{\partial \overline{u_i' u_j'}}{\partial x_j} + \frac{1}{\mathrm{Ro}} \varepsilon_{3ji} u_j' = -\frac{\partial p'}{\partial x_i} + \frac{1}{\mathrm{Re}} \frac{\partial^2 u_i'}{\partial x_j \partial x_j} + \theta_v' \delta_{i3} \tag{B.1.1}$$

Multiplying the above expression by the fluctuating velocity u_k' and performing a time average gives

$$\overline{u_k' \frac{\partial u_i'}{\partial t}} + \overline{u_k' \frac{\partial U_i u_j'}{\partial x_j}} + \overline{u_k' \frac{\partial u_i' U_j}{\partial x_j}} + \overline{u_k' \frac{\partial u_i' u_j'}{\partial x_j}} - \overline{u_k' \frac{\partial \overline{u_i' u_j'}}{\partial x_j}} + \frac{1}{\mathrm{Ro}} \overline{u_k' u_j'} \varepsilon_{3ji} = -\overline{u_k' \frac{\partial p'}{\partial x_i}} + \frac{1}{\mathrm{Re}} \overline{u_k' \frac{\partial^2 u_i'}{\partial x_j \partial x_j}} + \overline{u_k' \theta_v'} \delta_{i3} \tag{B.1.2}$$

Since $\partial \overline{u_i' u_j'} / \partial x_j$ is a constant, the fifth term in Eq. B.1.2 reduces to 0 since $\overline{u_k'} = 0$:

$$-\overline{u_k' \frac{\partial \overline{u_i' u_j'}}{\partial x_j}} = -\overline{u_k'} \frac{\partial \overline{u_i' u_j'}}{\partial x_j} = 0 \tag{B.1.3}$$

Equation B.1.2 then simplifies to

$$\overline{u_k' \frac{\partial u_i'}{\partial t}} + \overline{u_k' \frac{\partial U_i u_j'}{\partial x_j}} + \overline{u_k' \frac{\partial u_i' U_j}{\partial x_j}} + \overline{u_k' \frac{\partial u_i' u_j'}{\partial x_j}} + \frac{1}{\mathrm{Ro}} \overline{u_k' u_j'} \varepsilon_{3ji} = -\overline{u_k' \frac{\partial p'}{\partial x_i}} + \frac{1}{\mathrm{Re}} \overline{u_k' \frac{\partial^2 u_i'}{\partial x_j \partial x_j}} + \overline{u_k' \theta_v'} \delta_{i3} \tag{B.1.4}$$

A second energy is developed by simply switching the i and k indices in B.1.4:

$$\overline{u_i'\frac{\partial u_k'}{\partial t}} + \overline{u_i'\frac{\partial U_k u_j'}{\partial x_j}} + \overline{u_i'\frac{\partial u_k' U_j}{\partial x_j}} + \overline{u_i'\frac{\partial u_k' u_j'}{\partial x_j}} + \frac{1}{\mathrm{Ro}}\overline{u_i' u_j'}\varepsilon_{3jk} = -\overline{u_i'\frac{\partial p'}{\partial x_k}} + \frac{1}{\mathrm{Re}}\overline{u_i'\frac{\partial^2 u_k'}{\partial x_j \partial x_j}} + \overline{u_i'\theta_v'}\delta_{k3} \quad \text{(B.1.5)}$$

Adding Eq. B.1.4 and Eq. B.1.5 and simplifying yields the full budget equation. The following simplifications can be made. Note that $\partial U_j/\partial x_j = \partial u_j'/\partial x_j = 0$ through incompressible continuity.

- Temporal variation

$$\overline{u_i'\frac{\partial u_k'}{\partial t}} + \overline{u_k'\frac{\partial u_i'}{\partial t}} = \frac{\partial \overline{u_i' u_k'}}{\partial t}$$

- Production

$$\begin{aligned}\overline{u_i'\frac{\partial U_k u_j'}{\partial x_j}} + \overline{u_k'\frac{\partial U_i u_j'}{\partial x_j}} &= U_k\overline{u_i'\frac{\partial u_j'}{\partial x_j}} + \overline{u_i' u_j'}\frac{\partial U_k}{\partial x_j} + U_i\overline{u_k'\frac{\partial u_j'}{\partial x_j}} + \overline{u_k' u_j'}\frac{\partial U_i}{\partial x_j} \\ &= \overline{u_i' u_j'}\frac{\partial U_k}{\partial x_j} + \overline{u_k' u_j'}\frac{\partial U_i}{\partial x_j}\end{aligned}$$

- Advection by mean flow

$$\begin{aligned}\overline{u_i'\frac{\partial u_k' U_j}{\partial x_j}} + \overline{u_k'\frac{\partial u_i' U_j}{\partial x_j}} &= \overline{u_i' u_k'}\frac{\partial U_j}{\partial x_j} + U_j\overline{u_i'\frac{\partial u_k'}{\partial x_j}} + \overline{u_k' u_i'}\frac{\partial U_j}{\partial x_j} + U_j\overline{u_k'\frac{\partial u_i'}{\partial x_j}} \\ &= U_j\overline{u_i'\frac{\partial u_k'}{\partial x_j}} + U_j\overline{u_k'\frac{\partial u_i'}{\partial x_j}} \\ &= U_j\frac{\partial \overline{u_i' u_k'}}{\partial x_j}\end{aligned}$$

- Turbulent diffusion

$$\begin{aligned}\overline{u_i'\frac{\partial u_k' u_j'}{\partial x_j}} + \overline{u_k'\frac{\partial u_i' u_j'}{\partial x_j}} &= 2\overline{u_i' u_k'\frac{\partial u_j'}{\partial x_j}} + \overline{u_i' u_j'\frac{\partial u_k'}{\partial x_j}} + \overline{u_k' u_j'\frac{\partial u_i'}{\partial x_j}} \\ &= \overline{u_i' u_j'\frac{\partial u_k'}{\partial x_j}} + \overline{u_k' u_j'\frac{\partial u_i'}{\partial x_j}} \\ &= \frac{\partial \overline{u_i' u_k' u_j'}}{\partial x_j} - \overline{u_i' u_k'\frac{\partial u_j'}{\partial x_j}} \\ &= \frac{\partial \overline{u_i' u_k' u_j'}}{\partial x_j}\end{aligned}$$

- Pressure terms

$$\begin{aligned}\overline{u_i'\frac{\partial p'}{\partial x_k}} + \overline{u_k'\frac{\partial p'}{\partial x_i}} &= \frac{\partial \overline{u_i' p'}}{\partial x_k} - \overline{p'\frac{\partial u_i'}{\partial x_k}} + \frac{\partial \overline{u_k' p'}}{\partial x_i} - \overline{p'\frac{\partial u_k'}{\partial x_i}} \\ &= \frac{\partial \overline{u_i' p'}}{\partial x_k} + \frac{\partial \overline{u_k' p'}}{\partial x_i} - \overline{p'\left(\frac{\partial u_i'}{\partial x_k} + \frac{\partial u_k'}{\partial x_i}\right)}\end{aligned}$$

- Viscous terms

$$\begin{aligned}\overline{u_i'\frac{\partial^2 u_k'}{\partial x_j \partial x_j}} + \overline{u_k'\frac{\partial^2 u_i'}{\partial x_j \partial x_j}} &= \frac{\partial}{\partial x_j}\overline{u_i'\frac{\partial u_k'}{\partial x_j}} - \overline{\frac{\partial u_i'}{\partial x_j}\frac{\partial u_k'}{\partial x_j}} + \frac{\partial}{\partial x_j}\overline{u_k'\frac{\partial u_i'}{\partial x_j}} - \overline{\frac{\partial u_k'}{\partial x_j}\frac{\partial u_i'}{\partial x_j}} \\ &= \frac{\partial}{\partial x_j}\overline{\left(u_i'\frac{\partial u_k'}{\partial x_j} + u_k'\frac{\partial u_i'}{\partial x_j}\right)} - 2\overline{\frac{\partial u_i'}{\partial x_j}\frac{\partial u_k'}{\partial x_j}} \\ &= \frac{\partial^2 \overline{u_i' u_k'}}{\partial x_j \partial x_j} - 2\overline{\frac{\partial u_i'}{\partial x_j}\frac{\partial u_k'}{\partial x_j}}\end{aligned}$$

Combining the above simplifications and the other simple terms yeilds the full turbulent kinetic energy budget (Eq. 4.3.1):

$$\begin{aligned}\frac{D\overline{u_i'u_k'}}{Dt} =& \frac{\partial \overline{u_i'u_k'}}{\partial t} + U_j\frac{\partial \overline{u_i'u_k'}}{\partial x_j} \\ =& + \overline{u_i'\theta_v'}\delta_{k3} + \overline{u_k'\theta_v'}\delta_{i3} \\ & - \overline{u_i'u_j'}\frac{\partial U_k}{\partial x_j} - \overline{u_k'u_j'}\frac{\partial U_i}{\partial x_j} \\ & - \overline{\frac{\partial u_i'u_k'u_j'}{\partial x_j}} \\ & - \frac{2}{\mathrm{Re}}\overline{\frac{\partial u_i'}{\partial x_j}\frac{\partial u_k'}{\partial x_j}} \\ & + \frac{1}{\mathrm{Re}}\frac{\partial^2 \overline{u_i'u_k'}}{\partial x_j \partial x_j} \\ & + \overline{p'\left(\frac{\partial u_i'}{\partial x_k} + \frac{\partial u_k'}{\partial x_i}\right)} \\ & - \overline{\frac{\partial u_i'p'}{\partial x_k}} - \overline{\frac{\partial u_k'p'}{\partial x_i}} \\ & + \frac{1}{\mathrm{Ro}}\left(\varepsilon_{kj3}\overline{u_i'u_j'} + \varepsilon_{ij3}\overline{u_k'u_j'}\right)\end{aligned}$$

B.2 Scalar Flux Budget

The scalar flux budget equation is derived in a similar fashion to the kinetic energy transport equation. The averaged scalar transport equation given by Eq. A.0.3d is subtracted from Eq. A.0.2d and yields a transport equation for q_w':

$$\frac{\partial q_w'}{\partial t} + \frac{\partial u_j'\overline{q_w}}{\partial x_j} + \frac{\partial U_j q_w'}{\partial x_j} + \frac{\partial u_j' q_w'}{\partial x_j} - \frac{\partial \overline{u_j' q_w'}}{\partial x_j} = \frac{1}{\mathrm{Re}\,\mathrm{Sc}}\frac{\partial^2 q_w'}{\partial x_j \partial x_j} \tag{B.2.1}$$

Multiplying the above expression by u_i' and averaging yields

$$\overline{u_i'\frac{\partial q_w'}{\partial t}} + \overline{u_i'\frac{\partial u_j'\overline{q_w}}{\partial x_j}} + \overline{u_i'\frac{\partial U_j q_w'}{\partial x_j}} + \overline{u_i'\frac{\partial u_j' q_w'}{\partial x_j}} - \overline{u_i'\frac{\partial \overline{u_j' q_w'}}{\partial x_j}} = \frac{1}{\mathrm{Re}\,\mathrm{Sc}}\overline{u_i'\frac{\partial^2 q_w'}{\partial x_j \partial x_j}} \tag{B.2.2}$$

Note that the fifth term in the expression is zero since $\overline{u_i'}$ is zero. A second equation is formed by multiplying the equation governing velocity fluctuations (Eq. B.1.1) by q_w' and applying a time average:

$$\overline{q_w'\frac{\partial u_i'}{\partial t}} + \overline{q_w'\frac{\partial U_i u_j'}{\partial x_j}} + \overline{q_w'\frac{\partial u_i' U_j}{\partial x_j}} + \overline{q_w'\frac{\partial u_i' u_j'}{\partial x_j}} - \overline{q_w'\frac{\partial \overline{u_i' u_j'}}{\partial x_j}} + \frac{1}{\mathrm{Ro}}\overline{q_w' u_j' \varepsilon_{3ji}} = -\overline{q_w'\frac{\partial p'}{\partial x_i}} + \frac{1}{\mathrm{Re}}\overline{q_w'\frac{\partial^2 u_i'}{\partial x_j \partial x_j}} + \overline{q_w'\theta_v'}\delta_{i3} \tag{B.2.3}$$

Once again, the fifth term drops out using the same argument formulated in Eq. B.1.3. Adding the results of Eq. B.2.2 and B.2.3 yields the full budget for the scalar flux $\overline{u_i' q_w'}$. The following simplifications are made:

- Temporal variation

$$\overline{u_i'\frac{\partial q_w'}{\partial t}} + \overline{q_w'\frac{\partial u_i'}{\partial t}} = \frac{\partial \overline{u_i' q_w'}}{\partial t}$$

- Production

$$\begin{aligned}\overline{u_i'\frac{\partial \overline{q_w} u_j'}{\partial x_j}} + \overline{q_w'\frac{\partial U_i u_j'}{\partial x_j}} &= \overline{q_w}\overline{u_i'\frac{\partial u_j'}{\partial x_j}} + \overline{u_i' u_j'}\frac{\partial \overline{q_w}}{\partial x_j} + U_i\overline{q_w'\frac{\partial u_j'}{\partial x_j}} + \overline{q_w' u_j'}\frac{\partial U_i}{\partial x_j} \\ &= \overline{u_i' u_j'}\frac{\partial \overline{q_w}}{\partial x_j} + \overline{q_w' u_j'}\frac{\partial U_i}{\partial x_j}\end{aligned}$$

- Advection by mean flow

$$\begin{aligned}\overline{u_i'\frac{\partial q_w' U_j}{\partial x_j}} + \overline{q_w'\frac{\partial u_i' U_j}{\partial x_j}} &= \overline{u_i' q_w'}\frac{\partial U_j}{\partial x_j} + U_j\overline{u_i'\frac{\partial q_w'}{\partial x_j}} + \overline{q_w' u_i'}\frac{\partial U_j}{\partial x_j} + U_j\overline{q_w'\frac{\partial u_i'}{\partial x_j}} \\ &= U_j\overline{u_i'\frac{\partial q_w'}{\partial x_j}} + U_j\overline{q_w'\frac{\partial u_i'}{\partial x_j}} \\ &= U_j\frac{\partial \overline{u_i' q_w'}}{\partial x_j}\end{aligned}$$

- Turbulent diffusion

$$\begin{aligned}\overline{u_i'\frac{\partial q_w' u_j'}{\partial x_j}} + \overline{q_w'\frac{\partial u_i' u_j'}{\partial x_j}} &= 2\overline{u_i' q_w'\frac{\partial u_j'}{\partial x_j}} + \overline{u_i' u_j'\frac{\partial q_w'}{\partial x_j}} + \overline{q_w' u_j'\frac{\partial u_i'}{\partial x_j}} \\ &= \overline{u_i' u_j'\frac{\partial q_w'}{\partial x_j}} + \overline{q_w' u_j'\frac{\partial u_i'}{\partial x_j}} \\ &= \frac{\partial \overline{u_i' q_w' u_j'}}{\partial x_j} - \overline{u_i' q_w'\frac{\partial u_j'}{\partial x_j}} \\ &= \frac{\partial \overline{u_i' q_w' u_j'}}{\partial x_j}\end{aligned}$$

- Pressure terms

$$\overline{q_w'\frac{\partial p'}{\partial x_i}} = \frac{\partial \overline{q_w' p'}}{\partial x_i} - \overline{p'\frac{\partial q_w'}{\partial x_i}}$$

- Viscous terms

$$\begin{aligned}\frac{1}{\mathrm{Re\,Sc}}\overline{u_i'\frac{\partial^2 q_w'}{\partial x_j \partial x_j}} + \frac{1}{\mathrm{Re}}\overline{q_w'\frac{\partial^2 u_i'}{\partial x_j \partial x_j}} &= \frac{1}{\mathrm{Re\,Sc}}\left[\frac{\partial}{\partial x_j}\overline{u_i'\frac{\partial q_w'}{\partial x_j}} - \overline{\frac{\partial u_i'}{\partial x_j}\frac{\partial q_w'}{\partial x_j}}\right] + \frac{1}{\mathrm{Re}}\left[\frac{\partial}{\partial x_j}\overline{q_w'\frac{\partial u_i'}{\partial x_j}} - \overline{\frac{\partial q_w'}{\partial x_j}\frac{\partial u_i'}{\partial x_j}}\right] \\ &= \frac{1}{\mathrm{Re\,Sc}}\left[\frac{\partial}{\partial x_j}\left(\frac{\partial \overline{u_i' q_w'}}{\partial x_j} - \overline{q_w'\frac{\partial u_i'}{\partial x_j}}\right) - \overline{\frac{\partial u_i'}{\partial x_j}\frac{\partial q_w'}{\partial x_j}}\right] \\ &+ \frac{1}{\mathrm{Re}}\left[\frac{\partial}{\partial x_j}\left(\frac{\partial \overline{u_i' q_w'}}{\partial x_j} - \overline{u_i'\frac{\partial q_w'}{\partial x_j}}\right) - \overline{\frac{\partial u_i'}{\partial x_j}\frac{\partial q_w'}{\partial x_j}}\right] \\ &= \left(\frac{1}{\mathrm{Re\,Sc}} + \frac{1}{\mathrm{Re}}\right)\left[\frac{\partial^2 \overline{u_i' q_w'}}{\partial x_j \partial x_j} - \overline{\frac{\partial u_i'}{\partial x_j}\frac{\partial q_w'}{\partial x_j}}\right] \\ &- \frac{1}{\mathrm{Re\,Sc}}\frac{\partial}{\partial x_j}\overline{q_w'\frac{\partial u_i'}{\partial x_j}} - \frac{1}{\mathrm{Re}}\frac{\partial}{\partial x_j}\overline{u_i'\frac{\partial q_w'}{\partial x_j}} \\ &= \left(\frac{1}{\mathrm{Re\,Sc}} + \frac{1}{\mathrm{Re}}\right)\left[\frac{\partial^2 \overline{u_i' q_w'}}{\partial x_j \partial x_j} - \overline{\frac{\partial u_i'}{\partial x_j}\frac{\partial q_w'}{\partial x_j}}\right] \\ &- \frac{1}{\mathrm{Re\,Sc}}\left[q_w'\frac{\partial^2 u_i'}{\partial x_j \partial x_j} + \overline{\frac{\partial u_i'}{\partial x_j}\frac{\partial q_w'}{\partial x_j}}\right] - \frac{1}{\mathrm{Re}}\left[u_i'\frac{\partial^2 q_w'}{\partial x_j \partial x_j} + \overline{\frac{\partial u_i'}{\partial x_j}\frac{\partial q_w'}{\partial x_j}}\right] \\ &= \left(\frac{1}{\mathrm{Re\,Sc}} + \frac{1}{\mathrm{Re}}\right)\left[\frac{\partial^2 \overline{u_i' q_w'}}{\partial x_j \partial x_j} - 2\overline{\frac{\partial u_i'}{\partial x_j}\frac{\partial q_w'}{\partial x_j}}\right] \\ &- \frac{1}{\mathrm{Re\,Sc}}\overline{q_w'\frac{\partial^2 u_i'}{\partial x_j \partial x_j}} - \frac{1}{\mathrm{Re}}\overline{u_i'\frac{\partial^2 q_w'}{\partial x_j \partial x_j}}\end{aligned}$$

Combining the above simplifications yields the full budget equation for the scalar flux $\overline{u_i' q_w'}$ as given by Eq. 6.4.2:

$$
\begin{aligned}
\frac{D\overline{u_i' q_w'}}{Dt} =& \frac{\partial \overline{u_i' q_w'}}{\partial t} + U_j \frac{\partial \overline{u_i' q_w'}}{\partial x_j} \\
=& + \overline{q_w' \theta_v'} \delta_{i3} \\
& - \overline{u_i' u_j'} \frac{\partial \overline{q_w}}{\partial x_j} - \overline{q_w' u_j'} \frac{\partial U_i}{\partial x_j} \\
& - \frac{\partial \overline{u_i' q_w' u_j'}}{\partial x_j} \\
& - \left(\frac{2}{\mathrm{Re\,Sc}} + \frac{2}{\mathrm{Re}} \right) \overline{\frac{\partial u_i'}{\partial x_j} \frac{\partial q_w'}{\partial x_j}} \\
& + \left(\frac{1}{\mathrm{Re\,Sc}} + \frac{1}{\mathrm{Re}} \right) \frac{\partial^2 \overline{u_i' q_w'}}{\partial x_j \partial x_j} \\
& + \overline{p' \frac{\partial q_w'}{\partial x_i}} \\
& - \frac{\partial \overline{q_w' p'}}{\partial x_i} \\
& + \frac{1}{\mathrm{Ro}} \varepsilon_{ij3} \overline{q_w' u_j'} \\
& - \frac{1}{\mathrm{Re\,Sc}} \overline{q_w' \frac{\partial^2 u_i'}{\partial x_j \partial x_j}} - \frac{1}{\mathrm{Re}} \overline{u_i' \frac{\partial^2 q_w'}{\partial x_j \partial x_j}}
\end{aligned}
$$

APPENDIX C

HIGH-ORDER CLOSURE MODEL - CASE B2

In §5.4, third and fourth-order velocity and temperature moments were related back to the second-order variances and the skewness of both temperature and velocity. It was shown that a range of values for a_i and d_i in Eq. 5.4.2 can be used to accurately model the higher-order terms.

Presented here are the results for Case B2. Figure C.1 shows the explained variance of the third-order moments as a function of a_i and d_i (for i and $d = 1 - 2$). The closure of $\overline{w'^2\theta'}$ behaves similar to the results of Case B1 though a slight increase in the optimum values of a_1 is seen. Subplot (b) shows that the range of acceptable values for d_2 decreases (a narrowing of the contours). As with Case B1, the recommended values of Gryanik and Hartmann (2002) perform poorly for the third-order terms. The fit of model in comparison to the DNS for $\overline{w'^2\theta'}$ and $\overline{w'\theta'^2}$ are shown in Fig. C.2(a) and (b) respectively.

Contours for the fourth-order moments are shown in Fig. C.3. a_i and d_i for $i = 3, 5, 6$ all show similar behavior to Case B1 results with only a slight contraction in the range of acceptable values when stratification is stronger. The largest deviation of the Case B2 results from those of Case B1 are seen in a_4 and d_4. Not only is the total region covered by the contour smaller (compare Fig. C.3(b) with 5.32(b)), but a significant shift is seen in the optimal value of both empirical constants. For Case B2, the recommended values of a_4 and d_4 are much closer those recommended by Gryanik and Hartmann (2002) (see Table 5.3). Using the optimum values for a_i and d_i shown in Fig. C.3, the fit of the DNS data with the model of Eq. 5.4.2 is shown in Fig. C.4.

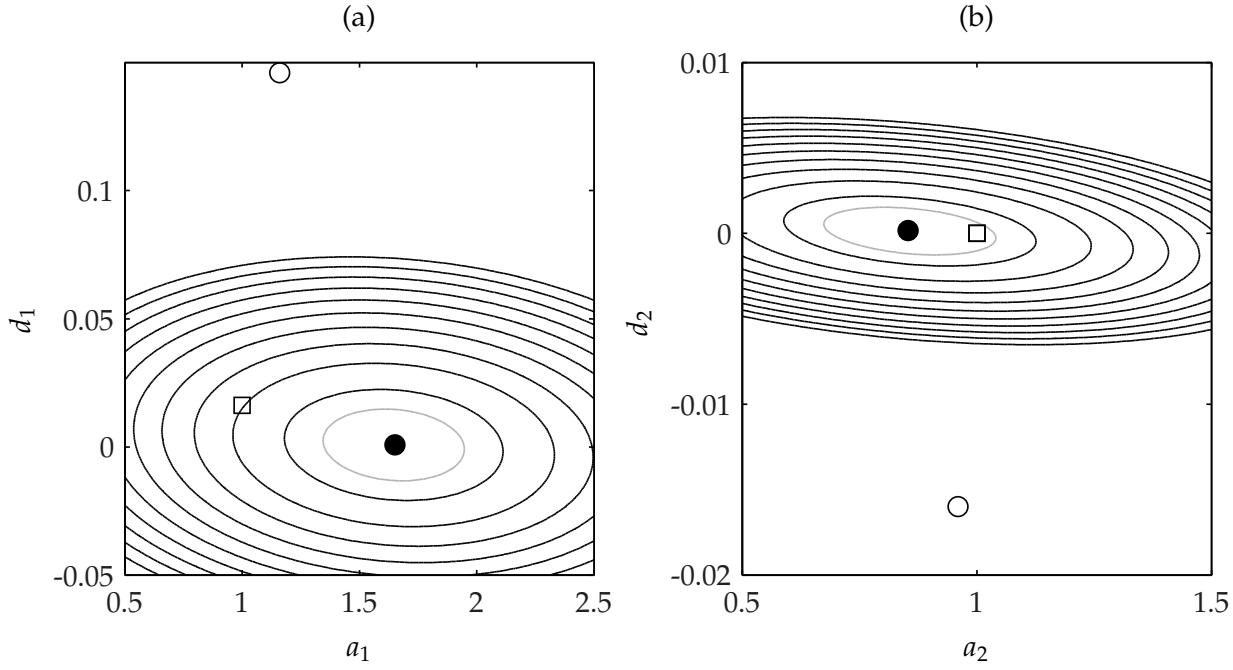

Figure C.1: Calculation of empirical constants for third-order moments. Contours give explained variance as calculated by Eq. 5.4.6. (a) $\overline{w'^2\theta'}$, (b) $\overline{w'\theta'^2}$. Contour interval is $\Delta = 0.1$ for the black contours; gray contour gives $\sigma_f^2 = 0.95$. Open circles, Gryanik and Hartmann (2002); open squares, Zilitinkevich et al. (1999); closed circles, Case B2.

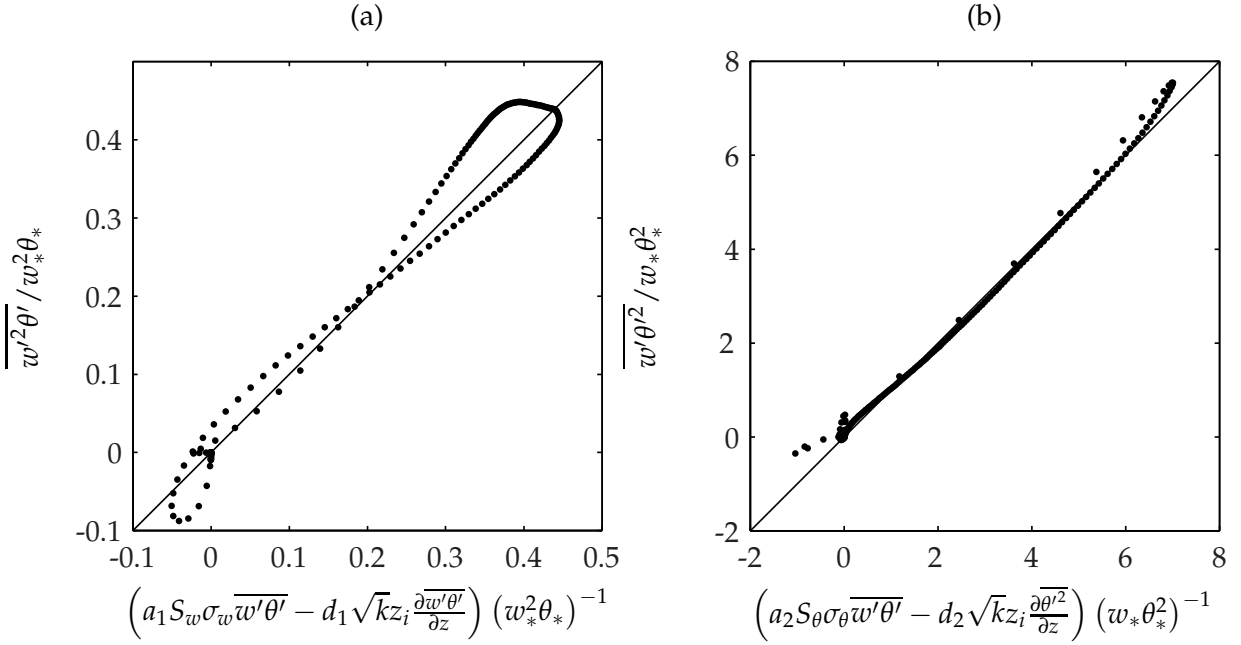

Figure C.2: Third-order moments: (a) $\overline{w'^2\theta'}$, $a_1 = 1.44$, $d_1 = -1.17 \times 10^{-3}$; (b) $\overline{w'\theta'^2}$, $a_2 = 0.894$, $d_2 = 1.67 \times 10^{-4}$. Dots are Case B2 data and the line is unity.

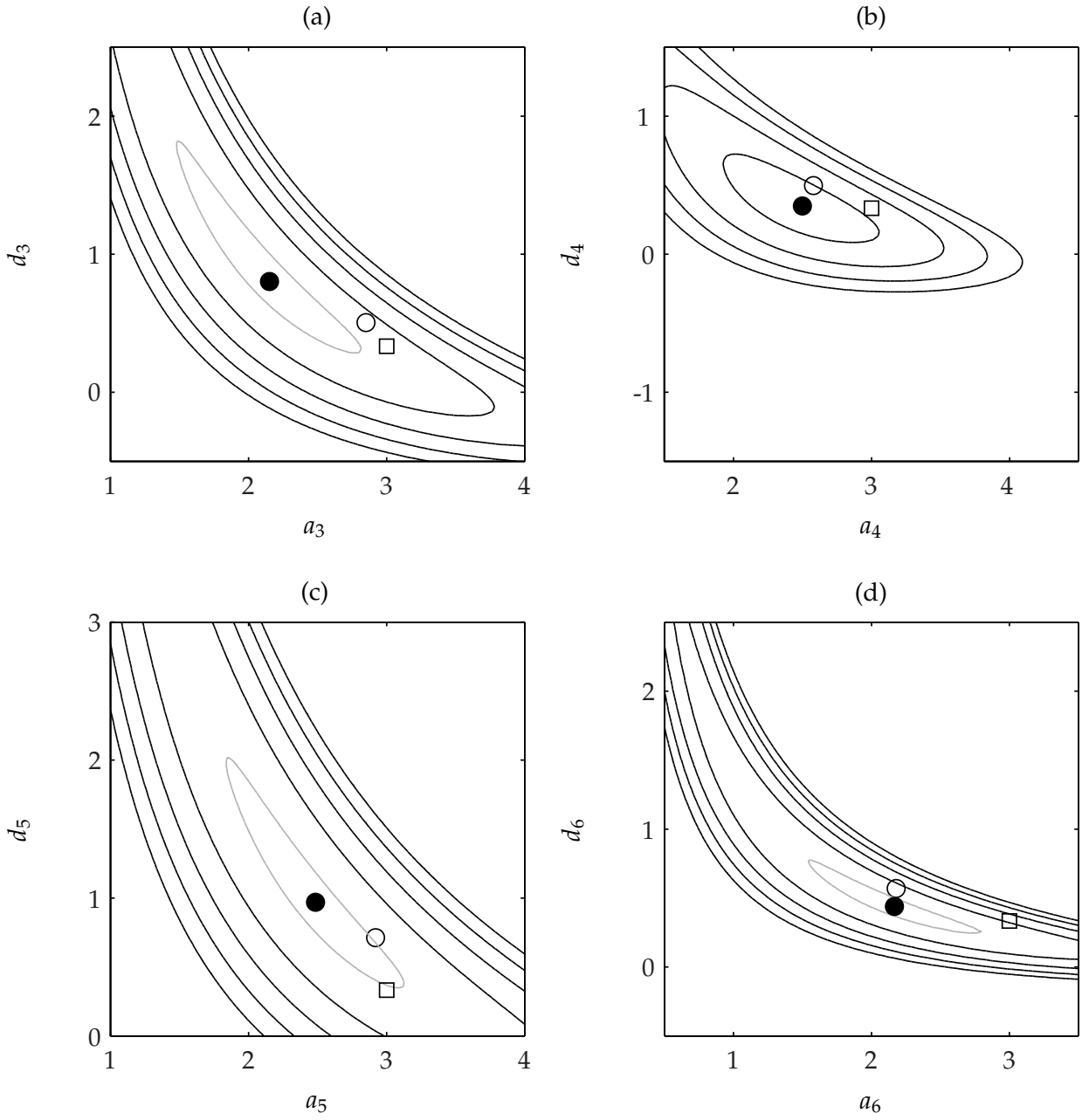

Figure C.3: Calculation of empirical constants for fourth-order moments. Contours give explained variance as calculated by Eq. 5.4.6. (a) $\overline{w'^4}$, (b) $\overline{\theta'^4}$, (c) $\overline{w'^3\theta'}$, (d) $\overline{w'\theta'^3}$. Contour interval is $\Delta = 0.05$ for the black contours (minimum of $\sigma_f^2 = 0.8$); gray contour gives $\sigma_f^2 = 0.99$. Open circles, Gryanik and Hartmann (2002); open squares, Zilitinkevich et al. (1999); closed circles, Case B2.

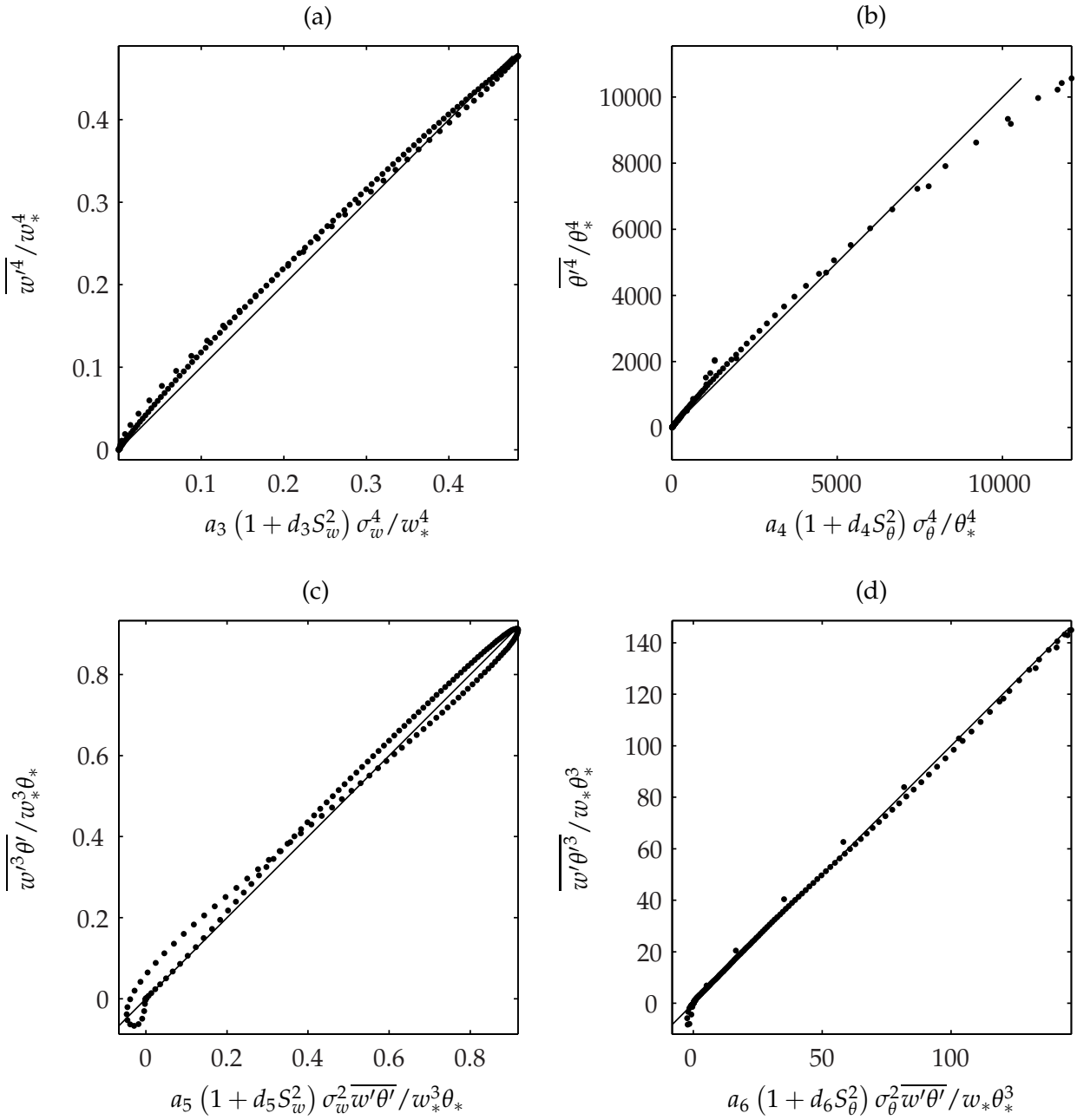

Figure C.4: Fourth-order moments: (a) $\overline{w'^4}$, $a_3 = 2.36$, $d_3 = 0.742$, $\sigma_f^2 = 0.998$; (b) $\overline{\theta'^4}$ $a_4 = 2.95$, $d_4 = -7.58 \times 10^{-2}$, $\sigma_f^2 = 0.986$; (c) $\overline{w'^3\theta'}$, $a_5 = 2.42$, $d_5 = 0.879$, $\sigma_f^2 = 0.996$; (d) $\overline{w'^3\theta'^2}$, $a_6 = 2.11$, $d_6 = 0.470$, $\sigma_f^2 = 0.995$. Dots are Case B2 data and the line is unity.